Integrative methods for mapping brain connectivity



Silei Zhu

New College

University of Oxford

A thesis submitted for the degree of

Doctor of Philosophy

Hilary 2025

Acknowledgements

This thesis and my DPhil work have been completed with the great support, help and guidance from my amazing supervisors, colleagues, friends and family.

First, I am incredibly grateful for my supervisors, Professor Karla Miller and Dr. Amy Howard. It has been a great honour working with both of you, who definitely have made this research journey truly amazing and enjoyable. Your professionalism and enthusiasm for science have always inspired me since day one and when going forward. I still remember the first time I was introduced to BigMac - I was so fascinated by such beautiful work, and that's how my PhD journey began. I really appreciated the guidance you gave me to help me explore my curiosity and great flexibility in choosing the research directions I would like to pursue. When I first joined FMRIB, I was shy and lacked confidence and thank you for always being supportive and giving me time and a platform to learn and grow. Every time I struggled, you always had faith in me and encouraged me with kind words. Thank you for being not only my role models in research but also my mentors in life, and someone I really want to become.

A huge thanks go to WIN's Physics and Analysis groups. This work is a collaborative effort, with help from many people. Professor Saad Jbabdi offered invaluable advice and guidance on the projects. Istvan Huszar made great contributions to the MRI and histology registration. Nicola Dinsdale provided super useful advice on deep learning methods. Thanks to Steve Smith and Fidel Alfaro Almagro for their work on the UK BioBank. A special thanks to everyone who contributed to acquiring and processing the BigMac dataset. In addition, Wenchuan Wu, Rezvan Farahibozorg, Gwenaelle Douaud, Rick Lange, Ziyu Li, Michiel Cottaar and many others from our group provided advice and insights on diffusion MRI, functional MRI and anatomy which have been incredibly helpful. I also feel fortunate to have had the support of friends throughout my PhD journey. A big thank you to Hanjun, James, Christiana, Ben, Xi, and all the wonderful people within and outside of the WIN physics group.

I am super grateful for my family for being there for me as always. Huge thanks to my parents for always letting me choose whatever I love and passionate about. You have given me full

flexibility and support to make my own decisions while giving me chance to learn. A special thanks to my dear sister, Sherry, for being by my side since the day we were born. Even though you don't understand MRI and the brain, and I don't get finance, we never get tired of sharing every little detail about our work and lives with each other. Thank you for always being my biggest support. Your love and encouragement make me brave enough to step forward, knowing you will always be there for me.

Last but not least, to my life partner Gus, it has been a journey navigating a long-distance relationship for four years together with an 8-hour time difference and 9,000 km between us. Thank you for making sacrifices and always being my mental support. Every time I struggled, felt upset or got overwhelmed, you always knew how to make me feel better. Your thoughtfulness, optimism and sense of humour have helped me get through many tough times. I have learned so much from you, and it's made me a better person.

1

Motivation

Table of Contents

1.1 Thesis outline 6

Foreword

As a dynamic and intricate network, the brain comprises billions of neurons working in synchrony to support complex functions. White matter, accounting for approximately half of the brain volume (Ardesch et al., 2022), serves as communication highways, facilitating the transmission of neural signals across regions, and works in concert with grey matter, enabling the sophisticated functions that characterise human thought and behaviour. Brain connectivity can be measured across multiple scales, from the microscale of individual neurons to the macroscale of the entire brain. Advances in imaging techniques have provided new ways to map these connections, deepening our understanding of their structural architecture and functional roles.

Magnetic resonance imaging (MRI) has become a powerful non-invasive tool for investigating brain structure and function. Diffusion MRI (dMRI), specifically, enables the mapping of white matter pathways by measuring the diffusion of water molecules within tissue, thereby providing insights into brain connectivity. However, this technique relies on computational models that incorporate strong assumptions, and its spatial resolution is limited to millimetre-scale, posing

challenges for resolving fibre architecture at the micrometre level. While diffusion MRI allows for the estimation of fibre orientations and the reconstruction of white matter tracts, its specificity and accuracy remain limited. Advancing our understanding of diffusion MRI signals through data-driven approaches could significantly enhance the precision of in-vivo brain connectivity mapping, with broad implications for both neuroscience research and clinical applications, including surgical guidance.

Microscopy is widely used to investigate brain microstructure at the micrometre level or sub-micrometre level, providing highly detailed insights into neuronal and axonal architecture. Techniques such as light microscopy have applications ranging from fundamental neuroanatomical studies to the investigation of disease mechanisms. However, microscopy is typically restricted to ex-vivo or postmortem tissue sections and requires extensive processing, making whole-brain mapping time-consuming and often impractical, particularly in larger primates or human brains.

Integrating the complementary strengths of MRI and microscopy holds the potential to enhance our ability to map brain connectivity with greater precision and accuracy. This raises two critical questions we aim to address in this thesis: 1) Can MRI and microscopy be effectively combined to provide a more comprehensive understanding of neural architecture? 2) How can insights obtained from microscopy be translated to in-vivo brains where microscopy is not available?

1.1 Thesis outline

This thesis investigates how to integrate the advantages of microscopy and MRI to improve brain connectivity mapping. It includes a background chapter (**Chapter 2**) followed by four research chapters (**Chapter 3 – Chapter 6**) and a future direction chapter (**Chapter 7**), an overview of which is provided below.

In **Chapter 3**, we develop a data-fusion method to combine diffusion MRI and microscopy in a way that can maximise the unique benefits of each modality (the high resolution of microscopy and the 3D information from diffusion MRI), while overcoming their limitations (the 2D nature

of microscopy and the low resolution of MRI). Diffusion MRI and microscopy are combined in a joint model where microscopy provides the 2D fibre orientation within the microscopy plane, while diffusion MRI provides through-plane orientation information, creating "hybrid MRI-microscopy" fibre orientations that are 3D and at high spatial resolution. The method is applied to data from the BigMac dataset, where high quality postmortem diffusion MRI and co-registered multi-contrast microscopy (polarised light imaging, myelin and Nissl stains) are available. Our novel approach enables "hybrid MRI-microscopy" fibre tracking across the whole brain, with higher accuracy than MRI, and at high microscopy resolutions (~1000s times higher than the mm-scale MRI), unattainable through the microscopy or MRI alone. Crucially, our microscopy-informed fibre tracking preserves the advantages of microscopy including detailing intricate patterns of axonal organisation and improving tracking accuracy in the cortical mantle, as demonstrated in the Chapter 3. Further, we show that the hybrid method is generalisable and compatible with multiple microscopy contrasts. This means that it can be readily applied to both existing and forthcoming datasets, including both animal models and human brains. Together, the hybrid MRI-microscopy method can provide important neuroanatomical insights, comprehensive maps of the brain connectome and play a vital role in advancing fundamental brain connectivity investigations across species.

In **Chapter 4**, we go beyond the hybrid MRI-microscopy approach and aim to transfer its benefits to datasets that have in-vivo MRI but without microscopy. To achieve this, we design a deep learning framework to predict fibre orientation from MRI, negating the need for a biophysical model typically used in diffusion MRI fibre orientation estimation. The network is trained using hybrid orientation as ground truth, enabling it to learn microscopy-informed fibre orientations and enhance fibre accuracy. Crucially, we used domain adaptation to train the network on both high-quality postmortem MRI and in-vivo MRI from the same brain, ensuring its applicability to both postmortem MRI and in-vivo MRI data. This work extends microscopy-derived knowledge beyond datasets where MRI and microscopy are acquired from the same brain to typical in-vivo MRI in another macaque brain. Our approach preserves the strengths of microscopy resolving fine-scale axonal organisation and improving fibre tracking while ensuring broad applicability across dMRI datasets. Notably, the network is designed to only require single-shell data and remains agnostic to acquisition parameters (such as resolution or the

number of gradient directions), allowing it to be applied to diverse existing datasets with a range of different acquisition protocols. Collectively, we present an approach leveraging hybrid MRI-microscopy methods to refine brain connectivity, integrating microscopy information into non-invasive imaging.

Chapter 5 demonstrates how our microscopy-informed network can be adapted for and applied to in-vivo human dMRI. Our aim was to investigate whether the microscopy-like fibre orientation estimated by the network can address the limitations of conventional methods. To achieve this, we implemented an unsupervised domain adaptation method allowing the transfer of knowledge from a labelled macaque domain to an unlabelled human domain. It reduces the gap between the two domains by aligning their feature distributions and generalising across species. We first demonstrate how the model can predict microscopy-informed fibre orientations in single-shell human dMRI data. We show that our fibre orientations can be used to reconstruct known major white matter tracts and superficial white matter tracts within the brain that follow neuroanatomical expectations. Interestingly, our network tractography is different from tract reconstruction using the more conventional diffusion model-based method. This presents a challenge as it is difficult to know which is more neuroanatomically correct. Here we investigate this using orthogonal information from resting-state functional MRI (rsfMRI) which can also tell us about tract terminations if we assume cortices that are functionally connected share similar axonal connectivity. We demonstrate that the network tractography enhances the structural-functional alignment and thus better captures the tract termination. The precise tract termination varies across individuals and an accurate mapping of termination can become a valuable individual biomarker. Our network shows promise for both clinical diagnostics and research into brain networks.

In **Chapter 6,** we investigate whether our network is capable of achieving super-resolution. Microscopy provides fibre orientations at high spatial resolution; therefore, a network trained on microscopy data at resolutions exceeding that of MRI has the potential to super-resolve the MRI-derived fibre orientations. We adapted the network introduced in **Chapter 5**. Instead of generating a single FOD per voxel, the modified network produces a 2x2x2 spatially resolved grid of FODs per voxel, effectively doubling the resolution of the input MRI. This is achieved by

integrating fibre directional information from dMRI with the high-resolution spatial details from structural MRI while training the network to approximate microscopy-informed fibre orientations at high resolution. The network was trained using data from BigMac and applied to unseen MRI data from both human and macaque brains. Our results demonstrate super-resolved FODs across in-vivo and postmortem data. The network's ability to enhance fibre orientation resolution without requiring microscopy data makes it a valuable tool, as super-resolution facilitates more precise tract localisation and improves the mapping of brain connectivity.

Chapter 7 concludes the thesis with a summary and an outline of future research.

2

Background

Table of Contents

2.1 Brain connectivity *12*
2.1.1 Brain macrostructures and microstructures 12
2.1.2 White matter and brain connectivity 15
2.2 Invasive methods for studying brain connectivity *17*
2.2.1 White matter dissection 18
2.2.2 Polarised light imaging 19
2.2.3 Histological staining 22
2.2.4 Tracer 23
2.2.5 Electron microscopy 25
2.3. Diffusion MRI *25*
2.3.1 Diffusion MRI basics 25
2.3.2 Diffusion tensor imaging 31
2.3.3 Constrained spherical deconvolution 33
2.3.4 Ball and Stick model 34
2.3.5 Tractography 36
2.3.6 Postmortem diffusion MRI 37
2.3.7 Challenges of tractography 38
2.4 Combining MRI and microscopy *41*
2.4.1 Registration 42
2.4.2 Using histology for the dMRI validation 42

2.4.3 Joint analysis of MRI and microscopy 44
2.5 Deep learning 44
2.5.1 Introduction of deep learning 44
2.5.2 Using deep learning for fibre orientation estimation and tractography 47

Foreword

This chapter provides essential background for the thesis. First, it presents an overview of brain connectivity, including neuronal connections at the microscale level and white matter tracts at the macroscale level. Second, it reviews the development of brain connectivity mapping technologies, focusing on invasive approaches. Third, we introduce diffusion magnetic resonance imaging (dMRI), a non-invasive method widely utilised in clinical diagnostics, including its key concepts, physics basis and fibre tracking techniques. Fourth, we highlight how these technologies complement one another and, through the integration and validation of multiple modalities, collectively deepen our understanding of the brain connectome. Finally, we discuss the potential of deep learning techniques to improve the brain connectome estimation.

2.1 Brain connectivity

Brain connectivity refers to the network linking different brain regions, forming a “wiring diagram” that underlies cognition and neuropsychological processes. The complete and point-to-point connectivity maps are known as the **brain connectome** (Sporns et al., 2005), which can be characterised in terms of functional connectivity, representing brain regions that activate or deactivate in synchrony, or structural connectivity, reflecting brain regions physically connected by white matter tracts. The structural connectome is a key determinant and constraint of the functional connectome (Melozzi et al., 2019). To gain a better understanding of brain function and how it is affected by disruptions in structural connectivity, it is crucial to obtain an accurate and detailed map of the structural connectome.

Mapping the brain structural connectome has become a key topic of research in neuroscience, aiming to characterise the architecture of axonal connections within the brain. The connectome can be measured across various length scales, from the nanoscopic level of synapses to the macroscopic scale of the entire brain. To date, a whole body connectome has been mapped in Caenorhabditis elegans (C. elegans), which has 302 neurons and has been fully reconstructed using electron micrographs of serial sections (White et al., 1986). The mouse brain connectome has been mapped at both the cellular and mesoscale levels through enhanced green fluorescent protein (EGFP) labelling of neurons (Oh et al., 2014). However, the connectome of larger brains, particularly those of non-human primates and humans at the whole-brain level remains poorly characterised due to the immense scale of the data and technological limitations, which will be elaborated in this Chapter. Mapping the entire human brain connectome involves approximately 86 billion neurons and their projections.

2.1.1 Brain macrostructures and microstructures

At the macroscopic level, the brain is comprised of three distinct tissue types: grey matter (GM), white matter (WM), and cerebrospinal fluid (CSF) (Hedges, 2022) (Figure 2.1). Grey matter, primarily found in the cerebral cortex, consists mainly of neural cell bodies and dendrites, while white matter is predominantly composed of axonal fibres and supporting glial cells. The different compositions of these tissues result in distinct appearances, with grey matter appearing darker

due to the higher density of cell bodies, and white matter appearing lighter due to the myelinated axons.

Historically, grey matter has been the focus of most research because of its direct involvement in cognitive functions such as language, memory and decision-making, as well as its fundamental role in processing sensory input and generating motor output. White matter, located beneath the grey matter, initially was regarded as a supporting role for grey matter. Contemporary neuroimaging techniques have revealed the essential role of white matter in transmitting neural signals between different regions of the brain. Comprising approximately half of the total brain volume, white matter is crucial for efficient neural communication and overall brain function emerging as a key focus in neuroscience research.

Neurons

Neurons, the fundamental functional units of the brain, were first described at the microscopic level by the pioneering neurophysiologist Santiago Ramón y Cajal (Ramón y Cajal, 1995). He delineated the architecture of neurons, consisting of three main components: the cell body, axons, and dendrites (Figure 2.1). Dendrites, with their tree-like branching structure, are responsible for receiving signals from other neurons, while axons are long projections that transmit electrical impulses to distant cells. Axons are surrounded by the myelin sheath, a lipid- and protein-rich layer that insulates the axons. This myelination enables the rapid and efficient transmission of neural signals by forming tightly packed membranes, allowing signals to travel up to 100 times faster than in unmyelinated axons, while also reducing metabolic energy consumption. The cell body, or soma, which contains the nucleus and organelles, is responsible for metabolic functions, including protein synthesis and other cellular processes. Communication between neurons occurs at the synapse, the small gap between two neurons (or between a neuron and a target cell such as a muscle cell). Neurotransmitters are released from the presynaptic neuron and bind to receptors on the dendrites of the postsynaptic neuron. The signal is processed within the cell body. Signal transmission within neurons occurs through electrical impulses known as action potentials.

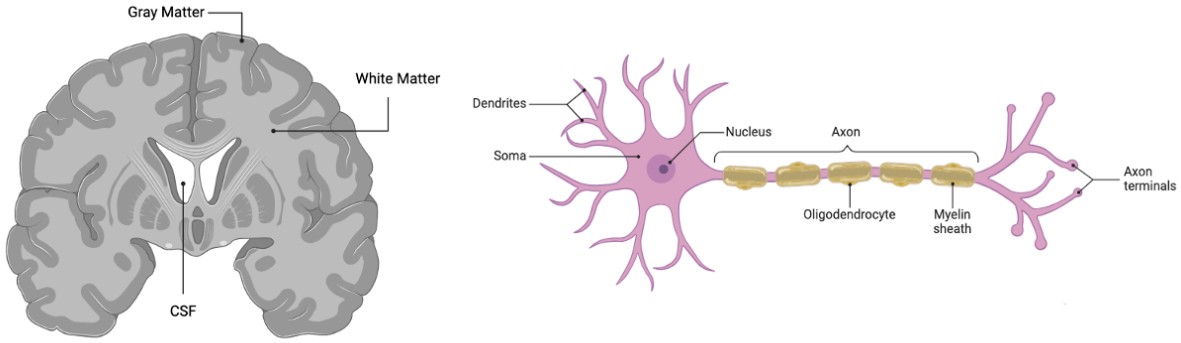


Figure 2.1: Left: Macroscopic brain structures, including grey matter, white matter and cerebrospinal fluid (CSF). Right: A neuron, the basic cellular unit of the brain, depicting its key structures: dendrites, soma (cell body) and myelinated axon.

Grey matter

Grey matter is found in the cerebral cortex as well as in subcortical structures, including the basal ganglia and thalamus. Connections between subcortical nuclei and cortical regions play a crucial role in relaying sensory and motor information and supporting higher-order brain functions like cognition and emotion. The cerebral cortex is folded into gyri (ridges) and sulci (grooves) through a process known as gyrification during brain development (Chi et al., 1977). This folding increases the cortical surface area relative to volume, which enables more neurons without proportional increases in brain volume. Additionally, gyrification reduces the distance between brain areas, making communication more efficient. In this Chapter and Chapter 3, we will consider how the gyrification of the brain leads to specific challenges in mapping the structural connectome with MRI.

Different cortical regions are specialised for distinct functions. For example, the primary motor cortex, located in the precentral gyrus, is responsible for the motor control of various body parts (Figure 2.2). The motor cortex exhibits a “homunculus” pattern (Latin: “little person”), a topographical representation mapping the motor control to different body regions, including the face, upper limbs, and lower limbs (Penfield and Boldrey, 1937). This organisation of the motor cortex serves as a well-defined model for evaluating tractography methods, as demonstrated in Chapter 3 and 4.

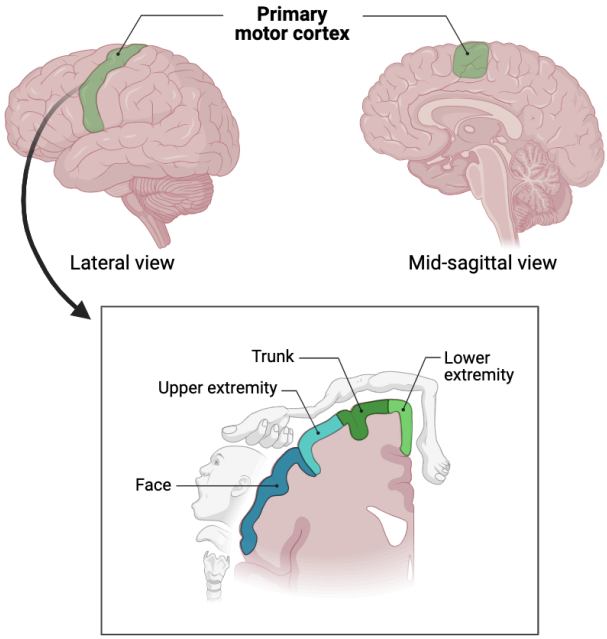


Figure 2.2: The primary motor cortex, located in the precentral gyrus, exhibits a homunculus pattern. Different regions of the motor cortex control movement in specific body parts, arranged in a medial-to-lateral order: the lower extremities (eg., toes), followed by the trunk, upper extremities (eg., arm, fingers), and face. The figure is adapted from Purves et al. (2019) *Neuroscience*(Purves et al., 2019).

2.1.2 White matter and brain connectivity

White matter consists of millions of axons organised into fibre bundles, or "tracts", facilitating neural communication (Miller et al., 1980). These tracts connect different regions of grey matter and enable the rapid transmission of neural signals between them. In addition to neurons, glia cells, including microglia and oligodendrocytes, provide critical support to neurons in the white matter. Among these, oligodendrocytes are responsible for generating myelin to ensheathe axons.

White matter tracts are essential for brain function, playing a crucial role in cognition and behaviours. For example, in order to coordinate limb movements, the primary motor cortex sends signals to peripheral nerves along the corticospinal tract, which travels through the internal capsule and along the spinal cord (Morecraft et al., 2002). Disruptions to white matter integrity, such as myelin degradation and axonal damage, are linked to various neuropathologies including cognitive decline (Filley and Fields, 2016), neurodegenerative diseases (Saini et al., 2022) and multiple sclerosis (Van Waesberghe et al., 1999). Additionally, white matter undergoes structural

changes due to aging (Rojkova et al., 2016), brain development (Knickmeyer et al., 2008) and learning (Scholz et al., 2009).

Classification

White matter tracts can be categorised into projection, commissural and association fibres based on the types of regions they connect (Figure 2.3). Projection fibres establish connections between the cortex and lower brain regions or the spinal cord, such as the corticospinal tract (Konstantopoulos and Giakoumettis, 2023). Association fibres connect cortical areas within the same hemisphere, including short association fibres (or "U" fibres) linking adjacent gyri, and long association fibres connecting distant regions, such as superior longitudinal fasciculus. Commissural fibres interconnect corresponding regions across hemispheres, with the corpus callosum being the largest commissural fibre.

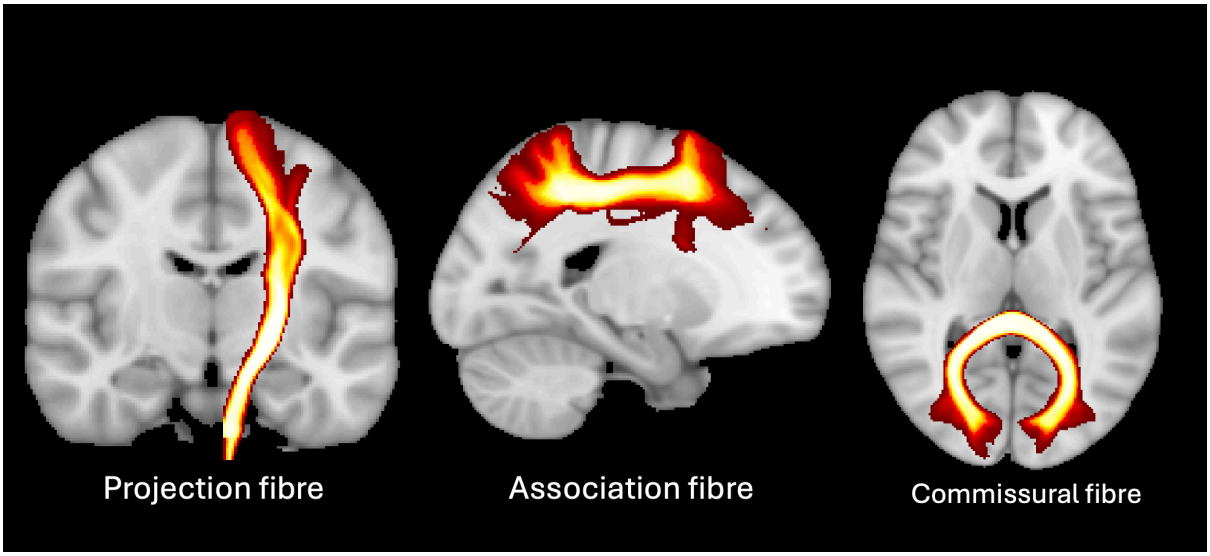


Figure 2.3: The categorisation of white matter. Projection fibre (corticospinal tract), association fibre (superior longitudinal fasciculus 1), commissural fibre (forceps major).

Beyond the major classifications of white matter, the superficial white matter (SWM) tracts are a subset of association fibres that connect adjacent gyri and are located in the outermost layer of white matter, just beneath the cortical surface. They are also known as U-fibres. Due to their small size, high curvature, and proximity to the grey matter, accurately tracking SWM tracts presents significant challenges and thus compared to the deep white matter, SWM is less characterised. The SWM undergoes late maturation during neurodevelopment and is susceptible

to demyelination processes associated with aging (Wu et al., 2014a). In addition, disruptions to SWM integrity are implicated in various neurological and neurodegenerative disorders, including autism spectrum disorder, epilepsy, and Alzheimer's disease(Phillips et al., 2016).

White matter across species

Brain connectivity varies significantly across species in terms of size, complexity, and cortical folding. For example, neuronal count varies by three orders of magnitude between the human brain (86 billion neurons) and mouse brains (70 million), with macaques in between (6 billion) (Friedrich et al., 2021). Despite these differences, many white matter tracts are conserved among higher primates such as cingulum and uncinate fasciculus (Thiebaut De Schotten et al., 2012). Notable variations in the branching patterns of these tracts reflect evolutionary adaptations related to specific brain functions, meaning that white matter anatomy reflects both shared neural architecture and evolutionary specialisation (Mars et al., 2018, 2014). Importantly, much of our understanding of brain connectivity is derived from invasive techniques, such as anatomical tracers and genetic modifications that can only be used in animal models like mice and macaques. Combined with non-invasive techniques like MRI in humans, these methods have significantly enhanced our understanding of the brain connectome (Van Essen et al., 2019). A key challenge is linking our understanding of brain connectivity across species, which requires approaches that integrate these tools.

2.2 Invasive methods for studying brain connectivity

Over recent decades, progress in neural imaging techniques has greatly advanced our understanding of fibre architecture and brain connectivity. Sections 2.2 and 2.3 review various methods used to study brain connectivity across scales, ranging from single neurons to the entire brain, spanning the microscale to the macroscale and incorporating both invasive and non-invasive techniques (Figure 2.4).

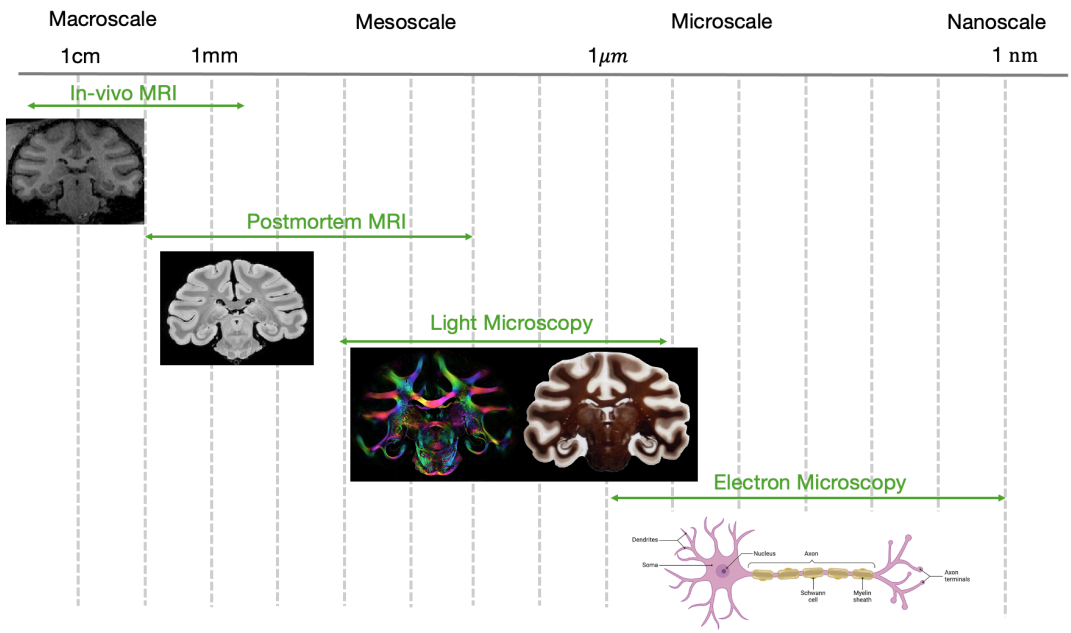


Figure 2.4: Brain connectivity can be assessed at various scales using different technologies. In-vivo MRI provides macroscale brain connectivity, capturing whole-brain networks and white matter tracts. Postmortem MRI offers higher resolution, enabling the study of smaller-scale fibre architecture. Light microscopy provides detailed myeloarchitecture and cytoarchitecture at the microscale, while electron microscopy achieves nanoscale resolution, allowing analysis at the single-cell level of neurons.

2.2.1 White matter dissection

The earliest advances in white matter anatomy were based on direct observational techniques. In the early 19th century, Johann Christian Reil first mapped white matter tracts through dissections, identifying connections between cortical regions ("Das Balken-System oder die Hirnschenkel-Organisation im großen Gehirn.," 1809). This work was followed by Karl Friedrich Burdach, who introduced a standard nomenclature for these tracts, including terms still in use today, such as the arcuate fasciculus and uncinate fasciculus (Meyer, 1970). In 1935, Klingler developed a dissection technique involving the freezing of fixed human brains, which facilitated the separation of nerve fibres through ice crystal formation (Klingler, 1935). This method improved the peeling process and allowed for three-dimensional visualisation of major white matter tracts, forming the foundation for much of our current understanding of white matter architecture. Even today, dissections are an essential tool for validating non-invasive methods, such as diffusion MRI tractography (Wysiadecki et al., 2019). However, white matter dissection requires substantial anatomical expertise, is time-consuming, and typically focuses on individual fibre tracts.

2.2.2 Polarised light imaging

Light microscopy is a powerful technique for investigating biological tissue at both millimetre and micrometre scales, commonly using either brightfield or fluorescence methods (Thorn, 2016). In brightfield light microscopy, contrast is generated through the measurement of light absorption and scattering within the tissue. In contrast, fluorescence microscopy utilises fluorophores that absorb light at one wavelength and emit it at a longer wavelength, improving both specificity and contrast. As it is beyond the scope of this thesis to review all the different microscopy techniques, below we detail one specific brightfield microscopy technique, Polarised Light Imaging (PLI), that is used extensively in this thesis.

PLI visualises structures by leveraging birefringence (or double refraction). Birefringence is an optical property in which light splits into two distinct rays refracting at different angles due to variations in the refractive indices along different axes (Figure 2.5 Left). The lipid bilayer of the axonal myelin membrane exhibits birefringence, with the optical axis aligning with the fibre orientation (Axer, 2011; Axer et al., 2001, 2011a). As described in detail below, PLI involves transmitting polarised light through the tissue, measuring changes in the light's polarisation state and enabling quantification of birefringence. Therefore, PLI specifically allows for the orientation estimation of myelinated fibres without the need for staining.

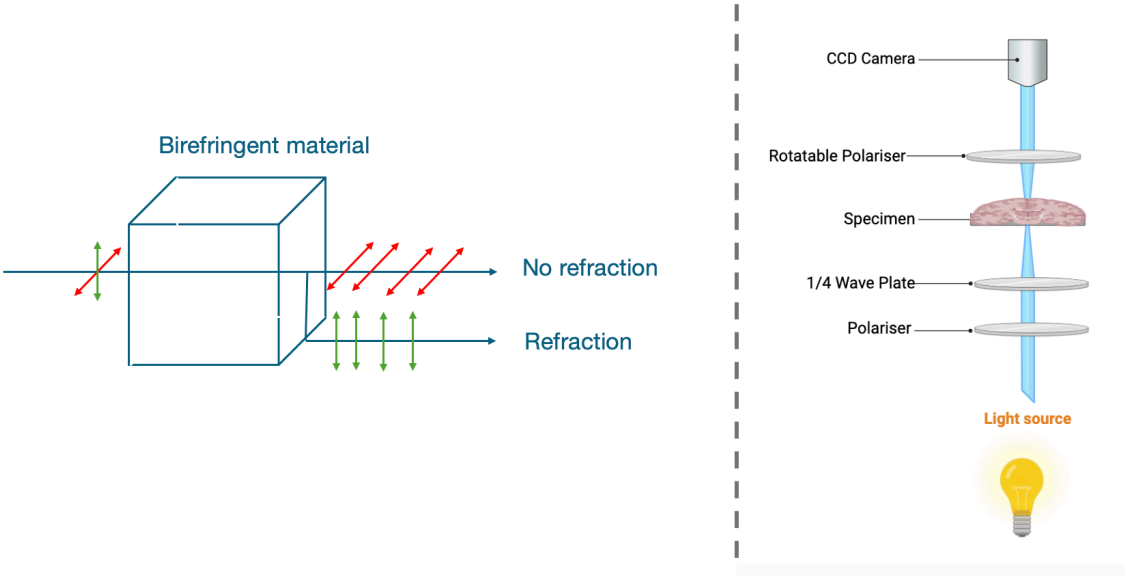


Figure 2.5: Left: Birefringence (double refraction) mechanism. When light passes through a birefringent material, it splits into two rays that travel at different speeds and refractive angles due to the material's anisotropic internal structure. **Right: PLI setup**. Light from the source passes through a linear polariser and a quarter-wave plate. The brain specimen induces a phase shift, and light intensity is measured at various rotation angles using a rotatable polariser.

The PLI setup can be adapted from confocal microscopy, starting with an LED light source, which emits unpolarised light (Figure 2.5 Right). A linear polariser is then used to convert the unpolarised light into polarised light which subsequently passes through a quarter-wave plate (retarder) and is converted into circularly polarised light. When this circularly polarised light interacts with the myelin lipids, a phase shift occurs, resulting in the light becoming elliptically polarised. After passing through the sample, it reaches a rotatable polariser (or analyser). As the analyser rotates, the intensity of the transmitted light varies sinusoidally with respect to the rotation angles. Finally, a camera is positioned to capture the transmitted light intensity. Multiple images are acquired for each sample as the rotatable polariser is rotated at a 10°~20° angular resolution generating a sinusoidal measurement of light intensity. When the polariser is aligned with the primary axis of the elliptically polarised light, it produces the maximum intensity value, and when it is aligned with the minor axis of the ellipse, it produces the minimum intensity. By analysing the phase of this sinusoidal variation, the in-plane orientation of the underlying fibres can be determined (Axer, 2011).

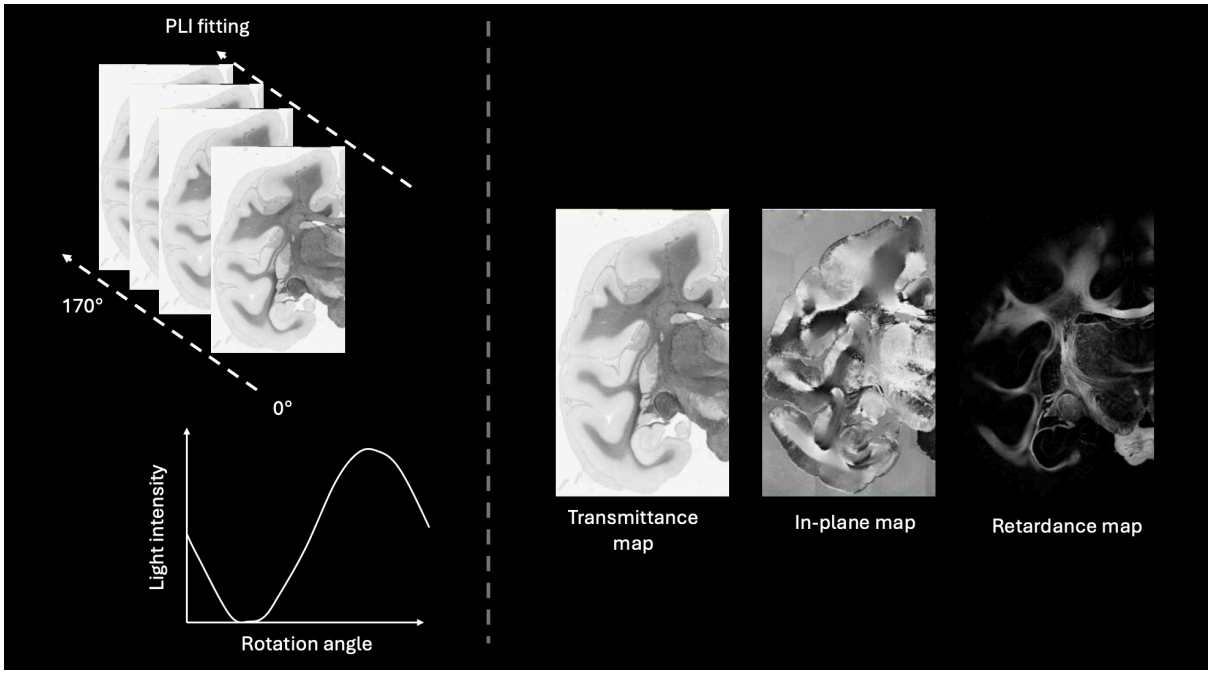


Figure 2.6: Left: PLI intensity is measured at different rotation angles using a rotatable polariser. The resulting intensity variation can be fitted to a sinusoid function. Right: Derived PLI parameter maps, including the transmittance map (intensity), in-plane map (phase of the sinusoid function) and retardance map (dependent on both myelin content and inclination angle).

For each microscopy pixel, the intensity (I) can be characterised by the following equation:

$$I = \frac{I_0}{2} \cdot [1 + \sin(2\rho - 2\varphi) \cdot sin\delta]$$

The relationship between the rotation angles (ρ) and measured light intensity (I) at each pixel can be fitted with a sinusoid function, from which key parameters are extracted (Figure 2.6). Here, I_0 is the light transmittance denoting the light intensity affected by local extinction due to absorption and scattering in brain tissues, apart from birefringence. The phase of the sinusoidal function encodes the in-plane fibre orientation φ (i.e. the orientation in the xy plane)(Axer et al., 2011a). The ellipticity of the polarisation determines the retardation $|\sin\delta|$ which reflects the normalised amplitudes of the light intensity (I/I_0).

Retardance is affected by both the myelin content and the orientation angle relative to the imaging plane (i.e., the inclination angle, α):

$$\delta \approx 2\pi \cdot \frac{d \cdot \Delta n}{\lambda} \cdot \cos^2 \alpha$$

Where λ is the wavelength of light, d is the thickness of the tissue section, and Δn represents the birefringence of myelin. A limitation of this setup is the ambiguity in determining d, Δn and the sign of the inclination angle. The derived inclination angle ranges from 0 to 90 degrees without a specified sign. To address the ambiguity of the sign, a tilting stage was introduced. By slightly tilting the brain section, fibre architecture can be imaged stereoscopically from different angles allowing for a more accurate determination of the inclination angle. The tilting stage enables a more precise quantification of fibre orientation in three dimensional space(Axer et al., 2011b).

With PLI, fibre orientation is characterised as a vector field, with each orientation represented by a vector in the fibre orientation map (FOM). Given an accurate estimation of the inclination angle α, a reliable 3D reconstruction of fibre orientation can be obtained, allowing for tractography of continuous fibre pathways and the mapping of fibre tracts(Axer et al., 2011b). However, the acquisition of 3D PLI data using the tilting stage approach is typically constrained by the limited field of view, lengthy acquisition times and the sophisticated experimental setup. As a practical alternative, 2D PLI enables straightforward measurement of in-plane fibre orientations over a larger field of view.

2.2.3 Histological staining

Histology staining is a technique to enhance the visualisation of cellular structures within tissue sections under a microscope. It plays an essential role in both research, for studying anatomical structures, and clinical practice, for diagnosing disease in excised tissue samples. A range of dyes is available to highlight distinct tissue components. For example, Camillo Golgi pioneered a silver-staining technique, known as the Golgi stain, which selectively binds to neuronal cell bodies and dendrites. This method was crucial in enabling Santiago Ramon y Cajal to first delineate the intricate architecture of neurons in 1906 (Glickstein, 2006). Alternative to chemical staining, immunostaining techniques can specifically target proteins of interest such as MAP2, which is primarily expressed in the dendrites (Soltani et al., 2005).

This thesis focuses on two types of histology techniques. The first type of technique, myeloarchitecture staining, uses compounds that bind to the myelin sheath and axons, enhancing the visualisation of myeloarchitecture and enabling the identification of structural alterations such as demyelination during pathological processes (Garman, 2011). A commonly used myeloarchitecture staining is the Gallyas silver stain. The second type of histological staining technique is cytoarchitecture staining. Cresyl violet is utilised to stain Nissl bodies—granular structures within neurons, primarily associated with the rough endoplasmic reticulum and ribosomes—enabling clear visualisation of neuronal cell bodies (Kádár et al., 2009).

Structure tensor analysis

Structure tensor analysis is a method of analysing histological images that enables the extraction of local orientations, intensity and anisotropy metrics. It is commonly used in histology to assess the organisation of neural fibres within tissue sections. The structure tensor is a matrix that quantifies the spatial gradient of image intensities. The gradient represents the rate of intensity changes, capturing information about the direction and magnitude of intensity variations in the image. In a 2D image I (x,y), the structure tensor at each point (x,y) is expressed as follows:

$$J = \begin{bmatrix} < f_x , f_x > \omega & < f_x , f_y > \omega \\ < f_x , f_y > \omega & < f_y , f_y > \omega \end{bmatrix}$$

where f_x and f_y represent the gradients of the image intensity, calculated as the spatial derivatives with respect to the x and y axes respectively. ω represents the local region over which the structure tensor components are computed. Practically, these spatial derivatives are calculated by convolving the image with a Gaussian kernel with the kernel size defined by σ(Budde and Annese, 2013). The fibre orientation is then determined using the formula:

$$\theta = \frac{1}{2}\arctan\left(2\,\frac{< f_x , f_y > \omega}{< f_y , f_y > \omega - < f_x , f_x > \omega}\right)$$

Structure tensor analysis also provides additional metrics, such as anisotropy and intensity, which are analogous to those derived from diffusion tensor imaging (DTI) in dMRI (Section 2.3.2). By analysing local image regions, it offers detailed and spatially resolved information on fibre orientation and tissue microstructure(Budde and Frank, 2012a).

2.2.4 Tracer

Tracer techniques are widely used for investigating neural connectivity and mapping neuronal circuits. Tracers leverage in-vivo cellular transport to label neuronal projections, enabling the precise mapping of neural pathways and connectivity across the brain. Tract tracers can be classified into two categories: chemical agents, which are passively taken up by axonal fibres and transported along them, and genetically encoded viral tracers, which utilise cellular transport mechanisms for greater directional specificity. These tracers can further be categorised based on

their directionality: anterograde tracers, which move from the cell body to the axon terminals, and retrograde tracers, which travel from the axon terminals back to the cell body(Guo et al., 2022).

Anatomical tracers are injected into a specific brain region of interest in an anaesthetised animal and after several days of recovery, the brain is extracted for histological processing and imaging. The tissue is then sectioned into thin slices for analysis. Tracer signals in consecutive sections are reconstructed to visualise continuous neuronal trajectories or to identify the terminal location of tracer projections within the grey matter (Figure 2.7). Thus, this approach enables precise and accurate mapping of axonal projections and is useful for identifying neural structures that were previously unknown (Markov et al., 2012a). Tracer has been used to validate dMRI tractography, which will be elaborated in Section 2.4.2.

However, tracers are limited to one or a few injection sites per animal and cannot be directly applied to humans, making it challenging to obtain a complete map of whole-brain connectivity. To address this limitation, data from multiple animals are combined to create a more comprehensive map of axonal projections. However, this approach ignores the individual variability in neural connectivity. For example, the Allen Mouse Brain Connectivity Atlas provides a mesoscale connectivity map of the adult mouse brain. With projection signals from 469 injection sites (469 injected brains) to 295 target non-overlapping grey matter regions, a connectivity matrix has been created and made openly available, which details the projection intensity from each injection site to different cortical regions (Oh et al., 2014).

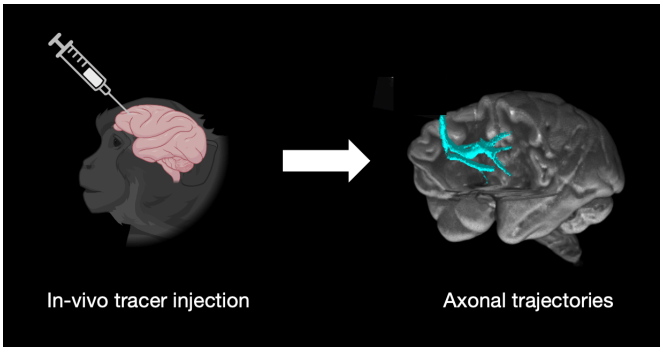


Figure 2.7: Anatomical tracers are injected in-vivo, followed by a recovery period to allow tracer propagation. The brain is then extracted for histological processing, enabling visualisation of axonal trajectories.

2.2.5 Electron microscopy

Electron microscopy (EM) enables imaging at the nanometre scale. Unlike light microscopy, which uses visible light as the illumination source, EM utilises a focused beam of electrons which is accelerated and transmitted through the specimen, allowing for the detection of fine structural details. Since the wavelength of an electron is much shorter than visible light - approximately 100,000 times shorter - EM can visualise cellular structures and molecular complexes at resolutions that light microscopy cannot achieve (Nahirney and Tremblay, 2021).

One of the most notable achievements of electron microscopy is the ability to resolve the structure of synapses (Gray, 1969). For example, recent work successfully mapped a comprehensive synaptic circuitry in the human temporal cortex at nanometre-scale resolution, capturing neurons, glial cells, myelin, and vasculature across all cortical layers(Shapson-Coe et al., 2024). However, due to lengthy acquisition times and large data volumes, their data acquisition was constrained to a small tissue volume of just 1 mm^3.

2.3. Diffusion MRI

Diffusion magnetic resonance imaging (dMRI) is a non-invasive imaging technique enabling the in-vivo study of white matter architecture in the human brain, unlike the very high-resolution but invasive methods described above. Diffusion MRI has become an important tool to investigate brain connectivity and neurological diseases, widely utilised in both clinical and research settings.

2.3.1 Diffusion MRI basics

MR physics

MRI is based on the principles of nuclear magnetic resonance (NMR), which describes the behaviour of hydrogen nuclei (i.e. protons) in the presence of a magnetic field. The MRI process relies on three essential magnetic fields: the main magnetic field (B_0), the transverse magnetic

field (B_1), and the spatial encoding field gradients. In the presence of the main magnetic field B_0, proton spins tend to align with the field. This alignment results in a net magnetisation in the direction of the main magnetic field. When a radiofrequency (RF) pulse (B_1 field) is applied perpendicular to B0, it rotates the magnetisation away from B0 and into the transverse plane, a process called “excitation”. The angle of rotation depends on the strength and duration of the RF pulse, most commonly aiming to achieve a 90-degree rotation (“flip angle”) to place the magnetisation orthogonal to B0 (in the transverse plane). As will be seen later, having the magnetisation fully in the transverse plane generally results in maximal signal (Figure 2.8B). Following the RF pulse, the spins begin to “precess” (rotate) around the main magnetic field direction at an angular frequency proportional to the field strength. This phenomenon is described by the equation below:

$$\omega = \gamma B$$

where ω is the precession frequency, B is the magnetic field strength and γ is the gyromagnetic ratio, a constant specific to the type of nucleus. The magnetisation of a collection of spins can only be detected when they are precessing, as it induces a changing magnetic field, generating an oscillating signal. The component of the magnetisation in the transverse plane contributes to this signal inducing a current in the receiver coil which can be detected. As the spins precess, inhomogeneities in the magnetic field cause slight variations in their precession frequencies. When the components of spins in the transverse plane are oriented in different directions with incoherent precession (“dephasing”), their signal can interfere, reducing the net detected signal. (Figure 2.8C). This dephasing can be reversed by applying a 180-degree RF pulse, which flips the spins, causing them to rephase and allowing spins sharing coherent precession again. The signal (or echo) is then detected (Figure 2.8F). This process, referred to as the spin echo effect, was first discovered by Edwin Hahn in 1950 and remains fundamental to modern MRI technology.

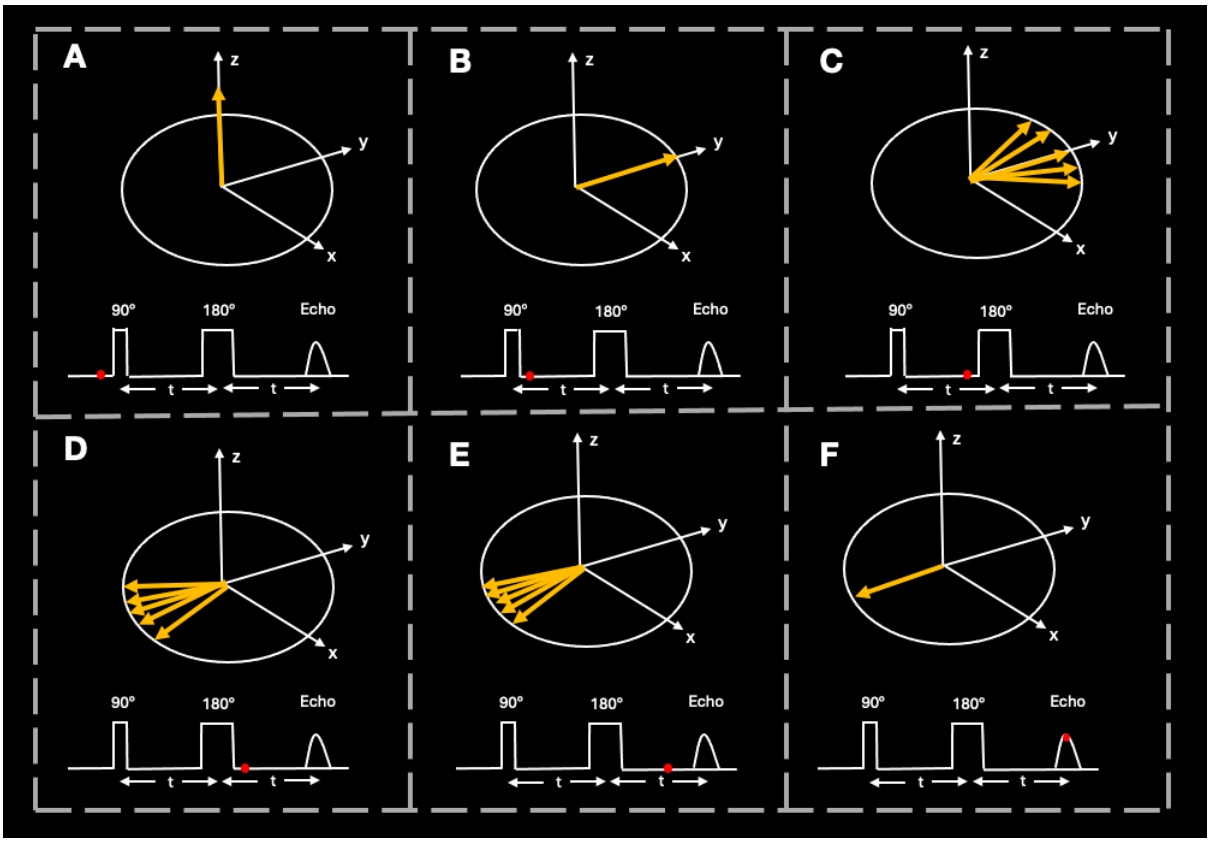


Figure 2.8: Spin echo. A) Proton vectors align with the main magnetic field. B) After applying a 90° RF pulse, proton vectors rotate into the xy-plane and precess in phase. C) Due to magnetic field inhomogeneities, proton vectors diphase at different rates, causing signal decay. D) After a time t, a 180° RF pulse is applied, flipping the proton vectors. E) The proton vectors are rephrasing. F) After a time 2t, all proton vectors are back in phase, maximising the signal in the xy-plane and generating the spin echo, which is measured.

Another important concept in MRI is the spatial encoding gradient, which is a variation in the magnetic field strength that creates a position-dependent variation in the spin precession frequency. This allows signals from different positions to be emitted at different frequencies. As described in Figure 2.9, spins accumulate a phase that depends on their spatial position. Spatial encoding gradient fields are primarily used in MRI to encode spatial position when forming an image, but they are not the focus on this thesis and will not be elaborated. The following paragraphs will explore how gradients are used to encode water diffusion, elucidating fibre structure in the brain.

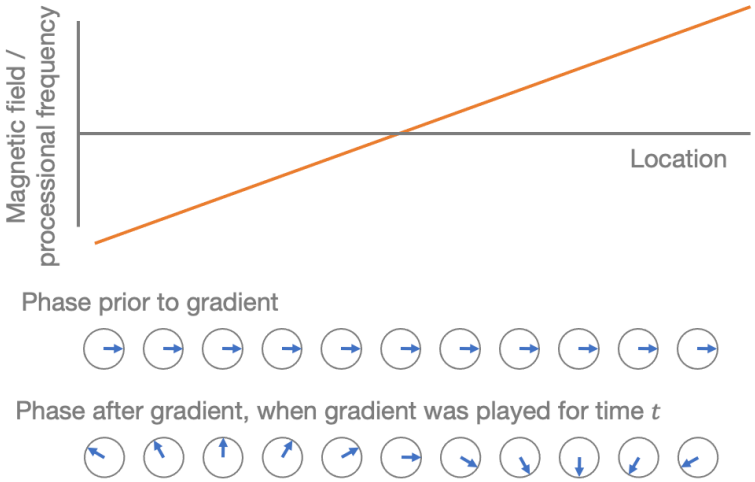


Figure 2.9 MR gradients. The precession frequency of spins depends on the local magnetic field. After gradients are applied, the spins exhibit a phase distribution that varies spatially. Many thanks to Amy Howard for providing the figure(Howard, 2020).

What is diffusion?

The phenomenon of diffusion was first observed by Robert Brown in 1827 when he noticed the erratic motion of pollen grains suspended in water under a microscope. This random motion is now known as Brownian motion (Brown, 1828). Water molecules similarly undergo Brownian motion in three-dimensional space, with each molecule following a distinct and random trajectory influenced by thermal energy. While it is challenging to directly measure the behaviour of an individual water molecule, the collective diffusion behaviour of a large number of water molecules can be effectively characterised. Albert Einstein first introduced the concept of "displacement distribution" (Einstein, 1905), and the squared displacement of water molecules from their initial position r^2 can be described as below:

$$r^2 = 2nDt$$

Where n is the number of dimensions, t indicates the observation time and D represents the self-diffusion coefficient. In unrestricted Brownian motion, water molecules diffuse freely in all

directions, and the ensemble-averaged probability function that describes molecular movement over time follows a Gaussian distribution.

Diffusion-weighted MRI

MRI can be made sensitive to diffusion based on the principles described by Einstein's equation, which relates the displacements of molecules to the diffusion coefficient. In diffusion-weighted MRI (dMRI), molecular displacement over time is measured to infer the diffusion coefficient. The motion of water in biological tissues is described by the apparent diffusion coefficient (ADC), which replaces the diffusion coefficient D.

To measure the diffusion displacement of water molecules in MRI, we introduce “diffusion-sensitising gradients” into the sequence. Specifically, a gradient field is temporarily applied before and after the 180-degree pulse, as shown in Figure 2.10 (blue). Crucially, the duration and amplitude of these gradient fields are equal and share the same polarity. If the spins remain stationary, any phase shift induced by the first gradient is completely reversed by the second gradient due to the refocusing effect of the 180-degree pulse. Thus, there is no signal loss for stationary water molecules. However, when spins diffuse, they end up in different locations during the first and second gradient applications. Consequently, the phase of spins during second gradient differs from that in the first gradient, and the accumulated phase shift is proportional to the spatial displacement. Under random diffusive motion, this phase shift varies from proton to proton, leading to net dephasing and, consequently signal attenuation. Greater dephasing results in increased signal loss, indicating faster diffusion, which corresponds to a higher ADC. Conversely, slower diffusion causes less dephasing and reduced signal loss (Bihan, 2007) (Figure 2.10).

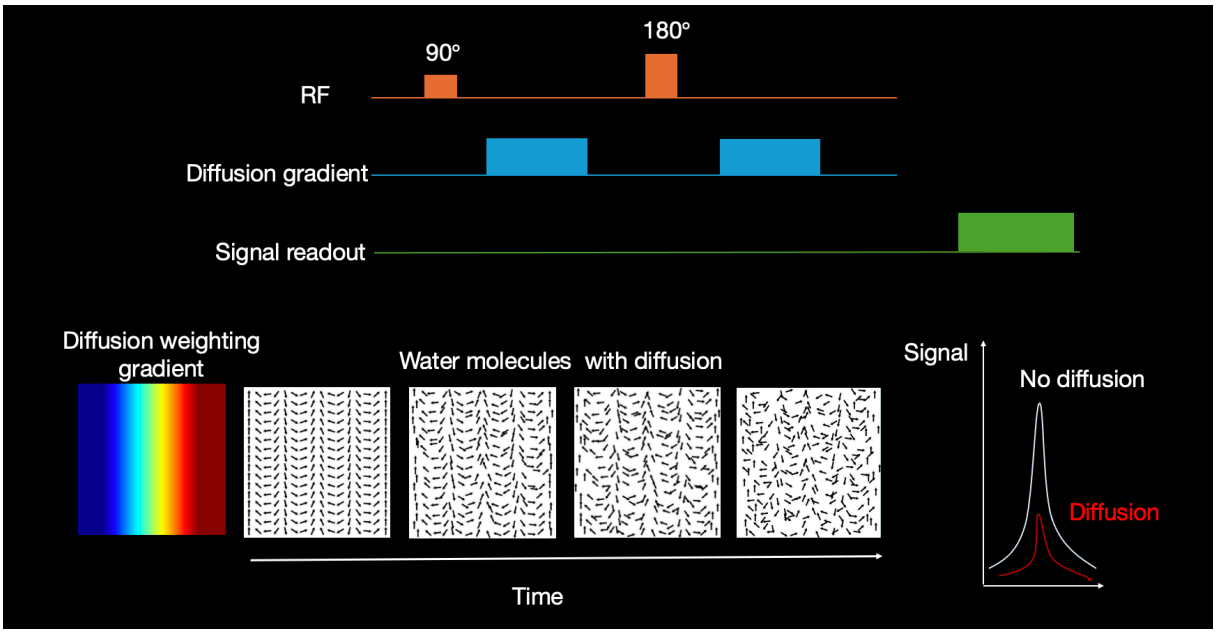


Figure 2.10: Mechanism of diffusion-weighted imaging (DWI). Following the application of a 90° RF pulse and a 180° refocusing pulse, diffusion-sensitising gradients are applied along the left-right direction. When water molecules diffuse, they experience dephasing leading to signal attenuation.

When molecular displacement follows a Gaussian distribution, the resulting signal attenuation in dMRI can be quantified by the equation below:

$$\frac{S_b}{S_0} = \exp(-b \cdot ADC)$$

S_b is the diffusion-attenuated signal and S_0 is the baseline MR signal obtained without diffusion gradients. The factor **b**, known as the **b-value**, quantifies the sensitivity to diffusion. The b-value can be calculated using the following equation:

$$b = \gamma^2 \int_0^{TE} [\int_0^t G(t')dt']^2 dt$$

Where $G(t')$ represents the time-dependent amplitude of the diffusion gradient, and the integrals account for its cumulative effect from time 0 to t over the entire echo time (TE). For rectangular gradients, the equation simplifies to:

$$b = \gamma^2 G^2 \delta^2 (\Delta - \delta/3)$$

where b is determined by the factors including the duration of the gradient (δ), the gradient amplitude (G), and the time interval between the paired gradients (Δ).

Higher b-values lead to larger signal attenuation, thereby increasing sensitivity to diffusion and enhancing contrast. However, higher b-values also result in a reduced signal-to-noise ratio (SNR). In contrast, lower b-values typically provide a higher SNR but reduced diffusion contrast.

The diffusion gradient is always applied along a specific direction in space, the direction in which the signal becomes sensitive to diffusion. This is often called the b-vector, or simply the diffusion direction. To accurately characterise the complex fibre configurations, it is necessary to measure the dMRI signal along many different diffusion directions, thus providing higher angular resolution. When many gradient directions are acquired at a single b-value, they form a sphere in q-space, known as a shell. Acquisition with multiple b values (two or more non-zero b values) is known as multi-shell.

Diffusion and brain microstructure

Brain microstructure affects water diffusion within the brain, and as a result, diffusion MRI provides a non-invasive method to investigate the orientation of water diffusion and cellular compartments in brain tissues. When water diffusion is equal in all directions, it is isotropic, which is commonly observed in CSF. In grey matter, reduced diffusivity may be detected compared to CSF due to the restriction imposed by cellular structures. In white matter, axonal membranes restrict or hinder diffusion perpendicular to the axons compared to diffusion along the axon direction. This results in constrained diffusion in one direction and faster diffusion in another, a phenomenon known as anisotropic diffusion.

2.3.2 Diffusion tensor imaging

A single value of the diffusion coefficient (or ADC) is insufficient to fully characterise the anisotropic features of water diffusion as measured by diffusion MRI. Therefore, more advanced diffusion MRI signal models are needed. In diffusion tensor imaging (DTI), the diffusion process

is described by a tensor, given by a symmetric 3x3 matrix D, as shown below(Basser et al., 1994):

$$D = \begin{matrix} D_{xx} & D_{xy} & D_{xz} \\ D_{xy} & D_{yy} & D_{yz} \\ D_{xz} & D_{yz} & D_{zz} \end{matrix}$$

The diffusion tensor describes the covariance of diffusion displacements in 3D. The tensor is constrained to be symmetric, with diagonal elements representing diffusion variances along three orthogonal axes, and off-diagonal elements capturing covariances between diffusion displacements (eg. D_{xy} reflects the correlation between displacements along the x- and y- axis). The diagonalisation of the diffusion tensor matrix D produces three mutually orthogonal eigenvectors and their corresponding eigenvalues ($\lambda 1, \lambda 2, \lambda 3$), describing the apparent diffusivities along the axes. The first eigenvector represents the principal diffusion direction. The diffusion tensor may form an ellipsoid when the diffusion is anisotropic with the major eigenvector aligning with the dominant fibre orientation. When the diffusion is isotropic, the tensor forms a sphere with three eigenvalues nearly equal.

It turns out that a range of metrics derived from the tensor are clinically useful. For example, mean diffusivity (MD), the average of the eigenvalues, reflects overall diffusivity within a voxel. Fractional anisotropy (FA) quantifies the fraction of the tensor's magnitude that is anisotropic. FA is obtained from the normalised variance of the tensor's eigenvalues as shown below. FA provides insights into white matter integrity, with reduced FA values observed in neurodegenerative processes or injury(Assaf and Pasternak, 2008).

$$FA = \sqrt{\frac{3}{2}} \frac{\sqrt{(\lambda_1 - \lambda)^2 + (\lambda_2 - \lambda)^2 + (\lambda_3 - \lambda)^2}}{\sqrt{\lambda_1^2 + \lambda_2^2 + \lambda_3^2}}$$

A limitation of DTI is its inability to capture more complicated signal behaviour. When multiple fibre populations are present within a voxel, DTI fails to distinguish between fibre architectures such as crossing, bending, or fanning fibres. Each millimetre-scale MRI voxel contains hundreds

of micrometre-scale axonal fibres with diverse orientations. Furthermore, DTI cannot model the departure of mono-exponential signal decay. While the tensor model approximates diffusion well under Gaussian-like (ellipsoidal) conditions, it struggles with non-Gaussian diffusion behaviours. Non-gaussian behaviour is usually caused by factors such as fibre dispersion, axial diffusivity and interactions between water, phospholipids and proteins. By using multi-shell data with multiple b values, we can more accurately estimate multiple diffusivities within each voxel, providing a better model of non-Gaussian signal behaviour. These limitations highlight the need for advanced models to more accurately characterise complex fibre geometries and non-Gaussian diffusion patterns (Le Bihan and Johansen-Berg, 2012).

2.3.3 Constrained spherical deconvolution

Instead of assuming a single primary orientation per voxel, using a continuous function of fibre orientation distribution (FOD) can better describe more complex fibre configurations and properties, including crossing fibres. FODs are usually described by spherical harmonics, a representation of data distribution on the sphere in three-dimensional space. Spherical harmonic basis functions form a complete and orthonormal set, and different complex functions defined on the sphere can be expressed as a linear combination of these basis functions. Constrained spherical deconvolution (CSD) builds on this as a method for estimating FODs(Tournier et al., 2004).

CSD models the diffusion signal as a sum of contributions from multiple fibre populations, with each contribution weighted by its corresponding fibre volume fraction. It assumes that all fibre population share the same diffusion signal profile, referred to as the fibre response function (FRF). Mathematically, the diffusion signal in each voxel is the convolution of the response function (as the kernel) with the FOD. The FRF is typically derived from voxels with high fractional anisotropy, which are likely to contain a single fibre population. By performing spherical deconvolution of the diffusion signal with the FRF, the FOD can be derived (Figure 2.11). The spherical harmonics fitting process is constrained to minimise negative peaks, as the volume fraction of any fibre population cannot be negative (Tournier et al., 2007). CSD can be applied to single-shell high angular resolution diffusion imaging (HARDI) data or multi-shell data. FODs obtained from CSD have been shown to more accurately track crossing fibres in

regions where the corpus callosum and corticospinal tract intersect (Dell'Acqua and Tournier, 2019). Additionally, CSD-derived metrics can reveal white matter alterations that are not detectable using DTI metrics (Dell'Acqua et al., 2013).

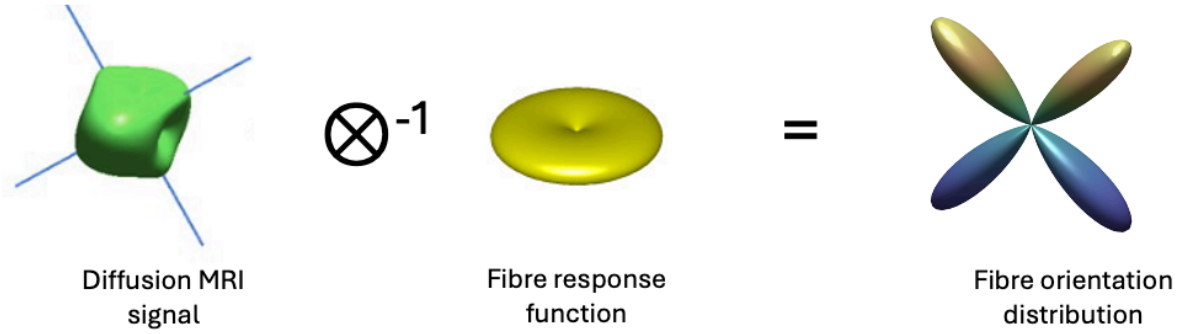


Figure 2.11: Constrained spherical harmonics in diffusion MRI. By assuming that all the fibre populations share the same signal profile, fibre orientation distribution can be calculated with the deconvolution of the diffusion signal with the FRF.

A limitation of CSD is the assumption that a single FRF applies uniformly across all brain regions, which implies that all the fibre orientations share the same microstructural properties. However, an FRF estimated from WM will not be applicable in GM and CSF, which have entirely different microstructures (Jeurissen et al., 2014). To address this limitation, multi-shell multi-tissue CSD incorporating separate compartments for each tissue type, enables more accurate characterisation of tissue-specific signal contributions (WM/CSF/GM). However, even within white matter, fibre populations differ in shape, packing density, and microstructural properties, and these variances have been validated through microscopy studies (Schilling et al., 2019c) but are not explicitly accounted for by CSD.

2.3.4 Ball and Stick model

The Ball and Stick model (BAS), as the name suggests, models the diffusion signal in each voxel using two types of compartments: an isotropic "ball" compartment and an anisotropic "stick" compartment (Behrens et al., 2007). The stick represents diffusion within and around axons, and the ball compartment models the diffusion of free water in the voxel (Figure 2.12). The total

signal measured in each voxel is described as the sum of the weighted signal from the two types of compartments, as shown below:

$$S = (1-\sum_{j=1}^{N} f_j) \cdot S_{iso} + \sum_{j=1}^{N} f_j \cdot S_{aniso}$$

Where S_{iso} and S_{aniso} are the signal contributions from the ball and stick compartments respectively. f_j represents the fraction of the signal contributed by the j^{th} fibre orientation in the anisotropic compartment and N is the total number of fibre orientations being modelled in the voxel. The signal contribution from the isotropic compartment for a given gradient direction i is given by:

$$S_{iso} = S_0 \cdot \exp(-b_i D)$$

Where S_0 is the measured signal without diffusion weighting, b_i is the b value for gradient i, and D is the unknown diffusivity. The signal contribution from the anisotropic compartment for a given gradient direction i can be written as:

$$S_{aniso} = S_0 \cdot \exp\left(-b_i D (x_i{}^T v_j)^2\right)$$

Where the anisotropic compartments are assumed to have a zero radius, modeled as sticks, with only axial diffusivity but no radial diffusivity. x_i represents the unit vector in the direction of the gradient for gradient i and v_j is the unknown j^{th} fibre orientation. The diffusivity of the isotropic compartment is assumed to be equal to that of the anisotropic compartment in the BAS model.

The model is fitted using a Bayesian framework through the Markov Chain Monte Carlo (MCMC) method, which is a sampling technique (MCMC is mentioned here because it was the method used in the original paper). MCMC estimates samples from the posterior distribution, providing both parameter values and their associated uncertainties (Behrens et al., 2003). Furthermore, the BAS model can account for multiple fibre populations per voxel and decides the number of fibre populations using a model selection technique called Automatic Relevance Determination (ARD). This ensures that the model complexity (in terms of fibre populations) is

limited to what the data actually supports. For example, in voxels with a single dominant fibre orientation, such as those in the corpus callosum, additional fibre populations are penalised if they are not supported by the data (Behrens et al., 2007).

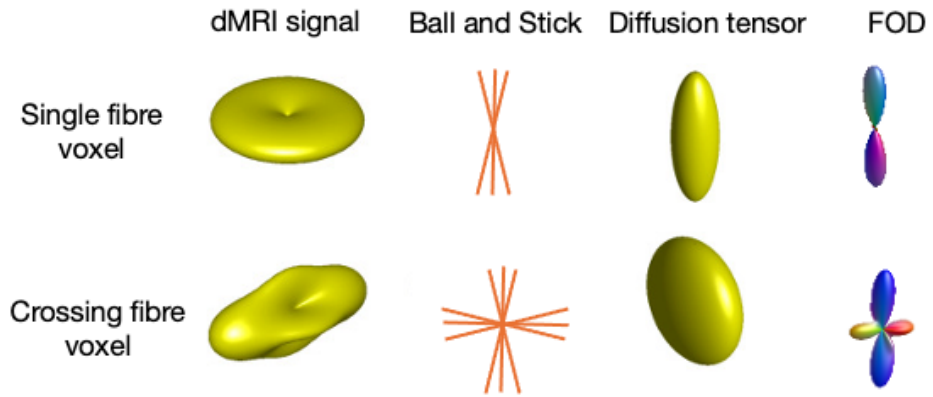


Figure 2.12: Diffusion modelling of fibre orientation within a voxel for single and crossing fibres. Left: dMRI signal demonstrating signal decay along fibre orientations. Middle left: Ball and Stick model for estimating fibre orientations. Middle right: Primary fibre orientation estimated using DTI. Right: fibre orientation distribution (FOD) derived from constrained spherical deconvolution.

2.3.5 Tractography

Local fibre orientation information, as measured by dMRI modelling, can be utilised to reconstruct white matter tracts by iteratively following the most aligned and collinear directions from one voxel to its neighbouring voxels. This process, known as **tractography**, assumes that the direction of highest diffusivity corresponds to the white matter pathway. Tractography generates streamlines that are grouped into fibre bundle.

Deterministic and probabilistic tractography

Tractography algorithms include deterministic and probabilistic tractography. Deterministic tractography propagates along a unique fibre orientation per voxel, typically following the principal direction of diffusion. A single pathway is generated from each seed point. However, dMRI data are susceptible to noise and artifacts which can propagate through fibre tracking. In addition, errors in fibre orientation estimation can occur due to suboptimal assumptions in the diffusion model or limited resolution. Deterministic tractography disregards these uncertainties and artefacts, typically resolving only the most dominant fibre orientation. Therefore,

deterministic tractography often struggles to resolve crossing or complex fibre configurations and is particularly susceptible to noise and errors. In comparison, probabilistic tractography considers uncertainty in fibre orientation within each voxel. It generates multiple possible trajectories from each seed point by sampling from an orientation distribution derived from fibre orientation models such as the Ball and Stick model and tracing fibre bundle (Girard et al., 2025). Pathways with higher densities indicate greater reliability and reproducibility of connections.

2.3.6 Postmortem diffusion MRI

Diffusion MRI of postmortem tissue acts as an intermediate link between in-vivo dMRI and microscopy: it shares the same tissue characteristics with microscopy and the same signal properties as in-vivo dMRI. Postmortem MRI offers several advantages in measuring brain connectivity (Schilling et al., 2025). First, it is not constrained by scan time or affected by motion artifacts. Second, without time limitations, postmortem dMRI can achieve high spatial resolution, often down to a few hundred micrometres, enabling better visualisation of anatomical structures, such as the grey matter-white matter boundary and subcortical structures (Yendiki et al., 2022). However, to preserve tissue integrity postmortem dMRI requires chemical fixation, which alters tissue properties. Fixed tissue shows reduced relaxation times, leading to reduced SNR. Additionally, due to microstructure changes in the tissue, postmortem dMRI exhibits lower fractional anisotropy and ADC values.

Due to the reduced diffusivity observed in postmortem dMRI caused by factors such as temperature change (Berger et al., 2022) and tissue fixation (D'Arceuil et al., 2007), higher b-values are usually required during postmortem imaging (a b-value of 4500 s/mm^2 needed to achieve contrast comparable to in-vivo imaging at b values of 1000-1500 s/mm^s based on the changes in diffusivity) (Miller et al., 2011). While 2D single-shot echo planar imaging (ss-EPI) remains the most commonly used pulse sequence for in-vivo dMRI, postmortem dMRI benefits from more advanced methods (Yendiki et al., 2022). For example, 3D multi-shot techniques allow for shorter echo times and improved SNR, which can achieve a submillimetre resolution in the postmortem human brain (Miller et al., 2011).

2.3.7 Challenges of tractography

Despite being a widely used non-invasive method for mapping the human brain connectome, dMRI tractography has several limitations which are addressed in this thesis by combining MRI and microscopy.

Crossing fibre problem: One of the most extensively studied challenges is the "crossing fibre problem" which describes multiple and distinct white matter tracts intersecting in a single voxel. Crossing fibres are prevalent in white matter and have been estimated to have fractions ranging from 30% to 90% of white matter voxels (Schilling et al., 2017a). The crossing fibres are particularly common in primate brains due to the higher complexity of white matter structures compared to the non-primate brain (eg. mice) (Georgiadis et al., 2023). Advanced fibre orientation estimation methods, such as the spherical deconvolution (Dell'Acqua et al., 2007) or the Ball and Stick model mentioned in section 2.3.4 can better disentangle the crossing fibre problem compared to DTI. In addition, high spatial resolution and high angular resolution show the potential to better resolve crossing fibres (Schilling et al., 2017a).

Gyral bias problem: Tractography streamlines are found to preferentially terminate at the gyral crowns instead of taking a sharp turn toward the gyral walls (the walls of sulci)(Schilling et al., 2017b). The sharply curved axon bundles are evident in myelin-stained microscopy but are not accurately represented in tractography (Figure 2.13). The fibre orientation radially oriented to the white matter-grey matter boundary is difficult to capture. One explanation for this bias is the large voxel size of dMRI at the millimetre scale, making the gyrus which approximates grey matter susceptible to partial volume effect. Thus, it is challenging to disentangle myelin-specific information in each dMRI voxel.

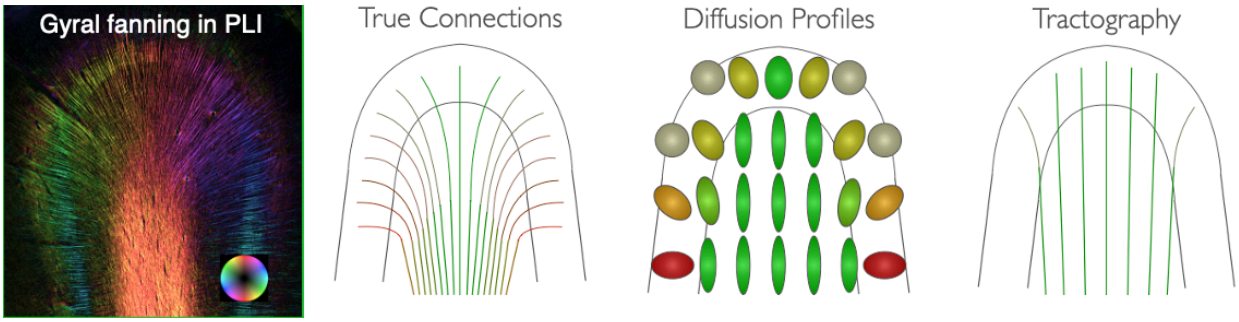


Figure 2.13: Gyral bias. The ground truth gyral fanning is demonstrated using PLI. The true connections capture the sharp turn toward the gyral walls. The diffusion MRI profiles and tractography trajectories (streamlines) predominantly terminate at the gyral crowns but fail to turn into the gyral wall. Many thanks to Karla Miller for kindly providing this figure.

Superficial white matter challenges: The superficial white matter (SWM) introduced in Section 2.1.2 poses challenges for tractography. SWM refers to short association fibres ("U-fibres") that connect adjacent cortical regions within the same hemisphere. Tracking SWM tracking is difficult due to its intricate anatomy characterised by looping, large curvature and its proximity to grey matter (Guevara et al., 2020). Particularly, SWM closely follows cortical folding patterns which also differ significantly across individuals, adding more variability.

Bottleneck problem: The bottleneck problem occurs when multiple white matter bundles originate and terminate at different locations but converge in the middle within a single voxel with parallel orientations (Figure 2.14). Due to the limited spatial and angular resolution, tractography fails to unambiguously follow the paths of individual axons and often struggles to distinguish patterns of crossing, fanning, or kissing in a single voxel, all of which create intermingle patterns. An example bottleneck region is the internal capsule, where fibres projecting from the frontal and parietal lobes and terminating in midbrain nuclei such as the corticospinal tract and superior thalamic radiations converge in the middle (Schilling et al., 2022). The bottleneck problem remains unsolved and is one of the challenges our research aims to address. To mitigate the bottleneck problem, anatomical priors from histology or high-resolution dMRI will assist in precise fibre tracking and fibre orientation better informed by microstructure also shows great potential (Girard et al., 2017).

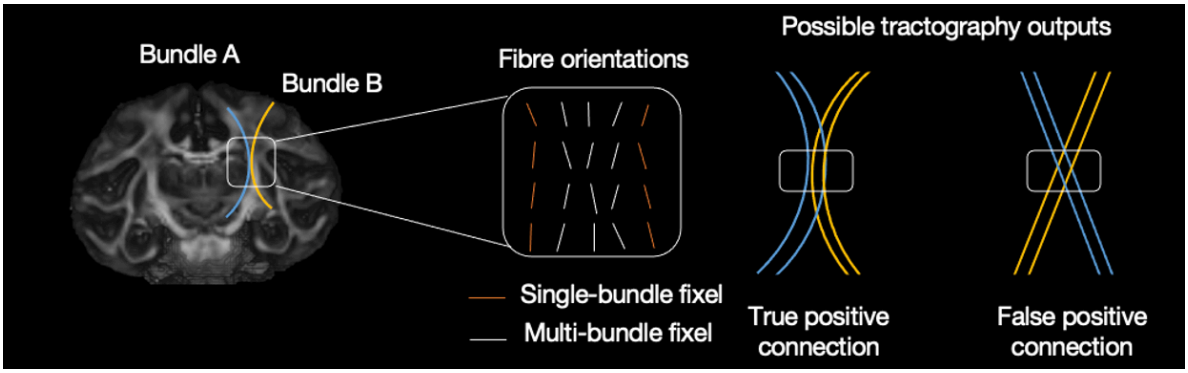


Figure 2.14: Bottleneck problem. An example in the internal capsule (IC) is shown. Two fibre bundles, originating and terminating at different locations converge with similar orientations within the bottleneck region (truth axonal connection). Fixels (fibre orientations per voxel as described in Figure 2.15) are classified based on the number of fibre bundles passing through each fixel: multi-bundle fixels (white) have multiple associated fibre bundles and single-bundle fixels have a single associated fibre bundle (orange). The bottleneck region, identified as the multi-bundle fixel where streamlines become indistinguishably mixed, generates the false positive connection. As a result, a single FOD pattern can produce two probabilistic tractography outputs.

The prevalence of bottleneck regions throughout the brain has been studied using fixel-based analysis (FBA) (Dhollander et al., 2021). A "fixel" refers to a fibre population within a single voxel. Fixel-based analysis provides advantages over traditional voxel-based analysis by enabling fibre-specific measurements (Figure 2.15). Fixels are derived by segmenting the continuous FODs into distinct fibre populations, allowing for fibre-specific microstructural measurements at the subvoxel level. These fibre-specific measurements obtained through FBA have demonstrated significant correlations with various neurological diseases (Raffelt et al., 2012). For example, fibre density reflects intra-axonal volume (Raffelt et al., 2012) and its reduction has been observed in patients with cerebral small vessel disease (Petersen et al., 2022). When FBA is used to map the distribution of bottleneck regions, it reveals that bottlenecks account for approximately 50–70% of the fixels in the white matter of the human brain (Schilling et al., 2022). We use FBA to evaluate whether our approach combining MRI and microscopy improves the bottleneck problem in Chapter 3.

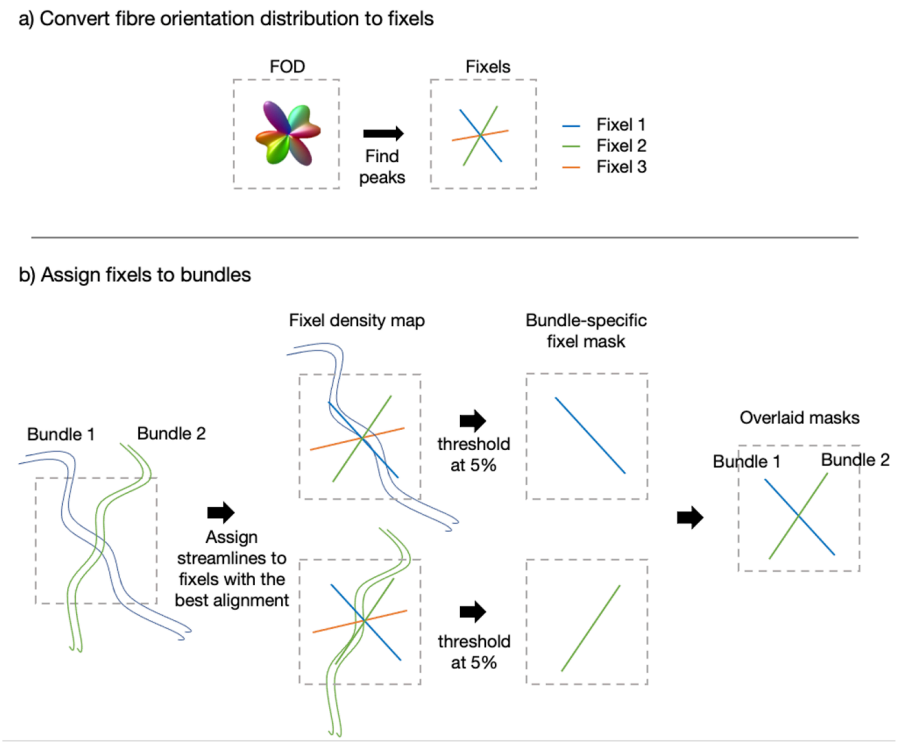


Figure 2.15: a) The fibre orientation distribution can be subdivided into "fixels", each of which describes a specific fibre population within the voxel. b) Each streamline is assigned to a specific fixel. This allows us to compute a fixel density map for each fibre bundle. The fixel density map is calculated for each fibre bundle independently and describes the number of streamlines from a given fibre bundle that passes through each fixel. The density map is converted into a fixel mask by setting a threshold. We can then combine the masks across fibre bundles to visualise whether they pass through the voxel with different orientations (as shown) or the same fibre orientations (indicating a bottleneck).

2.4 Combining MRI and microscopy

Various invasive techniques (Section 2.2) and non-invasive techniques (Section 2.3) for mapping brain connectivity offer complementary information across a range of length scales. Microscopy enables the visualisation of axons at the micrometre scale over limited fields-of-view, whereas MRI captures larger structures over the whole brain, such as the entire white matter fibre tracts. Furthermore, microscopy provides direct observation and measurement of myeloarchitecture and cytoarchitecture, in contrast to MRI, which relies on model-based assumptions to derive surrogate measures of microstructure. By combining the two approaches in the same tissue, we can leverage the complementary strengths of MRI and microscopy to: 1) validate dMRI measurements using microscopy, with microscopy widely regarded as the 'gold standard'(Axer, 2011); 2) combine dMRI and microscopy for more accurate analysis; and 3) transfer knowledge

gained from microscopy to improve dMRI techniques. While the first aim (validation of MRI with microscopy) is the most common use case of combining the two methodologies, in this thesis, we focus on the latter two concepts. In Chapter 3, we present a novel joint analysis, whereas Chapter 4-6 deal with microscopy-to-MRI knowledge transfer.

2.4.1 Registration

The meaningful comparison and combination of MRI and microscopy data are predicated on accurate spatial correspondence between the different imaging modalities. Ideally, this would be achieved through multi-modal registration, which refers to the process of transforming images from one space (e.g. microscopy space) to the other space (e.g. MRI space). In addition, challenges such as tissue deformations, shrinkage, and other artifacts that conventional MRI-MRI registration tools do not address need to be handled with MRI-histology registration.

The registration solutions vary depending on the microscopy sectioning method(Tullo et al., 2018). For example, in 2D serial histological sectioning, undistorted histological block face photographs are often obtained before each sectioning step, which act as reference points. By aligning anatomical landmarks between sections and block face photographs, the 2D histological slices can be accurately stacked into a 3D volume and then transformed into the MRI space(Pichat et al., 2018). However, registering stand-alone histology images is typically more challenging due to in-plane deformations, significant manual inputs, etc. An open-access tool, the Tensor Image Registration Library (TIRL), has been developed and supports the registration of stand-alone histology images for both histology-to-MRI (slice-to-volume) and histology-to-histology(Huszar et al., 2023a). TIRL is fully automated, requiring no manual labelling making it suitable for large datasets and was used for analysing the BigMac dataset presented in Chapter 3.

2.4.2 Using histology for the dMRI validation

Microscopy has been widely used as a gold standard to validate dMRI measurements.

Fibre dispersion: Fibre dispersion is a simple metric used to characterise within-voxel fibre configurations, such as fanning. Better estimation of fibre dispersion can help the delineation of

white matter pathways during tractography (Rowe et al., 2013) and can also serve as a pathological biomarker (Kamagata et al., 2021). In dMRI, dispersion is quantified through diffusion modelling, which estimates the angular variability of the FODs to capture the spread of fibre orientations. In histology, fibre dispersion can be measured from microscopy-derived FODs specifically for myelin (Mollink et al., 2017a). Dispersion is observed to be higher in regions with crossing fibres and lower in regions with more aligned fibre structures such as the corpus callosum. A region-wise comparison of dispersion between dMRI and histology reveals a correlation coefficient of $r = 0.79$, indicating that dMRI captures the overall angular architecture of the FOD well. The dispersion model can be further improved by incorporating microscopy information (Mollink et al., 2017a).

Brain connectivity: Microscopy is also a powerful tool to validate dMRI tractography for brain connectivity mapping. While phantoms can be used to evaluate tractography streamlines quantitatively, they fail to reflect the complexity of brain circuitry (Fillard et al., 2011). Anatomical tracers offer an alternative by demonstrating axonal trajectories or their terminations across the brain. For instance, the IronTract Challenge used a dataset with dMRI and tracer injections performed on the same macaque brains to assess different tractography methods, allowing for voxel-wise comparison (Maffei et al., 2022a). It revealed common tractography errors (eg. branching into small bundles) and optimised strategies (pre-processing with denoising, Gibbs ringing correction, eddy-current distortions correction and Gaussian post-filtering etc). Additionally, tractography can be evaluated at the whole-brain level by comparing to the extensive connectivity matrices of cortico-cortical pathways from tracer injections (i.e., comparing the starting and termination points, rather than pathways within white matter). The connectivity matrices provide the quantitative weights (connection strength) and directional information (Felleman and Van Essen, 1991; Markov et al., 2012a).

Fibre response function: In CSD, the fibre response function, which represents the signal profile of a single fibre population, is conventionally derived from voxels with high fractional anisotropy, where a coherent and single fibre population is assumed (Tournier et al., 2007). Alternatively, to validate with 3D histological ground truth, the response function can be derived by deconvolving the dMRI signal using histology-based FODs. The resulting fibre response

functions vary across different brain regions (Schilling et al., 2019c). Therefore, the standard CSD assuming a global fibre response function fails to reflect the local anatomy and can be challenged, compromising the accuracy of tractography and connectivity analysis.

2.4.3 Joint analysis of MRI and microscopy

MRI and microscopy offer complementary insights into brain connectivity, each contributing unique information while also having inherent uncertainties. By leveraging the strengths of both modalities, a more accurate understanding of brain anatomy can be achieved. Several studies have successfully combined dMRI and microscopy, particularly in the mouse brain (Goubran et al., 2019; Johnson et al., 2023; Qu et al., 2022).

For instance, a data fusion framework combining MRI and myelin histology has been developed to address the degeneracy between fibre dispersion and radial diffusion (Howard et al., 2019). Specifically, a fibre population exhibiting high dispersion, but low radial diffusivity may produce a diffusion signal indistinguishable from that of a highly coherent fibre population with high radial diffusivity. Therefore, in CSD, variability in fibre dispersion cannot be accurately resolved due to the assumption of a global FRF. A joint analysis framework has been demonstrated to overcome this limitation by incorporating histological data to constrain the fibre orientation and dispersion within each MRI voxel, achieving more reliable estimations (Howard et al., 2019). In Chapter 3, we introduce a new data fusion framework designed to enhance the accuracy of fibre orientation estimation by integrating 3D whole-brain dMRI with 2D microscopy data.

2.5 Deep learning

2.5.1 Introduction of deep learning

Recent advances in machine learning have transformed the analysis and interpretation of large-scale neural imaging datasets. Deep learning, a type of machine learning, leverages a multi-layered neural network to progressively learn data representations from neuroimaging datasets. Each layer performs a non-linear transformation to learn a complex relationship between the input and output. As the depth of the network increases, the level of abstraction in data

representation also increases – that is, the network is able to capture increasingly complex image features that are relevant to the task the network is assigned.

A network generates predictions based on input data, with each layer characterised by a set of parameters. These parameters are iteratively updated in a data-driven manner. During training, a loss function evaluates the network's predictions – such as by comparing predictions to the ground truth in supervised learning – guiding the optimisation. The network learns feature representations through backpropagation, during which the error is propagated backwards to update the weights and parameters, thereby improving model performance. There are various architecture and training methods in deep learning. A common categorisation includes supervised, unsupervised and semi-supervised learning. In supervised learning, where there are labelled outputs, the loss function is defined by the difference between paired inputs and their target labels, enabling the model to learn explicit input-output mappings. In unsupervised learning, where there is no labelled data, the loss function is optimised based on specific tasks such as clustering and dimensionality reduction. Semi-supervised learning, on the other hand, leverages a combination of a small amount of labelled data and a large amount of unlabelled data, using the labelled data to guide the learning while extracting patterns from the unlabelled data (Alom et al., 2019; Alzubaidi et al., 2021; Pouyanfar et al., 2019)

A convolutional Neural Network (CNN) is a widely used deep learning architecture that utilises kernels to perform localised convolution. In contrast to fully connected layers (also known as multi-layer perceptron) where each neuron (a computational unit that processes input data and passes the result to the next layer) is linked to every neuron in the preceding layer, neurons in CNN are connected only to specific localised regions of the input (Figure 2.16). This localised connectivity not only reduces computational complexity but also enables the learning of spatially relevant features, making CNN suitable for image analysis. The networks used in this thesis employ a CNN structure.

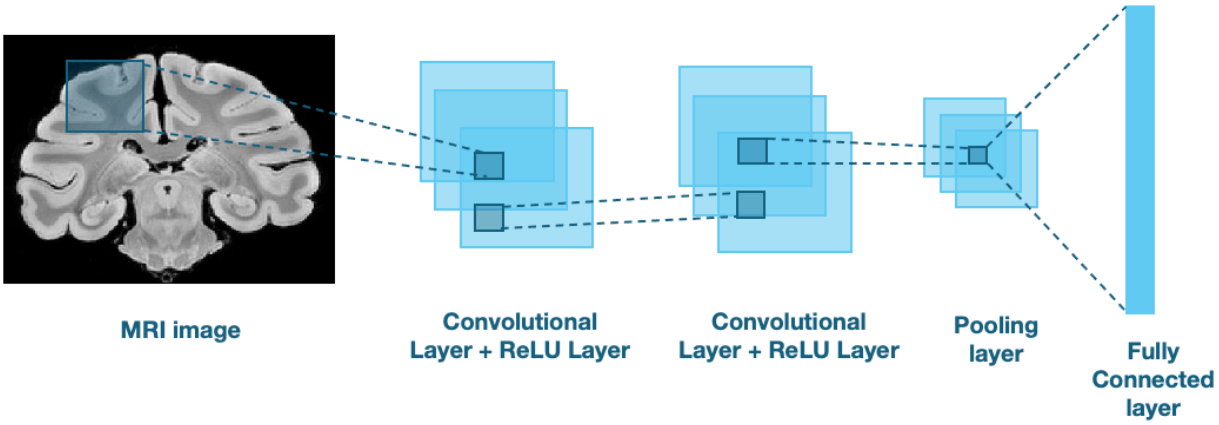


Figure 2.16: Example of a convolutional Neural Network architecture. Convolutional Kernels are applied to extract local features from input data. The extracted features are then flattened and passed to a fully connected layer.

In our work, we focus on a specific type of deep learning: transfer learning. When training and testing data come from different distributions, transfer learning aims to address model performance degradation on testing data due to this distribution shift. It involves using a model trained on the training data (source domain) and adapting it to the testing data (target domain). By transferring learned representations from the source domain and fine-tuning them on the target domain, the model can generalise better and improve performance on the testing data when labelled data in the target domain is limited or when the target task is more complex (Guan and Liu, 2022). For instance, a model can be trained to predict the progression of mild cognitive impairment from MRI imaging, and transfer learning can allow this model to generalise to PET imaging (Cheng et al., 2015).

Domain adaptation is a specialised form of transfer learning where the source task and target task are the same, but differences in data distribution between the source and target domains present a key challenge in model training. For example, variations in resolution, contrast, and signal-to-noise ratios can lead to distribution shifts, limiting the generalisability and applicability of DL models. To address this, domain adaptation techniques train the network to identify and align a shared feature space between the two domains, thereby improving performance on the target

domain despite data discrepancies (Guan and Liu, 2022). Deep learning methods for domain adaptation are used in Chapter 4,5 and 6 of this thesis.

2.5.2 Using deep learning for fibre orientation estimation and tractography

Recent developments in machine learning and data-driven methods have provided a novel solution for estimating brain connectivity from dMRI signals (Wasserthal et al., 2018a). There are two advantages of using deep learning. 1) As mentioned in section 2.3, the reliability of brain connectivity estimation largely depends on the diffusion model and often requires strong assumptions. In comparison, deep learning is model-free and thereby avoids imposing biophysical assumptions. 2) Deep learning method offers the potential for accurate fibre orientation estimation from limited diffusion data (i.e., less data than required by model-based methods). For example, DL can estimate multi-shell dMRI-derived FODs from single-shell data (Nath et al., 2020a), and improve the angular resolution of FODs from dMRI with a limited number of diffusion gradient directions (Zeng et al., 2022).

3

Imaging the structural connectome with hybrid MRI-microscopy tractography

Table of Contents

3.1. Introduction *50*

3.2. Methods *53*

3.2.1 MRI and microscopy data acquisition **53**

3.2.2 Constrained spherical deconvolution **55**

3.2.3 MRI-Microscopy data co-registration **55**

3.2.4 Hybrid MRI-microscopy fibre orientations **55**

3.2.4.1 Hybrid orientation reconstruction 55

3.2.4.2 Hybrid fibre orientation distributions (FODs) 58

3.2.4.3 Gelatine artefact 59

3.2.5 Experiments **59**

3.2.5.1 Tractography 59

3.2.5.2 Gyral bias 61

3.2.5.3 Bottleneck regions 62

3.2.5.4 Comparison with anatomic tracers 63

3.3. Results *64*

3.3.1 Generating hybrid MRI-PLI fibre orientations **64**

3.3.2 Whole-brain hybrid MRI-PLI tractography. **66**

3.3.3 Hybrid tractography resolves the gyral bias at high resolution. **68**

3.3.4 Hybrid tractography preserve topography in bottleneck areas. **69**

3.3.5 Comparison between hybrid tractography and tracer data. **74**

3.3.6 Hybrid MRI-microscopy can be performed with various microscopy contrasts. **76**

3.4. Discussion *78*
Data and code availability **84**

Foreword

Mapping how neurons are structurally wired into whole-brain networks can be challenging, particularly in larger brains where 3D microscopy is not available. Multi-modal datasets combining MRI and microscopy provide a solution, where high resolution but 2D microscopy can be complemented by whole-brain but low-resolution MRI. However, there lacks unified approaches to integrate and jointly analyse these multi-modal data in an insightful way. To address this gap, we introduce a data-fusion method for hybrid MRI-microscopy fibre orientation and connectome reconstruction. Specifically, we complement precise "in-plane" orientations from microscopy with "through-plane" information from MRI to construct 3D hybrid fibre orientations at resolutions far exceeding that of MRI whilst preserving microscopy's myelin specificity, resulting in superior fibre tracking. Our method is openly available, can be deployed on standard 2D microscopy, including different microscopy contrasts, and is species agnostic, facilitating neuroanatomical investigation in both animal models and human brains.

Published work:

Silei Zhu, Istvan N. Huszar, Michiel Cottaar, Greg Daubney, Nicole Eichert, Taylor Hanayik, Alexandre A. Khrapitchev, Rogier B. Mars, Jeroen Mollink, Jerome Sallet, Connor Scott, Adele Smart, Saad Jbabdi, Karla L. Miller, Amy F.D. Howard, Imaging the structural connectome with hybrid MRI-microscopy tractography, Medical Image Analysis, 2025, 103498, ISSN 1361-8415, https://doi.org/10.1016/j.media.2025.103498.

Authorship contribution statement

My contributions to this chapter include hybrid MRI-microscopy pipeline development, conceiving of and performing analyses. INH: developed the TIRL software and protocol for co-registration of the MRI-microscopy data. MC, GD, TH, AK, RM, JM, CS, AS etc were involved in the acquisition and curation of the BigMac data. NE: advised on the cortical ROI drawing. SJ: study conceptualisation. KLM: study conceptualisation, advised on all processing

pipelines and analyses; evaluated the results. AFDH: study conceptualisation, advised on all processing pipelines and analyses; evaluated the results.

3.1. Introduction

Mapping brain structure through multiple modalities can improve our understanding of brain function, development, aging and diseases (Hansen et al., 2022; Smith et al., 2020; Sporns, 2013). Much effort has gone into creating comprehensive maps of brain connectivity using various methods from MRI to microscopy (Essen et al., 2013; Oh et al., 2014; Scheffer et al., 2020; White et al., 1986). However, mapping the whole-brain networks in larger brain is challenging. Different modalities can provide complementary information about the underlying tissue microstructure by probing different length scales and providing sensitivity to different tissue features. Notably, when multiple modalities are combined in the same tissue, this can offer new opportunities for multi-scale neuroscience.

Chemical tracers have been an important tool for mapping the pathways of neural connections in animal brains over many years (Jbabdi et al., 2015; Lein et al., 2007; Maffei et al., 2022b; Markov et al., 2012b). The tracer facilitates direct visualisation of axonal projection from an injection site, providing a highly specific and sensitive estimate of inter-regional brain connectivity (Markov et al., 2012b, 2010). However, tracers are limited to a single or a few injections per animal, where achieving whole-brain coverage requires sacrificing many animals, and combining information across subjects ignores important between-subject variability (Lein et al., 2007; Markov et al., 2012b, 2010). Further, tracers are prohibitive to use in humans.

Alternative microscopy techniques serve as crucial reference measurements for characterising fibre architecture at high spatial resolution (Mollink et al., 2017a). For microscopy to be useful in tract reconstruction, the microscopy must inform on the fibre orientations in 3D. Multiple microscopy methods can provide 3D information (e.g. 3D polarised light imaging [3D-PLI] (Axer et al., 2011b; Nicole Schubert et al., 2017; Reckfort et al., 2015), μ-CT (Dyer et al., 2017; Masís et al., 2018), SAXS (Georgiadis et al., 2020) or serial EM (Denk and Horstmann, 2004)), and synaptic organization at the cubic-millimetre level has been mapped in the human cortex (Shapson-Coe et al., 2024). However, their sophisticated hardware and long acquisition times limit widespread application. Consequently, microscopy orientations are often acquired in 3D

from only small tissue samples or in 2D from thin sections of brain tissue, thus precluding 3D tract reconstruction or whole-brain connectivity estimates in primate brains.

In comparison, diffusion MRI (dMRI) enables non-invasive mapping of structural brain connectivity (Edgar and Griffiths, 2009). By measuring the diffusive motion of water molecules through the tissue, we can infer underlying fibre orientations and reconstruct white matter (WM) fibre bundles or tracts via tractography methods (Beaulieu, 2002). This facilitates whole-brain estimation of white matter organisation but relies on fibre orientations estimated via computational models from millimetre-scale MR signals. Low resolution and inaccuracies in the models can introduce bias or noise in the inferred fibre orientations that contribute to false positives and negatives in downstream tractography outputs (Maier-Hein et al., 2017; Nath et al., 2020b; Schilling et al., 2017b; Thomas et al., 2014). Regardless, due to the substantial promise of the method for non-invasive brain connectivity imaging, extensive efforts have gone into both understanding and overcoming these tractography limitations, through validation studies and methodological advancements (Ambrosen et al., 2020; Aydogan and Shi, 2018; Caminiti et al., 2021; Côté et al., 2013; Delettre et al., 2019; Dell'Acqua, 2024; Donahue et al., 2016; Dyrby et al., 2007; Girard et al., 2020; Maffei et al., 2022b; Schilling et al., 2019a, 2019d; Yendiki et al., 2022; Zhang et al., 2022).

Here, we propose a data-fusion approach (Howard et al., 2019) to jointly analyse data from MRI and microscopy to perform whole-brain microscopy-informed tractography. Our framework leverages the complementary information these modalities provide to create hybrid MRI-microscopy fibre orientations that are both 3D and at high resolution (Figure 3.1), preserving the unique benefits of the microscopy whilst facilitating 3D tractography. We use 2D microscopy to provide detailed estimates of fibre orientation within the microscopy plane and MRI to provide the through-plane orientation. For the latter, we use models that estimate distributions of fibre orientations within MRI voxels (Behrens et al., 2003), rather than a single orientation per voxel (e.g. from diffusion tensor imaging) (Basser et al., 1994). By extracting the through-plane angle for the fibre within this distribution that best matches the in-plane orientation derived from microscopy, we can then estimate 3D fibre orientations at spatial resolutions that exceed the MRI data. The dMRI Ball and Stick (BAS) method produces many orientation samples per voxel. However, the precise sub-voxel spatial localisation of these fibre orientations is unknown. In our hybrid method, the microscopy essentially assigned the through-plane orientation of the 3D samples to their putative location within the voxel to

"super-resolve" the MRI information. Our hybrid MRI-microscopy method provides: 1) 3D fibre orientations; 2) whole-brain coverage; 3) high resolution information and estimation of complex fibre architecture as described by the microscopy. The hybrid orientations are then combined into fibre orientation distributions (FODs) at arbitrary resolutions that are input into existing tractography pipelines for tract reconstruction. When based on myelin-sensitive microscopy, the hybrid orientations likely provide a more "myelin-specific" fibre orientation distribution than MRI, where the MRI FOD can represent a range of microstructural features including axons, dendrites and glia processes (Alexander et al., 2019; Jespersen et al., 2007; Stanisz et al., 1997). These myelin-specific FODs may be advantageous for certain applications such as defining the "myelin connectome" or tracking myelinated fibres into the cortex.

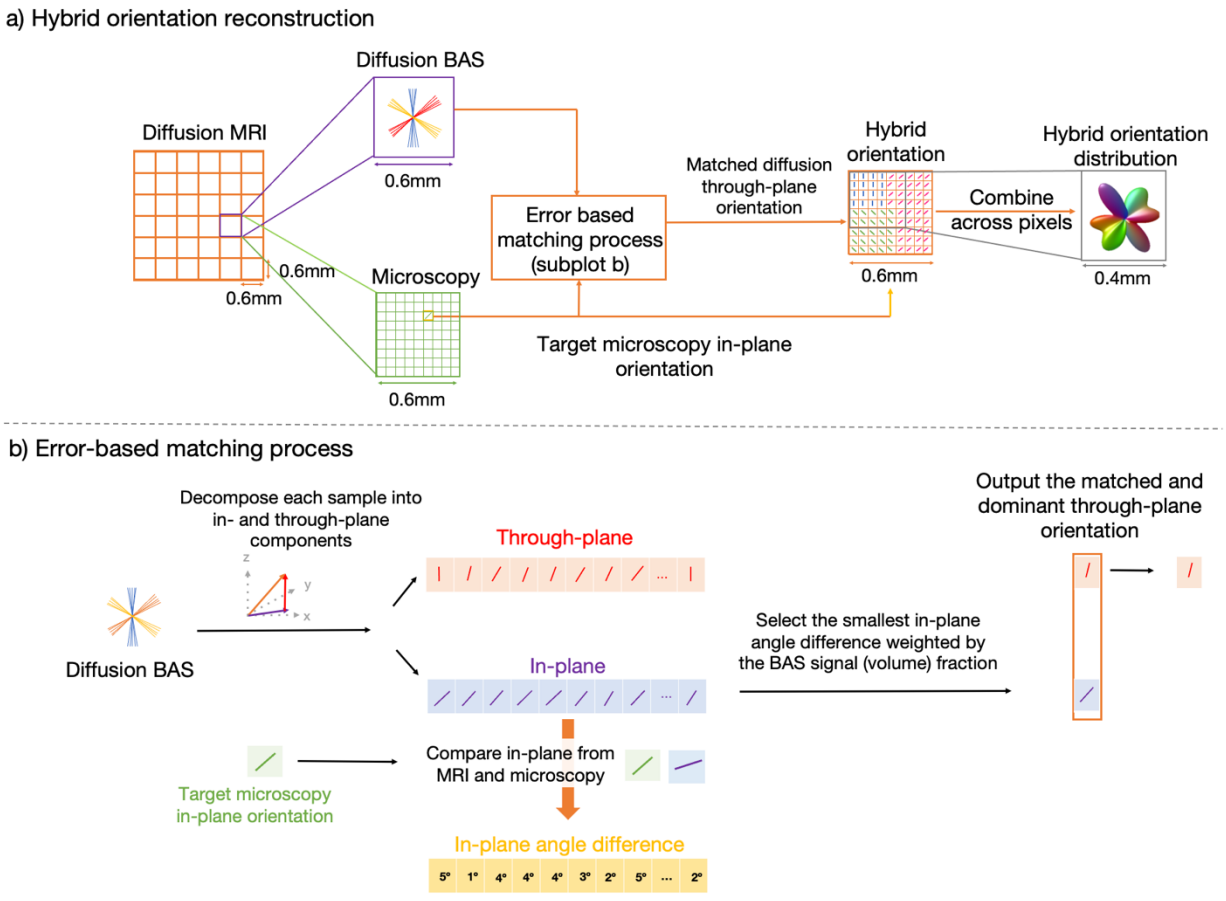


Figure 3.1: The hybrid MRI-microscopy approach.

a) Our data fusion method leverages the complementary strengths of diffusion MRI and microscopy. Each 2D microscopy orientation was warped to dMRI space and compared to the BAS samples in the same voxel, where the BAS samples were first projected onto the microscopy plane to facilitate fair comparison with the 2D microscopy. The microscopy through-plane information was then approximated using that from the BAS sample selected by the error-based matching process. b) The error based matching process. The diffusion BAS and microscopy in-plane orientation were used as inputs. The 3D BAS orientation was decomposed into the through-plane angle and in-plane angle by projecting onto the microscopy plane. The in-plane angle was compared to the

target microscopy in-plane orientation by quantifying the angle difference. We selected the BAS sample with the smallest in-plane angle difference weighted by the BAS signal fraction (related to the volume fraction where more dominant fibre bundles have higher signal fractions) and determined the matched through-plane angle.

We demonstrate our approach using the BigMac dataset (Howard et al., 2023), an open-access multi-modal resource that includes postmortem dMRI and microscopy data from a single macaque brain with whole-brain coverage. The microscopy includes polarised light imaging (PLI) (Axer, 2011; Larsen et al., 2007; Nicole Schubert et al., 2017) as well as myelin- (Gallyas, 1971) and Nissl-stained histology (Kádár et al., 2009; Pilati et al., 2008). Precise co-registration between microscopy and MRI has been conducted, which is essential for meaningful data fusion at the voxel-wise level (Huszar et al., 2023a). Applying our hybrid method to the MRI and PLI data, we first demonstrate how to perform hybrid tractography at different resolutions and reconstruct microscopy-informed tracts spanning the whole macaque brain. With confidence in our method, we then demonstrate how hybrid tractography can be beneficial in neuroanatomical and methodological investigations. Specifically, we utilise our hybrid outputs to investigate two known challenges in MRI-based tractography: the gyral bias (Schilling et al., 2017b) and bottleneck problem (Schilling et al., 2022), both of which are primarily driven by the limited spatial resolution of MRI data. By comparing our hybrid outputs to MRI results in the same brain, we investigate how these challenges are related to the resolution and contrast-generating mechanism of MRI. We then compare the hybrid tractography outputs to tracer data obtained from other animals (Markov et al., 2012b, 2010) to demonstrate that our hybrid method provides higher specificity in fibre tracking than MRI only tractography. Finally, we perform hybrid tractography using three different microscopy contrasts (PLI, myelin- and Nissl-stained histology) to demonstrate its application on different types of microscopy. Overall, our method retains the benefits of microscopy without relying on invasive tracers, meaning we can estimate dense, microscopy-informed structural connectivity from a single brain, using a method that is translatable across species, including humans.

3.2. Methods

3.2.1 MRI and microscopy data acquisition

The BigMac dataset was previously acquired and pre-processed as described in Howard et al., 2023. Relevant to this work, an adult rhesus macaque brain was scanned postmortem on a 7T small animal scanner. Structural images were acquired with multi gradient echo sequence at a

spatial resolution of 0.3 mm isotropic: FOV =76.8 × 76.8 × 76.8 mm, TE/TR = 7.8/97.7 ms, and flip angle = 30°.

Postmortem dMRI was acquired with spin echo 2D multi-slice sequence and single-line readout: 0.6 mm isotropic resolution data with 128 gradient directions at b=4 ms/μm^2 and 8 with negligible diffusion weighting, and 1 mm isotropic resolution data with 250 gradient directions at b=4 ms/μm^2 and 10 with negligible diffusion weighting.

After the scanning, the brain was sectioned into two blocks (anterior/posterior halves). Each block was sectioned into thin (50/100 μm) slices and allocated to one of six interleaved contrasts: polarised light imaging (PLI) (Axer, 2011; Axer et al., 2001, 2011b; Larsen et al., 2007), Cresyl violet staining for Nissl bodies (Kádár et al., 2009; Pilati et al., 2008), Gallyas silver staining for myelin (Gallyas, 1971) and three unassigned sections that were stored for longevity. The slice thickness was 50 μm for 5 out of the 6 sections (including PLI, Nissl and myelin-stained sections) with one section 100 μm thick. Each section of the same contrast was repeated every 350 μm.

PLI estimated the primary fibre orientation based on the birefringence of myelinated axons with a resolution of 4 μm per pixel (Axer, 2011; Axer et al., 2001, 2011b; Larsen et al., 2007). Images were acquired as the analyser (rotatable polariser) was rotated through 180°, with a 20° angular resolution. Images were background corrected after which a sinusoid was fitted to the measured intensity at each pixel (I) as a function of analyser rotation (ρ). The phase of the sinusoid described the in-plane fibre orientation. Retardance and transmittance maps were also calculated and here used only for visualisation and to drive the co-registration respectively.

Histology slides with Gallyas silver staining (myelin) and Cresyl violet staining (Nissl bodies) were digitised at a spatial resolution of 0.28 μm/pixel. 2D structure tensor analysis (Bigun et al., 2004; Budde and Annese, 2013; Budde and Frank, 2012b) of the stained sections (using a Gaussian kernel with sigma=10 pixels) was used to estimate the fibre orientations for each microscopy pixel.

3.2.2 Constrained spherical deconvolution

The diffusion MRI data was analysed using constrained spherical deconvolution (CSD) (Tournier et al., 2007). CSD is a common fibre orientation estimation method that uses diffusion MRI data only and where the CSD-derived FODs and downstream tractography could be directly compared to equivalent outputs from the hybrid method (both FODs are similarly described using spherical harmonics). Here, CSD was performed using the dhollander algorithm for fibre response function estimation(Dhollander et al., 2016; Tournier et al., 2007).

3.2.3 MRI-Microscopy data co-registration

MRI-Microscopy registration was performed using TIRL (v3.1.1), an automated pipeline facilitating the accurate registration of the histology sections to the whole brain MRI via a sequence of linear and non-linear transformations (see (Howard et al., 2023; Huszar et al., 2023a, 2023b, 2022) for further details). Here each PLI, myelin- and Nissl-stained slide was registered independently to the MRI space. The structural MRI was used as a reference due to its high resolution and good grey/white contrast. Separately, the structural and dMRI were co-registered using linear registration in FSL (FLIRT)(Jenkinson et al., 2002; Jenkinson and Smith, 2001). By combining the TIRL and FLIRT transformations, the microscopy pixels were mapped to voxel coordinates in dMRI space. Mapping of the microscopy fibre orientations (vectors) to dMRI space also accounted for local rotations according to the warp field.

3.2.4 Hybrid MRI-microscopy fibre orientations

3.2.4.1 Hybrid orientation reconstruction

To calculate the 3D hybrid MRI-microscopy orientations, microscopy provided the fibre orientations within the microscopy plane, and we approximated the through-plane angle (or inclination angle) with that from dMRI (BAS model). A schematic of the method is illustrated in Figure 3.1.

Estimating BAS orientations from diffusion MRI

The dMRI was analysed using the Ball and Stick (BAS) model (Behrens et al., 2003) to estimate ≤ 3 fibre populations with 50 orientation estimates (samples) per population. These sample orientations capture the uncertainty in the estimation of the 3 fibre populations, which in part reflects the distribution of fibre orientations throughout the dMRI voxel. Samples from BAS populations with signal fractions less than 0.05 were excluded from future analysis.

The BAS model was chosen due to its ability to estimate multiple fibre populations per voxel and provide discrete orientation samples that can be directly compared with those from microscopy. Other diffusion models providing estimation for the fibre orientation could also be used.

Extracting 2D orientations from microscopy

PLI maps of fibre orientation within the microscopy plane (in-plane angles estimated for each pixel) were used as input for the hybrid MRI-PLI tractography. In-plane orientations were estimated from myelin- and Nissl- stained histology using 2D structure tensor analysis. No other processing was applied, and all in-plane orientations were considered equally throughout the tissue.

Combing MRI and microscopy for hybrid orientation reconstruction

The microscopy in-plane orientations were first warped to dMRI space and compared with the co-registered BAS samples within the same voxel using an error-based matching process (Figure 3.1b). To facilitate fair comparison of in-plane dMRI and microscopy orientations, the 3D BAS orientation samples were decomposed into the through-plane angle and in-plane angle by projecting the BAS orientation onto the microscopy plane. This process was repeated for ≤150 BAS samples per voxel (≤ 3 fibre populations with 50 orientation samples per population). The in-plane angle of each sample was then compared to the target microscopy in-plane orientation by quantifying the angle difference (the “error-based matching process”, Figure 3.1b).

In our initial studies, we then selected the hybrid through-plane angle as that from the BAS sample with the smallest in-plane angle difference to the microscopy. This through-plane diffusion orientation was then combined with the in-plane microscopy orientation to reconstruct the hybrid orientation which is both 3D and at microscopic resolution.

However, this matching process, based solely on the in-plane angular difference, was found to result in through-plane fibre populations (related to fibre bundles tracking along the anterior-posterior axis) being underestimated, with a bias for in-plane fibre populations (i.e. going left-right, or inferior-superior) which are better captured by the microscopy. Appendix 3.1 shows fibre orientations in the cingulum with a strong left-right orientation, though the cingulum

primary bundle runs anterior-posterior. Consequently, the matching error was edited to be the combination of the angle difference and the signal fraction estimated from dMRI BAS (related to the volume fraction, where more dominant fibre bundles have higher signal fractions), to more accurately account for the relative contributions of different fibre populations. The probability, p_i, of selecting BAS sample i, was calculated as the product of the BAS signal fraction and the cosine of the angular difference between the dMRI in-plane angle and the PLI angles. This approach assigned higher selection probabilities to samples with larger signal fractions and smaller angular differences between the BAS in-plane and PLI angles. We then selected our BAS sample using cumulative probability distribution sampling, a widely used machine learning method that is used to sample items from a list where each element has a specific weight or probability associated with it. The probabilities were first normalised to sum to one. The cumulative probabilities, C, were then computed by sequentially summing the individual probabilities for all elements (BAS samples), $C[i] = \sum_{j=1}^{i} p_j$. A random number, r, was then generated between 0 and 1 and we selected the BAS sample with the smallest index such that $C[i] \geq r$. This approach ensured higher-probability elements were prioritised while maintaining randomness in the selection process. The selected BAS sample provided the through-plane angle for the hybrid orientation, as described above. With this approach, diffusion MRI has greater influence on the assignment of microscopy pixels to fibre populations, particularly when the in-plane angle is ambiguous (i.e. two distinct fibre populations have the same in-plane angle when projected onto the microscopy plane) and in regions where the fibre bundle runs primarily through the microscopy plane.

Figure 3.2 shows the in-plane, through-plane angle and angle difference maps for matched PLI and dMRI orientations for an example PLI slide, demonstrating good agreement of the in-plane BAS and microscopy orientations and thus validating our approach.

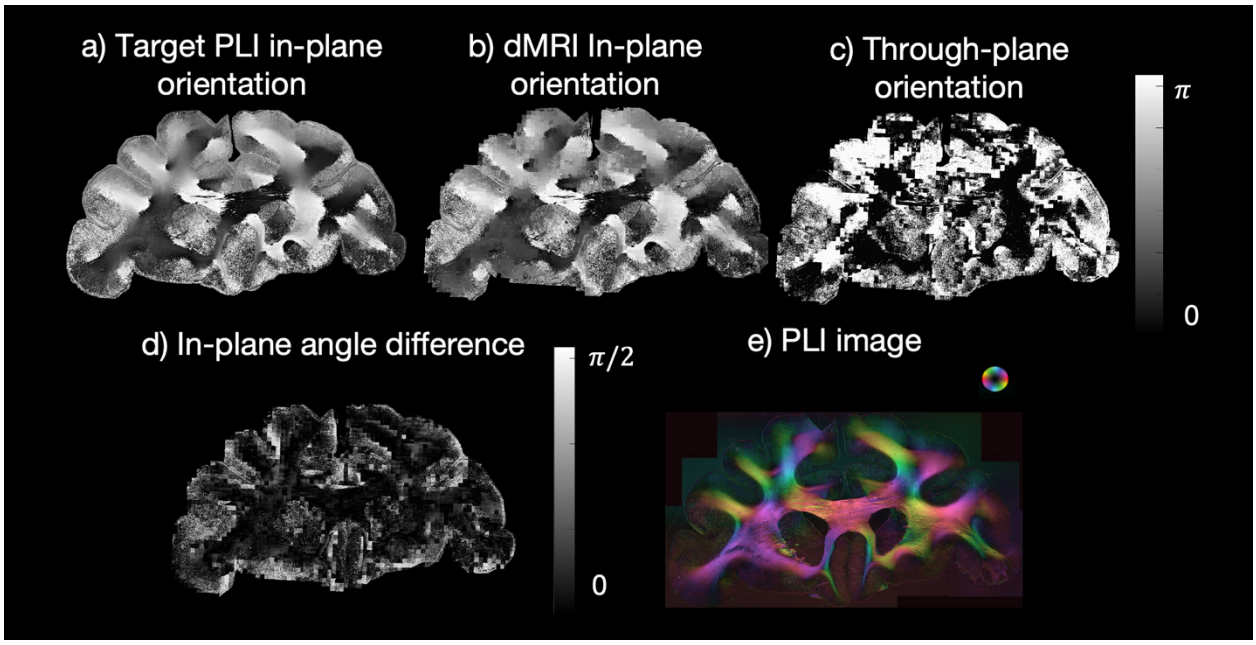


Figure 3.2: The angle component used in the hybrid orientation reconstruction.

a) The PLI in-plane orientation. b) The in-plane orientation from the diffusion BAS decomposition (represented by the angle of the 3D dMRI vector projected onto the microscopy plane). Here we show the in-plane angle of the BAS sample that is most similar to the PLI. c) The through-plane orientation from the diffusion BAS decomposition (inclination angle); d) The in-plane angle difference between the target PLI orientation and the most similar BAS fibre orientation showing a small angle difference. e) The PLI hue-saturation-value with the colour-coded orientations.

3.2.4.2 Hybrid fibre orientation distributions (FODs)

Our method generated a hybrid fibre orientation per microscopy pixel. To summarise the hybrid orientations within a 3D voxel, these orientations were combined over a local 3D neighbourhood (a voxel) into a fibre orientation distribution (FOD) similar to those from diffusion MRI. The spatial resolution of the voxel (a user-defined, largely arbitrary value) decided the size of the local neighbourhood over which orientations were combined (Appendix 3.2). As such, the same hybrid orientations could be combined into FODs at multiple spatial resolutions. In this work, FODs were reconstructed at the spatial resolution of 1.0, 0.6, and 0.4 mm isotropic. Voxels of the required spatial resolution were first defined in MRI space. The hybrid orientations within the local neighbourhood of each voxel were then combined into a 3D frequency histogram of orientations for 256 evenly spaced points across a sphere. Spherical harmonics of order 8 were fitted to the histogram. This order was chosen to make our results most comparable with other, existing datasets, where order 8 is usually the default. However, higher order spherical harmonics could be used. dMRI-derived (CSD) FODs are typically not normalised for the integral to sum to one. To ensure our hybrid FODs had amplitudes similar to those from dMRI (i.e. to make the tractography outputs comparable), the hybrid FODs were

scaled on a voxel-wise basis so that the amplitude of the maximum hybrid/ CSD FOD peak was equivalent. This scaling method was chosen based on the visual evaluation of comparable outputs from the hybrid and diffusion tractography. Alternative approaches may involve aligning the mean amplitudes of the hybrid and dMRI FODs by equating the first spherical harmonic coefficient, corresponding to the l=0, m=0 term.

In BigMac, there was a region in the centre of the brain (approx. 1.8-3 mm thick) with missing microscopy because the brain was sectioned in two halves (an anterior and posterior block). In this region, the missing data were filled with the FODs from the dMRI data estimated via CSD (Tournier et al., 2007) (Appendix 3.3). To fill the missing data of the hybrid orientation at 0.4 mm and 1 mm, the CSD FODs were up-/down-sampled as appropriate with MRtrix3(Tournier et al., 2019).

3.2.4.3 Gelatine artefact

In certain most anterior PLI sections, background birefringence is observed both inside and outside of the tissue that varies slowly across the slide (Appendix 3.4). This is due to the anterior PLI slides being coated in a small amount of gelatine which aids the mounting of tissue sections onto the glass slides but which is also birefringent (Tobolsky, 1955). The posterior PLI slides were mounted on plain glass slides without gelatine and so do not suffer from this artefact. In the affected slides, orientations from the grey matter are unreliable, though orientations from the highly myelinated white matter appear reasonable, as the birefringence of myelin appears to dominate (Menzel et al., 2015). When working with the hybrid FODs, it would be possible to mask out the affected regions and replace them with FODs from CSD, or use hybrid orientations from another microscopy (e.g. Gallyas staining that does not suffer from this artefact). We have not implemented that here as our results primarily focus on white matter reconstruction that does not primarily include these grey matter regions.

3.2.5 Experiments

3.2.5.1 Tractography

Tractography was performed using MRtrix3 and FODs either derived from the hybrid method above (hybrid tractography), or from CSD (Tournier et al., 2007) of the dMRI data (diffusion tractography). Whole-brain tractography was achieved using the iFOD2 algorithm (Tournier et

al., 2010) with the following parameters: 30 seeds per voxel in the white matter, step size of 0.2 mm, cut-off value of 0.05, maximal length of 120 mm, and minimal length of 5 mm. Fibre bundle segmentation was performed with inclusion and exclusion masks from XTRACT to extract 42 tracts spanning the whole brain, including association, commissural, limbic and projection fibres (Warrington et al., 2020). The masks were warped from standard (F99) space to the BigMac diffusion space (Van Essen and Dierker, 2007).

The reconstructed tracts were further refined to remove the spurious streamlines (Figure 3.3). First, each streamline within a given tract was compared to the tract probability map from the population-based XTRACT white matter atlas obtained from 6 macaque brains (Warrington et al., 2020). The streamline was assigned a score based on the mean probability value of the voxels the streamline intersected. If the mean probability of a streamline was lower than 0.2, it was discarded (Yeatman et al., 2012). Second, streamlines that were 4 standard deviations longer than the mean fibre length or deviated over 5 standard deviations relative to the core of the fibre were removed. The parameters were chosen based on the literature and were fine tuned for our data (Yeatman et al., 2012). The density map of each tract was calculated on a voxel-wise basis as the number of streamlines per voxel divided by the total number of streamlines of the tract.

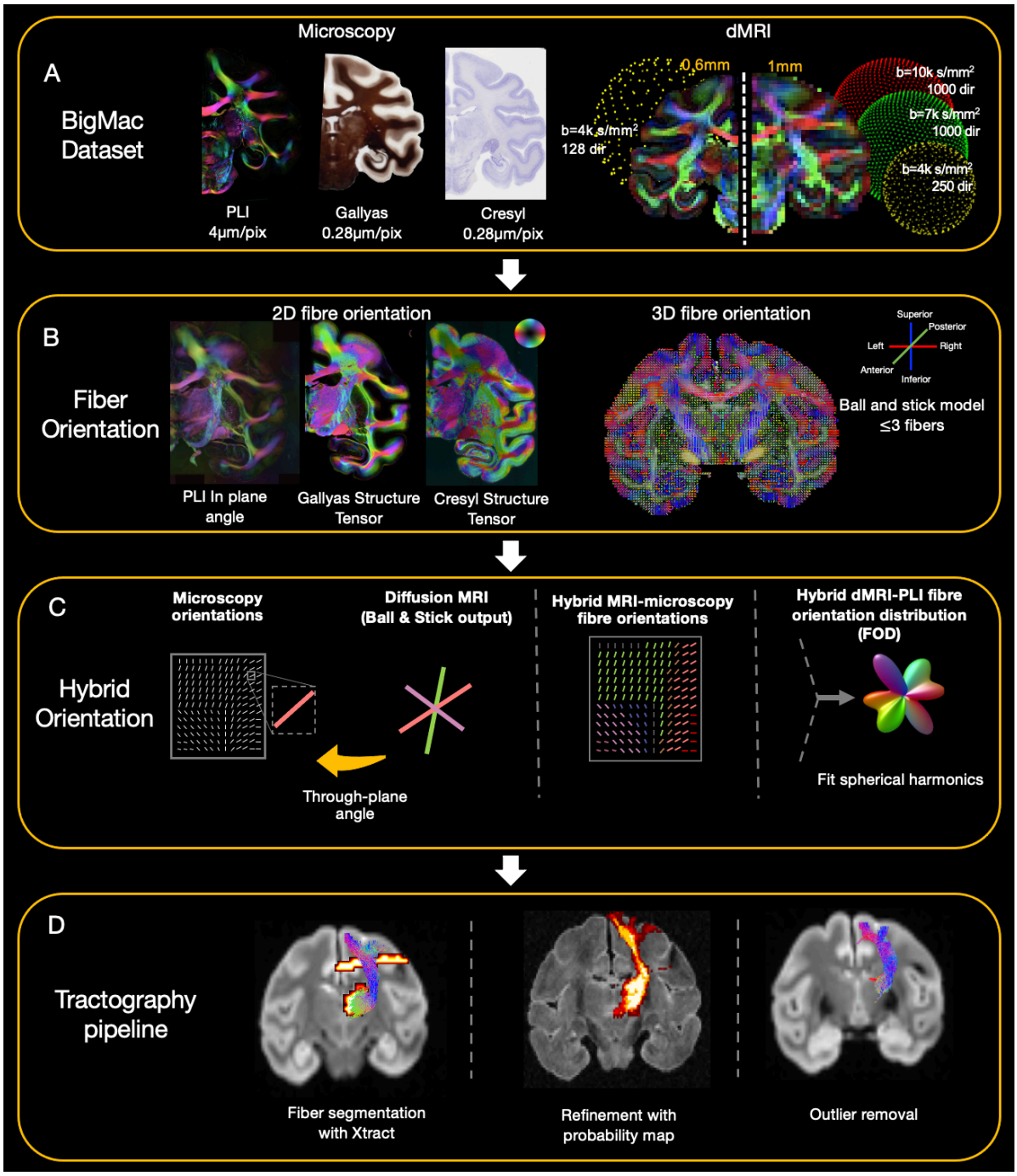


Figure 3.3: An overview of the analysis pipeline.

A) BigMac includes co-registered microscopy (PLI, myelin- and Nissl-staining) and postmortem MRI (dMRI/structural). B) Fibre orientations are extracted from each microscopy contrast (in-plane angle from PLI, structure tensor analysis from histology) and dMRI (Ball and Stick model). C) Hybrid orientations are generated with the in-plane orientation from microscopy and through-plane orientation from dMRI. D) The tractography results are optimized with XTRACT probability maps and outlier removal.

3.2.5.2 Gyral bias

Gyral crowns were defined as regions of high convexity and gyral walls were defined by their low curvature. FODs near the gyri and gyral streamline structure were examined for different spatial resolutions (0.4, 0.6 and 1 mm). Whole-brain tractography was then performed with the

parameters mentioned above, but now with 5 seeds per voxel to facilitate easier visualisation of streamlines near the cortex.

3.2.5.3 Bottleneck regions

We investigated two bottleneck regions within the motor network to determine whether hybrid tractography with different spatial resolutions can retain the topographic organisation of fibre bundles when passing through the bottleneck regions. First, we investigated whether the topographic medial-lateral representation of the trunk, arms and face areas across the motor cortex would be retained for fibres projecting through the internal capsule, as has been previously described (Kretschmann, 1988; Morecraft et al., 2002; Park et al., 2001). Second, we studied fibre bundles projecting from the primary motor and somatosensory motor cortex into the brainstem to determine whether the anterior-posterior distribution was retained (Asan et al., 2022).

The ROIs in the motor/somatosensory cortex were manually drawn on the structural MRI surface and then converted into volume space, warped to the dMRI and used for tractography seed masks. The internal capsule mask was obtained from the D99 atlas v2.0 (Saleem et al., 2021) and the brainstem mask was obtained from the subcortical atlas of the Rhesus Macaque (SARM) (Hartig et al., 2021). These atlases were selected over the F99 atlas because they provide templates that include subcortical brain regions. Both were warped to BigMac diffusion space. Seeding from the ROIs in the cortex, tractography was performed following the same parameters as above. Only streamlines going through the internal capsule or brainstem were retained. Tract density maps were generated for each ROI. The masks within the internal capsule and brainstem were colour-coded based on the ROI with the highest number of streamlines. The outputs in the internal capsule and brainstem were compared for both hybrid orientations and dMRI data.

To identify the bottleneck area, fixel-based analysis was performed with MRtrix3 (Tournier et al., 2019). A fixel describes a specific fibre population within a voxel. Tracts generated from each seed ROI were converted to fixel density maps using the tck2fixel command. Here the FOD was first segmented into discrete fixels and each streamline passing through a voxel was assigned to the fixel that exhibited best alignment (Dhollander et al., 2021). The fixel density map was then thresholded at 5% and converted into a fixel mask. The bottleneck area was

identified as the region where multiple fibre bundles use the same fixel when fibre tracking through the voxel (“multi-bundle fixels”).

3.2.5.4 Comparison with anatomic tracers

We compared our hybrid tractography to a weighted connectivity matrix derived from retrograde tracer data, which serves as a ground truth estimate of structural connectivity (Chad J. Donahue et al., 2016; Markov et al., 2012b, 2010). We used a weighted connectivity matrix constructed from tracer injections in 28 monkeys to examine the connectivity profiles of cortical-cortical pathways which is openly available on the Brain Analysis Library of Spatial maps and Atlases (BALSA) database (Van Essen et al., 2017). Tracers were injected into 29 regions of 91 cortical areas from the macaque atlas in the left hemisphere (Markov et al., 2010; Paxinos et al., 2024; Saleem and Logothetis, 2012), and the fraction of labeled neurons (FLNe), defined as the number of labeled neurons in each cortical area relative to the total number of neurons in the injection, was used to quantify connectivity. As we aimed to investigate the improvement of hybrid tractography over dMRI tractography with the tracer connectivity as a reference, we applied a threshold of 0.0001 to exclude very sparse tracer connections that are unlikely to be captured by tractography(Markov et al., 2012b). The cortical atlas was co-registered to BigMac space and hybrid/diffusion-only tractography was seeded from the 29 injection sites of the left hemisphere with the tractography parameters mentioned above. The number of streamlines projecting to each of the 91 cortical regions, divided by the total number of streamlines from that injection site, was used to construct the tractography connectivity matrix (29 x 91 areas). The connectivity matrix was generated for hybrid tractography at 0.4 mm, 0.6 mm and 1 mm.

To facilitate quantitative comparison via a ROC curve, the tracer matrix was first binarized using a threshold of 0.0001. The hybrid/diffusion-only connectivity matrices were then also binarized using thresholds ranging from 0 to 0.25 and the number of true positives (TP), false positives (FP), true negatives (TN) and false negatives (FN) counted for each threshold. The sensitivity was calculated as the true positive rate TPR=TP/(TP+FN) and specificity as the true negative rate TNR=TN/(TN+FP). The ROC curve was then plotted as sensitivity versus 1-specificity. The AUC value was calculated using MATLABs (2021a) perfcuve function. Overlap matrices (hybrid/diffusion tractography versus tracer) were then plotted for different tractography thresholds with the tracer in yellow, tractography in blue, and overlap in green. The correlation between tractography and tracer connectivity weights was evaluated by plotting

the data on a logscale to quantitatively assess the predictive power of tractography. Tracer data were thresholded at 1e-6 and tractography data were thresholded at 1e-4. The Pearson correlation coefficient (r) was calculated and reported.

3.3. Results

Note, we use the term MRI-microscopy to refer to the general method, as multiple microscopy contrasts can be used to create hybrid orientations. MRI-PLI is used to denote the hybrid orientations reconstructed using PLI which estimates the in-plane fibre orientation based on tissue birefringence (Axer, 2011; Axer et al., 2001, 2011b; Larsen et al., 2007).

3.3.1 Generating hybrid MRI-PLI fibre orientations

Hybrid MRI-microscopy orientations were estimated for each microscopy pixel and then combined over a local neighbourhood to create fibre orientation distributions (FODs). Figure 3.4 compares hybrid FODs at 0.6 mm isotropic to those obtained from dMRI using both the Ball and Stick model and constrained spherical deconvolution (CSD) where the latter also uses spherical harmonics making the FODs easy to compare. For the hybrid FODs, the microscopy mostly informed the orientations within the coronal plane, whilst the dMRI provided through-plane information in the sagittal and transverse views. We observe how the hybrid MRI-PLI FODs agree with the fibre orientations from Ball and Stick and CSD in all three views and faithfully depict U-shaped fibres connecting cortical areas between adjacent gyri. The fibre orientations are generally well aligned and follow expected anatomy, giving confidence in the fidelity of the hybrid outputs. This is true both for fibre orientations that lie primarily within the microscopy plane, such as the corpus callosum, and those that are primarily through the microscopy plane, such as the cingulum. The hybrid FODs are mostly narrower than CSD, indicating lower fibre dispersion (Howard 2019). Further, though crossing fibre populations are depicted in the hybrid FODs, they are less frequent, and the hybrid method estimates fewer, more dominant fibre populations compared to CSD. This is particularly evident at the white matter-grey matter boundary where the hybrid MRI-PLI FODs showed a more anatomically accurate pattern of fibres fanning into the cortex as frequently described in myelin-stained histology. We also observe fewer crossing fibres within some, but not all, white matter regions, including in parts of the centrum semiovale.

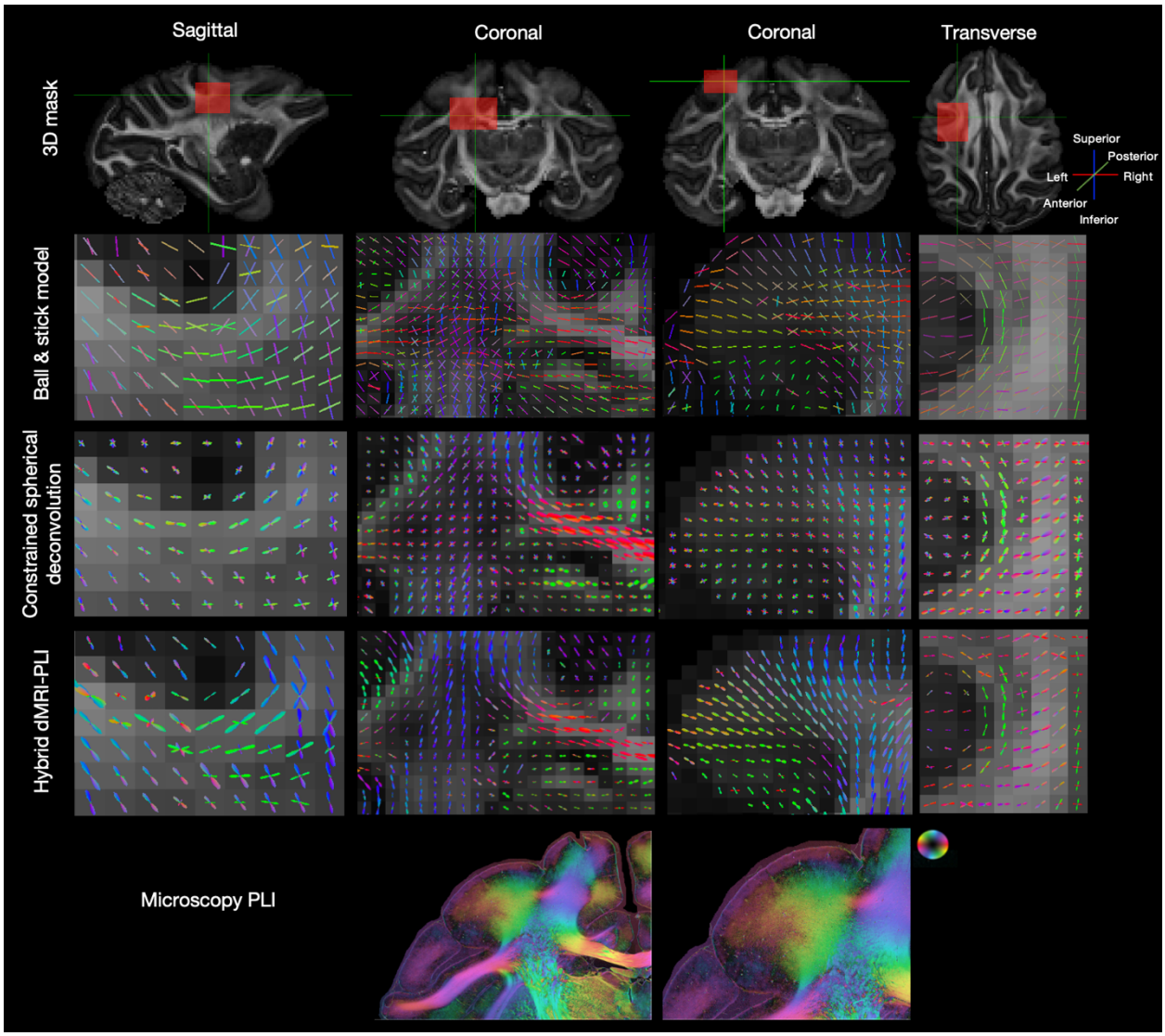


Figure 3.4: Comparison between dMRI FOD and hybrid MRI-PLI FOD.

The FOD generated from the Ball and Stick model (Top), constrained spherical deconvolution (Middle) and hybrid MRI-PLI (Bottom). The orientations in sagittal, coronal and transverse views are presented for U-fibres (left and right), a region covering the corpus callosum and centrum semiovale (middle left) and cortex (middle right). The PLI hue-saturation-value with the colour-coded orientations is provided at the bottom, and the contrast has been edited to highlight the grey matter. Note the colour schemes for the FODs and PLI are not equivalent.

One important feature of our hybrid method is that the hybrid FODs can be constructed at different resolutions from the same underlying data by changing the size of the combined neighbourhood region (Appendix 3.5). This allows us to investigate how spatial resolution affects tractography without confounding factors such as signal-to-noise ratio changes in MRI acquired at different resolutions. Appendix 3.5 demonstrates how using 0.6 mm resolution postmortem dMRI and PLI microscopy at 4 μm/pixel we created hybrid FODs at multiple resolutions: 1 mm isotropic, 0.6 mm isotropic, 0.4 mm isotropic, and 0.1x0.4x0.1 mm. In the

latter, the through-plane resolution (0.4 mm) was determined by the distance between consecutive PLI slices (0.35 mm).

3.3.2 Whole-brain hybrid MRI-PLI tractography.

Using fibre orientation estimates from the hybrid MRI-PLI, fibre bundles were reconstructed with a standard tractography pipeline (Figure 3.3). Figure 3.5 displays the reconstruction of three example tracts at the hybrid spatial resolutions of 0.4 mm, 0.6 mm, and 1 mm isotropic, alongside tractography using conventional dMRI-only analysis (CSD) at 0.6 mm. We specifically chose tracts that represent two extremes with respect to how the hybrid orientations relate to the underlying data: (i) the cortico-spinal tract predominantly runs in parallel to the microscopy plane such that microscopy is most informative; (ii) the optic radiation extends through the microscopy plane for which dMRI is most informative. Hybrid and dMRI tractography produce similar reconstructions of both tracts. Both tracts are characterized by intricate anatomical features: the cortico-spinal tract tracks through multiple crossing fibre regions, with branches extending to both superior and lateral regions of the motor cortex; the optic radiation contains a backward curving structure known as Meyer's Loop in the anterior portion (Chamberland et al., 2018). The hybrid method successfully reconstructs both complex structures. The uncinate fibre tract represents a case where the hybrid tractography does not perform so well. Most of the uncinate fibre can be robustly reconstructed with a clearly observed U shape structure extending from the anterior temporal lobe to the orbitofrontal cortex. However, the hybrid method fails to capture the most anterior part of the uncinate tracking through the orbitofrontal cortex, which is well reconstructed using dMRI-tractography. The limited anterior extent may be caused by registration inaccuracies due to the limited amount of brain tissue and less distinct anatomical features to drive the registration, or affected by the background gelatine in the most anterior part of the brain (c.f. 3.2.4.3 Gelatine artefact). The latter can likely explain differences in the tracts cortical terminations, rather than the tract core, as background gelatine was shown to predominantly affect PLI in the grey matter.

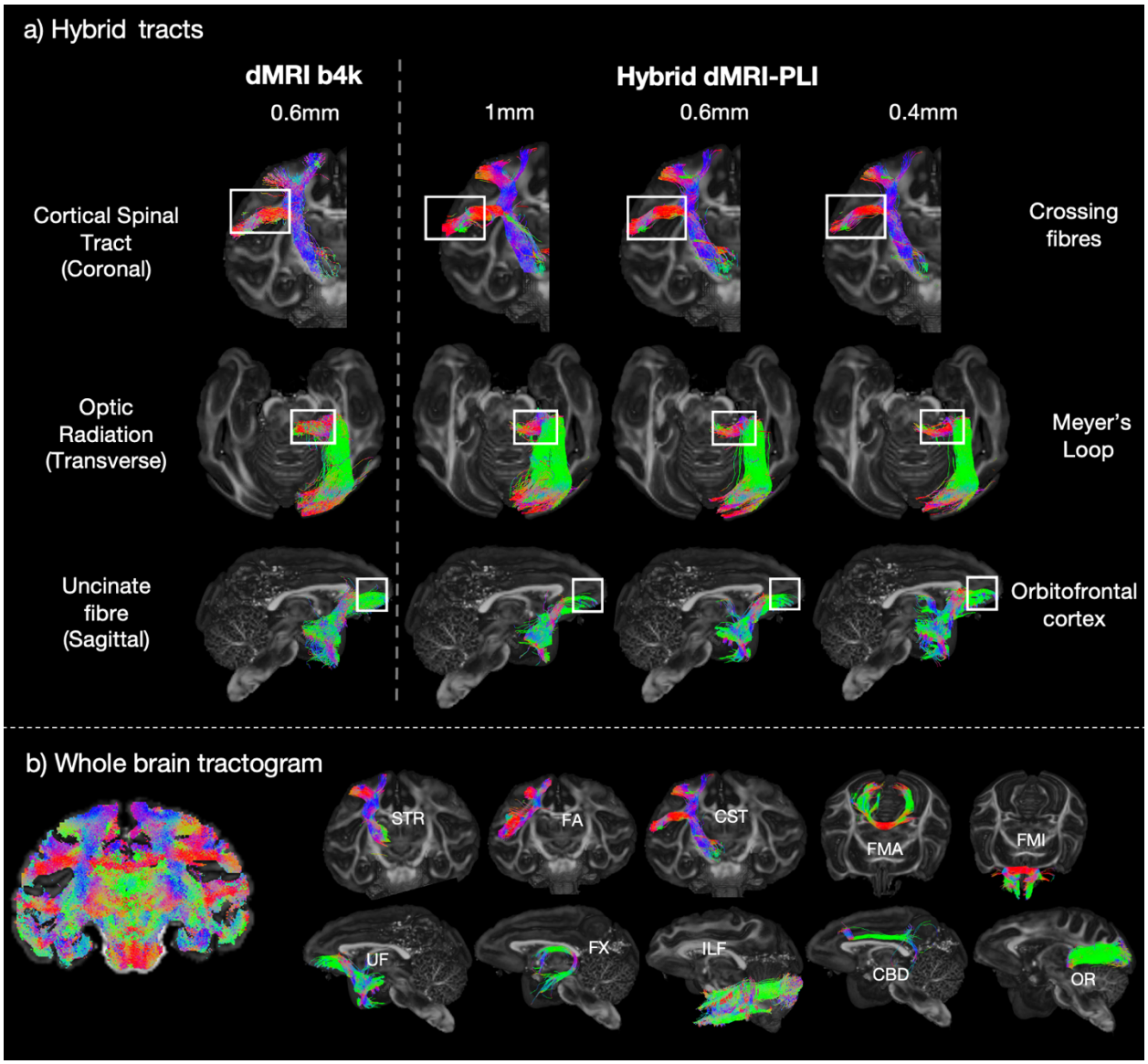


Figure 3.5: Tracts generated using the hybrid tractography.
a) The hybrid method can successfully reconstruct tracts throughout the brain including the corticospinal tract, an example tract within the coronal plane where microscopy is the most informative (Top), the optic radiation, a tract extending primarily along the anterior-posterior axis where dMRI provides most information (Middle), and the uncinate fibre (Bottom), a tract connecting the anterior temporal lobe and the orbitofrontal cortex. The anatomical features of interest are labelled with white boxes. The background anatomical image is the fractional anisotropy behind the tracts for visualisation. b) A whole-brain tractogram is shown. Ten example tracts generated from the hybrid tractography at 0.6 mm isotropic are illustrated including the superior thalamic radiation (STR), frontal aslant (FA), corticospinal tract in the coronal view, forceps major (FMA), forceps minor (FMI) in the axial view, uncinate fasciculus (UF), fornix (FX), inferior longitudinal fasciculus (ILF), cingulum subsection: dorsal (CBD), optic radiation (OR) in the sagittal view.

Having established that our method can provide reliable tract reconstructions, we then proceeded to reconstruct fibre bundles spanning the whole brain (Figure 3.5b & Appendix 3.6). The XTRACT toolbox was employed to define seed and target regions of interest (ROIs) for a

total of 42 tracts, comprising association, commissural, and projection fibres (Warrington et al., 2020).

The BigMac macaque brain was found to have a cerebral bleed in the right hemisphere, as observed in the MRI (loss of signal) and microscopy (missing tissue). This bleeding site primarily affected the grey matter but had some overlap with tracts including SLF2. Consequently, we observed asymmetry in the reconstruction of SLF2 between the left and right hemispheres (Appendix 3.7), where streamlines failed to track through the bleeding site on the right. Despite this limitation, other tracts were successfully reconstructed using the hybrid orientations, yielding anatomically expected structures (Figure 3.5b). The results further demonstrate that our method is applicable to a wide range of major white matter tracts and can reconstruct tracts spanning the whole macaque brain.

3.3.3 Hybrid tractography resolves the gyral bias at high resolution.

At the spatial resolution available to dMRI scans, the signal in voxels near the cortex is dominated by fibres projecting towards the gyral crowns. This causes streamlines to terminate at gyral crowns rather than accurately capturing sharp turns into gyral walls, leading to biases in connectivity mapping (Figure 3.6). This so-called gyral bias is in part due to the spatial resolution of dMRI (Schilling et al., 2017b; Tendler et al., 2022). Our hybrid method provides microscopy-informed fibre orientations that can be reconstructed at multiple spatial resolutions down to the near-native microscopy resolution. We investigated whether this approach can reduce or eliminate the gyral bias problem. In Figure 3.6, the gyral bias is evident in the 1 mm hybrid data, with fibres preferentially terminating at the gyral crown. However, with increased spatial resolution we observe an increasing number of streamlines extending towards the gyral walls, aligned with previous observations from microscopy (Tendler et al., 2022). The dMRI-only data shows similar trends of reduced gyral bias with increased spatial resolution, though with a less clean fanning pattern than that observed in the hybrid results. These results suggest that increasing the spatial resolution in both diffusion and hybrid tractography can overcome the gyral bias problem which is consistent with previous findings (Schilling et al., 2017b; Tendler et al., 2022).

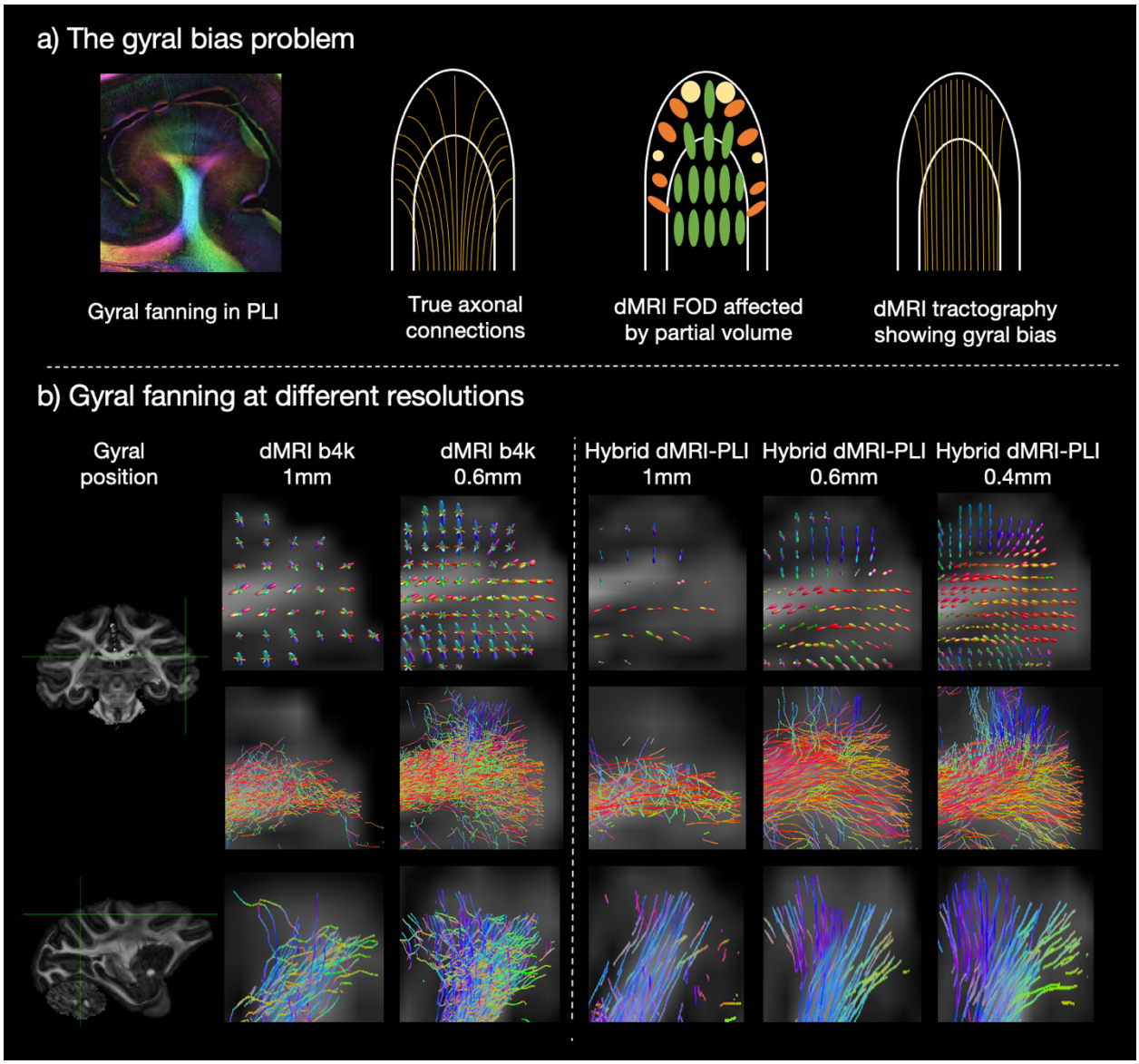


Figure 3.6: High resolution hybrid tractography eliminates the gyral bias.

a) Gyral bias. Diffusion tractography trajectories (streamlines) predominantly terminate at the gyral crowns but fail to turn into the gyral wall. The ground truth gyral fanning is demonstrated using PLI and a schematic representation of fibre connections. b) Gyral fanning at different resolutions. FODs (Top) and tractography streamlines of two gyri which primarily lie within (Middle) and through (Bottom) the microscopy plane. Outputs are shown for dMRI and hybrid MRI-PLI reconstructed at different isotropic resolutions. The gyral bias problem is present in the 1 mm, whilst the high spatial resolution of 0.4 mm successfully delineates the expected fibre fanning.

3.3.4 Hybrid tractography preserve topography in bottleneck areas.

Another limitation of dMRI tractography is the bottleneck problem. In bottleneck regions, multiple fibre bundles merge causing streamlines to become indistinguishably mixed at the spatial resolution of dMRI (Maier-Hein et al., 2017; Schilling et al., 2022). Without additional anatomical knowledge, it is difficult to retain information about the origin and termination of individual tracts passing through a bottleneck (Figure 3.7a). We further investigated the use of

hybrid method in tackling bottleneck regions to ask whether spatial resolution and/or the microscopy-informed fibre orientations can provide superior tract separation than typical dMRI analysis. Our first bottleneck of interest was the internal capsule (IC). This was motivated by the known topographic arrangement of fibres within this tract, mirroring the topography of the motor cortex. The medial-to-lateral functional organisation of the motor cortex has a topographic organisation, which is maintained along the anterior-to-posterior axis of the IC, with fibres originating from medial "trunk (and legs)" regions located anteriorly within the IC compared to those from lateral "face" regions (Kretschmann, 1988; Morecraft et al., 2002; Park et al., 2001). Streamlines were seeded from three ROIs defined on the precentral gyrus representing the trunk (and legs), arm and face regions with a medial-to-lateral distribution (Figure 3.7b). Figure 3.7c shows voxels in the IC colour-coded by the ROI with the highest streamline density. Figure 3.7d visualises the streamlines from each ROI projecting through the IC. Whilst dMRI mixes streamlines from distinct ROIs as they pass through the IC, the hybrid method consistently retains the strong topographic organisation of streamlines through the bottleneck region, where the order of trunk-arm-face regions along the anterior-posterior axis in the IC follows neuroanatomical expectations (Kretschmann, 1988; Morecraft et al., 2002; Park et al., 2001).

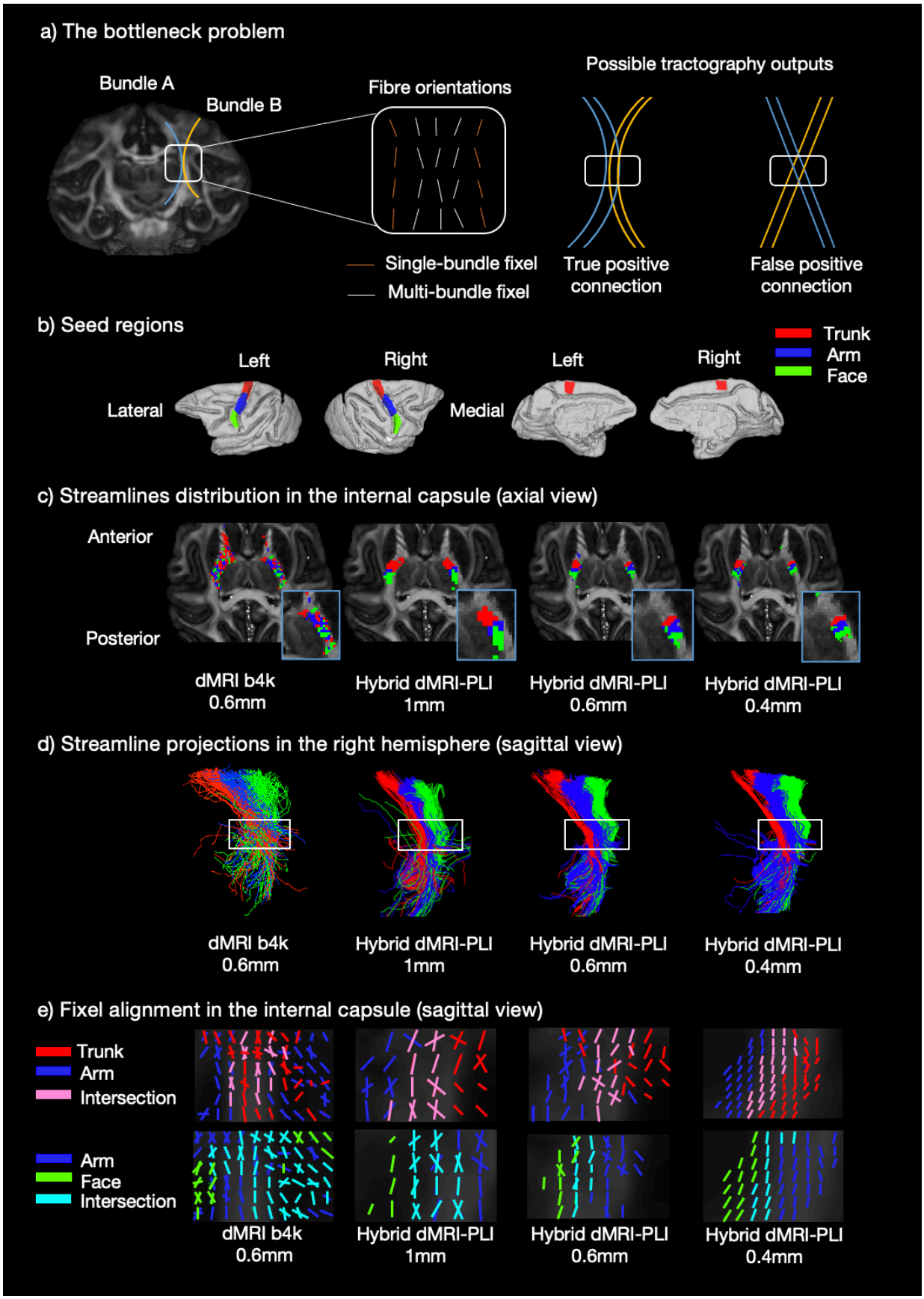


Figure 3.7: Hybrid tractography preserves topography in the internal capsule.

a) Bottleneck problem. An example in the internal capsule (IC) is shown as described in Chapter 2. b) ROIs relate to the functional representation of the trunk, arm and face regions shown for both medial and lateral parts of the

two hemispheres. Tractography was seeded from the ROIs to reconstruct streamlines passing through the IC. c) The density map and (d) streamline projections are shown. The blue box indicates a zoomed region in (c) and the white box in (d) is the bottleneck region of interest. The bottleneck problem is observed in the dMRI as streamlines from the ROIs are mixed. With the hybrid method, the streamlines from each ROI demonstrate a clear anterior-posterior distribution in the bottleneck region. e) Fixel-based analysis was performed to generate a fixel density map for each ROI in the internal capsule. The red, blue and green colours represent fixels associated with the trunk, arm and face regions respectively. Pink shows fixels associated with both the trunk (red) and arm (blue) ROIs. Cyan shows the intersection of fixels from both the arm (blue) and face (green).

Fixel-based analysis was then used to visualise the fibre populations in each voxel associated with each tract (Dhollander et al., 2021), quantifying tract orientation overlap within the bottleneck (as described in Chapter 2, section 2.3.7). In each voxel, the FOD was divided into discrete fibre populations, or "fixels". During tractography, each streamline passed through a voxel by following a specific fixel. Consequently, we can describe each streamline as a series of fixels projecting from our seed ROI. Combining across all streamlines in a given tract produced a fixel density map. This is analogous to a streamline density map, but now on a fixel rather than voxel basis. The density map was then converted into a tract-specific fixel mask using a 5% threshold.

Regions where a single fixel is transversed by multiple fibre bundles (referred to as a "multi-bundle fixel") are defined as bottleneck regions. Conversely, fixel associated with a single bundle is termed "single-bundle fixel" (Schilling et al., 2022). In Figure 3.7e, single-bundle fixels are colour coded using red, blue and green according to the ROI from which they are seeded (red=trunk, blue=arm, green=face). Multi-bundle fixels exhibit overlapping colours such as pink resulting from the overlap between the red (trunk) and blue (arm) fixels, or cyan resulting from the overlap between blue (arm) and green (face) fixels. In the dMRI analysis, we observe a large number of multi-bundle fixels (i.e. a large bottleneck region). This suggests that streamlines originating from different motor cortex ROIs tend to jump from one tract to the other. In the hybrid results, there is a clear separation of the ROIs on either side, with an intersecting bottleneck region in the middle where the two pathways run parallel to each other with shared orientations. This pattern is most evident in the 0.4 mm, as with increased spatial resolution, the bottleneck region decreases in size and the separation becomes clearer.

Together, the results demonstrate how, irrespective of the spatial resolution, microscopy-informed tractography mitigates the bottleneck problem in the IC. Interestingly, this holds even for the 1 mm hybrid reconstruction, a coarser resolution than that of the dMRI data used in this comparison (0.6 mm).

A second bottleneck region in the brainstem was studied using tractography seeded from ROIs in the primary motor and somatosensory cortex (Figure 3.8) (Asan et al., 2022). As above, density maps and tractography results are presented for dMRI and hybrid orientation at different spatial resolutions. The bottleneck problem is observed in both the dMRI and the hybrid method at 1 mm as streamlines from the two ROIs are mixed. In the hybrid high-resolution results (0.4 mm and 0.6 mm), the streamlines from each ROI demonstrate a separable distribution. Streamlines from the primary motor ROI are observed to be more anterior to those from the somatosensory ROI, mirroring the anterior-posterior topographic organisation of the cortex. As in the IC, the fixel-based analysis indicates how at higher spatial resolution there are fewer fixels associated with the bottleneck (pink), facilitating better tract separation.

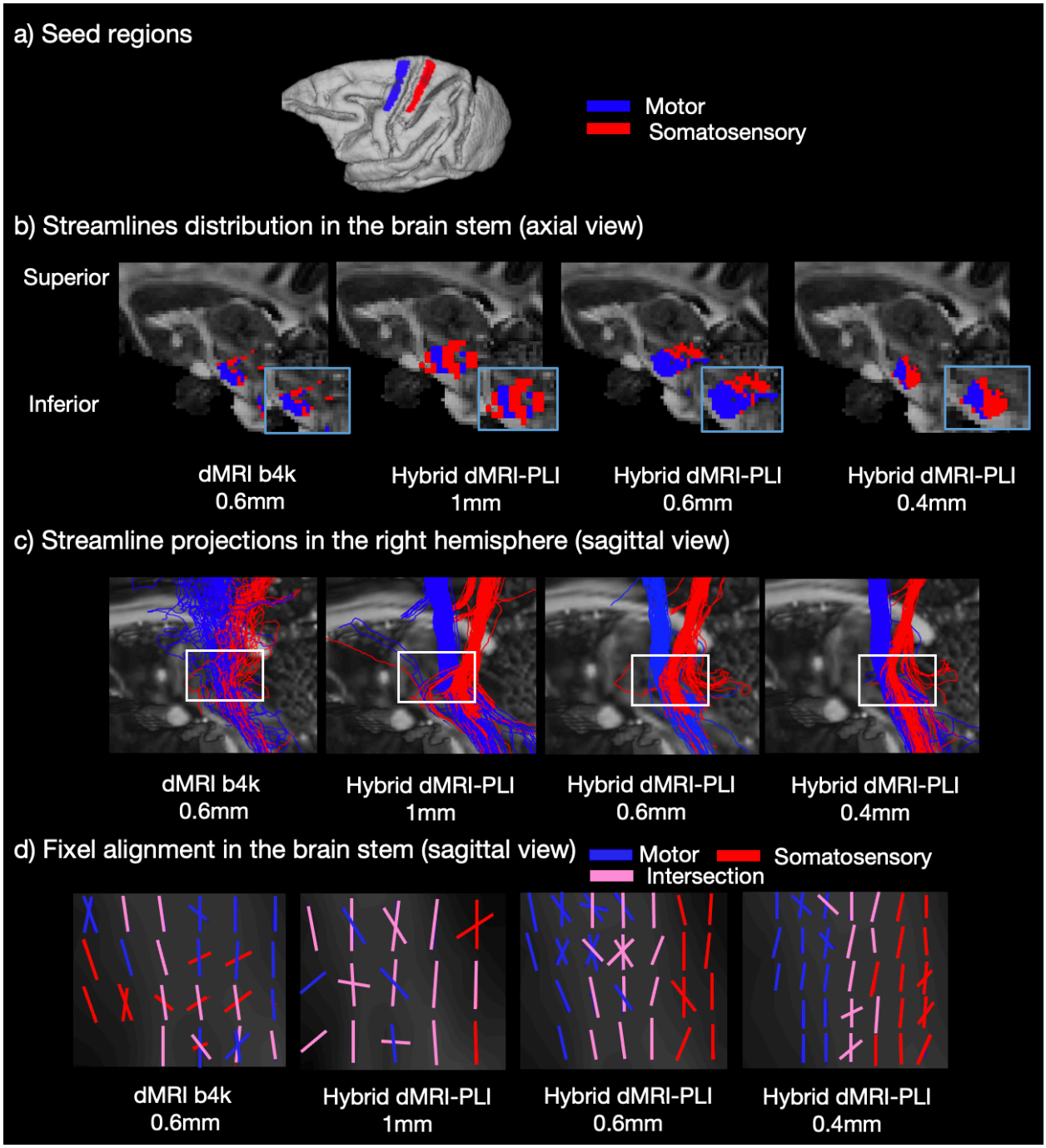


Figure 3.8: Hybrid tractography preserves topography in the brainstem.
a) ROIs in the primary motor (blue) and somatosensory (red) cortex. Tractography was seeded from the ROIs to reconstruct streamlines passing through the brainstem. b) The density map in sagittal view and (c) the streamline projections are shown. The blue box indicates a zoomed region in (b) and the white box in (c) is the bottleneck region of interest. The bottleneck problem is observed in the 0.6 mm dMRI and 1 mm hybrid method as streamlines from the two ROIs are mixed. In the hybrid method at higher resolution (0.6 and 0.4 mm), the streamlines from each ROI demonstrate a separable distribution in the brainstem. d) Using fixel-based analysis, fixels from primary motor cortex (blue), somatosensory cortex (red), and overlapping fixels (pink) are shown (d).

3.3.5 Comparison between hybrid tractography and tracer data.

To investigate the neuroanatomical accuracy of hybrid MRI-PLI tractography, Figure 3.9 uses a tracer-based connectivity matrix as an estimation of ground truth structural connectivity (Chad J. Donahue et al., 2016; Markov et al., 2012b, 2010). Figure 3.9b visually compares the normalized connectivity matrix from the tracer to those generated from dMRI and hybrid MRI-PLI tractography at 0.6 mm. As visual comparisons are difficult, we then binarized the tracer matrix using a threshold of 0.0001 and generated a receiver operating characteristics (ROC) curve to quantitatively evaluate the sensitivity and specificity of tractography in detecting brain connectivity relative to the tracer (Figure 3.9c). The hybrid method shows larger AUC (area under the ROC curve) with superior sensitivity compared to dMRI for the same level of specificity, and superior specificity for the same level of sensitivity, except for when specificity is very high and sensitivity is low where the methods become similar. Figure 3.9d shows overlap matrices between diffusion/hybrid tractography and tracer for different tractography thresholds. Tracer, tractography, and overlap are visually represented using distinct colours, allowing visualization of false positive, false negative, and true positive connections. At lower thresholds, the hybrid method demonstrates fewer false positive connections compared to dMRI tractography. Figure 3.9e correlates the tracer and tractography connection strengths, with similar correlation coefficients for the hybrid method ($r = 0.6150$) compared to dMRI ($r = 0.6343$) both of which are comparable to the correlation coefficient reported in previous studies (Chad J. Donahue et al., 2016). Similar results are found for hybrid MRI-PLI tractography at 1 mm and 0.4 mm (Appendix 3.8). These results suggest the hybrid method demonstrates neuroanatomical accuracy in estimating brain connectivity above that of typical diffusion tractography.

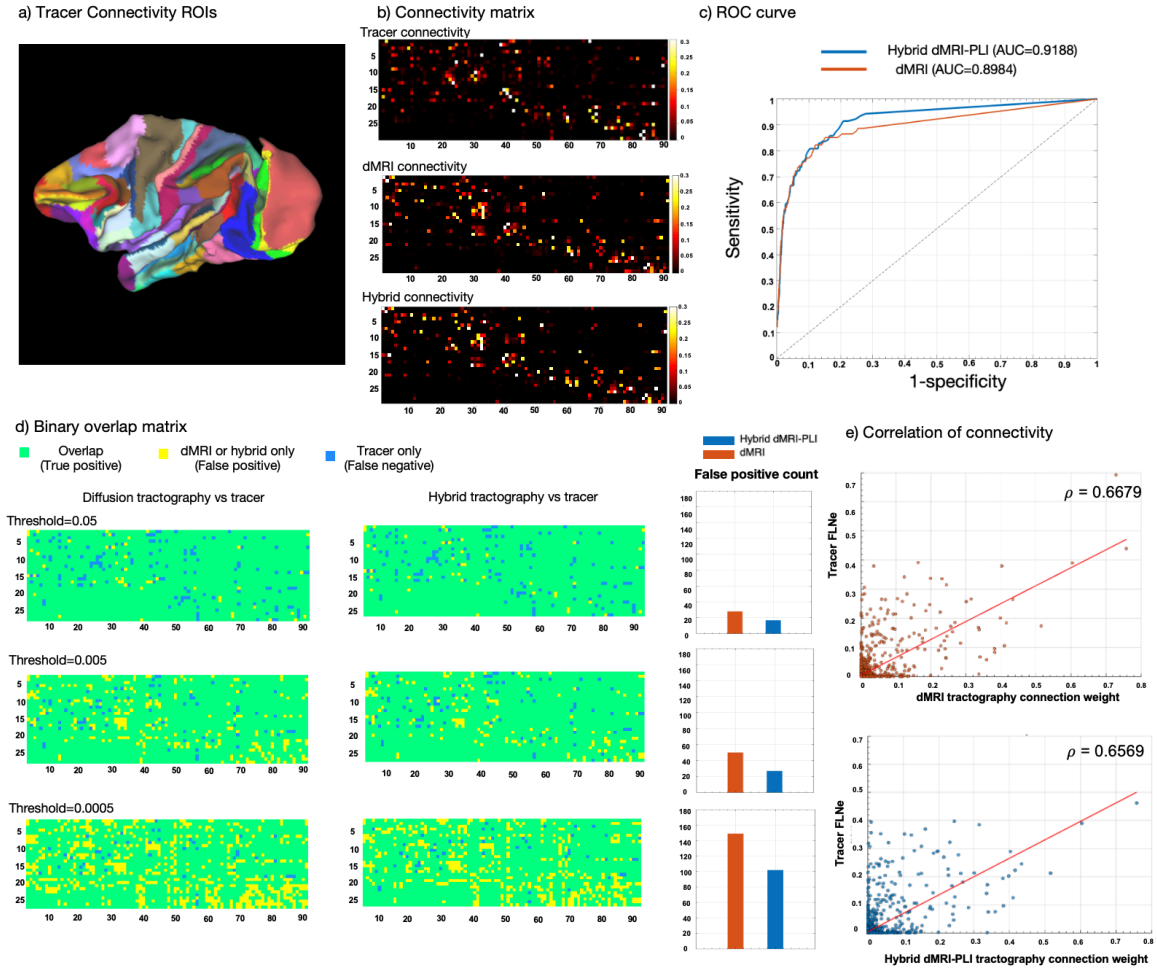


Figure 3.9: Comparisons of 0.6 mm hybrid and dMRI tractography to tracer data.

a) The 91 cortical areas of M132 surface parcellation are shown for the left hemisphere. b) Weighted matrices of size 29 x 91 are shown for the tracer, dMRI tractography, and hybrid tractography. c) An ROC curve illustrating the specificity and sensitivity of hybrid/diffusion-only tractography relative to the tracer connectivity. Different thresholds were applied to the tractography ranging from 0 to 0.25 and the true positive and false positive rates were calculated. d) Binary overlap matrices for different tractography thresholds where tracer only connections are represented in blue (false negative), tractography only in yellow (false positive), and overlap in green (true positive and negative). False positive connectivity was counted for dMRI and hybrid tractography. e) Scatter plot comparing tracer data with tractography (both dMRI and hybrid dMRI-PLI). Tractography data were thresholded at 1e-4 and tracer data were thresholded at 1e-6. Correlations were investigated for several different threshold for tractography (0.0005, 0.005, 0.05), producing similar results (data not shown). The red line denotes the least absolute residual fit, and ρ is the Pearson correlation coefficient. Data points on the x- and y- axis (x=0 or y=0) were excluded from the correlation analysis.

3.3.6 Hybrid MRI-microscopy can be performed with various microscopy contrasts.

The hybrid orientations can also be reconstructed from other microscopy contrasts that provide 2D fibre orientation information. Here we demonstrate this using structure tensor outputs from

myelin- and Nissl-stained histology also included in the BigMac dataset (Gallyas silver and Cresyl violet stains respectively) (Bigun et al., 2004; Budde and Annese, 2013; Budde and Frank, 2012b; Seehaus et al., 2015). Figure 3.10 shows how the resulting hybrid FODs at the 0.6 mm isotropic resolution are consistent among microscopy contrasts and follow our neuroanatomical expectations. We observe U-shaped fibres, also known as short arcuate fibres, connecting different gyri for three different microscopy contrasts with a consistent curving structure even in the through-plane orientation, the most challenging orientation for the hybrid method. Interestingly, we also observe notable differences in the hybrid outputs from the different microscopy contrasts, where both myelin- and Nissl-stains estimate considerably more crossing-fibre voxels than PLI, as quantified by the crossing fibre ratio calculated across the whole brain. Nonetheless, all three microscopy contrasts facilitate tractography reconstruction of the corticospinal tract, providing preliminary results on, and giving confidence in, the generalisability of the method. The application of the method to different microscopy contrasts provides opportunities for other multi-model datasets to reconstruct 3D fibre tractography.

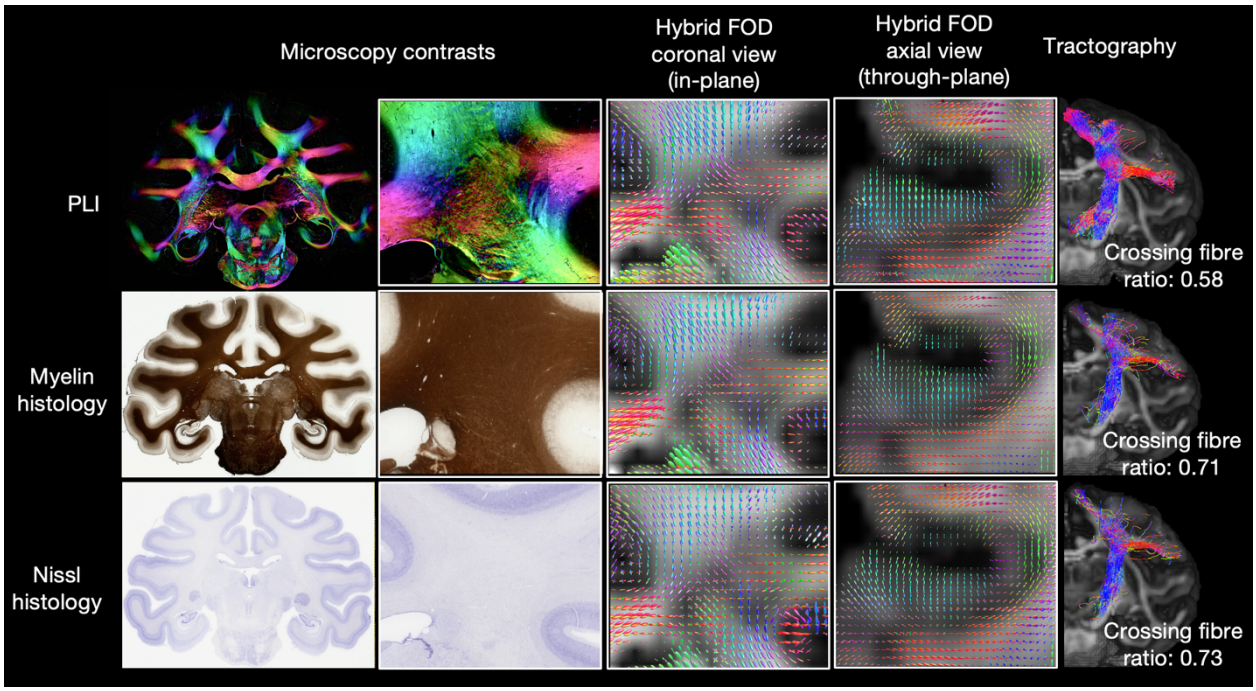


Figure 3.10: Multiple microscopy contrasts can inform hybrid tractography.
Hybrid fibre orientation distributions reconstructed at 0.6 mm resolution from different microscopy contrasts: PLI, myelin- and Nissl-stained histology (Gallyas silver/Cresyl violet-stained). All three contrasts show fibre orientations aligned with neuroanatomical expectations. Noticeably, the histology FODs depict more multi-fibre voxels (crossing fibre ratio = $N_{wm,multi-fibre}/N_{wm,voxels\ with\ fibre}$). These FODs can be fed into tractography to reconstruct white matter tracts (example corticospinal tract shown).

3.4. Discussion

We develop a method that facilitates microscopy-informed tract reconstruction across the whole brain without relying on 3D microscopy or invasive tracers. Our method requires data (diffusion MRI and light microscopy) that is readily attainable, meaning our method is translatable across datasets and species, including into humans. Utilising whole-brain, densely-sampled MRI and microscopy data in the macaque, we construct hybrid MRI-microscopy fibre orientations that are both informed by high-resolution microscopy and provide 3D information at the whole-brain level. By combining both modalities in our hybrid reconstruction we assigned the through-plane orientation of the BAS samples to their precise sub-voxel localisation and informed the 3D configuration of fibre orientations from the microscopy. By utilising a dMRI fibre reconstruction method that produces multiple fibre estimates per voxel, our hybrid method could "super-resolve" 3D fibre orientations at a resolution higher than the native MRI. We demonstrate how the hybrid orientations can be used by tractography algorithms for neuroanatomical investigation. Further, we show how the hybrid outputs (FODs and tractography) based on high fidelity microscopy can be directly compared to dMRI equivalents within the same subject, making the hybrid method a valuable resource for the dMRI modelling community. Notably, the hybrid orientations can be reconstructed at different spatial resolutions using the same underlying data, facilitating meaningful tractography comparisons across different resolutions without signal-to-noise confounds. This allows for novel insights into tractography performance that can potentially inspire future algorithms or study design. In addition, the high-resolution and myelin-specific tractography achievable via the hybrid method can provide neuroanatomical insight, such as interesting patterns of axonal organisation within larger white matter tracts, or reconstruction of the myelinated connectome.

Our data fusion method uses microscopy information to drive tractography-based tract reconstruction with minimum reliance on the dMRI. This is advantageous as it enforces the outputs to be maximally informed by and at the high resolution of the detailed microscopy. This mindset is considerably different from previous approaches that aim to determine optimal tractography protocols by first performing tractography, comparing these outputs to microscopy/tracing, and using this comparison for parameter up-date or to study how various parameter combinations or methods influence the tractography sensitivity and accuracy (Yendiki et al., 2022). Microscopy-informed connectome reconstruction of smaller brains can

alternatively be achieved from 3D microscopy data alone. However, to date this has not been achieved at the whole-brain level in larger primate or human brains, as 3D microscopy methods are typically restricted to imaging millimetre scale samples (Georgiadis et al., 2020; Masís et al., 2018; Reckfort et al., 2015), and tracers are typically limited to one or two injection sites per animal. This work provides whole-brain, microscopy-informed connectomics in the macaque, a primate model with complex white matter similar to humans. This white matter complexity is important as it means that models trained on this bespoke dataset may benefit in vivo tractography in human brains where microscopy is not available. In comparison, rodent brains have far fewer crossing-fibre voxels, meaning that models trained on rodents may be less suitable for application to humans.

We investigated whether the hybrid method could address two known challenges in dMRI: the gyral bias and bottleneck problem. Existing dMRI model-based solutions to the gyral bias problem often rely on assumed knowledge of fibre architecture over a canonical gyrus which are often obtained from invasive imaging methods such as microscopy, involving separate brains or even species (Aydogan and Shi, 2018; Wu et al., 2020). For example, St-Onge et al. incorporated cortical surfaces derived from anatomical images to model the sharp turn of fibres, as fibres were constrained to be radial to the cortical surface (St-Onge et al., 2018). Alternatively, Cottaar et al. modelled fibre orientation using a vector field, constraining the orientations with the anatomical geometry (Cottaar et al., 2021). In comparison, the hybrid method directly uses high spatial resolution microscopy data in the same brain. The results (Figure 3.6) suggest the gyral bias can be reduced and the expected pattern of fibre fanning can be realised with improved spatial resolution (Schilling et al., 2022). We observe similar trends in both hybrid and diffusion tractography, though the results are more striking in the hybrid method. This may result from the hybrid fibre orientations being more directly related to myelinated axons which in microscopy follow clear fanning patterns across the gyrus ex vivo. In comparison, dendrites complicate dMRI modelling for fibres projecting into the cortex. Considering the global volume difference between humans and macaques (macaque brain volume is ~1/12 of the human brain volume), the spatial resolutions we used (1 mm, 0.6 mm and 0.4 mm) are approximately equivalent to the 2.5, 1.5, and 1 mm in humans, roughly corresponding to resolutions achievable in the clinic, in typical research data and among the highest achievable resolution so far. Consequently, the resolution examined here in the macaque may provide guidance on solving some tractography challenges in the human brain.

Our hybrid method showed particularly promising results when applied to bottleneck regions, where the hybrid tractography resolved patterns of white matter organisation that mirrored the topographic organisation of the cortex (Figure 3.7). Bottleneck regions – where multiple fibre bundles converge and share the same orientations – are prevalent in the brain and have been shown to affect a large proportion of white matter tracts leading to false positive streamlines (Maier-Hein et al., 2017; Schilling et al., 2022). Existing solutions relying on anatomical priors or microstructural characteristics demonstrate the potential to identify bundle-specific fibre orientations, which have been shown to effectively reduce false-positive streamlines (Schiavi et al., 2020; Wasserthal et al., 2018b). For example, Girard et al. addressed ambiguities in fibre configurations through microstructure modelling (Girard et al., 2017), and Rheault et al. enhanced tracking specificity by integrating both anatomical and orientational priors (Rheault et al., 2019). However, these approaches remain susceptible to errors in estimating fibre orientations from dMRI data. In contrast, our method directly utilizes microscopy data, thereby bypassing microstructural assumptions and model-based limitations to address the bottleneck problem more accurately. First, we investigated the bottleneck problem in the internal capsule, a relatively thin white matter structure where multiple tracts intermingle to pack within a small volume. Our ability to conserve the order of the motor cortex projections along the anterior-posterior axis in the internal capsule was evaluated. The topographic organisation was conserved in the hybrid tractography at all resolutions including 1 mm but lost in the diffusion tractography with 0.6 mm. This implies that our ability to resolve the anterior-posterior pattern of white matter organisation in the internal capsule is related to some specific feature of the hybrid FODs, rather than simple improvements in spatial resolution. For example, the hybrid FODs often have lower dispersion or fewer crossing fibres than the dMRI (likely due to their high specificity to myelin) which may result in streamlines leaving the cortical seed region and following a smooth and continuous fibre bundle instead of jumping between different tracts. Second, we studied the bottleneck region at the brainstem where PLI has been shown to be superior to dMRI when identifying smaller fibre bundles such as pyramidal tracts (Axer, 2011). Our ability to retain the order of primary motor and somatosensory cortex along the anterior-posterior axis of the brainstem was demonstrated with the hybrid method at higher resolutions (0.6 or 0.4 mm), but not in the 1 mm hybrid outputs or diffusion tractography at 0.6 mm. These results suggest that improved spatial resolution combined with our hybrid specificity can again help to resolve the bottleneck problem. Together, hybrid results present a novel way of investigating the bottleneck problem. Our method has the potential to resolve

topographic patterns of white matter organisation within major fibre bundles that are currently considered relatively homogeneous or where long-standing hypotheses regarding white-matter topography are currently still lacking empirical evidence (Belyk et al., 2021).

The hybrid MRI-PLI tractography is generally well aligned with that of dMRI, though there are also some noticeable differences. To better understand whether the hybrid outputs better reflect ground truth anatomy, we compare the connectivity of dMRI and hybrid tractography to tracer connectivity data from other macaque brains (Markov et al., 2012b). Our analysis reveals that the hybrid method outperformed dMRI tractography in terms of simultaneously achieving sensitivity and specificity, as indicated by the ROC curve (Figure 3.9). We hypothesise this may be because the hybrid FOD is based on myelin-sensitive microscopy and so is fairly myelin-specific, whilst the dMRI FOD is influenced by multiple tissue features (e.g. dendrites, glia, and extra-cellular space) (Alexander et al., 2019; Jespersen et al., 2007; Stanisz et al., 1997). Consequently, the hybrid FODs may allow for superior tracking, particularly in regions with considerable partial voluming such as in the cortical ribbon or in and around subcortical structures.

We demonstrate how our method can be applied to different microscopy contrasts, each of which may provide subtly different orientational information (Figure 3.10). Here, we observe a lower crossing fibre ratio in the hybrid MRI-PLI FODs, when compared to hybrid FODs reconstructed from either myelin or Nissl-stained histology. Note, this can also be observed when comparing 2D structure tensor and PLI data, suggesting it is a primarily a characteristic of the inputted microscopy data, rather than a feature of the hybrid method itself. This difference in crossing fibres is likely due to the nature of PLI which becomes less informative when a pixel (covering a volume of 4x4x50 μm with 50 μm being the tissue thickness) contains multiple fibre populations in which case PLI tends to output the orientation of the more dominant fibre population (Dohmen et al., 2015). In comparison, the histology data has a finer spatial resolution at 0.28 μm/pixel, where around 200 histology pixels fit into a single PLI pixel (4 μm/pixel), and so can likely better delineate crossing fibre populations (Rowe et al., 2013). The crossing fibre ratio may also be impacted by the size of the Gaussian kernel used in the structure tensor analysis, where in BigMac we used a kernel of $\sigma = 10$ pixels ~ 3 μm, the effect of which warrants further investigation. Future studies should focus on further validating the hybrid outputs across different microscopy contrasts, including comparisons with tracer connectivity data where our hybrid FODs provide new opportunities for validating the structure

tensor parameters. Careful consideration should be taken when choosing the microscopy data for hybrid analysis as different microscopy contrasts can produce different results and provide specificity to different microstructural features. For example, the myelin-stain histology only includes myelinated structures, missing contributions from unmyelinated axons. Nissl-stain in the white matter, on the other hand, visualises glial cell bodies, where oligodendrocytes and astrocyte soma tend to be oriented in parallel to the surrounding axons (Baumann and Pham-Dinh, 2001; Johansen-Berg and Behrens, 2014). Future work into hybrid outputs from different microscopy contrasts may provide novel neuroanatomical insight into microstructure organisation.

The hybrid MRI-microscopy method has several limitations. First, it relies on the combined analysis of MRI and microscopy which should be carefully co-registered. We found that tracts reconstructed from the hybrid FODs in the most anterior part of the brain such as the uncinate fasciculus in Figure 3.5 had less anterior reach compared to the dMRI reconstructions, which in this case more closely followed neuroanatomical expectations. This may be related to errors in the dMRI-microscopy co-registration in this region and/or errors in PLI orientations affected by background gelatine on the anterior slides, though this was primarily found to affect orientations the grey matter rather than the more myelinated white matter where tissue birefringence tended to dominate (Appendix 3.9). dMRI-microscopy co-registration in BigMac was achieved via a state-of-the-art registration tool called TIRL (Huszar et al., 2023a). However, due to the limited anatomical information at the most anterior or posterior brain (where sections show little or no white/grey matter contrast), the registration accuracy with these sections is lower. Second, the hybrid method does not provide ground truth information about the tract structure, thus requiring careful consideration when interpreting the neuroanatomical implications of its outputs. Other technology such as micro-CT can provide fibre orientations in both 2D and 3D at micrometer level, and so may provide validation opportunities for the hybrid tractography (Karamov et al., 2020; Masís et al., 2018). Third, our hybrid orientations will be affected by the spatial resolution of the dMRI. BAS model provides multiple orientations per voxel, capturing the range of fibre directions but not their spatial locations, and microscopy data "super-resolve" dMRI information. There is a trade-off during dMRI acquisitions between higher spatial resolution and higher angular resolution within a limited time. The former reduces partial volume effects, and the latter improves crossing fibre estimation and SNR. The optimal trade-off for hybrid tractography likely depends on the fibre tract, with high spatial resolution

benefiting smaller tracts and high angular resolution aiding crossing fibre regions (Jones et al., 2020). Fourth, direct in vivo translation of the hybrid method presented here would be challenging, as it is difficult to obtain microscopy data in vivo. To circumvent these limitations, ongoing work in our lab focuses on using machine learning methods to translate the benefits of the hybrid method in vivo, when only limited dMRI is available.

There is ongoing work to further improve the hybrid MRI-microscopy method. First, in our current method, each hybrid orientation is considered independently from its surrounding neighbours. Here some similarity or neighbourhood constraint could be used to enforce local smoothness for very high-resolution reconstructions. Second, the BigMac data we used to reconstruct hybrid orientation has only semi-dense sampled microscopy, with a gap of 350 μm between consecutive PLI slides. Therefore, our microscopy only partially explains the fibre orientations within a voxel and our ability to reconstruct FODs at high resolution is limited by the effective through-plane resolution (350 μm gap). As BigMac includes both Nissl- and myelin-stained histology as well as PLI, future work can combine the three microscopy contrasts into a single hybrid FOD to further increase the through-plane resolution/sampling. Third, one benefit of our method is that we have both high spatial and angular resolution for the hybrid orientations. As such, we may benefit from fitting higher-order spherical harmonics to our hybrid FODs which may further improve our ability to capture small separation angles between multiple fibre populations. Fourth, our current method for hybrid orientation estimation did not consider the PLI retardance, which could inform the accuracy of the PLI orientation estimation. This could be considered in future implementations to down weight the microscopy orientation information in regions of higher uncertainty.

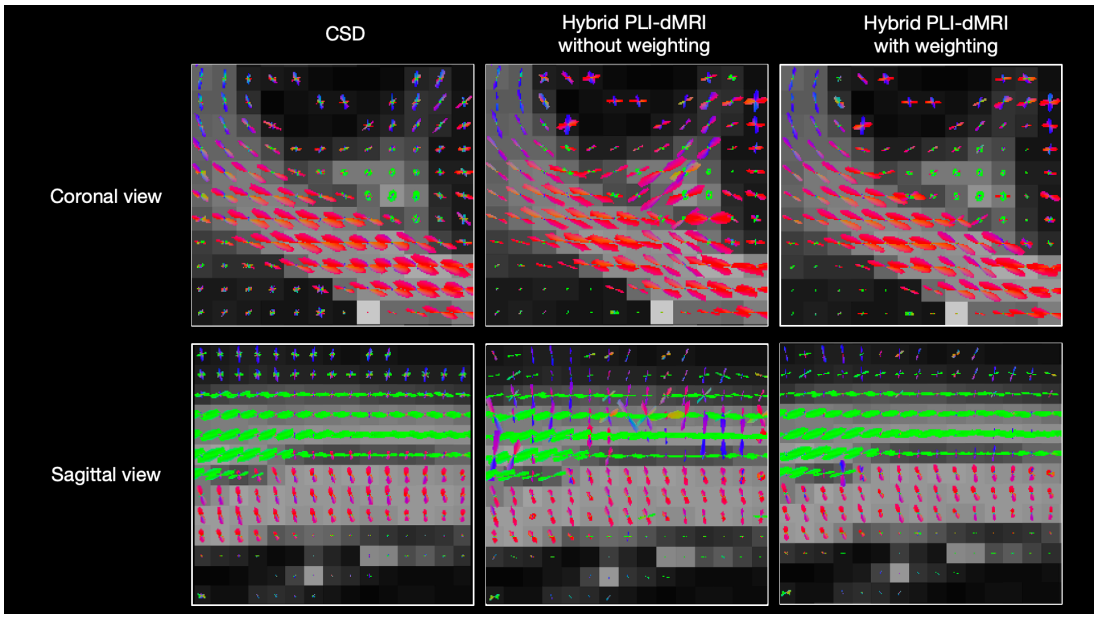
The hybrid outputs (FODs at different resolutions, provided as NIFTI files) are made openly available to the wider community and offer new opportunities for microscopy-informed, whole-brain tractography. The outputs can be utilised for novel neuroanatomical investigations, or to validate and drive in vivo MRI acquisition and analysis (e.g. by helping define the spatial resolution required to observe certain characteristics of the white matter). For example, future work could use the hybrid method to study the superficial white matter (Guevara et al., 2020) that connect neighbouring cortical regions with a U-shaped trajectory, as well as fibre tracking within subcortical regions (Maller et al., 2019). Though these regions represent challenging areas for diffusion tractography, the hybrid method based on high-resolution microscopy, coupled with the high specificity to axons, may provide superior fibre tracking.

The successful application of our method to different microscopy contrasts opens avenues for hybrid tractography to be performed on other multi-modal datasets that previously could not be used to perform 3D tract reconstruction (Budde and Annese, 2013; Mollink et al., 2017a). This includes data acquired from other species facilitating cross-species investigations into structural connectivity, and small tissue blocks that focus on a single white matter bundle or region of interest (Schilling et al., 2019b; Tendler et al., 2022). For a microscopy dataset without dMRI, it is even possible to input dMRI data from another brain or atlas into the model, though the results may be less reliable due to the mismatch of the underlying brain microstructure. Crucially, our method relies on data that can and are being acquired in the human brain (eg. Big Brain project) (Amunts et al., 2013). Future whole-brain suitable human data will provide exciting opportunities for hybrid reconstruction of the microscopy-informed human connectome, and cross-species comparisons using the macaque data presented here.

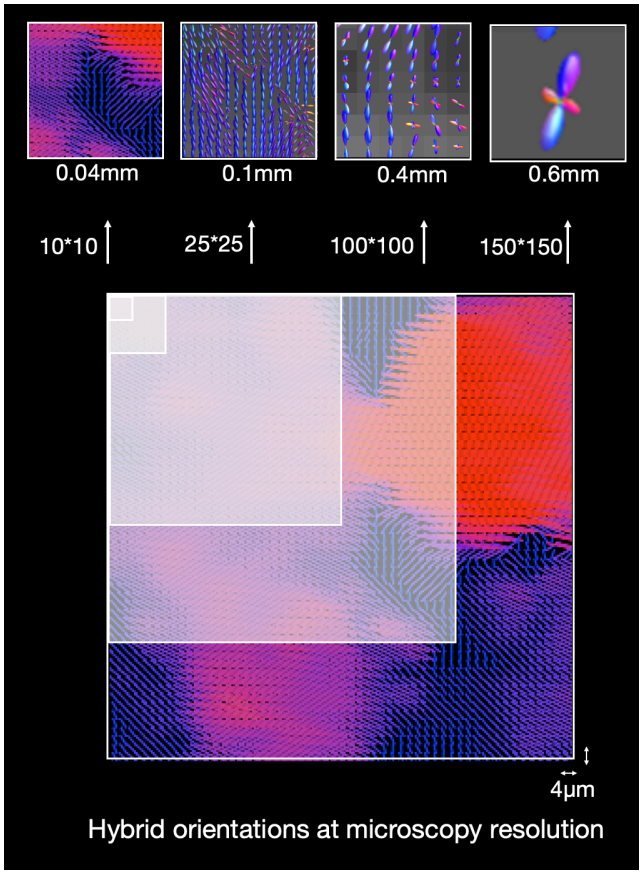
Data and code availability

The pre-processed BigMac data with MRI and microscopy has been previously made openly available via the Digital Brain Bank (https://open.win.ox.ac.uk/DigitalBrainBank/#/). Whole-brain volumes of the fibre orientation distributions output from the hybrid method will be made openly available on the Digital Brain Bank via a data sharing agreement to ensure the data is used for purpose which satisfy research ethics and funding requirements. This includes dMRI-PLI, dMRI-Gallyas, dMRI-Cresyl FODs at multiple spatial resolutions (1, 0.6 and 0.4 mm isotropic), and dMRI FODs at 0.6 mm. The code for constructing the hybrid orientation from dMRI and microscopy is accessible via (https://git.fmrib.ox.ac.uk/srq306/hybrid_microscopy_dmri). The code was written in MATLAB with further tutorial documentation and code explanation provided at (https://open.win.ox.ac.uk/pages/srq306/hybridtractographydoc/). The MATLAB scripts can be edited for other datasets with fairly minimal effort while future efforts aim to package it into a more widely applicable toolbox.

Appendix

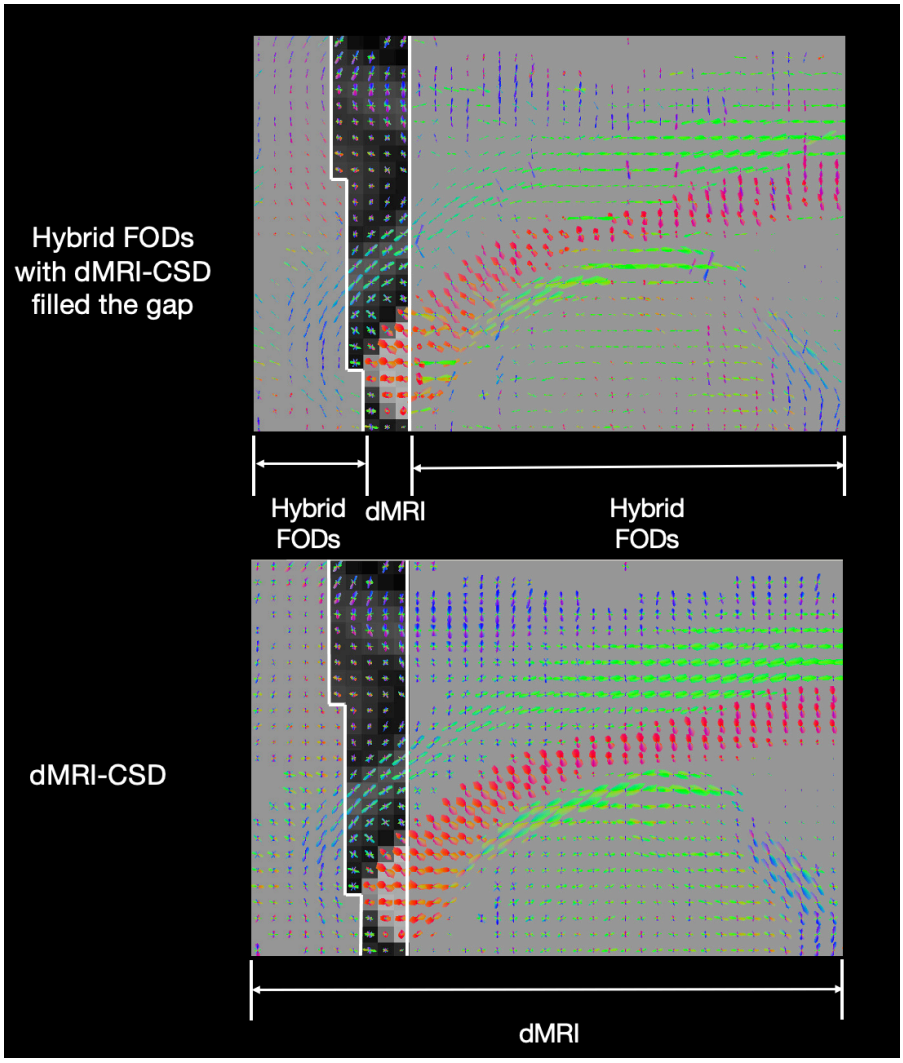


Appendix 3.1: Resolving orientation bias in the Cingulum using Ball and Stick (BAS) signal fraction weighting.
In the cingulum, the dominant fibre orientation is anterior-posterior, as shown by the CSD reconstruction (Left). During the error-based matching process, selecting the through-plane angle from the BAS sample with the smallest in-plane angle difference to the microscopy introduces a bias toward the in-plane angle (Middle), which is more readily captured by microscopy. To address this, the matching error was refined by combining the angle difference with the signal fraction estimated from dMRI BAS. This adjustment effectively resolves the observed bias, enabling more accurate orientation mapping (Right).

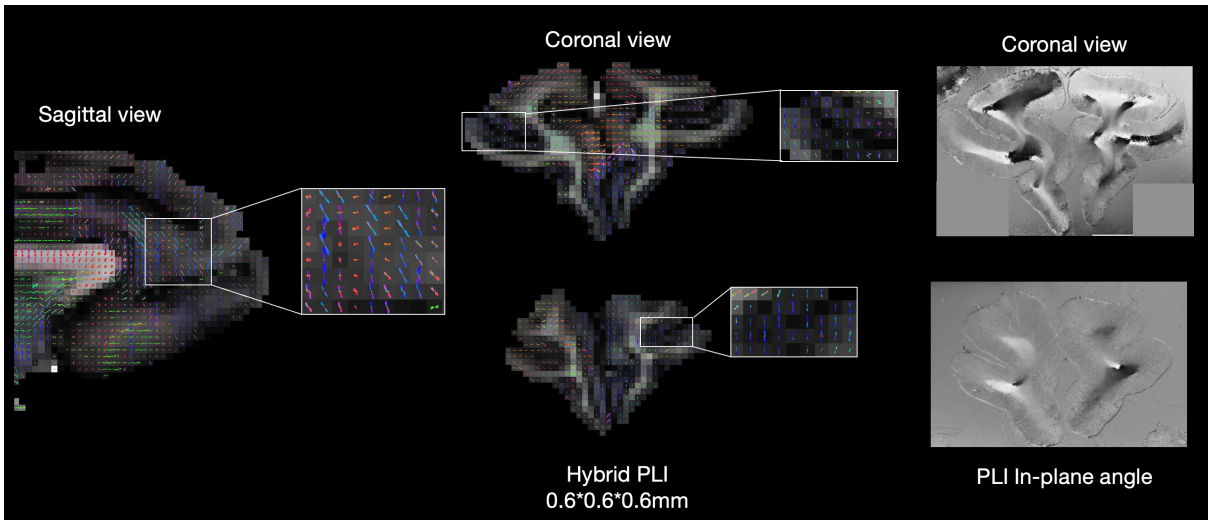


Appendix 3.2: Hybrid orientations at different resolutions.

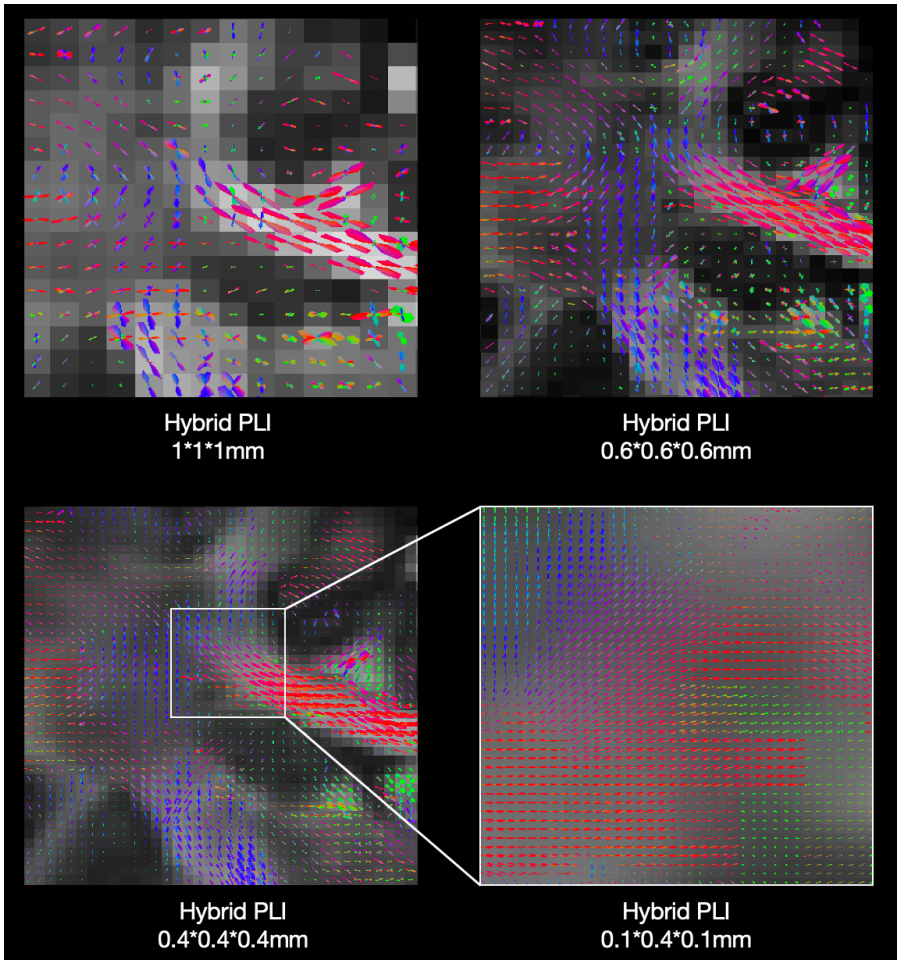
The hybrid method generates 3D fibre orientations at the resolution of the microscopy data that can then be combined over a local neighbourhood into a fibre orientation distribution (FOD). The resolution of the hybrid FOD depends on the size of the combined region. Using 4µm resolution microscopy, we demonstrate how a 0.04mm FOD can be generated by combining 10*10 pixels, 0.1mm with 25*25 pixels, 0.4mm with 100*100 pixels or 0.6mm with 150* 150 pixels.



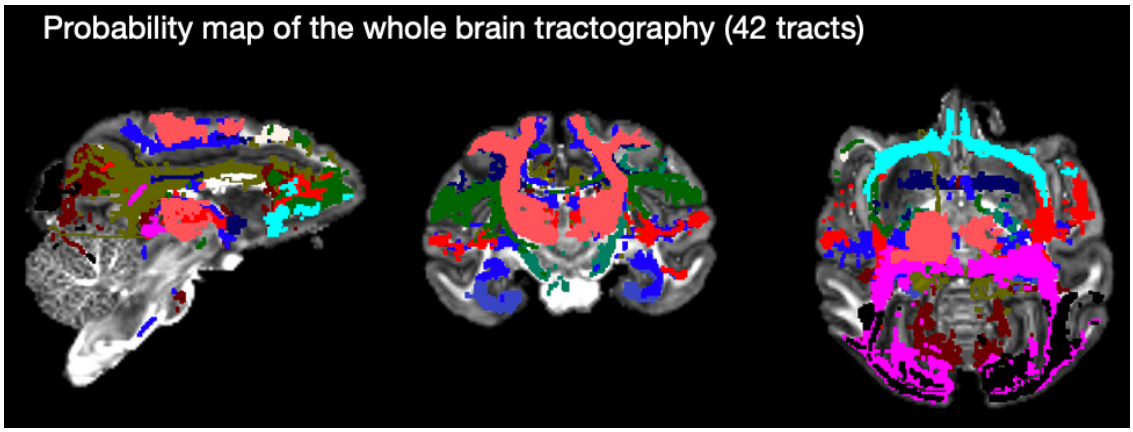
Appendix 3.3: Missing microscopy filled with dMRI CSD.
The BigMac brain was sectioned into two halves (anterior & posterior), resulting in a gap of approximately 3-5 voxels without microscopy data in the centre of the brain. To facilitate whole-brain tractography using the hybrid method, these voxels were filled by FODs from dMRI-CSD. The continuity and similarity of the FODs after filling (Top) is shown in comparison with dMRI CSD (bottom).



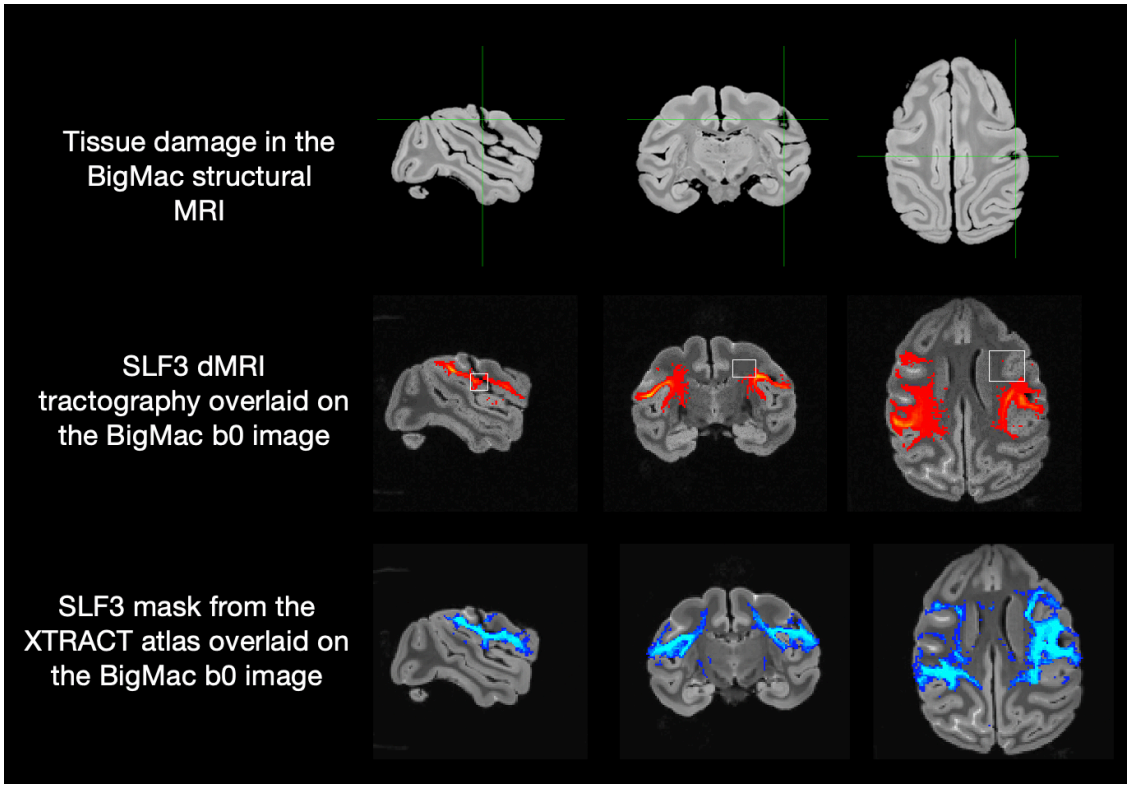
Appendix 3.4: Fibre orientations in the anterior brain.
In specific regions of the anterior brain, the accuracy of fibre orientation within the grey matter is compromised. Two representative slides in the coronal view are shown as examples. This is due to the slides being coated in gelatine which is also birefringent. While PLI effectively captures fibre orientation information in myelinated white matter, the presence of gelatine in the grey matter introduces uncertainty in determining fibre orientation.



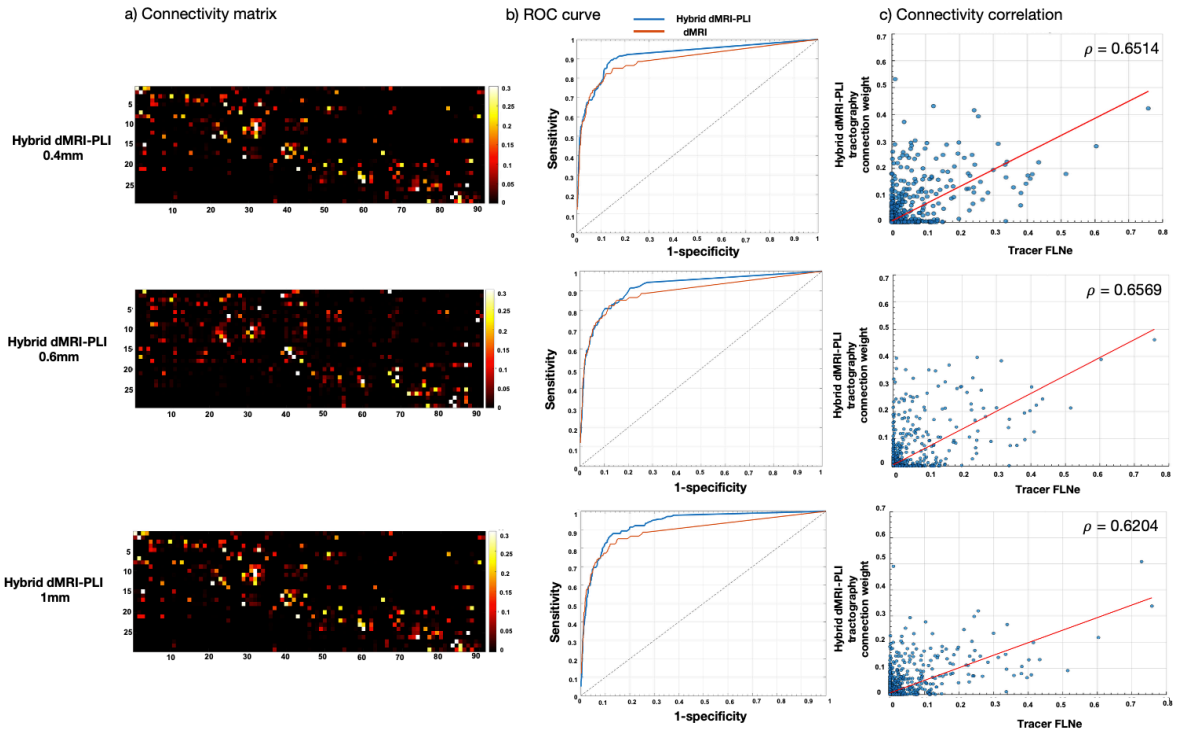
Appendix 3.5: Hybrid fibre orientation distributions reconstructed at different spatial resolutions.
Here we show example outputs for 1*1*1mm, 0.6*0.6*0.6mm, 0.4*0.4*0.4mm and 0.1*0.4*0.1mm (XYZ). X-Z denotes the coronal plane where microscopy was acquired with a native resolution of 4 μm/pixel, whilst Y denotes the axis along which the brain was sectioned, where microscopy sections of similar contrast are repeated every 0.35mm throughout the brain. Hence the asymmetric 0.1*0.4*0.1mm voxels. The fibre orientations vary smoothly at all resolutions.



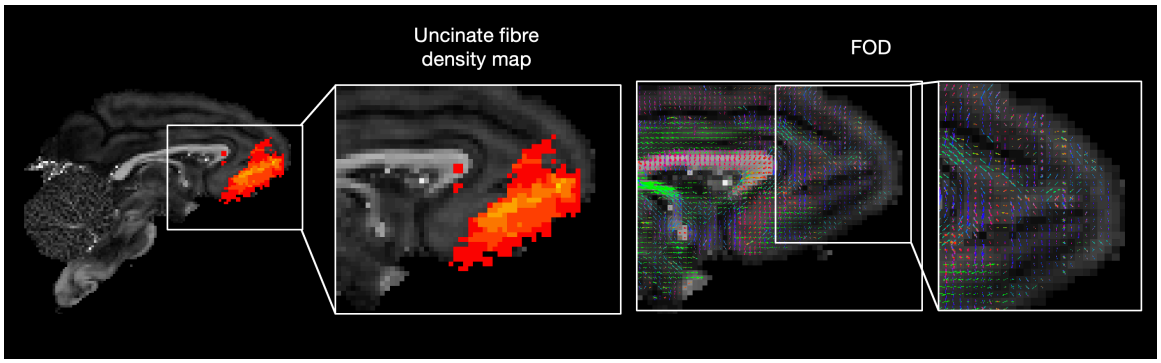
Appendix 3.6: Tracts spanning the whole brain reconstructed using hybrid dMRI-PLI at 0.6mm.
XTRACT was used to reconstruct 42 major white matter tracts using the hybrid FODs. Here we overlay tract masks to demonstrate the substantial coverage of the 42 tracts across the brain.



Appendix 3.7: Bleeding site in the BigMac dataset.
The tissue damage in the left hemisphere is evident in the postmortem MRI structural image (Top). This affected the tracking of the superior longitudinal fasciculus 3 (SLF3) (middle) compared to the XTRACT atlas (bottom), with missing regions indicated by the white boxes.



Appendix 3.8. Quantitative tracer assessment across varying resolutions.
a) Connectivity matrix; b) ROC curve; c) Connectivity correlation. The results show that the conclusions remain consistent across these resolutions, with an improved ROC curve for hybrid dMRI-PLI compared to dMRI CSD.



Appendix 3.9: Anterior extent of uncinate fasciculus.
The uncinate fasciculus in Figure 3.5 has less anterior extent than dMRI tractography. This may be related to errors in the dMRI-microscopy co-registration in this region or errors in PLI orientations affected by background gelatine on the anterior slides. Here, the effect of the gelatine can be seen in the FODs which often have a SI (blue) orientation. Note, this was primarily found to affect orientations the grey matter rather than the more myelinated white matter where tissue birefringence tended to dominate.

4

Estimating microscopy-informed fibre orientations from in-vivo dMRI using a domain adaptation framework

Table of Contents

4.1 Introduction *93*
4.2 Methods *95*
4.2.1 Data: the BigMac dataset 95
4.2.2 Hybrid dMRI-microscopy orientations 97
4.2.3 The network 97
4.2.4 Tractography 100
4.3 Results *102*
4.3.1 Network structure and domain separation 102
4.3.2 Network application to macaque 103
4.3.3 The network improves the specificity of white matter organisation 105
4.3.4 The network improves tracking in another in-vivo macaque dataset 106
4.3.5 Comparison with anatomical tracers 107
4.4 Discussion *109*

Foreword

White matter provides the underlying structure for neural communication, and changes in white matter due to demyelination or dysconnectivity are implicated in many brain diseases. In pursuit of better methods for imaging structural brain connectivity, multiple efforts are going into acquiring bespoke datasets that combine MRI and microscopy. MRI remains the most commonly used non-invasive method for in-vivo brain connectivity mapping. Microscopy measures the axonal architecture directly and is often considered the gold standard. However, accurately resolving the complex anatomy of white matter remains challenging, especially in-vivo due to limited acquisition times and indirect measures of brain microstructure through diffusion MRI. We need methods that can: 1) leverage microscopy information and can be applied to MRI without accompanying microscopy, 2) bridge postmortem and in-vivo MRI which have very different tissue properties, and 3) work in humans, where most ex-vivo datasets are acquired from animal models. Here we propose a deep learning network to achieve the above (Figure 4.1). The network takes MRI as input and outputs fibre orientations learned directly from microscopy data during training. We use a domain adaptation framework to create a network which is invariant to tissue state (postmortem versus in-vivo). This cross-tissue and cross-modality framework enables the application of microscopy-derived insights to in-vivo dMRI data, where microscopy is not attainable. Here we demonstrate the network applied to in-vivo and postmortem data from the macaque. In the next chapter, we extend the method for application to in-vivo human MRI. Our results demonstrate the potential of the method for more precise and data-driven connectivity mapping which may benefit tractography applications in the clinic.

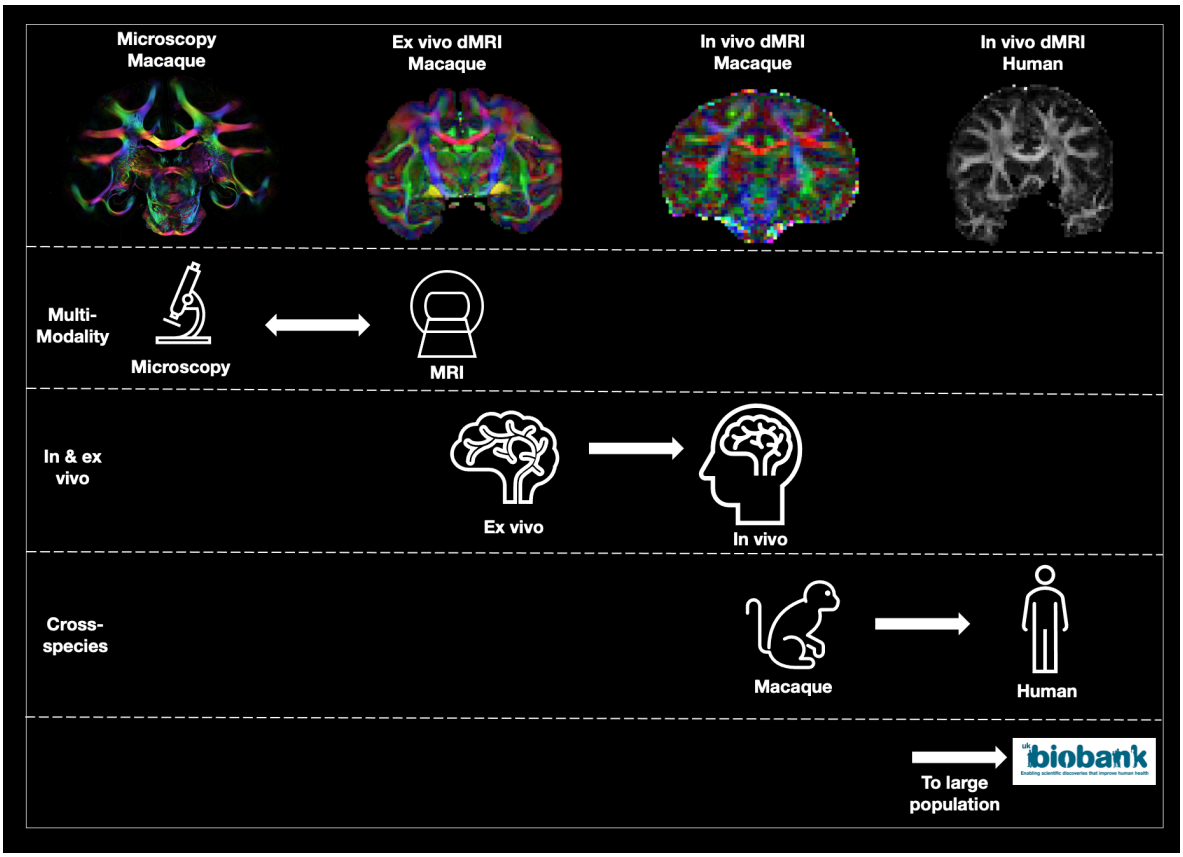


Figure 4.1. Knowledge transfer in microscopy-informed fibre orientation.
Transferring microscopy information to in-vivo human dMRI data involves three main steps. First, microscopy and postmortem dMRI fibre orientations are combined through our data-fusion hybrid MRI-microscopy method (Chapter 3) which converts the microscopy orientations into 3D orientations with whole-brain coverage. These orientations are then combined into FODs that are comparable to those estimated from dMRI. Second, information from our postmortem dataset is translated to in-vivo dMRI via a domain adaptation network. The network allows the estimation of microscopy-informed orientations from both postmortem and in-vivo dMRI data with equivalent performance (Chapter 4). Third, the network trained on macaque brain data is adapted for human in-vivo dMRI data ensuring the effective transfer of features learned from microscopy (Chapter 5).

Published work

Conference

Silei Zhu, Nicola K. Dinsdale, Saad Jbabdi, Karla L. Miller, Amy F.D. Howard, Estimating microscopy-informed fibre orientations from in-vivo dMRI using a domain adaptation framework, ISMRM Annual Meeting 2024, Oral.

Individual contributions to this thesis chapter

My contributions to this chapter include network design, training, and testing, data processing, fibre orientation visualisation, tractography, manuscript writing, editing and review.

Steps for conceptualisation, data processing and network design were advised by Nicola K. Dinsdale, Saad Jbabdi, Karla L. Miller and Amy F.D. Howard.

4.1 Introduction

With the goal of developing better methods for probing the mesoscopic structure of the brain's network, researchers are increasingly acquiring datasets that link MRI to microscopy within the same brains. Diffusion MRI (dMRI) is the only non-invasive method for mapping brain structural connectivity and is sensitive to tissue alterations due to diseases which is crucial for clinical diagnosis (Basser and Jones, 2002; Jbabdi et al., 2015). However, its reliance on indirect measures of water diffusion within tissue can lead to inaccuracies in reconstructing complex white matter pathways. This challenge is particularly pronounced in in-vivo settings, where limited hardware and acquisition time result in limited resolution when combining data across hundreds or thousands of axons. Additionally, diffusion microstructural information is limited due to noise and suboptimal model assumptions. Conversely, microscopy techniques offer high-resolution ground truth measurements, allowing for the precise identification of axonal architecture and fibre orientations. Microscopy is widely used to validate dMRI and serves as a gold standard for structural connectivity studies (Mollink et al., 2017b). However, microscopy is typically limited to postmortem studies, with most available microscopy datasets derived from non-human species (e.g. rodents and non-human primates) (Choe et al., 2012; Mollink et al., 2017b). These limitations constrain its direct use in in-vivo studies and clinical applications. Ideally, we could leverage such data to improve in-vivo tractography. We introduce a deep-learning model trained on macaque data, to predict microscopy-informed fibre orientation distributions (FODs) from diffusion MRI (dMRI), transferring microscopy information to in-vivo when microscopy is not available.

Recently, deep learning has shown potential for advancing dMRI estimation of fibre orientations (Liang et al., 2023; Zeng et al., 2022). One of the primary challenges with dMRI is its requirement for computational modelling to extract fibre orientations. These models

typically require assumptions such as modelling axons as sticks or assuming a single fibre response function across the brain, which can lead to inaccuracies as introduced in Chapter 2. Deep learning approaches have recently demonstrated potential for advancing dMRI fibre orientation estimation through data-driven methods that eliminate the need for a biophysical model. However, a key challenge in deep learning methods is their heavy reliance on the distribution of training data which undermines their generalisability (LeCun et al., 2015). This constraint poses difficulties in translating models from postmortem to in-vivo settings, as most existing dMRI-microscopy datasets are derived from postmortem brain tissues. While postmortem dMRI typically achieves higher spatial resolution and superior data quality due to longer scan times, substantial differences exist between in-vivo and postmortem tissue states. For instance, postmortem tissue exhibits reduced diffusivity and altered relaxation times. These disparities create a distribution mismatch, making models trained exclusively on postmortem dMRI unsuitable for direct application to in-vivo data.

Domain adaptation in deep learning offers a potential solution for translation between in-vivo and postmortem MRI. Crucially, the domain adaptation framework is designed to make the network invariant to inputs with different data distributions, addressing the heterogeneity of datasets (Guan and Liu, 2022; van Opbroek et al., 2015; Wachinger and Reuter, 2016). It has been previously used to ensure applicability to data acquired from different centers, scanners, and subject population as well as with various acquisition protocols. Here, we explore its application to create a network invariant to tissue state differences between in-vivo and postmortem (Howard et al., 2023). We use a unique dataset comprising co-registered in-vivo dMRI, postmortem dMRI, and microscopy data from the same brain (Howard et al., 2023). Thus, the network generates feature representations that are invariant to tissue states, preserving the benefits of high-quality postmortem data while ensuring generalisability to in-vivo settings.

In this work, we develop a domain adaptation network that takes MRI as input and outputs fibre orientations directly derived from microscopy, with the network being invariant to tissue states. For optimal performance, our network requires training data that satisfy three criteria. First, we require microscopy and dMRI data from the same brain, where the microscopy provides “ground truth” information about fibre orientations during training. Both modalities should be acquired from the same subject to avoid microstructural mismatches due to inter-subject differences in brain structure, which could hinder accurate MRI-microscopy mapping.

Second, we require a dataset with in-vivo and postmortem MRI from the same brain. Postmortem dMRI serves as an intermediate bridging the gap between in-vivo dMRI and postmortem microscopy, providing higher resolution, higher signal-to-noise ratio (SNR) than in-vivo MRI, making it easier for the network to learn the MRI-microscopy mapping. Having the in-vivo MRI is crucial for translating the model to in-vivo settings through the domain adaptation framework. Third, for our network to eventually be suitable for human applications, we require data from primate brains rather than rodent brains, as the primate white matter architecture exhibits complexity comparable to that of humans. Approximately 30% to 90% of white matter voxels contain crossing fibres (Schilling et al., 2017a) and rodent brains have comparatively simpler white matter with fewer crossing fibres/multi-fibre voxels compared to human brains, such that networks trained on rodent data may have limited applicability to humans (Kuan et al., 2015).

The network is trained on the openly available data, the BigMac dataset (Howard et al., 2023), which uniquely provides co-registered in-vivo dMRI, postmortem dMRI and high-resolution microscopy (polarised light imaging, PLI) data from the same macaque brain, satisfying the criteria outlined above. The network is designed to accept either in-vivo or postmortem dMRI data as input and output microscopy-informed FODs. Hybrid dMRI-microscopy FODs, computed previously, serve as the training ground truth and drive the model to learn myelin-specific information. During inference, the network generates microscopy-informed FODs from unseen dMRI data, without the need for concurrent microscopy. We validate our network using unseen postmortem and in-vivo macaque data. Notably, the predicted FODs successfully replicate white matter organisation patterns observed in microscopy (Schilling et al., 2022) and reconstruct the anatomically complex U-shaped fibres.

4.2 Methods

4.2.1 Data: the BigMac dataset

The BigMac dataset was acquired and pre-processed as described in Howard et al., 2023 and Chapter 3. An adult rhesus macaque brain was scanned both in-vivo and postmortem.

In-vivo diffusion MRI was acquired using echo-planar imaging on a 3T whole-body scanner at two time points with TE/TR=100 ms/8.2 s, a spatial resolution of 1 mm isotropic and a b-

value of 1 ms/μm^2. In the first session, 1100 diffusion gradient directions were acquired, including 81 unique gradient directions and 144 images with negligible diffusion weighting. For the second session, 361 diffusion gradient directions were obtained, including 61 unique gradient directions and 38 images with negligible diffusion weighting. Structural images were acquired in both sessions using an MP-RAGE sequence with a spatial resolution of 0.5 mm, TE/TR = 4.01 ms/2.5s and 128 slices.

Postmortem MRI (as described in Chapter 3) was acquired on a 7T preclinical scanner, with 0.3 mm isotropic structural images and 0.6 mm isotropic dMRI at b=4 ms/μm^2 with 128 gradient directions and 8 images with negligible diffusion weighting. In addition, postmortem dMRI was acquired at a lower resolution of 1.0 mm isotropic, 250 gradient directions b=4 ms/μm^2.

After scanning, the postmortem brain was sectioned into slices along the anterior-posterior axis and assigned to different microscopy contrasts. This work uses only the polarised light imaging (PLI) data from sections with a thickness of 50 μm repeated every 350 μm. PLI utilises the birefringence properties of myelin to estimate primary fibre orientation estimation, here acquired at a resolution of 4 μm. Co-registration of MRI-Microscopy was performed using TIRL (v3.6) (Howard et al., 2023; Huszar et al., 2023a, 2023b, 2022).

Additionally, in-vivo dMRI from another macaque brain was acquired using the same protocol as the BigMac in-vivo dMRI session 1 from the PRIME-DE dataset (Noonan et al., 2014; Sallet et al., 2020).

Datasets for training, validation and testing

The training dataset included postmortem diffusion data at 0.6 mm isotropic resolution and in-vivo diffusion data at 1 mm isotropic (the first session), with co-registered hybrid FODs at the same corresponding resolution for postmortem and in-vivo data. The postmortem and in-vivo data were not co-registered and were treated separately during model training for fibre orientation estimation. The training dataset was partitioned into training (80%) and validation (20%) sets, with voxels outside the brain mask excluded to avoid background.

The testing datasets used to evaluate the network's generalisability and performance included three unseen datasets: (1) postmortem data from the same macaque at 1.0 mm isotropic resolution, 250 gradient directions b=4 ms/μm^2, which was not included in training; (2) in-vivo data from the same macaque, which was the second session of the BigMac dataset and (3) in-vivo data from another macaque.

The diffusion signal was normalised by S0 (the signal with negligible diffusion weighting) to mitigate T2 effects before being input into the network. The signal attenuation was then fitted using spherical harmonics of order 8, resulting in a channel size of 45. This spherical harmonic representation offers the advantage of being independent of the exact gradient orientation and number of gradient directions sampled, assuming at least 45 gradient directions can be sufficiently described by lmax=8. This representation is more robust to data noise and also does not require b-values and b-vectors as input, enabling its application to be broader. Brain volumes were subsampled into 3*3*3 blocks to incorporate shared information from neighbouring voxels.

4.2.2 Hybrid dMRI-microscopy orientations

Hybrid dMRI-microscopy FODs were reconstructed by combining information from diffusion MRI and microscopy, following the method described in Chapter 3. Polarised light imaging provided fibre orientations within the microscopy plane and postmortem diffusion MRI using the ball and stick model (BAS) (Behrens et al., 2003) was used to approximate the through-plane angle. FODs were reconstructed at spatial resolution of 0.6 mm and 1 mm isotropic in the space of postmortem dMRI. The hybrid FODs at 1 mm were registered to the BigMac in-vivo dMRI space with the MRtrix3 command mrregister, with FODs reoriented according to the warp field (Raffelt et al., 2011).

4.2.3 The network

Network architecture

We developed a domain adaptation network with 3 components: a feature extractor, a predictor and a classifier[10]. The feature extractor and predictor generated predicted FODs from dMRI, while the domain classifier ensured invariance between postmortem and in-vivo data. (Figure 4.2). The network received small blocks of MRI data as input and output microscopy-informed FODs, trained using the hybrid dMRI-microscopy FODs introduced in

Chapter 3[15]. Instead of processing individual voxels, the network input a cube of voxels, with local neighbourhood information, which was combined through the convolutional layers. Both the input and output were represented using spherical harmonics. The spherical harmonic representation provides a low-dimensional basis to approximate the diffusion signal on a sphere while improving robustness to noise and accommodating datasets with variable diffusion gradient directions. The domain classifier facilitated domain adaptation by determining whether the input data originated from postmortem MRI (the source domain) or in-vivo MRI (the target domain). During training, the domain classifier enforced the feature extractor to learn a latent representation that was agnostic to tissue state (i.e. ensuring that in-vivo and postmortem MRI data were mapped to a common feature space).

The training procedure followed a two-step adversarial training approach inspired by Dinsdale et al., 2021 (Dinsdale et al., 2021). In the first stage, the feature extractor and predictor were optimised to learn the primary task of microscopy-informed fibre orientation estimation, while the feature extractor and domain classifier were simultaneously trained to distinguish between in-vivo and postmortem MRI inputs. In the second stage, the feature extractor was trained to confuse a well-trained domain classifier while keeping the domain classifier parameters fixed. This enforced domain invariance in the latent feature representation at the output layer of the feature extractor. Meanwhile, the feature extractor and predictor were optimised to estimate the microscopy-informed fibre orientation.

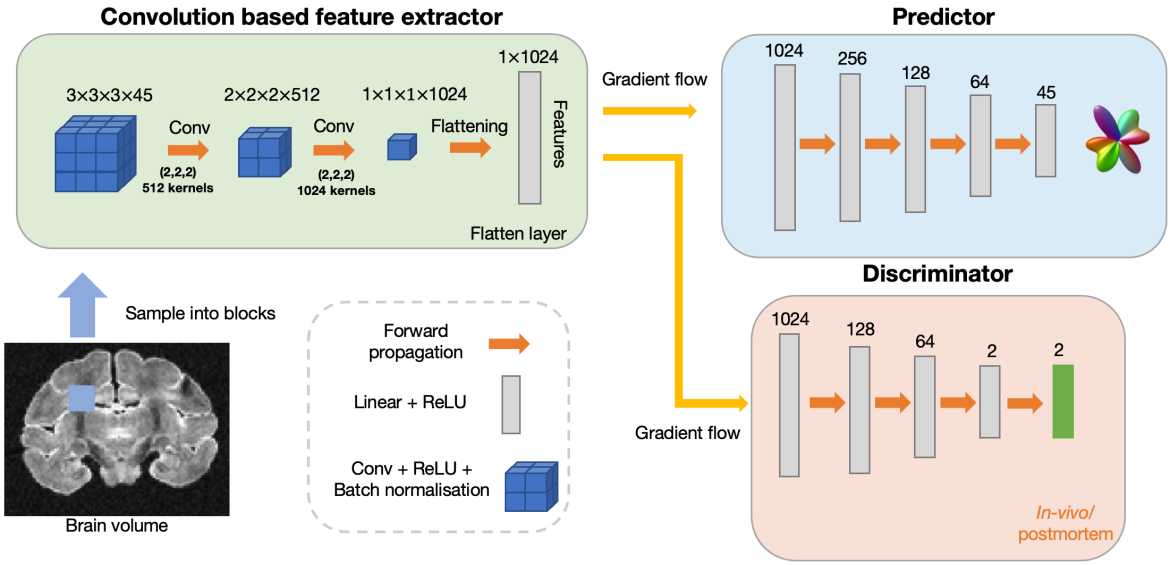


Figure 4.2. In-vivo translation of microscopy-informed FODs via deep learning.

Our domain adaptation network estimates microscopy-informed fibre orientations from dMRI signals from both postmortem and in-vivo MRI. There are three main components: 1) a feature extractor, 2) a predictor and 3) a domain classifier. Using domain adaptation, the model was trained to be invariant to the postmortem and in-vivo dMRI data inputs.

Different loss functions were used at each stage of training. In the first stage, the loss function for the main task was defined as the mean square error between the predicted and ground truth spherical harmonics amplitude (the spherical harmonic coefficients were first converted to amplitudes). The loss was minimised to optimise fibre orientation estimation. Meanwhile, a domain loss, formulated as binary cross-entropy, was used to train the domain classifier. Domain labels were encoded using one-hot encoding (eg. the label for the source domain is [0,1] and the label for the target domain is [1,0]). The domain classifier received softmax output values, which represent probabilities for each class. By minimising the cross-entropy, the classifier maximised its ability to distinguish between the source and target domains. In the second stage, adversarial training was implemented. A confusion loss was defined as the negative sum of normalised log-probabilities of the domain classifier predictions. This loss was designed to induce domain invariance in the final layer of the feature extractor. While keeping the discriminator's parameters fixed, gradients from the confusion loss were backpropagated to update the feature extractor. This process maximised the entropy in domain predictions, forcing them towards a uniform distribution and effectively removing domain-specific information. To preserve fibre orientation estimation performance, the feature extractor and predictor were simultaneously fine-tuned using the same mean square error loss function from the first stage. Thus, the two-stage adversarial training framework balanced two opposing objectives: the domain loss aimed to distinguish between in-vivo and postmortem MRI inputs, while the confusion loss aimed to eliminate these differences, ensuring domain invariance in the learned representations.

Spatial misalignment between MRI and microscopy data, or between hybrid FODs and MRI, could result in a slight rotation of the hybrid FOD relative to the ground truth. To address this, the predicted FODs were rotated along the x, y and z axes by a range of small angles (<10 degrees in each axis) during the loss function calculation in network training. Each rotated FOD was then compared to the hybrid FOD ground truth, and the loss was defined as the smallest mean square error across all rotations. This approach ensured that minor angular misalignment due to registration discrepancies between MRI and microscopy were accounted for during network training.

Domain separation
T-distributed stochastic neighbour embedding (t-SNE) was used to visualise the separation of features before and after unlearning (Maaten and Hinton, 2008). This dimensionality reduction technique transformed high-dimensional feature representations from the output of the feature extractor into a two-dimensional space, allowing a comparison of similarity between different domains.

Fibre orientation estimation
FODs were derived from the network. For benchmarking, FODs were computed using constrained spherical deconvolution (CSD) implemented in MRtrix3 (v3.0.3) (Tournier et al., 2019) following the same method as in Chapter 3 (Tournier et al., 2007).

Network FODs post-processing
FODs generated by the network were scaled on a voxelwise basis to ensure that the FODs had amplitudes comparable to those from CSD. The FODs were scaled such that the peak amplitude of the network-derived FODs matched that of the dMRI-CSD FODs. This scaling method was chosen based on the visual evaluation of the network and CSD outputs and used to ensure their comparability in tractography analysis.

4.2.4 Tractography

White matter tractography
White matter tractography was conducted to evaluate the ability of network-derived FODs to estimate structural connectivity. The tractography results were compared with those obtained from CSD-derived FODs. Tractography was performed using the MRtrix3 tractography pipeline (Markov et al., 2012b). Whole-brain fibre tractography was performed using the iFOD2 algorithm (Tournier et al., 2010) with the following parameters: seeding from the white matter with 30 seeds per voxel, a step size of 0.2 mm, a cut-off value of 0.05, a maximal length of 120 mm, and a minimal length of 5 mm. Fibre bundle segmentation was performed using inclusion and exclusion masks from XTRACT (Warrington et al., 2020). These masks were transformed from standard (F99) space to the BigMac postmortem and in-vivo diffusion data space using warp fields generated using FSL FLIRT/FNIRT.

White matter organisation in the internal capsule

We investigated white matter organisation within the internal capsule (IC) following our previous work using hybrid fibre orientations (Chapter 3) (Zhu et al., 2025). The motor cortex can be subdivided into regions corresponding to distinct functional representations, including the trunk, arm and face regions with a medial-lateral organisation. White matter tracts originating from these regions and passing through the internal capsule are known to maintain a topographic anterior-posterior representation within the internal capsule. The preservation of this pattern was demonstrated in Chapter 3 using hybrid FODs, but not CSD-based tractography. Therefore, we investigated whether this topographic organisation could be retained using the network-derived fibre orientations (Park et al., 2001).

The ROIs in the motor cortex and the internal capsule mask were warped into both postmortem and in-vivo dMRI space. The same tractography methods were used as described in Chapter 3.

U-shape fibre tractography

U-shape fibres are short association fibres that connect neighbouring gyri with high curvature. In macaques, these fibres were tracked using surface masks from neighbouring gyri. The cortical surface was reconstructed using Freesurfer (Fischl, 2012) from the structural T1-weighted image. The surface boundary was then registered to both postmortem and in-vivo dMRI spaces. For U-shape fibre tractography, seed and target masks were placed on the cortical surface of adjacent gyri. Vertices were extracted from the white matter and grey matter interface. The spherical seeding method in MRtrix3 (Tournier et al., 2019) was used, which generates seeds from a list of vertices with a small radius centered around each vertex coordinate. Only streamlines that tracked to the target mask in the neighbouring gyrus were retained.

Comparison to retrograde tracer connectivity

Network and CSD-derived connectivity matrices were compared to the same tracer weighted connectivity matrix as in Chapter 3 using similar methods (Chad J. Donahue et al., 2016; Markov et al., 2012b, 2010). The cortical atlas was co-registered to BigMac in-vivo and postmortem space. Tractography using both network-derived and CSD-derived FODs was seeded from the 29 injection sites in the left hemisphere using the same tractography parameters mentioned previously and the connectivity matrix (29 x 91 areas) was calculated and normalised.

4.3 Results

4.3.1 Network structure and domain separation

The domain adaptation network architecture was trained to generate microscopy-informed FODs from dMRI signals. The training process was designed to utilise information from postmortem data (source domain) to enhance fibre orientation estimation in in-vivo data (target domain).

Figure 4.3 evaluates domain separation. The t-SNE plot (Maaten and Hinton, 2008) (left) shows the clear differences in the distribution of input data from the source and target domain. After the initial training step, domain separation was evaluated at the last layer of the feature extractor which was trained to effectively separate data from the source and target domains (middle). Following the unlearning step (right), the t-SNE plot shows that feature representations from both inputs are entirely mixed, suggesting that tissue status information has been removed, making the embeddings of postmortem and in-vivo data indistinguishable.

The t-SNE plots demonstrate that the unlearning process altered feature representations. Before unlearning, the network was trained to extract domain-specific features, making it possible to differentiate between postmortem and in-vivo data. After unlearning, the network identified features invariant to domain differences, ensuring a more generalisable feature representation in the final layer of the feature extractor.

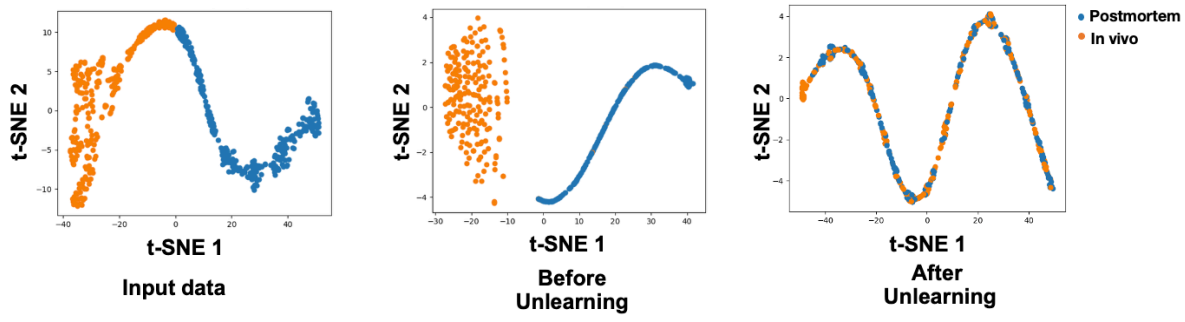


Figure 4.3. t-SNE visualisation of domain separation.
The left plot shows distinct input distributions between source and target domains. After initial training (middle), the discriminator classified data by tissue status at the last layer of feature extractor. Following unlearning (right), tissue status information was removed, making postmortem and in-vivo embeddings indistinguishable, ensuring feature space generalisation.

4.3.2 Network application to macaque

The network was first applied to postmortem macaque data acquired with different parameters at 1.0 mm isotropic resolution and 250 gradient directions b=4 ms/μm^2 (Figure 4.4). The network-estimated FODs were comparable to the CSD FODs, and both aligned with anatomical expectations, demonstrating the validity of the network for postmortem macaque data.

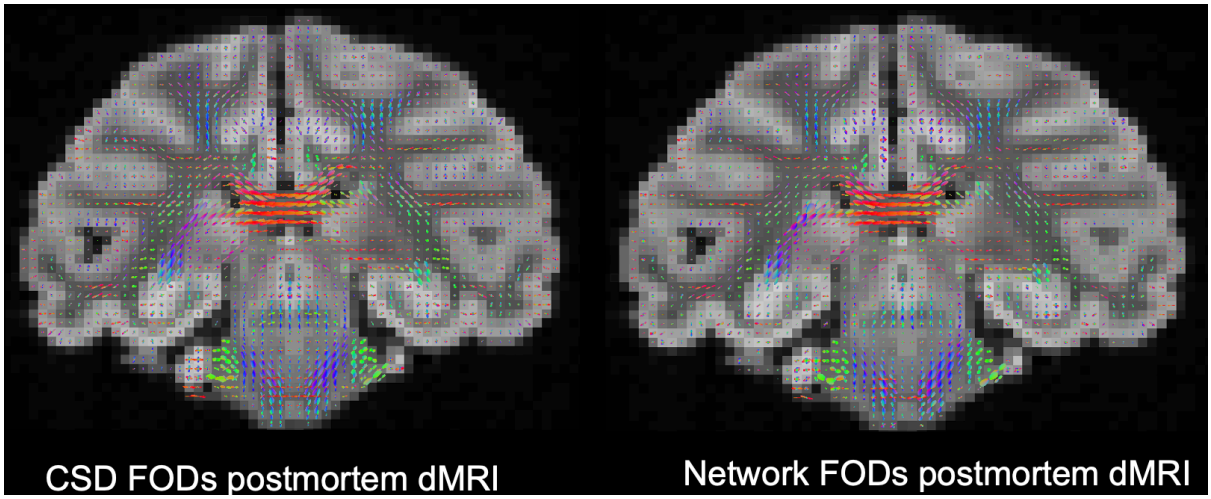


Figure 4.4. Network application to postmortem macaque data.
FODs estimated using the network are compared to CSD-derived FODs in postmortem dMRI data from the same macaque, acquired at a different resolution not included in the training data. A similar FOD pattern is observed at the whole-brain level.

The network was next applied to in-vivo macaque data from the same subject as the training dataset but acquired in a separate session which was not used during training. We evaluated whether the network or CSD-estimated FODs could reconstruct the expected fibre orientation fanning patterns within the gyrus, as observed in microscopy where fibres predominantly exhibit a radial organisation across the cortex, perpendicular to the gyral walls. Figure 4.5 shows improvements near the white matter/grey matter boundary where the network estimated FODs more accurately depict fibre trajectories as they fan into the cortex, whereas CSD generates spurious peak estimates that lack anatomical feasibility.

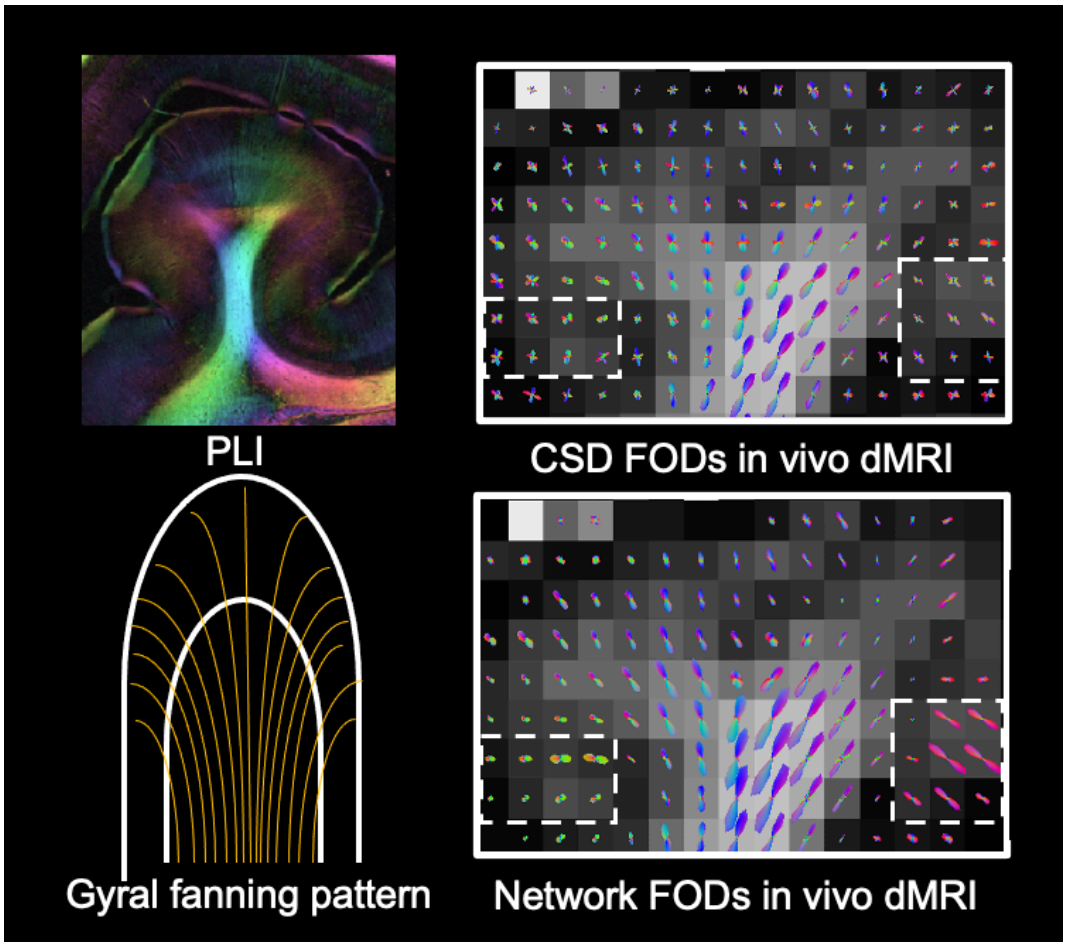


Figure 4.5. FODs estimated with the network in the in-vivo macaque brain. FODs estimated using the network are compared to CSD FODs in the in-vivo dMRI at the grey matter and white matter boundary. A better fanning pattern is observed in the network FODs with orientations perpendicular to the gyral wall that align with expectations from microscopy.

We further evaluated whether the improved in-vivo network-estimated FODs facilitated anatomically meaningful tractography, a key validation criterion for assessing FOD accuracy. Figure 4.6A illustrates the reconstruction of the forceps major and superior thalamic radiation using both network-derived and CSD-derived FODs. Notably, when tracking near cortical regions, the network-estimated FODs produce less noisy streamlines and more clearly delineate projections branching into distinct gyri.

Figure 4.6B shows the reconstruction of U-fibres, which are readily visualised in microscopy but are often challenging for dMRI tractography. Our results highlight an example where both network-estimated FODs and CSD FODs successfully delineate U-fibre trajectories, capturing their characteristic branching patterns into neighbouring gyri (Figure 4.6B Left). Furthermore, in another gyrus where CSD FODs fail to reconstruct U-fibres (Figure 4.6B

Right), the network successfully generates the streamlines. This difference can be attributed to differences in the underlying FODs, with the network-estimated FODs showing better spatial continuity and smoothness, whereas CSD FODs appear noisier.

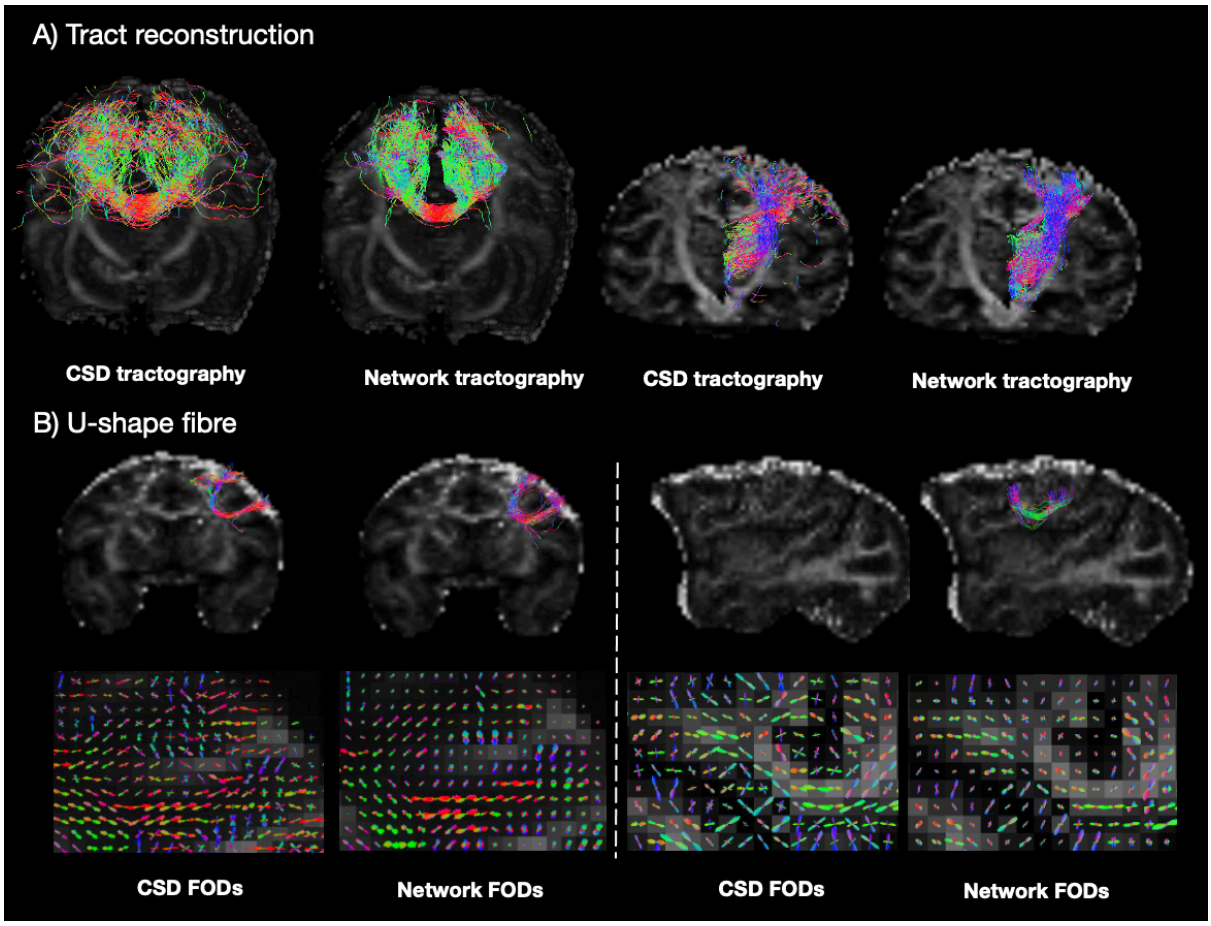


Figure 4.6 Validation of tractography in the in-vivo macaque dMRI data.
A) White matter tracts from XTRACT were reconstructed with network and CSD FODs. Two example tracts, the forceps major and superior thalamic radiation, are shown. B) The network demonstrated superior ability in reconstructing U-fibres compared to CSD. Notable differences were observed in the underlying FODs with less noise and better specificity.

4.3.3 The network improves the specificity of white matter organisation

Next, we investigated whether the network FODs in the in-vivo macaque could recreate the anterior-posterior distribution of motor trunk-arm-face regions within the internal capsule, as previously demonstrated using hybrid FODs in Chapter 3. Figure 4.7 shows how conventional CSD tractography fails to differentiate tracts originating from different motor cortex regions, leading to mixed streamlines within the internal capsule. In contrast, the network-derived FODs demonstrate a clearly separable pattern along the anterior-posterior

axis which is remarkably similar to the organisation observed using the hybrid dMRI-microscopy method in postmortem data in Chapter 3.

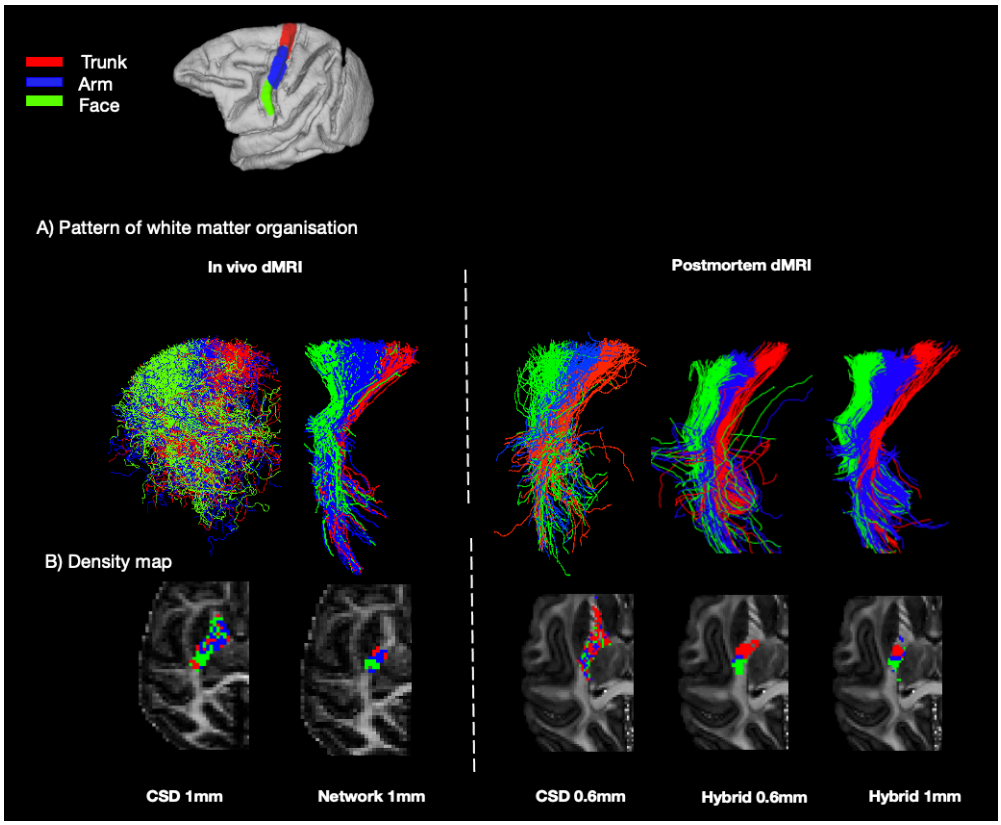


Figure 4.7. Network improves the specificity of white matter organisation.
The organisation of white matter fibres projecting from the motor cortex and through the internal capsule is studied with fibres classified as originating from the trunk(red), arm (blue) and face (green) regions of the motor cortex. Streamlines are shown in A, whilst B colour codes voxels according to the maximum intensity. For the in-vivo dMRI data, different projections are intermingled together for CSD but the network demonstrates an anterior-posterior distribution in the internal capsule with a clearly separable pattern. This mirrors previous results from Chapter 3 where, in postmortem dMRI data, the CSD method led to a mixture of streamlines in the internal capsule but the hybrid method demonstrated an anterior-posterior distribution.

4.3.4 The network improves tracking in another in-vivo macaque dataset

Figure 4.8 shows the network's performance and generalisability on another in-vivo macaque dataset obtained from a different macaque. Notably, this dataset similarly had a low data quality (Figure 4.8A). Our goal was to assess whether the network could generalise to a different brain and accurately recover microscopy-informed features despite the low data quality. The network-derived FODs exhibit anatomically plausible orientations with fewer crossing fibres compared to CSD FODs. Tractography of the frontal aslant, which appears

noisy when reconstructed using CSD, shows improvement with network-estimated FODs which shows a similar difference observed above.

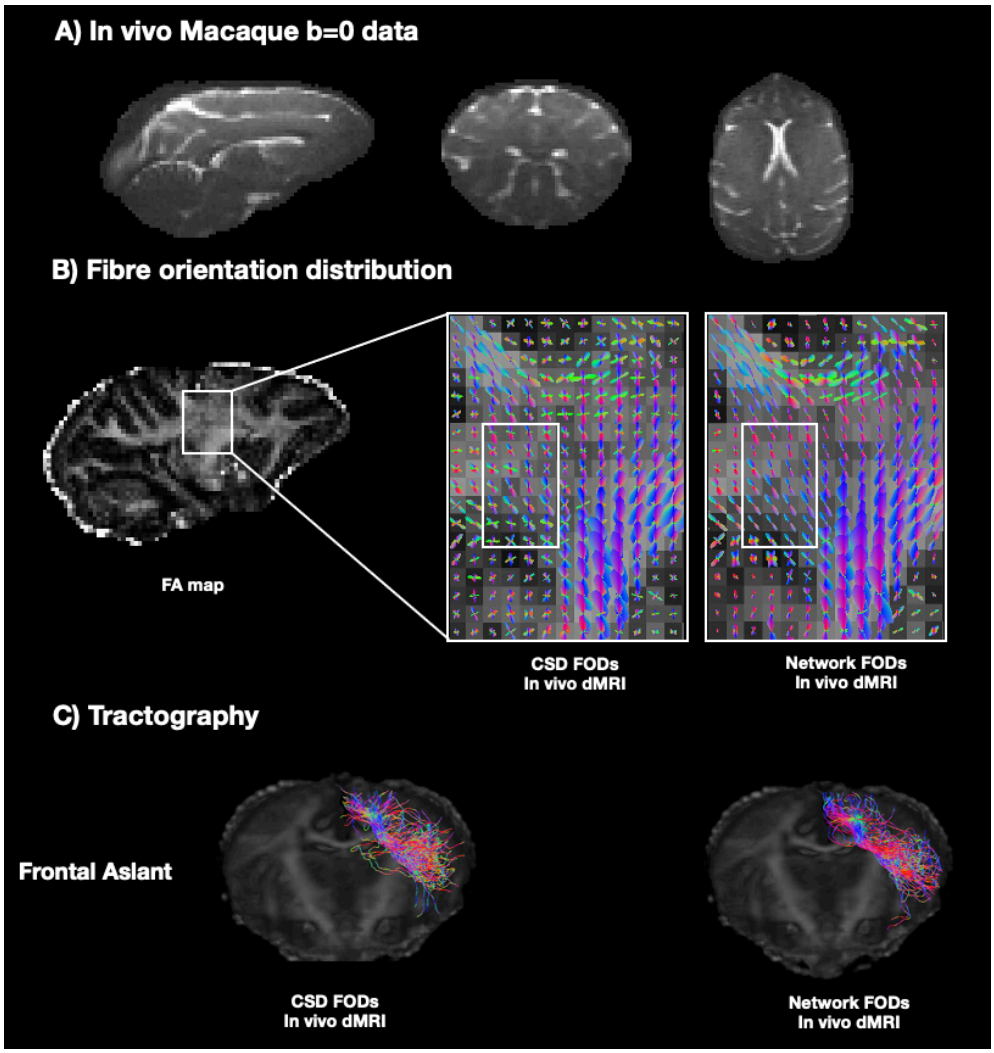


Figure 4.8 Application of the network to in-vivo macaque data from another macaque brain.
(A) In-vivo macaque b=0 data. (B) The FODs estimated by the network show anatomically plausible orientations, with fewer random peaks and crossing fibres compared to CSD FODs. (C) Tractography using the network FODs improves the reconstruction of the frontal aslant tract compared to the noisy results from CSD, demonstrating the network's potential to enhance tractography in very noisy data.

4.3.5 Comparison with anatomical tracers

Brain connectivity accuracy was evaluated by comparing tractography-derived connectivity matrices to tracer-based connectivity following a similar approach to Chapter 3. Figure 4.9 compares tracer-derived connectivity with tractography connectivity matrices obtained from postmortem CSD FODs, in-vivo CSD FODs, and in-vivo network FODs. Correlations

between tracer-based and tractography-derived connectivity matrices are presented in Figure 4.9B, demonstrating a higher correlation for network-derived FODs compared to CSD FODs in in-vivo dMRI. However, the correlation was lower than that observed in postmortem dMRI using CSD FODs, likely due to the higher data quality, SNR and higher resolution of the postmortem data. Additionally, when the tractography connectivity matrix was thresholded at 0.03, 0.05, and 0.07, network-derived FODs exhibited lower false positive rates than CSD FODs in in-vivo data. This suggests that network-derived FODs improve anatomical accuracy, though overall accuracy remains higher in postmortem dMRI compared to in-vivo dMRI.

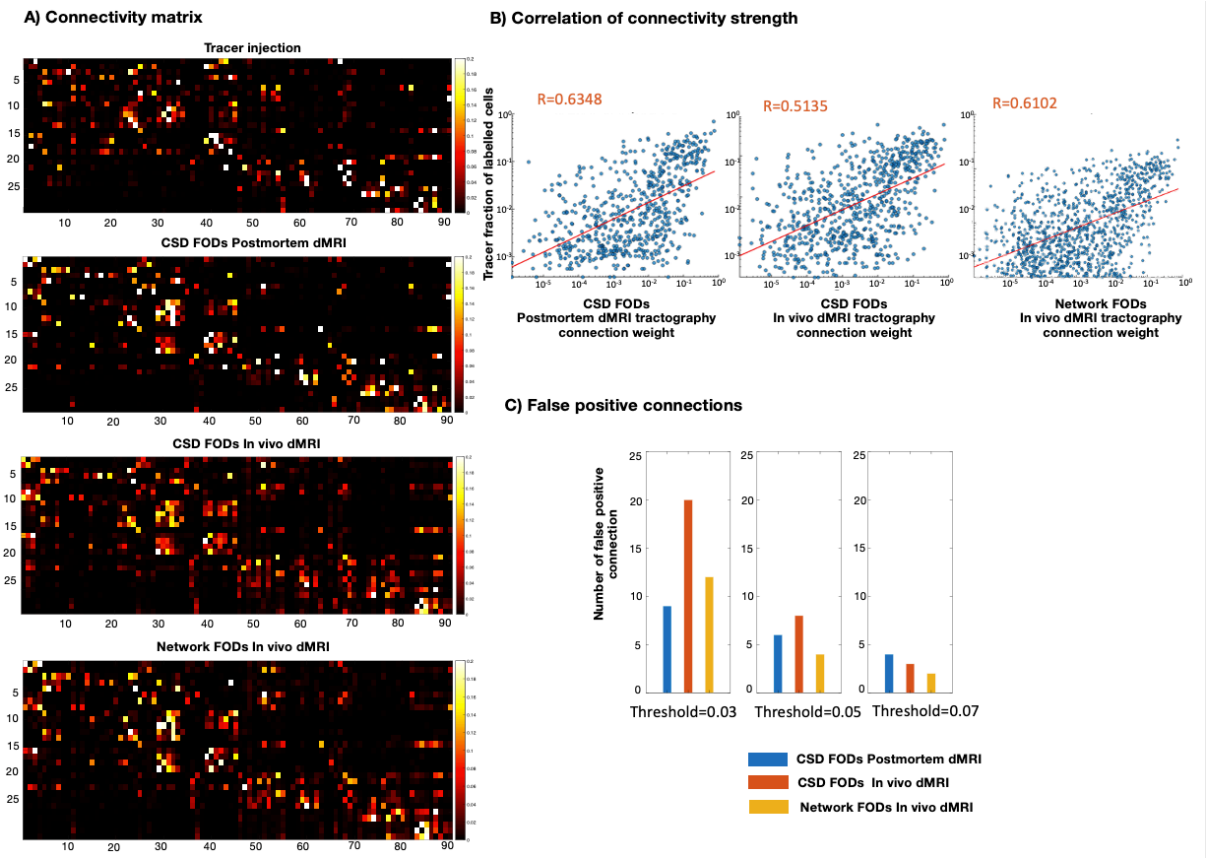


Figure 4.9 Comparison between tracer-and tractography-based connectivity matrices. A) The connectivity matrix of tracer injection is compared with those generated with the postmortem dMRI CSD FODs, in-vivo dMRI CSD FODs and in-vivo dMRI network FODs. B) Correlation of connectivity strength. The correlation between tractography and tracer connectivity weights was calculated by plotting the data on a logscale to quantitatively assess the predictive power of tractography. Tracer data were thresholded at 1e-6 and tractography data were thresholded at 1e-4. R indicates the Pearson correlation coefficient. C) False positive connections. The number of false positive connections was calculated at different thresholds (0.03, 0.05 and 0.07) for the tractography connectivity matrix and compared across the methods (postmortem dMRI CSD, in-vivo dMRI CSD and in-vivo dMRI network FODs).

4.4 Discussion

In this study, we present a domain adaptation network designed to transfer microscopy-based information to in-vivo diffusion MRI data, enhancing fibre orientation estimation in subjects where microscopy is not available. However, the transfer of information from microscopy to MRI and from postmortem to in-vivo dMRI is challenging due to differences in tissue properties and signal types. To address this, postmortem dMRI, which shares the same signal type as in-vivo dMRI and the same tissue properties as microscopy, serves as an effective intermediary. Compared to in-vivo dMRI, postmortem dMRI offers advantages such as a higher SNR, fewer artifacts, and the absence of motion. The network is designed with a domain adaptation structure to account for differences between postmortem and in-vivo dMRI, ensuring its applicability to both data types. Our results on postmortem and in-vivo macaque data demonstrate the successful transfer of information from postmortem microscopy to in-vivo macaque dMRI data.

The network effectively maps diffusion MRI signals to fibre orientations while preserving features of the fibre architecture described by the microscopy. For example, the network FODs successfully resolve white matter organisation patterns within the internal capsule that mirror those observed in the motor cortex, even in the in-vivo data. Furthermore, comparisons with tracer connectivity demonstrate that the network-derived FODs outperform CSD FODs in brain connectivity mapping, achieving higher correlation and lower false positive rates. Our network FODs exhibit lower dispersion (fanning) and fewer crossing fibres than CSD FODs, echoing results previously found when comparing microscopy and hybrid FODs to CSD (Zhu et al., 2025). This improvement likely results from the deep learning framework's ability to elucidate the complex relationship between diffusion MRI signals and FODs in a data-driven manner. In CSD, diffusion signals are modelled as the convolution of FODs with a fibre response function (FRF), where the FRF represents the diffusion signal for a single coherent fibre population. Several methods exist to estimate the FRF. One method estimates the FRF from voxels with high fractional anisotropy (FA) values, which are assumed to predominantly contain a single fibre population. In multi-shell data, CSD can estimate distinct response functions for different tissue types (e.g., grey matter, white matter, cerebrospinal fluid), but in single-shell data, it is constrained to a single response function, which can be suboptimal. The FRF is then applied across the entire white

matter or brain region. However, the assumption of a single brain-wide FRF has been challenged. Studies using 3D confocal microscopy have revealed significant variability in the shape and amplitude of response functions across different microstructures (Schilling et al., 2019c). Additionally, a generative joint dMRI-histology model has demonstrated that the response function depends on local anatomy and using a brain-wide response function leads to an overestimation of dispersion (Howard et al., 2019). Our network addresses this limitation by learning the relationship between dMRI signals and the FOD (essentially the FRF) directly from data. Without the constraint of a single FRF, the network may learn a range of FRFs depending on where the input MRI falls within the data distribution. This could help explain why we can more accurately estimate FODs that preserve the microscopy features in the cortex compared to CSD as we may learn tissue-specific FRFs.

Our results demonstrate how the network improves the tracking of U-shaped fibres. U-shaped fibres are a type of superficial white matter (SWM) that connect neighbouring gyri (Gahm and Shi, 2019). However, tracking U-shaped fibres through diffusion tractography is challenging due to their small size, large curvature and proximity to grey matter, which results in partial volume effects in diffusion signals. Traditional methods such as postmortem dissection have proven insufficient in fully characterising U-fibres because the fibre configuration is vulnerable when removed from the brain cortex (Guevara et al., 2020). To address these challenges, advanced techniques have been developed to improve U-fibre identification. Most approaches focus on enhancing fibre tracking instead of improving the underlying fibre orientations. For example, surface-based tracking uses the grey matter white matter interface for streamline seeding as an anatomical constraint (Gahm and Shi, 2019). Alternatively, clustering streamlines with similar morphology and terminations that are replicable across subjects has also been shown to improve U-fibre identification (Van Dyken et al., 2024). In this study, we aim to improve the underlying fibre orientation estimation near the grey matter boundary, thereby enhancing U-shaped fibre tractography. For the macaque brain, where established pipelines for U-shaped fibre tracking at the whole brain level are lacking, we seeded streamlines from one gyrus and tracked them to an adjacent gyrus to identify U-fibres. Our network improves the tracking of U-shaped fibres near the cortex, a task that often fails or is less optimal when using CSD FODs. This is likely due to our network, which is based on myelin-sensitive microscopy, having better information about how myelinated fibres are organised in the cortex, at the grey-white matter boundary, and in the U-fibres (or superficial white matter) below. This facilitates the improved reconstruction

of white matter fibres from these orientations. The deterioration of U-fibres has been implicated in neurological and neurodegenerative diseases (Phillips et al., 2016). As such, the improved delineation of U-fibres, if translated into in-vivo human data may have important implications for the diagnosis of these diseases.

Other deep learning methods have previously been developed to also estimate fibre orientations from dMRI, similarly addressing the limitations of suboptimal biophysical models. For example, Davood et al. demonstrated that a multilayer perceptron can effectively map from dMRI signals, interpolated onto a fixed spherical grid in q space, to FODs, improving accuracy in both phantom and real data (Karimi et al., 2021). Similarly, Lucena et al., used a 3D convolutional neural network to predict FODs comparable to those derived from multi-shell dMRI when using single-shell data, enabling more accurate fibre configuration resolution with time-limited acquisition protocols (Lucena et al., 2021). Additionally, deep learning approaches leveraging microscopy data have been explored. For example, Zifei et al., trained a network using tract-tracing data from the Allen Mouse Brain Connectivity Atlas and recapitulated the axonal connectivity in the hippocampus and cortex showing improved specificity (Liang et al., 2023). However, the applicability of their method to the human brain remains uncertain due to substantial differences in white matter organisation between the mouse and human brain. Our work is the first to utilise in-vivo, postmortem dMRI and microscopy within the same macaque brain with co-registered brain microstructures and complex enough fibre architecture. The network recapitulates previous results showing improved fibre tracking using hybrid output (compared to CSD) but now using in-vivo data. The next chapter will explore the adaptation of our network to in-vivo human data, highlighting its potential to transfer microscopy insights into living human brains. Improved precision in fibre tracking can better delineate the white matter alterations which further improve tractography diagnosis for neurological and neurodegenerative conditions such as seizure (Kreilkamp et al., 2017), schizophrenia (Deng et al., 2019), Parkinson's disease (Son et al., 2016) and tumor sugery (Panesar et al., 2019) showing potential for both diagnosis and surgical guidance.

The network has several limitations. First, the network was trained using data from only a single macaque, which may not provide enough training data to avoid overfitting, potentially leading to the lack of generalisability. In addition, the brain data doesn't include pathology, which means some pathological data may fall outside the data distribution. We also assume

no individual differences when mapping between diffusion signals and fibre orientations, without considering inter-individual variability. Second, the hybrid dMRI-microscopy FODs were reconstructed in the postmortem dMRI space. During training with in-vivo dMRI data, the hybrid FODs were registered to the in-vivo space, which may have introduced registration errors or rotations. To account for misregistration, a small angle rotation was tolerated when calculating the loss function. Alternative methods for better quantifying rotation and misregistration could further improve the accuracy of FOD estimation.

Conclusion

We developed a domain adaptation network to translate fibre information learnt from microscopy into in-vivo dMRI. Our data-driven network estimates fibre orientations without relying on complex biophysical modelling, recovering meaningful microscopy-based fibre features and improving the precision of fibre tracking. If we are able to demonstrate more precise tracking when applied to humans, the network has potentially important clinical applications where precision is fundamental to patient outcomes, such as the targeting of subcortical nuclei for brain stimulation or similar interventions.

5

Estimating microscopy-informed fibre orientations from dMRI data in the UK Biobank

Table of Contents

5.1 Introduction *115*
5.2 Methods *119*
5.2.1 Data 119
5.2.2 Unsupervised domain adaptation (UDA) 121
5.2.3 Fibre orientation estimation 123
5.2.4 Tractography 123
5.2.5 Structural-functional alignment 125
5.3 Results *128*
5.3.1 Network application to high-resolution human data 128
5.3.2 Network application to low-resolution single-shell dMRI in in-vivo human 129
5.3.3 The network enhances superficial white matter tractography 131
5.3.4 The network improves subcortical fibre tracking 132
5.3.5 Structural TTM and rsfMRI network alignment in the visual cortex 133
5.3.6 Whole-brain structural TTM and functional alignment 134
5.4 Discussion *138*

Foreword

There remains an unmet need for non-invasive methods to map mesoscale neuroanatomy in neuroscience. While diffusion MRI (dMRI) tractography is the most widely used approach, its ability to estimate fibre orientations - the basis for fibre tracking - is limited in accuracy. To address this, we developed a method that leverages co-registered microscopy, postmortem dMRI and in-vivo dMRI data to enhance in-vivo tractography. Our approach utilises a machine learning network to predict microscopy-informed fibre orientations directly from dMRI signals, improving tracking accuracy. Initially trained on macaque brain data, here the network was successfully adapted to in-vivo human datasets, as demonstrated using UK Biobank data. The network-estimated fibre orientations demonstrated close alignment with neuroanatomical expectations, enabling refined delineation of superficial white matter tracts and subcortical pathways. Compared to conventional methods, our approach produced tractography outputs that showed stronger correspondence with functional connectivity patterns suggesting improved capture of individual differences in white matter cortical termination. By bridging microscale anatomy and macroscale dMRI, our method advances the potential for more accurate, personalised and biologically meaningful mapping of brain connectivity.

Published work

Conference

Silei Zhu, Nicola K. Dinsdale, Saad Jbabdi, Karla L. Miller, Amy F.D. Howard, Estimating microscopy-informed fibre orientations from dMRI data in the UK BioBank, ISMRM Annual Meeting 2025, Digital Poster.

Silei Zhu, Nicola K. Dinsdale, Saad Jbabdi, Karla L. Miller, Amy F.D. Howard, Estimating microscopy-informed fibre orientations from dMRI data in the UK BioBank, ISMRM Diffusion Workshop 2025, Oral.

Individual contributions to this thesis chapter

My contributions to this chapter include network adaptation, fibre orientation estimation, tractography, rsfMRI network analysis, manuscript writing, editing and review. UK BioBank data were provided and pre-processed by the UK BioBank team(Miller et al., 2016).

Steps for conceptualisation, data processing, network design and manuscript editing were advised by Nicola K. Dinsdale, Saad Jbabdi, Karla L. Miller and Amy F.D. Howard.

5.1 Introduction

Advancing our understanding of human brain function and dysfunction requires precise characterisation of neuroanatomical connectivity. Diffusion MRI (dMRI) is the most widely used non-invasive method for mapping in-vivo brain connectivity, yet its resolution and accuracy remain limited by technical constraints such as noise, partial volume effects, and modelling assumptions (Johansen-Berg and Behrens, 2014). In contrast, postmortem microscopy techniques including electron microscopy (Gray, 1969), light-sheet microscopy (Johnson et al., 2023), and polarised light imaging (Axer, 2011; Axer et al., 2001) provide microscale visualisation of fibre architecture, offering insights into axonal organisation that are often considered the gold standard. However, microscopy is inherently restricted to postmortem tissue, limiting its applicability to living populations while dMRI enables large-scale in-vivo investigations. Bridging this gap is essential to enhance in-vivo connectivity mapping.

In this chapter, we adapted the deep learning framework introduced in Chapter 4 to in-vivo human dMRI data, transferring knowledge of fibre architecture derived from macaque microscopy to enhance in-vivo connectivity mapping. The method predicts microscopy-informed fibre orientation distributions (FODs) from in-vivo human dMRI, with the goal of improving fibre tracking accuracy in living humans. However, validating in-vivo tractography remains inherently challenging due to the absence of ground-truth connectivity data for the in-vivo human brain. Tracer-based methods, commonly used in non-human species to map axonal pathways, are ethically and practically infeasible in humans, as they require invasive injection before death (Maffei et al., 2022c; Yendiki et al., 2022). Microscopy, while valuable in visualising axons, is limited to small brain regions in humans, as whole-brain imaging at microscopic resolution remains prohibitively time-consuming and technically impractical. Consequently, validation relies on sparse postmortem samples, which are typically restricted to confirming major white matter tracts. Furthermore, the substantial interindividual variability in human brain structure, which is more pronounced than in other species, complicates the connectivity validation (Schilling et al., 2023). To address this lack of ground truth, we evaluated our approach using three tractography challenges based on

anatomical accuracy and assessed the individual variances of tractography through multimodal integration.

The first application focuses on our ability to successfully reconstruct the superficial white matter (SWM), which includes short cortico-cortical association fibres that are critical for brain function. SWM fibres are known to exhibit delayed myelination during neurodevelopment and are particularly vulnerable to demyelination in neurological disorders (Wu et al., 2014a), highlighting their clinical relevance. Despite this, the SWM remains understudied compared to deep white matter, largely due to imaging limitations. Its intricate curvature and proximity to grey matter pose challenges to conventional dMRI fibre orientation estimation algorithms (Jeurissen et al., 2014). Recent advances in postmortem quantitative ion beam microscopy (1 μm resolution) and in-vivo 7 Tesla MRI (400 μm isotropic) have enabled precise SWM mapping (Kirilina et al., 2020). However, such high-resolution imaging is impractical for clinical or large-scale studies. Lower-resolution dMRI (e.g., 2 mm isotropic) suffers from partial volume effects, where voxels containing SWM, grey matter, and deep white matter produce mixed signals, obscuring SWM-specific fibre orientations. Here, we evaluate whether our microscopy-informed network can disentangle SWM signals from low-resolution human dMRI. By leveraging data-driven methods, the network aims to isolate myelin-specific fibre orientations, enabling robust reconstruction of SWM architecture without requiring ultra-high-resolution acquisitions.

The second application relates to our ability to reconstruct subcortical connections, enabling more precise identification of subcortical nuclei for use as surgical targets in clinical practice. One example is deep brain stimulation (DBS), an established therapy for Parkinson's disease (Benabid, 2003). However, current DBS procedures face several challenges. Target localisation typically relies on histological brain atlases derived from population averages, which can introduce errors when applied to individual patients due to neuroanatomical variability (Anthofer et al., 2014). Additionally, subcortical nuclei are often small and closely positioned structures but serve distinct functions, requiring surgical precision at the millimetre scale (Wagle Shukla and Okun, 2014). For example, the ventral intermediate nucleus (VIM) and the ventral posterolateral nucleus (VPL) are two DBS target regions in the thalamus that are in close contact. While high-resolution dMRI, such as ultra-high-field imaging at 7T, holds promise for delineating subcortical connectivity(Patriat et al., 2023), its

clinical feasibility remains limited due to access and time constraints. Tractography of the pathways connecting to VIM and VPL has been shown to aid the identification of these nuclei based on their connectivity patterns. Therefore, better characterisation of subcortical connectivity is essential for precise localisation of subcortical nuclei and thus improving surgical outcomes (Yamada et al., 2010). In this work, we evaluated whether the microscopy-informed network can enhance subcortical fibre tracking.

The third application focuses on our ability to reconstruct the cortical terminations of white matter tracts, defined as the cortical regions where fibres originate and terminate. We use "tract termination" to describe both origination and termination as diffusion MRI cannot determine the direction of information transfer. In other words, our tract termination maps (TTMs) describe fibres tracking from the deep white matter to the cortex, regardless of their origin or the flow of information. Patterns of tract termination exhibit substantial variability across individuals, ages, and stages of brain development (Schilling et al., 2023). Crucially, changes in white matter connectivity and cortical termination are spatiotemporally synchronised, reflecting their collective role in brain maturation and cognitive function (Niogi, 2010)·(Deutsch et al., 2005). Despite this, most studies examine white matter tracts and cortical structures in isolation, leaving white matter cortical termination patterns relatively underexplored (Schilling et al., 2023). This gap is partly due to known limitations in dMRI which struggles to accurately map cortical termination patterns due to phenomena such as gyral bias (Schilling et al., 2017b). Mapping cortical termination faces two main challenges: 1) inter-subject variability, and 2) the absence of a ground truth for validation. To overcome these, we leverage complementary information from functional MRI, which provides insights into cortical boundaries and also helps mitigate the lack of a ground truth, allowing us to validate inter-subject variations in tract termination.

Brain regions are known to have functional specialisation, with different cortical areas supporting different perceptual and cognitive processes. Cortical regions involved in similar tasks display synchronised activity. This can be used to define local boundaries between neighbouring cortical regions, and to identify spatially separated regions involved in the same functional network (Eickhoff et al., 2018). The latter requires structural connectivity, either via direct white matter tracts linking the two regions, or indirect connections. Resting-state fMRI (rsfMRI) captures spontaneous neural activity through the blood-oxygen-level-dependent (BOLD) signal, a haemodynamic measurement for neuronal activation. Functional

connectivity (FC) quantifies statistical correlations in BOLD signals across regions, revealing networks with similar patterns of spontaneous brain activity, such as the visual, sensorimotor, and default mode networks (Lee et al., 2013). Critically, regions linked by structural connections typically exhibit shared functional activity (Honey et al., 2009), underpinning the structure-function relationship. However, tractography errors common in structural connectivity mapping can result in misalignment of cortical boundaries (defined by fMRI or tract termination maps). For example, a tract which should terminate across an entire gyrus may instead terminate in only a small portion of the gyral cortex (e.g., restricted to the gyral crown (Schilling et al., 2017b)) or may erroneously project to adjacent regions (Figure 5.1). This would result in the TTM to appear either overly constrained or expanded relative to the true cortical boundaries or functional connectivity map, assuming the latter provides accurate boundaries.

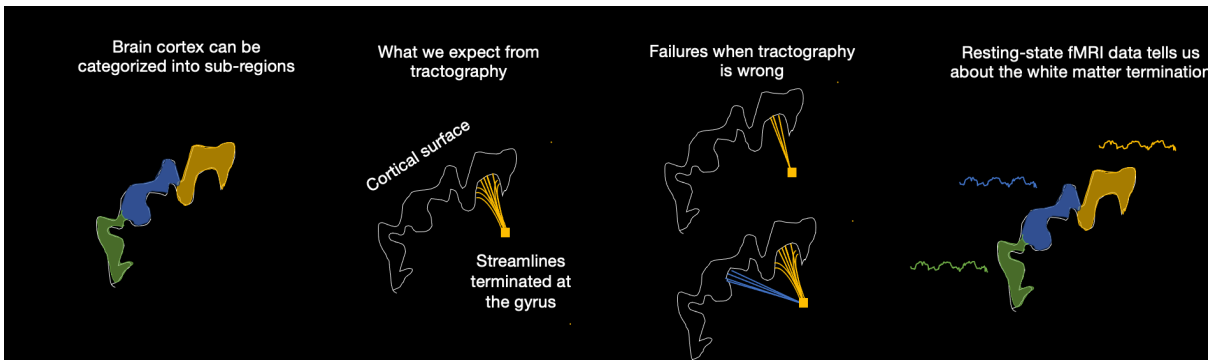


Figure 5.1 White Matter Tract Termination and rsfMRI Functional Activity Alignment. Brain regions comprise distinct functional subregions. White matter tract terminations - defined by tractography - help delineate these boundaries. However, tractography is prone to errors, as streamlines terminating within a gyrus may partially end in the crown or mistakenly project to adjacent regions. Since regions with similar structural connectivity exhibit similar rsfMRI activity, structural-functional alignment can help verify the accuracy of white matter tract terminations.

Since ground-truth termination boundaries remain unknown, we propose that the alignment between structural TTMs and rsfMRI can serves as a validation metric for tractography accuracy. Specifically, stronger alignment suggests that structural TTMs can accurately define regions with shared functional activity, reflecting biologically plausible connectivity pattern (D. Wang et al., 2015). This framework allows us to evaluate whether our microscopy-informed fibre orientations and the resulting tractography better identify individual termination variability compared to conventional methods, using in-vivo human MRI, where a microscopy ground truth is not available. These structural variations,

when accurately mapped, have the potential to serve as personalised biomarkers for brain development and dysfunction (Stephan et al., 2017). For instance, the spatial localisation of terminations may vary across individuals exhibiting expansion or contraction that is predictive of behavioural outcomes (e.g., visual discrimination performance (Baldassarre et al., 2012)·(Abraham et al., 2017)).

Together, this chapter modifies the microscopy-informed deep learning framework (Chapter 4) for in-vivo human dMRI via unsupervised domain adaptation. This approach enables the cross-species translation of microstructural information from macaque to human and integrates postmortem microscopy and in-vivo dMRI in humans. By bridging these modalities, the framework offers a potential tool for advancing connectivity studies in both research and clinic.

5.2 Methods

5.2.1 Data

The network was trained on macaque data from the BigMac Dataset as previously described (Chapter 4). Our method was then translated to and evaluated on two distinct in-vivo human dMRI datasets: (1) high-resolution data (1.25 mm isotropic voxels) and (2) standard-resolution data (2 mm isotropic voxels).

In-vivo human data at 1.25 mm

High-resolution dMRI data were obtained from the young adult cohort of the WU-Minn Human Connectome Project (HCP) (Essen et al., 2013). For this study, we selected a single female subject (age <30 years). Diffusion imaging was performed on a 3T Siemens scanner using a spin-echo echo-planar imaging (EPI) sequence with the following parameters: repetition time (TR) = 5520 ms, echo time (TE) = 89.5 ms, flip angle = 78°, and field of view (FOV) = 210 × 180 mm. Data were acquired across three diffusion weightings (b-values: 1000, 2000, 3000 s/mm²) with 90 diffusion-encoding directions per shell, supplemented by six non-diffusion-weighted (b=0 s/mm²) volumes. To mitigate phase-encoding distortions, acquisitions were repeated with opposing phase-encoding directions (right-to-left and left-to-right). The multi-shell data were subsampled to single-shell data (b = 1000 s/mm², 90 directions) since the network was designed for single-shell data more similar to clinically

feasible data. Notably, the acquisition time for the single-shell is approximately 20 minutes offering practical advantages over the multi-shell protocol (~60 minutes).

Consistent with the macaque data processing pipeline, diffusion-weighted signals were normalised by the non-diffusion-weighted signals (S0) to minimise T2-weighted contrast variability. Subsequently, normalised signals were fitted to the spherical harmonics (order = 8) to reduce noise sensitivity. This representation ensures invariance to rotational differences in gradient orientation and variations in the number of gradient directions, thereby facilitating cross-protocol generalisation. Consequently, the network was designed for single-shell dMRI data in spherical harmonics format, eliminating the need for b-values and b-vectors as input.

In-vivo human data at 2 mm

To evaluate the generalisability of our method at a lower resolution and with accelerated protocol which has more similar noise characteristics to clinically relevant data. We used the dMRI data (2 mm isotropic voxels) from the UK Biobank (Melissa Clare O'Donoghue et al., 2023). Additionally, we used structural MRI (T1-weighted) and resting-state functional MRI (rsfMRI) data from the same subjects. The tract terminations maps were validated against rsfMRI. Ten subjects from the UK BioBank were used in this Chapter.

Diffusion-weighted imaging was performed at 2 mm isotropic resolution (FOV = 104 × 104 × 72 mm^3) using a multi-shell protocol with b-values of 1000 and 2000 s/mm^2 (50 directions per shell). The acquisition included five non-diffusion-weighted volumes (b=0 s/mm^2) and three blip-reversed b0 volumes for distortion correction (anterior-posterior and posterior-anterior). Preprocessing included eddy current, susceptibility distortion, head motion correction and outlier-slices corrected using FSL (Jenkinson et al., 2012). For input to the network, the multi-shell data were subsampled to single-shell (1000 s/mm^2). The full multi-shell data, which provides richer diffusion contrasts and higher angular resolutions, were additionally used as a reference standard for fibre orientation estimation. As above, spherical harmonics were fitted to the diffusion attenuated signal (S/S0) prior to input to the network. The acquisition duration was approximately 7 minutes for multi-shell dMRI.

Resting-state functional MRI data were acquired at 2.4 mm isotropic resolution (FOV = 88 × 88 × 64 mm^3), using a repetition time (TR) of 0.735 s and an echo time (TE) of 39 ms. Preprocessing included motion correction, intensity normalisation, high-pass temporal

filtering, EPI unwarping, gradient distortion correction unwarping, and artefact removal (Miller et al., 2016).

T1-weighted structural MRI was acquired at 1 mm isotropic resolution (FOV = 208 × 256 × 256 mm^3) using a 3D MPRAGE sequence. T1-weighted scans were processed using FreeSurfer (Dale et al., 1999; Fischl et al., 1999) to reconstruct pial and white matter surfaces that were then registered to the MNI152 standard space via Multimodal Surface Matching (MSM) (Robinson et al., 2014). MSM leverages surface-based geometry to drive registration and improve cross-subject alignment, enhancing the accuracy of group-level analyses.

5.2.2 Unsupervised domain adaptation (UDA)

This study adapted our macaque-trained network for microscopy-informed fibre orientation estimation (Chapter 4) to human in-vivo data using an unsupervised domain adaptation (UDA) framework. Similarly, the domain adaptation approach was applied to address distributional shifts between the source and target domains (Ganin et al., 2017). These shifts, which arise from differences in data distribution, can lead to degraded model performance when models trained on a source domain (macaque data) are applied to a target domain (human data). UDA mitigates this discrepancy by jointly leveraging labelled source domain data and unlabelled target domain data, enabling cross-domain feature alignment (Liu et al., 2022). Unlike conventional retraining, our adaptation process used the pre-trained parameters from the original macaque-derived model as initialisation and then refined them for in-vivo human MRI using unlabelled human data.

The UDA framework operated in two phases: training and inference. During training, the model aligned feature representations between domains to minimise distributional shifts. The labelled macaque data provided direct supervision for fibre orientation estimation. The unlabelled human data guided the adaptation process to different species by informing the model of source-target variations. This process ensured the feature extractor learned species-invariant features, meaning the network performed similarly well on both human and macaque MRI inputs. During inference, the model then took unlabelled human dMRI data and predicted microscopy-informed FODs, without the requirement of microscopy from the same brain.

We used the same network architecture as in Chapter 4 consisting of a feature extractor, a predictor and a domain classifier. For the input and output of the data, the brain volumes were subsampled into 3×3×3 blocks incorporating shared information of neighbouring voxels. The adaptation pipeline comprised two sequential training stages designed to make the model species-invariant following a similar training approach with the same loss functions as described in Chapter 3 (Figure 5.2):

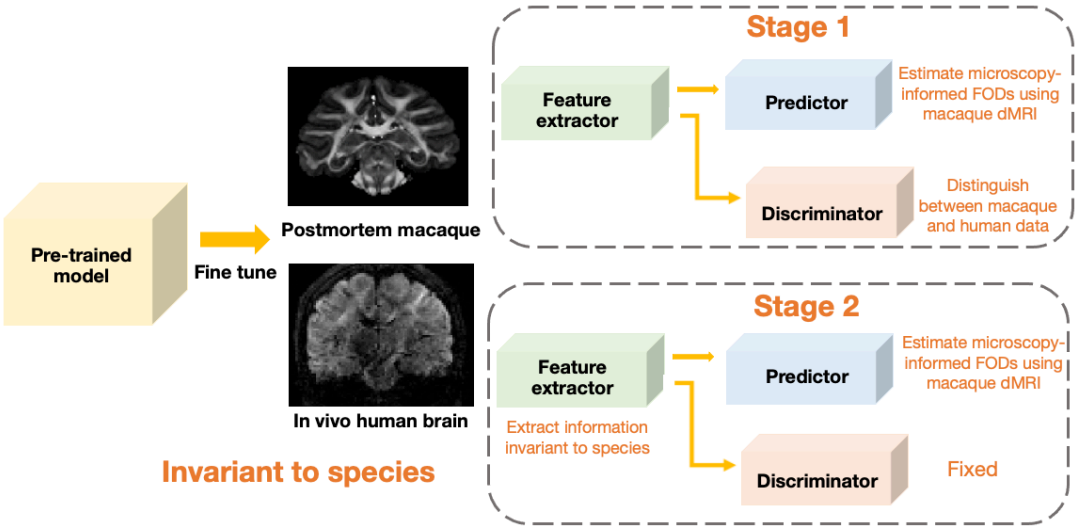


Figure 5.2 Unsupervised Domain Adaptation Framework.
The adaptation of the network to in-vivo human data establishes species invariance (macaque vs. human) through a two-stage training process: (1) The feature extractor and predictor are trained to derive microscopy-informed FODs from macaque dMRI, while a discriminator learns to distinguish between human and macaque dMRI. (2) With the discriminator fixed, the feature extractor is trained to capture species-invariant features, and both the feature extractor and predictor are optimised to estimate FODs.

Stage 1

1. The feature extractor took dMRI data as input and output a feature space (latent representation of the data). The predictor then took features as input and estimated microscopy-informed FODs. During training, hybrid dMRI-PLI fibre orientations were used as ground truth and were provided only for macaque data. Parameters in the feature extractor and predictor were optimised via a mean squared error.
2. The domain discriminator also took the features from the feature extractor and was trained to distinguish between human (target) and macaque (source) domains.

Stage 2

With the discriminator parameters fixed, the feature extractor and predictor were refined to make the network invariant to species:

1. The feature extractor was optimised to generate species-invariant features by minimising a confusion loss. The predicted domain labels were computed using the feature extractor and the fixed discriminator. The optimisation process ensures that the feature representations can confuse the discriminator, forcing the last layer of the feature extractor to be species-invariant.
2. The feature extractor and predictor continued training as before on the macaque dMRI data to preserve accuracy in microscopy-informed FOD estimation.

After training, the feature extractor produced species-invariant representations at its last layer, enabling consistent FOD prediction across species. A batch size of 128 was used. To address differences between datasets (resolution, noise etc), the network was independently adapted to high-resolution (1.25 mm) and low-resolution (2 mm) human acquisition protocols prior to FOD estimation. Critically, the adaptation process required only species labels (macaque/human) without the need for human-specific fibre orientation.

5.2.3 Fibre orientation estimation

FODs were derived from the adapted species-invariant network. For benchmarking, FODs were computed using constrained spherical deconvolution (CSD) implemented in MRtrix3 (v3.0.3) (Tournier et al., 2019). For multi-shell human data, the dwi2fod msmt_csd algorithm was applied, which estimated tissue-specific response functions for white matter, grey matter, and cerebrospinal fluid (CSF) (Jeurissen et al., 2014). For single-shell data, the dwi2fod csd command was utilised, generating a single white matter response function(Tournier et al., 2007). This analysis was performed for both high-resolution (1.25 mm) and standard-resolution (2 mm) human datasets.

5.2.4 Tractography

Major white matter tract tractography

Whole-brain probabilistic tractography was performed using FODs generated by both the network and CSD using the iFOD2 algorithm. Tracking parameters included seeding 30 streamlines per voxel, a step size of 0.2 mm, and termination criteria defined by an FOD amplitude threshold of 0.1, a maximum tract length of 120 mm, and a minimum tract length

of 5 mm. To isolate anatomically specific pathways, tract segmentation was performed using inclusion and exclusion masks from the XTRACT atlas (Warrington et al., 2020). For validation, two functionally critical tracts were reconstructed: the corticospinal tract (CST), essential for motor function, and the optic radiation (OR), central to visual processing. Streamlines intersecting the inclusion masks and not the exclusion regions were retained, ensuring anatomically plausible reconstructions.

Superficial white matter tractography

Superficial white matter (SWM) tracts form connectivity between adjacent cortical regions and are critical for neural processing. To reconstruct SWM pathways, we employed a validated pipeline (Shastin et al., 2022) comprising two sequential steps: whole-brain tractography and SWM-specific filtering.

Whole-brain probabilistic tractography was first performed using the iFOD2 algorithm in MRtrix3, generating an initial tractogram with 5 million streamlines. Parameters were constrained to prioritise short fibres characteristic of SWM, with a maximum streamline length of 40 mm to exclude long-range fibres and a FOD amplitude termination threshold of 0.05.

The tractogram was then iteratively filtered to isolate SWM fibres. First, a grey-grey matter filter retained only streamlines originating and terminating within cortical grey matter. Second, a hemisphere-hemisphere filter removed inter-hemispheric commissural fibres by restricting streamlines to a single hemisphere. Third, a white matter filter ensured streamlines traversed white matter, excluding superficial U-fibres confined to grey matter. This multi-stage filtering approach, validated in prior work (Shastin et al., 2022), enhances specificity to SWM while improving cortical coverage.

Cortical surfaces and tissue boundaries, derived from T1-weighted structural images using FreeSurfer, served as anatomical masks to remove any streamlines that did not meet the above criteria (Fischl, 2012). The pipeline was applied to FODs generated by both CSD and the network to enable comparative analysis of SWM reconstructions.

Subcortical tractography

Subcortical regions encompass deep grey matter structures (e.g., basal ganglia, thalamus) and their associated white matter pathways, which have critical functions such as motor control, emotion regulation, and decision-making (Patriat et al., 2023). To map connectivity between these structures, we performed subcortical tractography using region of interest (ROI)-to-ROI tracking with ROI masks derived from an atlas of 25 Parkinson's disease patients (Xiao et al., 2017). The atlas, aligned to the MNI ICBM152 space at 0.3 mm isotropic resolution, delineated subcortical nuclei: subthalamic nucleus, substantia nigra, red nucleus, globus pallidus internus (GPi), globus pallidus externus (GPe), putamen, and thalamus (Xiao et al., 2017).

Prior to tractography, atlas-defined masks were non-linearly registered to the individual in-vivo dMRI space using FSL FNIRT (Jenkinson et al., 2012), ensuring alignment with subject-specific anatomy. These masks served as inclusion regions for streamline seeding and propagation. Three functionally and clinically relevant pathways were reconstructed: (1) projections linking the thalamus to GPi, (2) nigrostriatal connections between the substantia nigra and striatum, and (3) rubrothalamic tract connecting the red nucleus to the thalamus(Petersen et al., 2018). Tractography was implemented identically for both network-derived and CSD-estimated FODs to enable direct comparison, with parameters optimised for subcortical anatomy (step size = 0.5 mm, FOD threshold = 0.1, maximum length = 50 mm).

5.2.5 Structural-functional alignment

To evaluate whether our network predicted microscopy-informed fibre orientations enhance the characterisation of white matter terminations and better identify individual variability, we compared tract termination maps (TTMs) derived from network-derived and CSD-derived FODs. TTMs represent the density distribution of streamline endpoints projecting from the white matter onto cortical grey matter. Structural-functional alignment was assessed by comparing TTMs with resting-state functional networks, defined as cortical regions exhibiting temporally correlated fMRI signals (Figure 5.3).

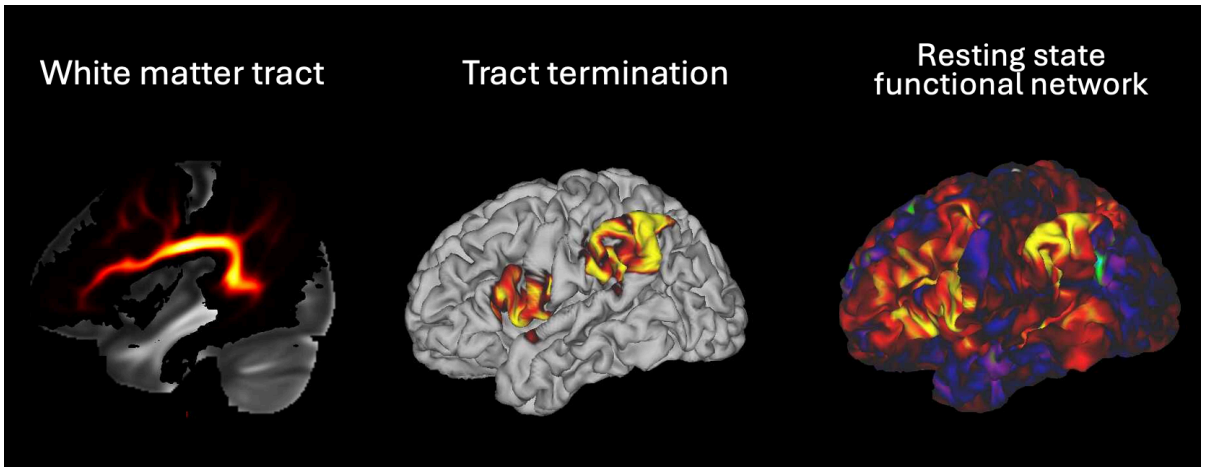


Figure 5.3 Structural-Functional Alignment Terminology.
The white matter tract density (left) is first obtained from tractography. The tract termination map (middle) describes terminations from this tract on the cortical surface. Regions sharing similar rsfMRI time series defines the rsfMRI network (Right).

Structural connectivity of the visual cortex

Here we compared the structure-function alignment of homotopic interhemispheric projections between the visual cortices. The visual cortices are structurally well-characterised and exhibit strong functional symmetry across hemispheres. This system provides an ideal system for evaluating structure-function alignment, as regions with robust structural connectivity are expected to display correlated functional activity.

Probabilistic tractography was seeded from the left visual cortex using the visual network mask from the UK BioBank volumetric resting-state networks with 25 component group ICA (Miller et al., 2016). The iFOD2 algorithm, with FOD amplitude threshold = 0.05, was applied to both CSD FODs and network FODs. TTMs on the right hemisphere were generated by normalising streamline endpoint counts by the total number of streamlines. This process was repeated for 3 subjects.

Functional maps

To derive the functional network associated with the visual cortex, we applied FSL's dual regression analysis (Nickerson et al., 2017). First, the left visual cortex mask (the same mask as the structural seed mask above) was used to extract the mean rsfMRI time series. The time series was then regressed against whole-brain rsfMRI data to identify voxels in the right hemisphere exhibiting temporally correlated signals. This produced subject-specific

functional connectivity maps, representing regions functionally synchronised with the left visual cortex.

We then quantified the spatial overlap between TTMs and the functional network in the right hemisphere. The overlap was measured using the Dice coefficient, which calculated the intersection of the binarised TTM (threshold = 0.001) and functional network (threshold = 0.2) normalised by their union. Higher Dice values indicated greater alignment between the structural TTM and rsfMRI network, following our neuroanatomical expectations. The structural-functional alignment in the visual cortex was evaluated across three subjects.

General linear model fitting

Above we explored structure-function relationships within a single cortical region. Here, we aim to develop a way to assess the alignment of structure and function across the whole brain. To achieve this, we generated TTMs for white matter tracts defined in the XTRACT atlas. A total of 23 white matter tracts were included, encompassing commissural fibres, as well as projection and association fibres from the left hemisphere. These TTMs provided the spatial basis for fitting 4D rsfMRI data using a general linear model (GLM) (Nickerson et al., 2017), using both CSD and network-derived FODs. We extracted the average time series for each TTM and regressed them against the rsfMRI. To evaluate the effectiveness of different methods (network versus CSD FODs) in capturing meaningful variance in the rsfMRI signal, we compared how well the spatial basis of TTMs explained the rsfMRI data by comparing the GLM residuals (Figure 5.4). To mitigate multicollinearity among the independent variables, we included TTMs exclusively from a single hemisphere. The GLM was formulated as follows:

$$Y(t) = \beta 0 + \sum_{i=1}^{n} \beta_i X_i(t) + \epsilon(t)$$

Where Y(t) is the resting-state time series at a given voxel, X_i(t) represents the tract-specific time series for tract i, β_i are the model parameters (regression coefficients), β_0 is the baseline time series and ϵ(t) is the residual error.

We fitted the GLM voxel-wise across the entire brain and extracted the residuals, which represent the unexplained portion of the voxel-wise time series. Smaller residuals suggest that

the TTMs provide a better low-dimensional representation of the rsfMRI (i.e. a better brain parcellation). The GLM was fitted, and residuals were calculated for ten subjects.

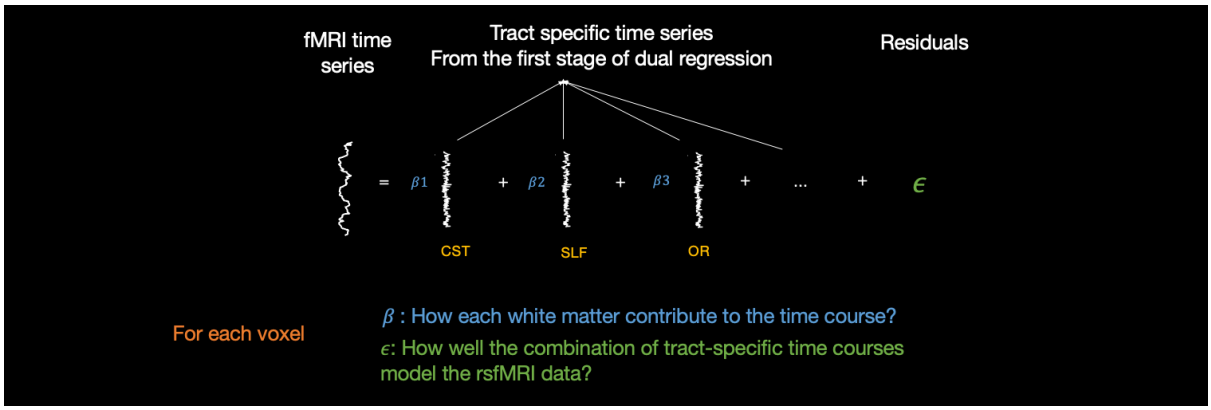


Figure 5.4 General Linear Model Fitting.
A general linear model was used to systematically and globally evaluate variance in rsfMRI data at each voxel. White matter tract-specific time series from the TTMs served as regressors (independent variables), while residuals quantified model fitting quality by capturing the difference between the predicted and measured voxel-wise fMRI time series. Lower residuals indicate a better low-dimensional representation of the rsfMRI data.

5.3 Results

5.3.1 Network application to high-resolution human data

Figure 5.5 shows the outputs from our network, which was trained on macaque and now adapted and applied to in-vivo human data from the HCP using unsupervised domain adaptation (Figure 5.2). The network-derived FODs exhibit strong agreement with those from CSD and follow neuroanatomical expectations. Tractography using the network FODs successfully replicates fine anatomical structures, such as the corticospinal tract branching into cortical gyri and the curved loop of the optic radiation. Together, these results suggest that the network has generalised effectively to human data and can produce biologically plausible tractography, guided by data-driven features rather than relying on explicit biophysical modelling. However, there are noticeable differences. Tractography using the network is more constrained and exhibits clear branching into distinct gyri. Moreover, while the network FODs contain fewer crossing fibres, these fibres are still present without interfering with crossing fibre tracking in the CST. These results highlight the network's potential for high-resolution data, demonstrating its ability to accurately depict brain structures and effectively describe brain connectivity compared to the model-based CSD method.

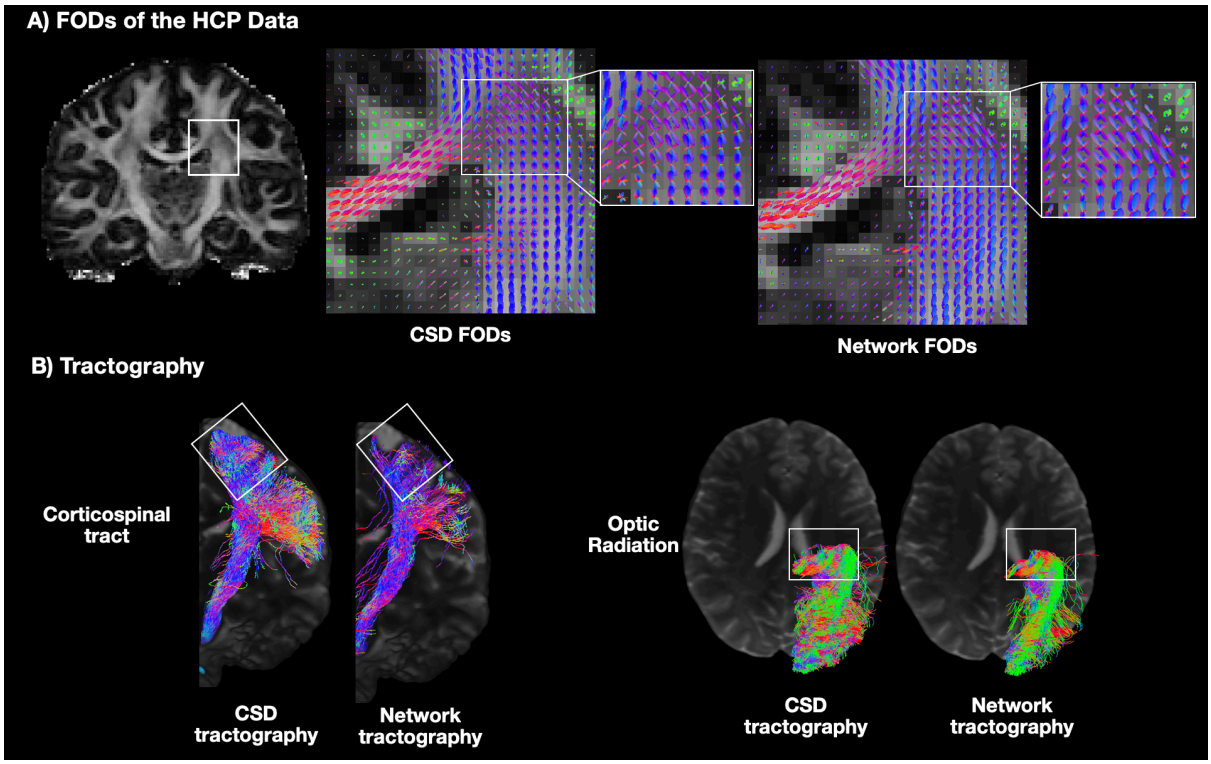


Figure 5.5 Application of network in the in-vivo human data with high quality.
The network was applied to high-resolution human data from the Human Connectome Project (HCP). A) Network FODs show good agreement with CSD FODs, following neuroanatomical expectations B) The corticospinal tract branching and the optical radiation with the backward curving structure (white box) were accurately depicted. This demonstrates the network's ability to produce biologically meaningful tractography, adhering to neuroanatomical expectations using data-driven FODs derived from microscopy data rather than biophysical modelling.

5.3.2 Network application to low-resolution single-shell dMRI in in-vivo human

To evaluate the network's utility in protocols with shorter acquisition times, we tested its performance on lower-quality single-shell dMRI data with 2 mm isotropic resolution from the UK BioBank.

Notably, the network produced FODs with enhanced robustness near grey matter-white matter boundaries compared to CSD. The network-derived FODs exhibit reduced noise and fewer spurious peaks (Figure 5.6), particularly in regions where CSD FODs show more random fibre orientations. Additionally, the network successfully captures anatomically plausible gyral fanning patterns, with primary fibre orientations aligning perpendicularly to gyral walls—a feature consistent with known microscopy neuroanatomy but often obscured

in low-resolution data. These results suggest that the network has the potential to mitigate limitations of conventional model-based methods (e.g. CSD) in low-quality datasets.

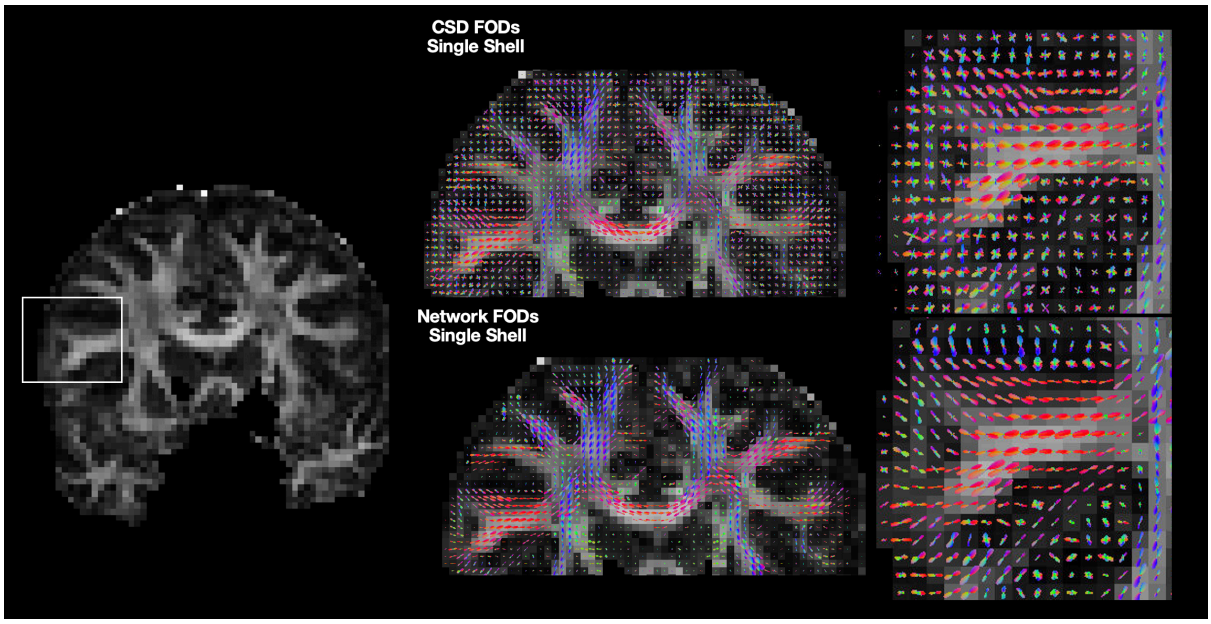


Figure 5.6 Application to UK BioBank dMRI.
The network was applied to in-vivo human data with single-shell dMRI at 2 mm resolution. Network-estimated FODs were compared to CSD FODs, showing reduced noise and better fanning patterns that echo myelin staining near the cortex.

Appendix 5.1 demonstrates the feasibility of reconstructing white matter tracts using network-derived FODs with both high-resolution (1.25 mm) data from the HCP and lower-resolution (2 mm) data from two UK BioBank subjects. Tractography successfully delineated representative tracts across three major anatomical categories including association fibres (inferior fronto-occipital fasciculus, IFO; frontal aslant tract, FA), commissural fibres (forceps minor, FMI), and projection fibres (superior thalamic radiation, STR). These results highlight the method's robustness to variations in data quality. Furthermore, Figure 5.7 illustrates tractography differences between tracts reconstructed from CSD and network FODs across three subjects. For example, the cortical projections of the corticospinal tract vary across individuals, with distinct termination patterns and densities. These differences are observed in both CSD and network tractography, though they manifest in different ways.

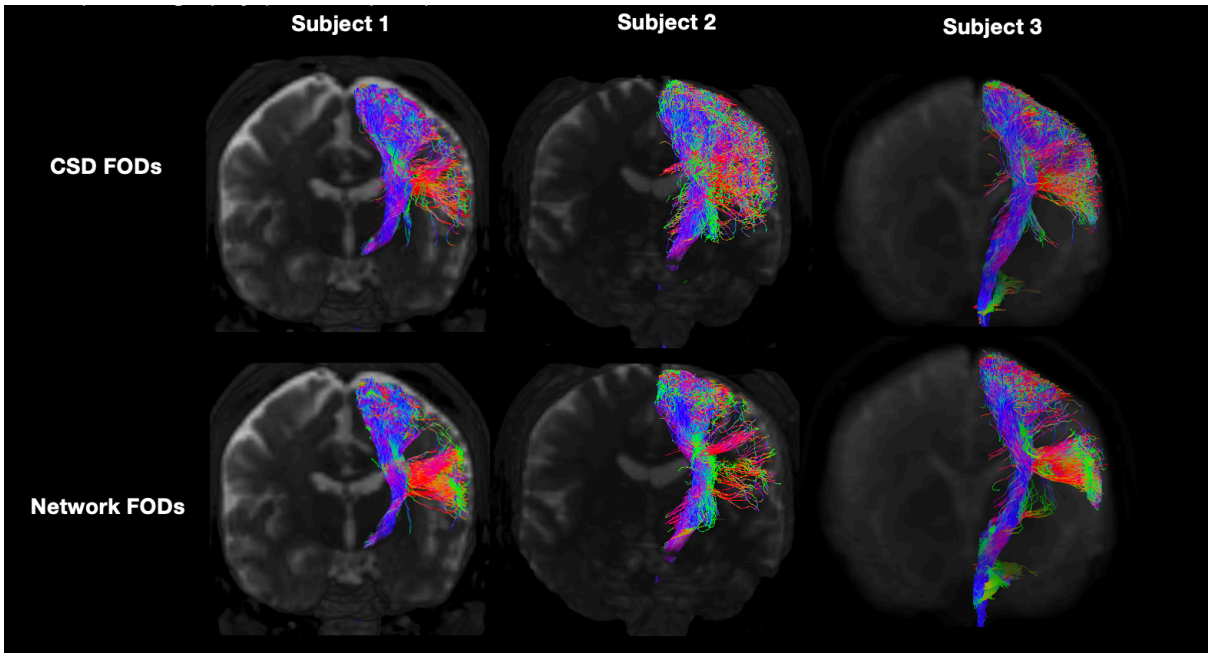


Figure 5.7: Individual variability in white matter cortical termination across three subjects from the UKB.
Distinct patterns in tract reconstruction were observed between CSD and network-derived FODs. The corticospinal tract exhibited subject-specific branching patterns among the three subjects. While both CSD and network tractography captured these inter-individual differences, the differences manifested differently between the two methods.

5.3.3 The network enhances superficial white matter tractography

Building on the network's ability to resolve fibre orientations near grey matter (Figure 5.6) and improve U-fibre tracking in macaques (Chapter 4), we evaluated its performance on SWM tracts in humans.

We utilised tractography from multi-shell CSD FODs as a state-of-the-art reference and compared it to outputs from the network and CSD FODs using only single-shell data (b = 1000 s/mm², 2 mm resolution).

Multi-shell CSD yielded coherent U-shaped SWM connections, consistent with known anatomy. However, single-shell CSD failed to resolve these patterns, producing spurious fibres (Figure 5.8). In contrast, the network recovered anatomically plausible U-fibres with sharp curvature, more closely matching the multi-shell results. Notably, improvements are less pronounced in frontal regions, likely due to susceptibility-induced field inhomogeneity degrading dMRI signal quality. Similar results are found across three subjects (Appendix 5.2)

demonstrating the network's ability to generalise across cohorts despite individual variability and data quality differences.

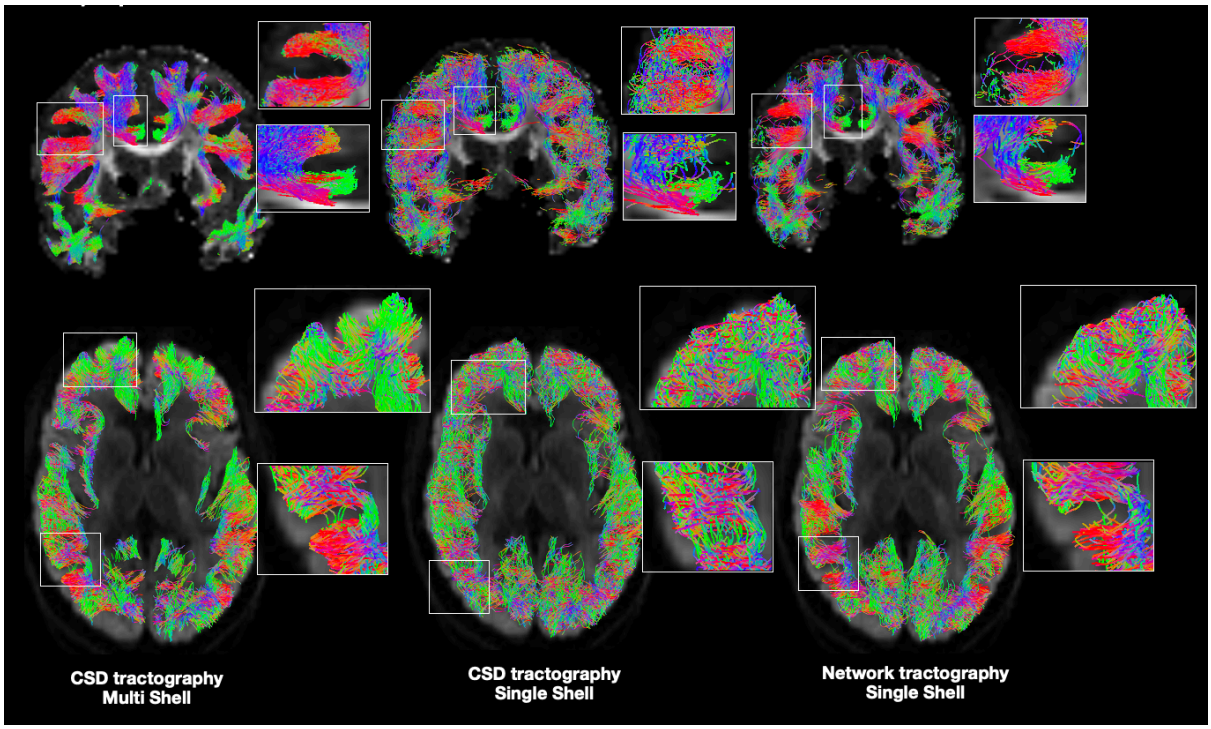


Figure 5.8. Superficial white matter tractogram of in-vivo human data.
The reconstruction of superficial white matter tracts derived from three methods: multi-shell tractography with CSD FODs, single-shell tractography with CSD FODs, and single-shell tractography with network FODs. The multi-shell CSD tractography serves as the reference for comparison. Notably, the single-shell network data reveals a better U-shaped structural pattern compared to the single-shell CSD tractography.

5.3.4 The network improves subcortical fibre tracking

We evaluated the network's ability to improve tractography in subcortical regions using ROI-to-ROI tractography (Figure 5.9). Both network- and CSD-derived FODs successfully reconstructed thalamus-GPi and substantia nigra-striatum connections which are established pathways with high curvature. However, for the connection between the red nucleus and the thalamus, the network uniquely resolved the projections from the red nucleus to the ventral intermediate thalamic nucleus, a pathway absent in CSD tractography. This pathway plays a critical role in cerebellar-thalamic motor circuits.

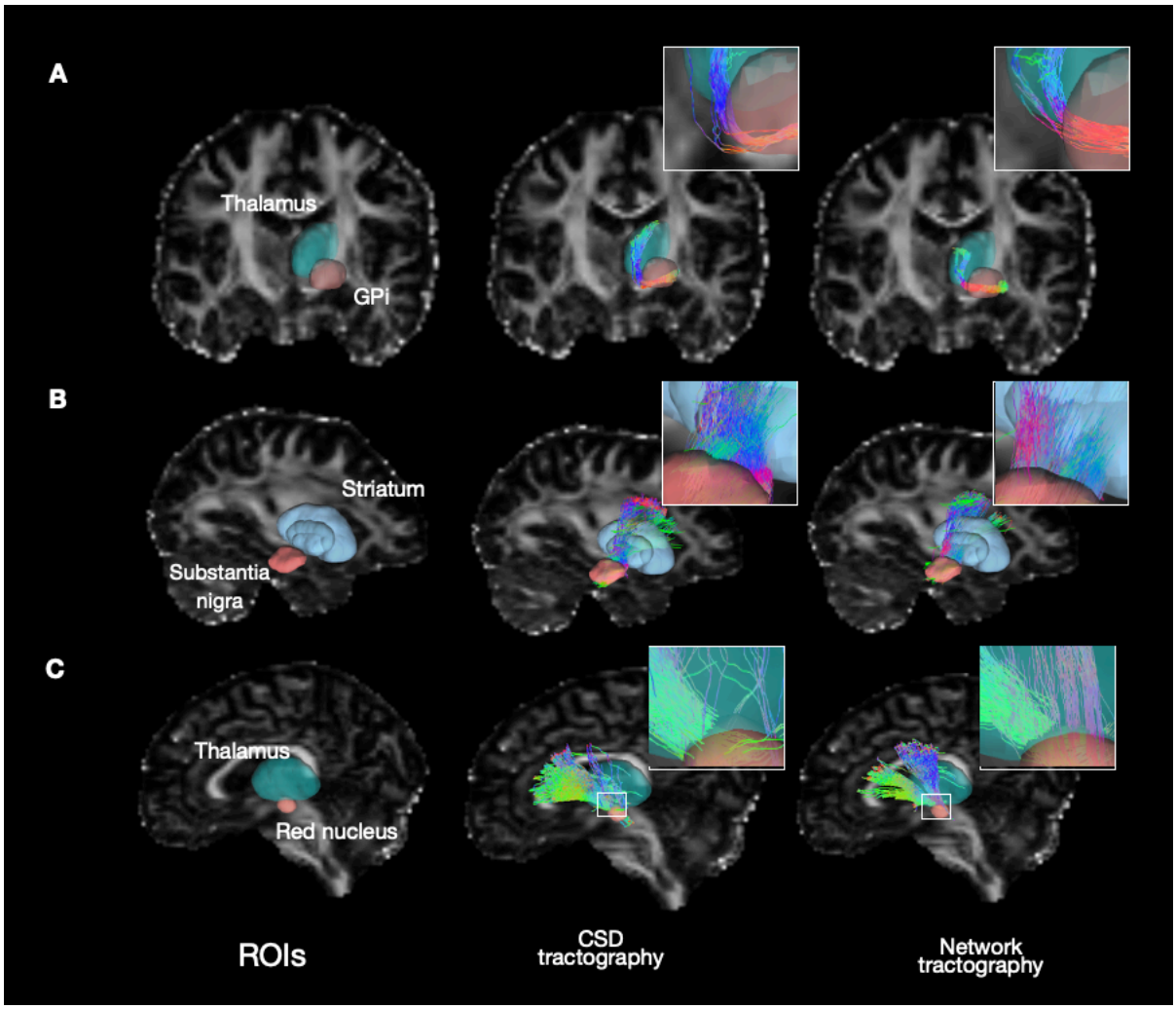


Figure 5.9. Improvement of Subcortical Tractography.
(A) Tractography connections between the thalamus and the globus pallidus interna (GPi) are reconstructed using both network FODs and CSD FODs, with both methods effectively capturing the structure's large curvature. (B) The connectivity between the substantia nigra and the striatum is clearly identified using both methods. (C) Fiber tracking from the red nucleus to the thalamus shows that the projection from the red nucleus to the ventral intermedius nucleus of the thalamus is observed in the network tractography but is missing in the CSD tractography. These results demonstrate the potential of our network approach to enhance fibre tracking in subcortical regions.

5.3.5 Structural TTM and rsfMRI network alignment in the visual cortex

Figure 5.10 examines whether the tractography differences observed between CSD and the network across subjects in Figure 5.7 are meaningful by assessing structure-rsfMRI alignment in the visual cortex. Compared to CSD, the network TTM defines a smaller and more localised region that excludes the anticorrelated resting-state region (blue). This follows

neuroanatomical expectations, as anticorrelated networks are typically not connected by direct structural pathways. The improved overlap is quantified by a higher Dice coefficient.

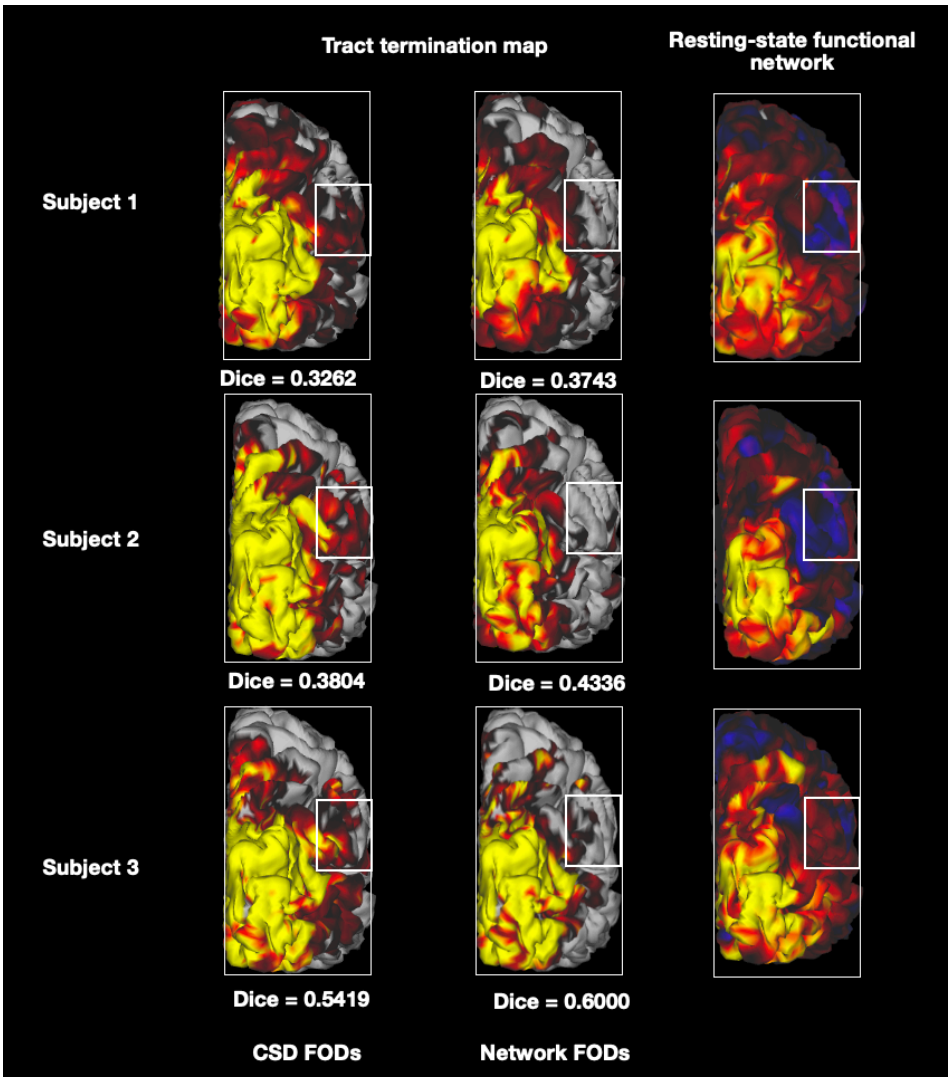


Figure 5.10. Alignment of white matter TTMs and rsfMRI Network in three subjects. Tractography was seeded from the left visual cortex to generate normalised density maps of white matter tract terminations in the right hemisphere. The resting-state network of the right hemisphere was identified using a left visual cortex mask applied in dual regression. The network tractography shows better alignment with the resting-state network compared to CSD with higher Dice coefficients in all three subjects.

5.3.6 Whole-brain structural TTM and functional alignment

TTMs from 23 white matter tracts across the brain were used as the spatial basis for rsfMRI GLM fitting. Figure 5.11 shows the maps of the residuals for two example subjects, where lower residuals indicate that tractography provides a better brain parcellation. In subject 1, lower residuals are observed in the superior occipital lobe with network TTMs compared to

CSD TTMs. In subject 2, lower residuals are observed in the frontal and parietal lobes with network TTMs compared to CSD TTMs.

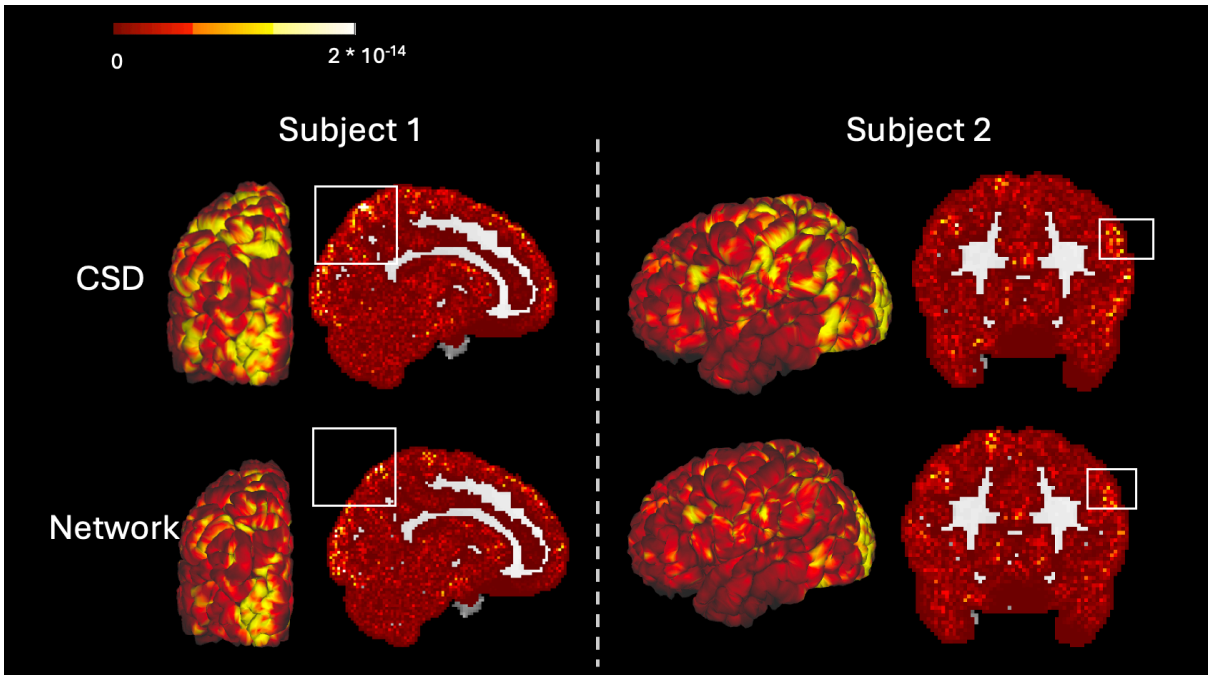


Figure 5.11: Residual maps of two example subjects.
Maps of the residuals for two subjects, comparing the rsfMRI data GLM model fitting of network-derived and CSD-derived TTMs. Lower residuals indicate better brain parcellation. In subject 1, reduced residuals are found in the superior occipital lobe using network TTMs compared to CSD TTMs. In subject 2, lower residuals are observed in the frontal and parietal lobes with network TTMs compared to CSD TTMs. The results suggest improved model fitting with network-derived TTMs.

Figure 5.12 displays the average residual map across 10 subjects. Network-based TTMs yielded lower residuals than CSD-derived TTMs, particularly in the frontal lobe and lateral occipital cortex, regions known for high inter-subject variability. Voxel-wise residual differences (CSD vs. network; Figure 5.12 Right) demonstrate the superior performance of network TTMs (with more blue than red) across most cortical areas. These results suggest that network-derived TTMs may better capture biologically meaningful individual variability in rsfMRI data and in defining cortical boundaries.

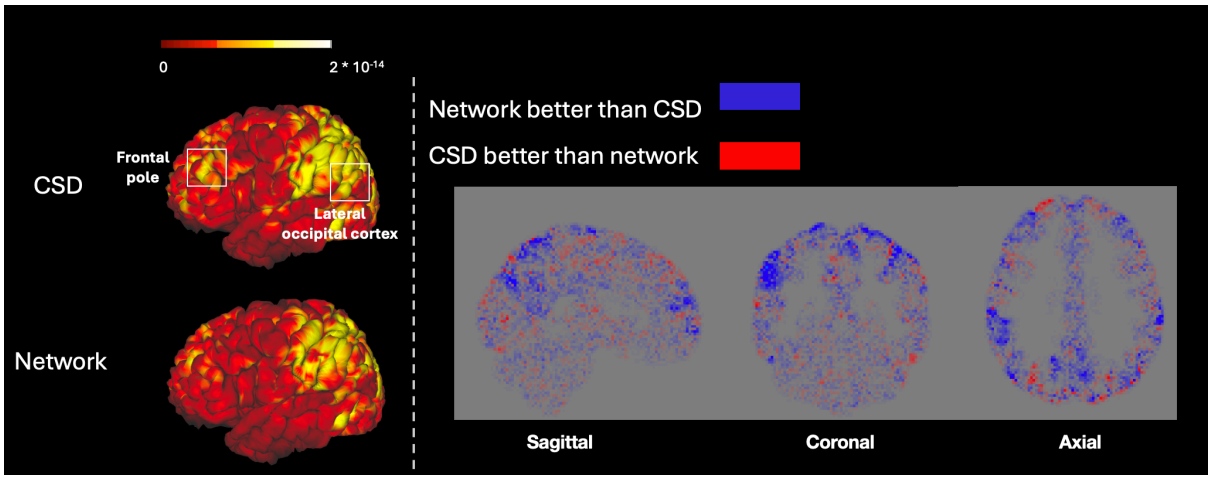


Figure 5.12: Group average residuals of rsfMRI Network (N=10)**.**
Left: TTMs were derived from 23 white matter tracts in the left hemisphere, covering the majority of cortical regions. Tract-specific time series were extracted from these TTMs and regressed against the rsfMRI data using a GLM. The residuals from the GLM are shown. Residuals from network-based TTMs were lower compared to those from CSD, particularly in the frontal and occipital lobes (N=10). Right: Residual difference between the network and CSD. This whole-brain map shows the difference in residuals between the residual map derived from network-based TTMs and derived from CSD TTMs. Lower residuals in network (shown in blue) are observed in the majority of brain regions, particularly in the parietal lobe and certain regions of the occipital lobe, indicating improved model fitting.

We hypothesise three potential factors contributing to improved structural-functional alignment and recued residuals in Figures 5.13. First, TTMs may be less susceptible to false-positive projections. For instance, in CSD tractography, the optic radiation is seen to project to the parietal lobe, whereas in network-based tractography, this misprojection is absent. Given that the optic radiation is expected to terminate in the primary visual cortex, network-based TTMs located in the medial occipital lobe may more accurately reflect anatomical connectivity (Figure 5.13A). Second, network-based TTMs exhibit more spatially localised termination compared to CSD, which shows broader, more spread-out projections (Figure 5.13B). Third, network-derived terminations demonstrate reduced overlap between neighbouring tracts, improving parcellation specificity (Figure 5.13C). Collectively, network-derived TTMs that better approximate functional boundaries provide a more accurate low-dimensional representation of rsfMRI data, leading to lower residuals and improved structure-function alignment.

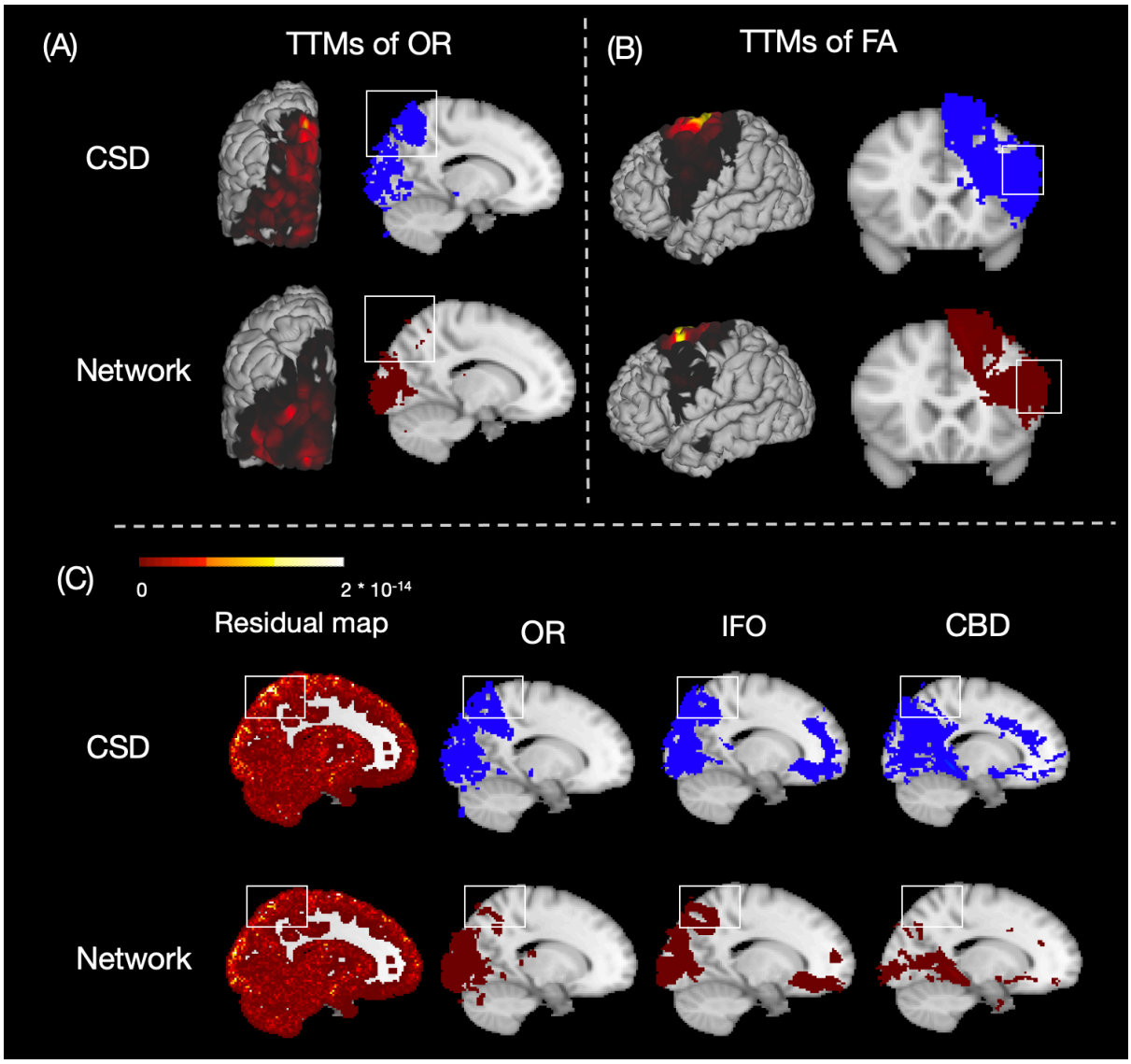


Figure 5.13 Mechanism underlying reduced residuals.
(A). CSD-derived TTMs incorrectly project the optic radiation (OR) into the parietal lobe, a region with higher residuals. In contrast, network-derived TTMs confine terminations to the primary visual cortex, aligning more closely with expected anatomy. (B). CSD-derived tractography exhibits widespread cortical terminations, whereas network-derived TTMs show more spatially localised patterns in the frontal aslant (FA) tract which primarily connects the inferior frontal gyrus and the supplementary motor cortex. (C) Network-derived TTMs demonstrate reduced overlap between distinct tracts, improving parcellation specificity. In the parietal lobe, where network FOD-based fitting resulted in lower residuals compared to CSD FODs-based fitting in this subject, CSD-derived TTMs exhibit overlapping projections from the OR, inferior fronto-occipital fasciculus (IFOF), and dorsal cingulum bundle (CBD). In contrast, network-derived TTMs show that parietal lobe terminations were predominantly from the IFOF, with minimal contributions from the OR and CBD.

5.4 Discussion

In this study, we adapted a network for microscopy-informed fibre orientation reconstruction that was initially trained on macaque dMRI data for in-vivo human datasets. The model was pre-trained using hybrid dMRI-PLI data (Chapters 3 & 4) and can transfer microscopy fibre orientation from postmortem brains to in-vivo brains. Through an unsupervised domain adaptation framework, the network becomes invariant to species differences between macaque and human brain. The network architecture features several key design principles which ensure meaningful cross-species translation. First, our network takes in small (3×3×3) blocks of voxels as input which capture local spatial smoothness while remaining sufficiently small to exclude species-specific anatomical information. Second, the shared white matter complexity between macaques and humans—particularly in regions with crossing fibres—ensures biological plausibility. Third, the domain adaptation network is designed to process single-shell dMRI data, represented using spherical harmonics, making it applicable to dMRI acquisitions with varying b-values and b-vectors. Furthermore, a similar network architecture can be trained for multi-shell dMRI data, facilitating its application to a broader range of diffusion imaging protocols.

The adapted network demonstrated three distinct advantages over conventional methods: (i) improved delineation of SWM tracts in single-shell dMRI at 2 mm resolution; (ii) successful reconstruction of subcortical pathways previously undetected by conventional tractography; and (iii) enhanced sensitivity to individual differences in cortical white matter termination patterns which correlated more strongly with functional connectivity. These results highlight the utility of cross-species domain adaptation in our network, enabling the transfer of microscopy-informed FOD properties to in-vivo dMRI in humans.

SWM, located between grey matter and deep white matter, presents unique segmentation challenges. While T1/T2-weighted imaging reliably identifies the grey-white boundary (Kirilina et al., 2020), distinguishing SWM from deep white matter remains problematic due to the lack of contrast in structural images. dMRI at low resolutions (e.g. 2 mm isotropic) suffers from partial volume effects which obscures tissue interfaces. By leveraging the higher myelin specificity of hybrid dMRI-PLI fibre orientations, our network produced cleaner fibre branching patterns near the cortical boundary similar to those observed in myelin-sensitive microscopy such as PLI on which the hybrid orientations are built. This resulted in superior

delineation of SWM compared to CSD-derived FODs. In comparison, existing SWM tractography methods (Van Dyken et al., 2024) impose assumptions regarding fibre architecture. For example, asymmetric fibre orientation helps reduce gyral bias thereby improving the accuracy of SWM tractography (Bastiani et al., 2017). In addition, surface-based tracking methods can constrain streamlines with the grey-white matter boundary, further refining the streamlines going to gyri (Van Dyken et al., 2024). Atlas-guided machine learning clustering can also incorporate useful anatomical priors(Zhang et al., 2018). However, these approaches have limitations: they either rely on predefined assumptions about fibre architecture or overlook individual variability in SWM morphology due to differences in gyral architecture and folding patterns (Wachinger et al., 2015). In contrast, our method directly infers fibre architecture from dMRI signals without relying on prior anatomical templates, and thus more likely to preserve inter-subject differences in SWM organisation. This suggests that the network mitigates the limitations of single-shell acquisitions, enhancing specificity in SWM reconstruction. The network demonstrates the potential to bridge the gap between research-grade and clinically feasible dMRI protocols for SWM mapping.

In addition to cortical-cortical connections, we investigated subcortical-subcortical connectivity including pathways linking the thalamus and red nucleus. These pathways are critical for motor and cognitive function and are implicated in neurodegenerative diseases such as Parkinson's, where deep brain stimulation (DBS) targets these regions. Current understanding of these circuits derives largely from tracer studies in non-human primates (Haber et al., 1993). However, in-vivo subcortical tractography remains challenging due to the small size and dense packing of subcortical structures. High-resolution dMRI provides one solution, facilitating the visualisation of the ventral intermediate thalamic nucleus, a key DBS target for tremor (Patriat et al., 2023). Alternatively, atlases combining 7T in-vivo dMRI with high-resolution postmortem dMRI and histology (BigBrain (Amunts et al., 2013)) have improved the delineation of subcortical structures, such as those involved in the auditory system (Sitek et al., 2019). However, these histology- or 7T-based approaches are typically unavailable in clinical settings. Our microscopy-informed framework circumvents these limitations by estimating fibre orientations directly from conventional dMRI data, without relying on histology or ultra-high field acquisitions. This enables the reconstruction of previously undetectable subcortical pathways. Notably, the anatomical accuracy of the subcortical pathways we have shown needs further evaluation through intervention methods

(Calabrese, 2016) or professional anatomist advice. These results highlight the network's potential to enhance tractography in clinically relevant subcortical networks, offering improved anatomical specificity.

To evaluate whether our microscopy-informed fibre orientations improve the identification of biologically meaningful cortical terminations, we assessed structural-functional alignment. Typically, structural connectivity (SC) constrains the neural communication between brain regions, thereby shaping functional connectivity (FC) (Hermundstad et al., 2013). However, the relationship between SC and FC remains complicated, with SC explaining only part of FC variance ($R^2 \approx 0.5$) (Honey et al., 2009). Several factors contribute to this discrepancy. First, functional connectivity may depend on indirect pathways. In such cases, two functionally related regions may not have direct structural connections but instead communicate through intermediary regions that are structurally linked to both (Nozais et al., 2023). Second, limitations in SC mapping accuracy such as tractography errors from false positives or incomplete fibre reconstruction can result in poor SC-FC alignment. Third, confounds in FC estimation such as noise, artefacts, and non-neural metabolic factors may obscure true functional relationships leading to discrepancies between SC and FC measurements. These findings suggest that refining SC mapping can improve structural-functional alignment (overcome point 2), even if not fully explain all the variance (points 1 and 3). In this work, we focus on the visual cortex where functional networks are tightly anatomically constrained. We found that conventional CSD-derived terminations projected into a region with anticorrelation rsfMRI signal – anatomically implausible patterns absent in our microscopy-informed FODs. This discrepancy likely stems from CSD's limited specificity in resolving cortical termination.

Our study has several limitations. First, the whole-brain functional-structural alignment analysis using GLM was conducted on a small cohort of 10 subjects. As a result, the whole-brain residual analysis presented here should be interpreted as a preliminary pilot study. Future research should focus on incorporating larger cohorts to enhance the robustness and generalisability of the findings. Second, the evaluation of SWM and subcortical pathway reconstructions relied on visual assessment of anatomical architecture rather than quantitative metrics. While this approach highlights qualitative improvements, standardised measures such as tract density imaging or streamline angular coherence are needed to rigorously benchmark performance (Shastin et al., 2022). Third, regarding the network, it was trained on

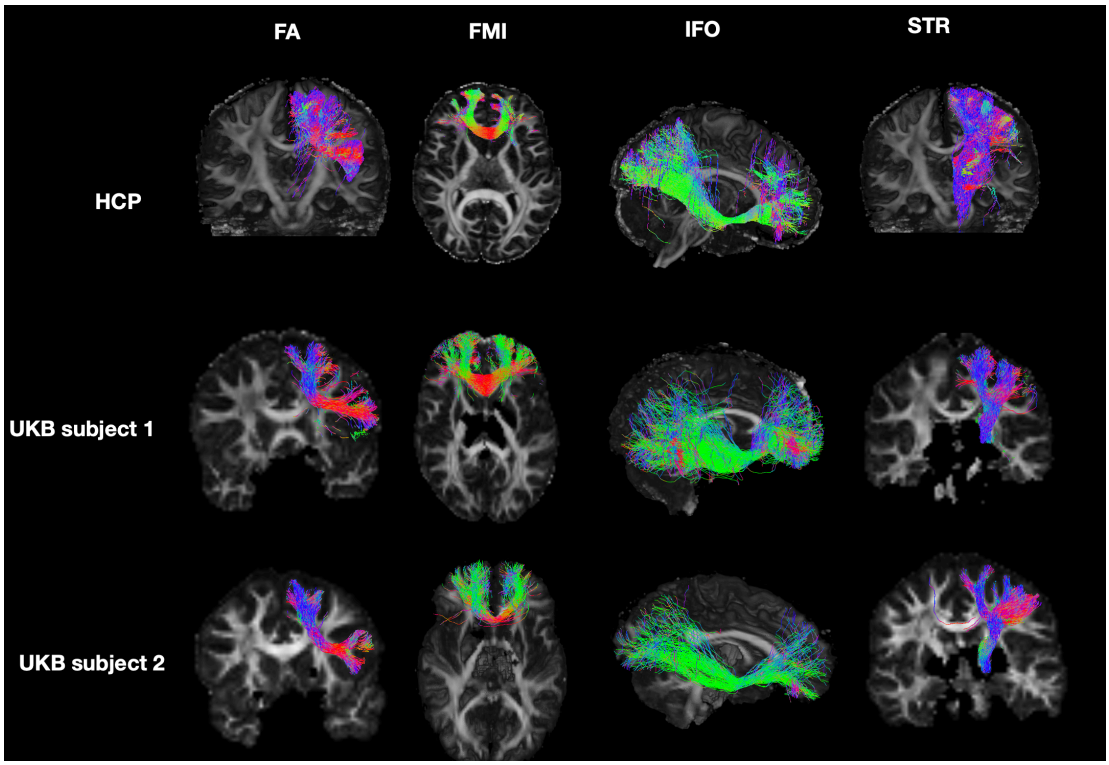
macaque data with a resolution of 0.6 mm, but when adapted to human data, the resolution was 1.25 mm or 2 mm. The difference in resolution alters the regions processed by the convolutional kernels, potentially affecting the network's performance. However, the impact of these resolution changes on the network performance has not been fully evaluated.

There are several future directions we would like to explore. First, while our method demonstrated notable improvements with low-resolution dMRI, the enhancement was less pronounced in high-resolution dMRI (1.25 mm of HCP data). To further explore its potential, we aim to incorporate other MRI modalities, such as T1-weighted MRI, which provides higher-resolution anatomical information. Second, to assess whether individual variations in white matter cortical termination are biologically meaningful, we employed structural-functional alignment as a measure. Future work will incorporate additional non-imaging phenotypes, such as age, sex, and physical characteristics. If the variability captured by network-based FODs in white matter TTMs significantly explains differences in these non-imaging phenotypes, it would support the biological relevance of our method and its potential as a biomarker. Third, further validation on other datasets with diverse dMRI acquisition protocols is necessary to assess generalisability. In this study, we adapted our network to single-shell dMRI at 1.25 mm resolution from HCP data and 2 mm resolution from UK BioBank data, both with b = 1000 s/mm², subsampled from multi-shell acquisitions. Future work should extend our approach to varying diffusion acquisition protocols such as multi-shell dMRI, dMRI acquisition with fewer gradient directions suitable for pre-operative tractography(Gersing et al., 2020), and larger populations to enhance robustness and broader applicability. The code and pre-trained network parameters will be made publicly available to support general use and enhance applicability.

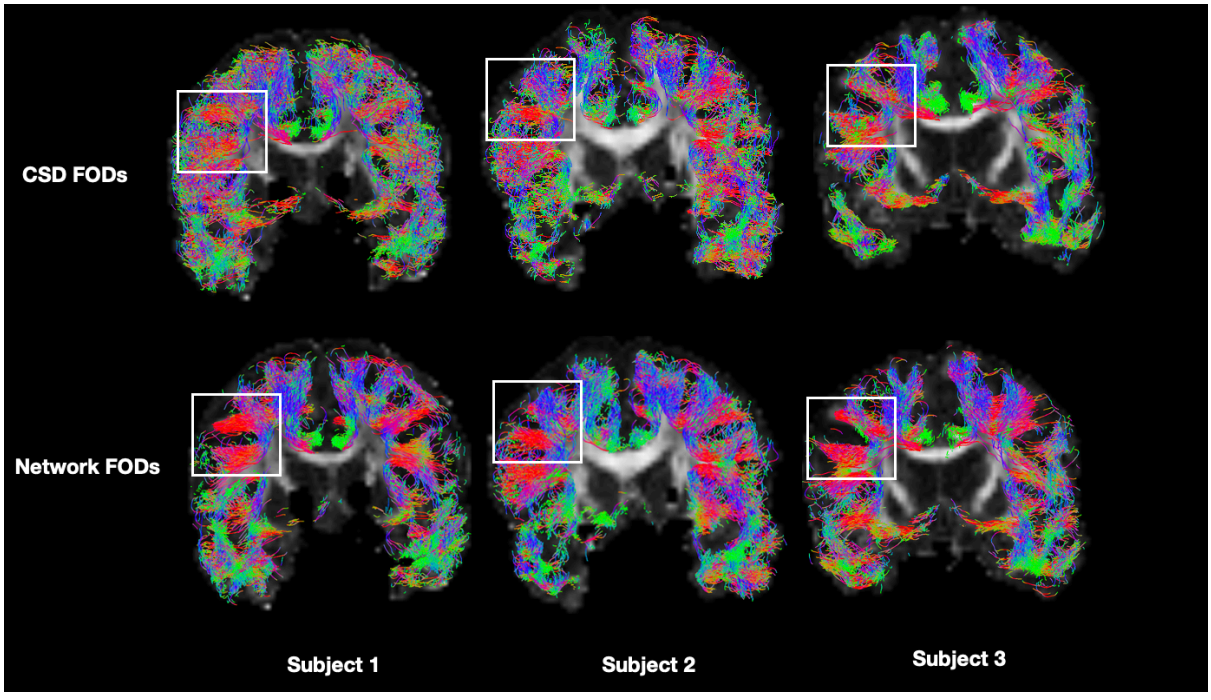
Conclusion

We developed a domain adaptation network that transfers microscopy information to in-vivo human dMRI, even in the absence of microscopy data. Our results demonstrate that our network enhances fibre tracking in superficial white matter and improves subcortical tractography. Additionally, our method is sensitive to individual variations in white matter cortical termination as supported by structural-functional alignment. These findings highlight the network's potential for improving the accuracy in single-shell clinical feasible dMRI applications.

Appendix



Appendix 5.1 Tracts reconstructed from the network FODs using different in-vivo human data.
The network was applied to high resolution HCP data (1.25 mm) and lower resolution UK BioBank data (2 mm). The network estimated FODs were used to reconstruct example tracts using XTRACT atlas including frontal Aslant (FA), forceps minor (FMI), inferior longitudinal fasciculus (IFO) and superior thalamic radiation (STR).



Appendix 5.2. Generalisability of the network in enhancing superficial white matter tracking.

The network was applied to in-vivo human dMRI data from three subjects, using single-shell dMRI at 2 mm resolution. The SWM tractogram generated from the network FODs is compared to the SWM tractogram obtained from the CSD FODs. The tractography using network FODs demonstrates improved clarity, and a distinct pattern of U-fibres compared to the CSD-derived SWM tractogram.

6

A microscopy-trained model to predict super-resolution fibre orientations from diffusion MRI

Table of Contents

6.1 Introduction *147*
6.2 Methods *150*
6.2.1 Network architecture 150
6.2.2 Pre-training on macaque data 153
6.2.3 Cross-species adaptation 154
6.2.4 Data 154
6.2.5 Fibre orientation distribution estimation 156
6.2.6 Tractography 156
6.3 Results *157*
6.3.1 Application to postmortem macaque MRI 157
6.3.2 Application to postmortem macaque data at 1 mm 158
6.3.3 Application to the in-vivo macaque data 162
6.3.4 Application to the in-vivo human data 163
6.4 Discussion *164*

Foreword

Diffusion MRI (dMRI) is constrained by spatial resolution, limiting its ability to accurately capture fibre orientations and structural connectivity. While microscopy provides fibre orientation at the micrometre scale, its use is typically restricted to postmortem tissue and small tissue sections prohibiting whole-brain connectomics. Inferring microscopic properties from in-vivo dMRI signals is challenging due to differences in signal types and alterations in tissues. To address this, we propose a deep learning framework that integrates dMRI, structural MRI, and microscopy to super-resolve fibre orientation distributions (FODs) from in-vivo dMRI signals. Our microscopy-informed network takes low-resolution single-shell dMRI as input and outputs FODs at twice the dMRI resolution (i.e. two-fold increase) with high-resolution structural MRI informing on the tissue boundary. Microscopy data serve as training ground truth, driving the model to learn high-resolution information about myelin fibre structure across the brain. Importantly, our network uses a domain adaptation to achieve cross-tissue (in-vivo and postmortem) and cross-species (macaque and human) generalisability. This means our network trained on postmortem macaque data is applicable to in-vivo human studies demonstrating how super-resolved FODs can reveal previously indistinguishable neuroanatomical features. This work is preliminary and demonstrates a novel multimodal synthesis approach, having the potential to advance high-resolution connectivity mapping for both basic and clinical neuroscience.

Published work

Conference

Silei Zhu, Karla L. Miller, Nicola K. Dinsdale, Saad Jbabdi, Amy F.D. Howard, A microscopy-trained model to predict super-resolution fibre orientations from diffusion MRI, ISMRM Annual Meeting 2025, Oral.

Silei Zhu, Karla L. Miller, Nicola K. Dinsdale, Saad Jbabdi, Amy F.D. Howard, A microscopy-trained model to predict super-resolution fibre orientations from diffusion MRI, ISMRM Diffusion workshop 2025, Power Pitch.

Individual contributions to this thesis chapter

My contributions to this chapter include super-resolution network design, training, and network applications on different datasets, visualisation and tractography as well as manuscript writing, editing and review.

Nicola K. Dinsdale, Saad Jbabdi, Karla L. Miller and Amy F.D. Howard advised on conceptualisation, data processing, network design and manuscript review.

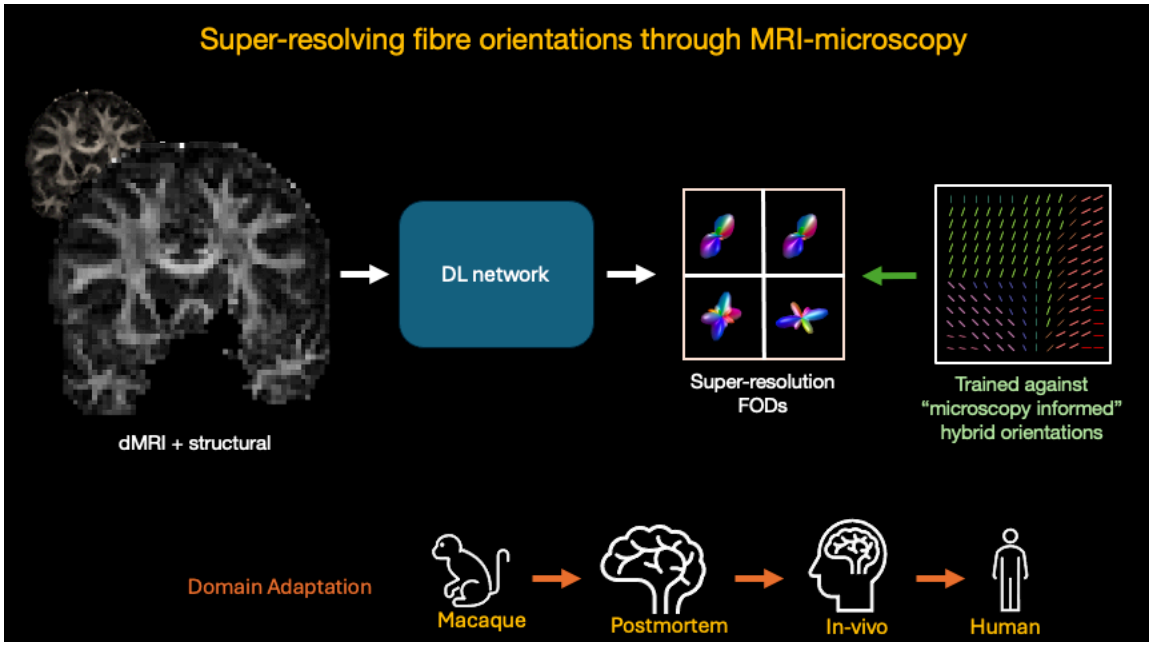


Figure 6.1 Schematic overview of the microscopy-informed super resolution network. We propose a deep learning framework that leverages low-resolution single-shell diffusion MRI to generate super-resolved fibre orientation distributions (FODs). Structural MRI provides anatomical tissue boundary constraints, while dMRI encodes directional information. The model is trained using hybrid dMRI-microscopy fibre orientation data at twice the resolution of dMRI, facilitating the super-resolution of FODs and enabling a more detailed reconstruction of white matter architecture.

6.1 Introduction

Diffusion MRI (dMRI) is a widely used non-invasive imaging technique for mapping brain microstructure and neuroanatomical connections, playing a crucial role in the diagnosis of white matter diseases, stroke and brain cancers. High-resolution dMRI provides significant advantages in delineating intricate white matter pathways and mitigating partial volume effects (Wu and Zhang, 2016). However, achieving high-resolution dMRI remains challenging due to several technical limitations. One major issue is the low signal-to-noise ratio (SNR), leading to inaccurate signal representation. Additionally, high-resolution acquisitions require dense sampling of K-space, resulting in prolonged scan times and increased susceptibility to subject motion.

Several MRI technologies and techniques have been developed to achieve high spatial resolution in dMRI. First, higher resolution can be achieved by optimising hardware, such as using ultra-high field strengths. Ultra-high field MRI provides stronger signals and a higher SNR compared to traditional 3T, enabling improved spatial resolution and finer structural details (Vu et al., 2015; Wu et al., 2016). For instance, 11.7T dMRI tractography has achieved a 40 μm resolution when imaging a hippocampus brain organoid, an in-vitro cellular model (Versace et al., 2024). When combined with advanced artefacts correction techniques, the ultra-high field has enabled high-quality in-vivo dMRI acquisition at 0.75 mm isotropic resolution in macaque using a 10.5 T scanner (Pisharady et al., 2024). In humans, high resolution at 1mm can be achieved at 7T using a three-dimensional multi-slab acquisition (Wu et al., 2016). However, despite the signal benefits, ultra-high field MRI has inherent limitations, including shorter T2 relaxation times, longer T1 relaxation times and increased susceptibility to field inhomogeneities (Barisano et al., 2019). Reduced T2 relaxation time leads to faster signal decay, potentially compromising image contrast. Second, novel acquisition and reconstruction methods facilitate high spatial resolution while preserving SNR and reducing scan times such as compressed sensing (Ning et al., 2015; Wu et al., 2014b) and parallel imaging reconstruction (e.g. SENSE (Pruessmann et al., 1999), GRAPPA (Block et al., 2007)). Compressed sensing reduces the number of data samples by utilising the sparsity of the data and parallel imaging reconstruction effectively accelerates acquisition and improves resolution through multiple receiver coils that simultaneously acquire data from different spatial locations. However, these methods are computationally expensive (eg. requiring long reconstruction times) and depend on prior knowledge and parameter tuning for optimal results. Third, postmortem imaging

provides unique opportunities for pushing high resolution, as it is not constrained by scan time or motion. For instance, complex fibre structures have been mapped in detail at 500 μm resolution in the postmortem human brain using a 7T MRI scanner (Tendler et al., 2022) and at 500 μm in the postmortem chimpanzee brain using a 9.4T preclinical MRI scanner (Eichner et al., 2024).

Alternatively, high spatial resolution can be attained with super-resolution techniques, which offer a promising approach for transforming low-resolution images into high-resolution images. For example, Calamante et al. proposed an interpolation method based on fibre tracking inside each voxel for super-resolution of track density imaging (Calamante et al., 2010). Additionally, techniques combining multiple scans which have small spatial shifts between acquisitions provide improved resolution (Greenspan et al., 2002). Furthermore, deep learning-based super resolution has demonstrated significant potential due to its ability to learn patterns directly from the data without requiring an explicit signal model or explicit assumptions about brain microstructures (Chen et al., 2018; Guerreiro et al., 2023). Deep learning has been effective in enhancing both spatial resolution (Chen et al., 2018; Guerreiro et al., 2023) and angular resolution (Aja-Fernández et al., 2023) in dMRI, leading to more accurate estimation of complex white matter architectures outperforming interpolation in resolution enhancement (Alexander et al., 2017).

Additional opportunities for deep learning-based super-resolution may be provided by combining multiple MRI contrasts acquired in the same subjects. MRI with different contrasts can provide rich and various structural information, where integrating data from multiple MRI modalities may provide benefits when investigating complex fibre architecture (Howard et al., 2019; Zhu et al., 2025). For instance, high-resolution T1-weighted has been used to enhance tissue boundary information and improve the quality of super-resolved dMRI (Cicimen et al., 2024; Zheng et al., 2017). Microscopy techniques, such as light and electron microscopy, provide high-resolution structural information at cellular and subcellular levels and can be used to super-resolve the dMRI fibre orientation through deep learning. Serial two-photon tomography, for example, has been utilised to enhance the resolution of FA images and T2-weighted images by learning tissue characteristics from microscopy contrast mainly reflecting myelinated white matter structures (Liang and Zhang, 2023). Nath et al. demonstrated the feasibility of training a neural network to map dMRI signals to white matter architecture measured by 3D confocal histology in two monkey brains. The network achieved higher

predictive accuracy in estimating histology-derived fibre orientations compared to traditional model-based methods (Nath et al., 2019). However, only 567 histological voxels were processed. Similarly, Zifei et al., proposed a deep learning network that maps dMRI signals to mesoscopic tract-tracing data from the Allen Mouse Brain Connectivity Atlas, further refining fibre orientation distribution (Liang et al., 2023). However, existing microscopy-informed super-resolution techniques developed in rodents have faced challenges in translation to human studies due to differences in fibre complexity. Additionally, studies based solely on ex-vivo data have encountered difficulties in in-vivo applications due to differences in data distribution.

In this Chapter, we present a deep learning network designed to estimate high-resolution microscopy-informed fibre orientations from low-resolution dMRI data. The network integrates information from two MR contrasts, leveraging directional information from dMRI and anatomical details from structural MRI as inputs. The hybrid dMRI-microscopy fibre orientations (introduced in Chapter 3), informed by polarised light imaging were used as a ground truth during training, providing fine anatomical details. This work builds on that presented in previous chapters. Similar to before, the network was first trained on macaque data and designed to be invariant to tissue types (postmortem and in-vivo, Chapter 4). Second, it was further refined to generalise across species (macaques and humans, Chapter 5). Our network was trained on multi-modal data from the BigMac dataset with PLI, postmortem MRI and in-vivo MRI all acquired from the same macaque brain with state-of-art MRI-microscopy co-registration. The co-registration enables precise alignment of brain microstructure across modalities. In Chapter 5, we demonstrated the feasibility of estimating microscopy-informed fibre orientations from in-vivo dMRI signals at the same resolution as the input dMRI data. The microscopy data (hybrid orientations) was constructed at microscopy high resolution and then combined to match dMRI low resolution. In this study, we extend the deep learning approach to super-resolve fibre orientations from dMRI to higher resolutions while incorporating microscopy information which facilitates the myelin-specific fibre orientation estimation. Overall, this data-driven method requires no assumptions or biophysical models to describe the fibre architecture, as with conventional dMRI models, providing a direct and robust approach for fusing multi-contrast information from dMRI and structural MRI and generating super-resolved fibre orientations that are mapped to microscopy data.

6.2 Methods

We designed a network that takes a cube of dMRI voxels with the size of 3×3×3 as input and outputs super-resolved fibre orientation distributions for the central voxel with the size of 2×2×2. As described in Chapter 4, a cube of dMRI was input rather than a single voxel to capture local neighbourhood information. The network was trained against "ground truth" FODs from our hybrid dMRI-PLI method, introduced in Chapter 3 (Zhu et al., 2025), to generate microscopy-informed FODs. We utilised a domain adaptation approach to train the network with the following key properties:

1) **Tissue invariance**: the network was designed to be robust to differences in tissue status accommodating both postmortem and in-vivo conditions;

2) **Cross-species adaptation**: the model was first trained on macaque data (MRI and microscopy) and later adapted for human MRI, whilst maintaining invariance to species differences (macaque vs human);

Here the network was further developed for:

1) **Super-resolution enhancement**: the output FODs were reconstructed at twice the native dMRI resolution, as were the hybrid FODs used for training.

2) **Multimodal feature fusion**: the network took both dMRI and structural MRI as inputs, complementing directional information from dMRI with higher-resolution anatomical context from structural MRI acquired in the same subject. Here structural MRI can benefit super resolution by providing information about tissue boundaries and partial voluming.

6.2.1 Network architecture

The proposed architecture comprised two core modules: (1) a diffusion-structural MRI fusion module and (2) a main domain adaptation network. The diffusion-structural MRI fusion module was trained together with the main domain adaptation network.

Diffusion-structural MRI fusion module

This module integrated high-resolution structural MRI with diffusion MRI for inputs to the main network (Figure 6.2). The structural MRI was represented as single-channel volume data (channel size = 1), with twice the spatial resolution of the dMRI. The dMRI signals were

normalised by the non-diffusion-weighted signals (S0) and described using spherical harmonics with 45 coefficients. Both modalities were sampled via overlapping sliding windows to maintain neighbouring information. Specifically, dMRI data were input into the network in 3×3×3 blocks of voxels. This resulted in patches of size 3×3×3×45. Structural MRI data were input as blocks of voxel with a size of 6×6×6×1, where the middle 2×2×2 neighbourhood of voxels overlapped with the central voxel of the dMRI. As the structural MRI was co-registered to the dMRI and at twice its resolution, this alignment ensured the structural and diffusion MRI shared the same underlying neuroanatomy. The network predicted fibre orientations for the central dMRI voxel at twice the dMRI resolution, generating a 2×2×2×45 output (8 FODs, each described by 45 spherical harmonics). This design effectively doubled the spatial resolution relative to the original dMRI voxel size 1×1×1×45.

The fusion process involves two parallel steps:

1. Spatial up-sampling of dMRI: A 3D transposed convolutional layer up-sampled the dMRI patches from 3×3×3×45 to 6×6×6×45 to match the structural MRI spatial resolution.
2. Channel expansion of structural MRI: A sequence of 1D convolutional layers with ReLU activations expanded the structural MRI patches 6×6×6×1 to 6×6×6×45 to match the 45 channels of the dMRI.

The diffusion and structural features were then concatenated along the channel axis and fused via a 3D convolutional layer, producing a unified 6×6×6×45 feature representation that integrated complementary dMRI-structural MRI information.

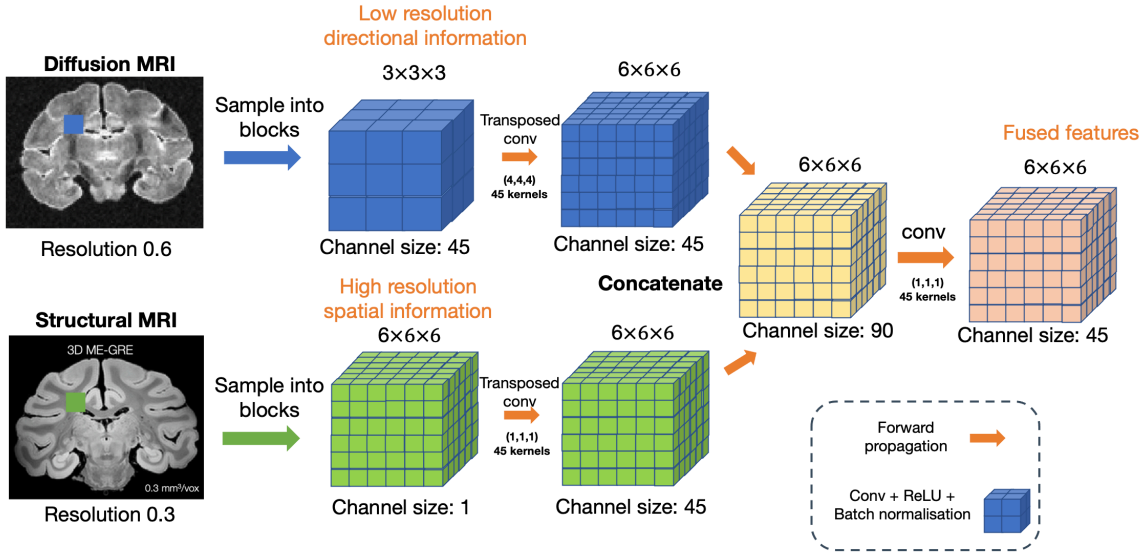


Figure 6.2: Feature fusion module.
This module integrates multi-modal inputs: diffusion MRI (dMRI) provides low-resolution (0.6 mm) orientation information, while structural MRI contributes high-resolution (0.3 mm) spatial details. Co-registered dMRI and structural MRI data are partitioned into blocks to extract fused features. The dMRI undergoes spatial upsampling via deconvolution layers, while structural MRI is upsampled along the channel dimension to match the dMRI's channel size. The features are then concatenated and fused through convolutional layers to generate fused representations, enabling cross-modal integration of directional and anatomical information.

Main domain adaptation module

The fused features were processed through the main domain adaptation network, which had an architecture analogous to the deep learning framework mentioned in Chapter 4. The network comprised three core components: 1) a feature extractor 2) a predictor and 3) a domain discriminator (Figure 6.3). An additional convolutional layer took the 6×6×6×45 input and downsampled it to 3×3×3×45 to match the size of the previous input. The output was also changed to be at twice the input dMRI resolution, with a 2×2×2×45 block of FODs predicted for the central dMRI voxel.

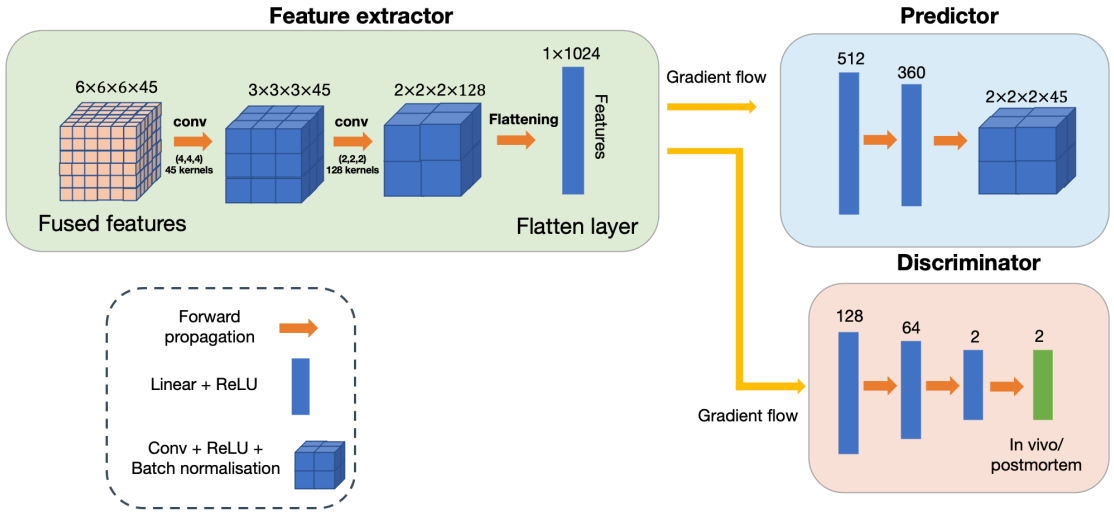


Figure 6.3: Main Network
The domain-adaptation network takes fused dMRI-structural MRI features as input and predicts microscopy-informed fibre orientations at twice the dMRI resolution. The network comprises three key components: (1) a **feature extractor** that takes fused features from dMRI and structural MRI inputs; by the end of training, it aims to learn representations that are invariant to tissue state or species; (2) a **predictor** that estimates microscopy-informed fibre orientations based on the extracted features; and (3) a **discriminator** that differentiates between postmortem and in-vivo tissue types, or macaque and human inputs.

6.2.2 Pre-training on macaque data

The network was pre-trained on macaque data due to the availability of co-registered microscopy, postmortem MRI and in-vivo MRI from the same brain. Similarly to the network training in Chapter 4, postmortem MRI was used as an intermediate, as it exhibits analogous tissue composition to microscopy while maintaining the same signal type as in-vivo MRI. During pre-training, the source domain comprised postmortem dMRI data at 0.6 mm and structural MRI data at 0.3 mm, and the target domain consisted of in-vivo dMRI at 1 mm and structural MRI data at 0.5 mm. The ground truth was hybrid dMRI-PLI fibre orientations at 0.3 mm for postmortem dMRI and 0.5 mm for in-vivo dMRI.

Similar to Chapter 4, the pre-training on macaque data was conducted in two stages. (1) the diffusion-structural MRI fusion module, the feature extractor and the predictor were trained to derive high-resolution microscopy-informed FODs, while a discriminator learned to distinguish between in-vivo and postmortem MRI. (2) With the discriminator fixed, the diffusion-structural MRI fusion module and the feature extractor were trained to capture species-invariant features by confusing the discriminator. Meanwhile, the fusion module, the feature extractor and the predictor were trained to super-resolve FODs. During the first stage,

the network identified tissue-specific features, while the second stage forgot/removed tissue-specific knowledge by maximising the misclassification. Consequently, the last layer of the feature extractor learned tissue-agnostic representations that aligned source and target distributions while preserving fidelity to super-resolve microscopy-derived orientation targets

6.2.3 Cross-species adaptation

Following pre-training in the macaque, the network was refined using unsupervised domain adaptation to generalise to human data, similar to the methodology outlined in Chapter 5. This step mitigated cross-species distributional shifts between macaque and human datasets. The source domain was the postmortem macaque data paired with labelled microscopy-informed FODs, while the target domain was the unlabelled in-vivo human MRI data. In the first stage, the network learned to distinguish between macaque and human data. In the second stage, the network was trained to extract features invariant to species which were then used for super-resolution.

6.2.4 Data

Macaque MRI Data

We used the same BigMac (Howard et al., 2023) data as described in Chapters 3&4. This included postmortem dMRI 1) High-resolution postmortem data: 0.6 mm isotropic resolution, 128 gradient directions, b=4 ms/μm^2 2) Low-resolution postmortem dMRI: 1.0 mm isotropic resolution, 250 gradient directions b=4 ms/μm^2 3) Low-resolution postmortem dMRI with higher b values: 1.0 mm isotropic resolution, 1000 diffusion gradient directions, b=10 ms/μm^2. Additionally, in-vivo dMRI were acquired in two sessions 1) Session 1: 1.0 mm with 1100 diffusion-weighted images with b=1 ms/μm^2 (81 unique gradient directions) and 144 non-diffusion weighted images. 2) Session 2 was acquired one year before the sacrifice of the animal with a similar MRI scan to session 1 but with shorter acquisition at 1.0 mm with 361 diffusion-weighted images with b=1 ms/μm^2 and 38 non-diffusion weighted images. Structural MRI data were acquired at 0.3 mm for postmortem imaging and at 0.5 mm for in-vivo imaging. Postmortem structural MRI at 0.3 mm was also down-sampled to 0.5 mm to pair with the dMRI at 1 mm.

Pre-processing

Spherical harmonics were fitted to preprocessed dMRI as previously described in Chapters 4 & 5. Structural MRI intensities were normalised to [0,1] via min-max scaling:

$$x' = \frac{x - \min(x)}{\max(x) - \min(x)},$$

where x denotes voxel intensities. This ensured numerical stability and accelerated neural network convergence.

Training, Validation and Testing Datasets

The network was trained on postmortem and in-vivo data (diffusion + structural MRI) at different resolutions. The high-resolution postmortem dMRI (0.6 mm) was paired with its structural MRI at 0.3mm, and the in-vivo dMRI from session 1 (1 mm) was paired with its structural MRI at 0.5mm. Each was partitioned into training (80%) and validation (20%) sets, with voxels outside the brain mask excluded to avoid background.

To assess generalisability, the testing dataset comprised four distinct subsets: 1) internal capsule regions from the left and right hemispheres of the high-resolution postmortem data. These internal capsule regions were explicitly excluded during training and validation to evaluate the network's ability to extrapolate to anatomically critical white matter structures; 2) low-resolution postmortem dMRI (1.0 mm), 3) low-resolution postmortem dMRI at higher b-values and more diffusion gradient directions (1.0 mm) 4) in-vivo dMRI (1.0 mm) from session 2.

Macaque microscopy data & Hybrid dMRI-PLI FODs

The hybrid fibre orientations (or microscopy-informed fibre orientations) were reconstructed as described previously where PLI provided the in-plane orientation and dMRI at 0.6 mm b=4 ms/μm^2 approximated the orientation going out of the plane (through-plane orientation). The hybrid fibre orientations were reconstructed at twice the dMRI resolution at 0.3 mm for postmortem and 0.5 mm isotropic for in-vivo training.

Human MRI data:

The network was applied to pre-processed human MRI data from the UK BioBank (Miller et al., 2016), previously described in Chapter 5. This included dMRI data at 2 mm (subsampled to single-shell dMRI with only the b=1000 s/mm^2 volumes and all non-diffusion weighted volumes) and structural MRI at 1 mm isotropic. Structural MRI was rigidly registered to

dMRI space using FSL tool FLIRT (Jenkinson and Smith, 2001). Following the methods applied to macaque data, dMRI signals were normalised by S0 and fitted to the spherical harmonics coefficient (order lmax=8). Structural MRI intensities were normalised to a [0,1] range using min-max scaling. As before, the network was adapted for the UK BioBank data using unsupervised domain adaptation to ensure species invariance and cross-species data generalisability. By leveraging domain-invariant features learned during adaptation, the network generated super-resolved microscopy-informed FODs for humans.

6.2.5 Fibre orientation distribution estimation

FODs estimated by the microscopy-informed super-resolved network were compared against conventional constrained spherical deconvolution (CSD) implemented in MRtrix3 (Dhollander et al., 2019) following methods previously described in Chapter 4.

To produce CSD FODs at the same resolution as the network-derived FODs, the dMRI data were first up-sampled to twice the resolution using linear interpolation. This approach approximated intermediate voxel intensities by assuming linear signal variation between adjacent voxels and was implemented via the mrgrid command in MRtrix3. Super-resolved FODs were estimated through CSD from the interpolated dMRI data.

6.2.6 Tractography

Anatomically-informed tractography was performed using the tckgen command in MRtrix3 (Tournier et al., 2019) to segment white matter fibre bundles using anatomical masks from the XTRACT for macaques. The tractography was seeded from the XTRACT seed mask, with streamlines passing through the target mask being retained, while those intersecting the exclusion mask were removed. The following parameters were applied: the iFOD2 algorithm, step size of 0.2 mm, cut-off value of 0.05, maximal length of 120 mm, and minimal length of 5 mm. In macaques, tractography was performed on network super-resolved FODs at 0.5 mm which were generated from 1 mm in-vivo dMRI data to evaluate the feasibility of running tractography on the super-resolved FODs.

6.3 Results

6.3.1 Application to postmortem macaque MRI

Figure 6.4 shows outputs from the network when applied to data from the internal capsule in high-resolution postmortem macaque data (0.6 mm dMRI and 0.3 mm structural MRI). Notably, this data was excluded from network training and validation as it was reserved as the testing dataset. The super-resolved FODs aligned well with anatomical expectations, effectively capturing the intricate architecture of the internal capsule. The network successfully reconstructed the anterior thalamic radiation fibres running in the anterior-posterior direction in the anterior limb, as well as corticospinal tract fibres exhibiting superior-inferior orientations in the posterior limb. Additionally, the anterior commissure, located anterior to the internal capsule, was correctly resolved with left-right fibre orientations. Overall, the network successfully reconstructed high-resolution FOD at 0.3 mm, accurately reflecting the complex organisation of the internal capsule and providing a detailed representation of its fibre architecture.

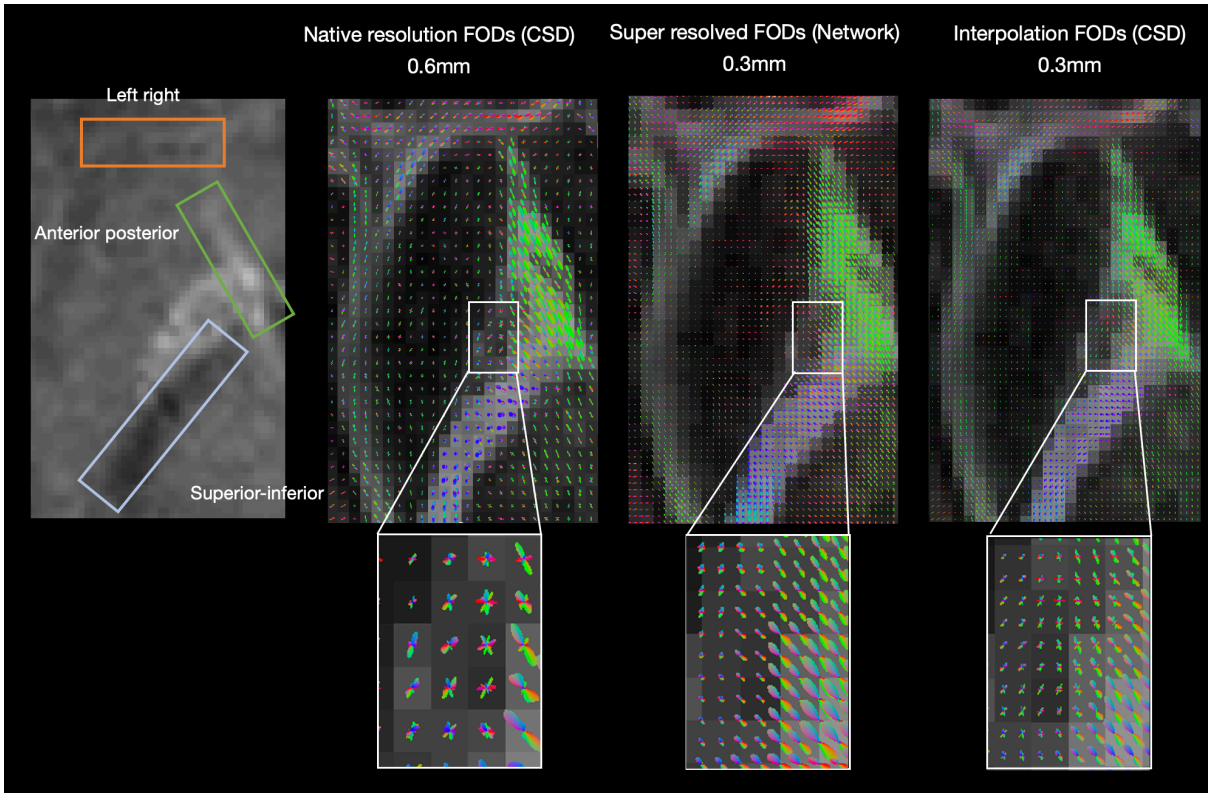


Figure 6.4: Super-resolved FODs in postmortem macaque data.
The network super-resolved FODs at 0.3 mm resolution were estimated using postmortem dMRI (0.6 mm) and structural MRI (0.3 mm) in the macaque. The network super-resolved FODs were compared to those derived from CSD with the dMRI at the native resolution and

with linear interpolation. The axial view of FODs in the internal capsule, which was excluded from model training, includes complex structures with different fibre orientations. The network super-resolved FODs have a half voxel shift relative to the underlying structure due to the visualisation issue which will be addressed in the future.

6.3.2 Application to postmortem macaque data at 1 mm

The network was further evaluated on lower-resolution postmortem macaque data (1 mm dMRI b=4 ms/μm^2 and 0.5 mm structural MRI) from the same brain which was not included in the training data. Figure 6.5 Top shows FODs in the corticospinal tract region with a similar fibre architecture pattern but fewer crossing fibres in the network super-resolved FODs compared to the interpolation CSD FODs. Furthermore, the network reconstructed significantly different crossing-fibre patterns in the thalamus compared to linear interpolation (Figure 6.5 Bottom). The linear interpolation FODs preserved spatial continuity but did not introduce new anatomical information. In contrast, the network allocated multiple fibre populations seen in crossing-fibre voxels at low resolution to distinct spatial locations at higher resolution while maintaining smooth spatial transitions between voxels. Furthermore, the network super-resolved FODs exhibited fewer voxels with multiple fibre populations. These differences demonstrate how the super-resolution achieved by microscopy-informed network extends beyond simple interpolation, potentially due to the microscopy features of FODs learned during training.

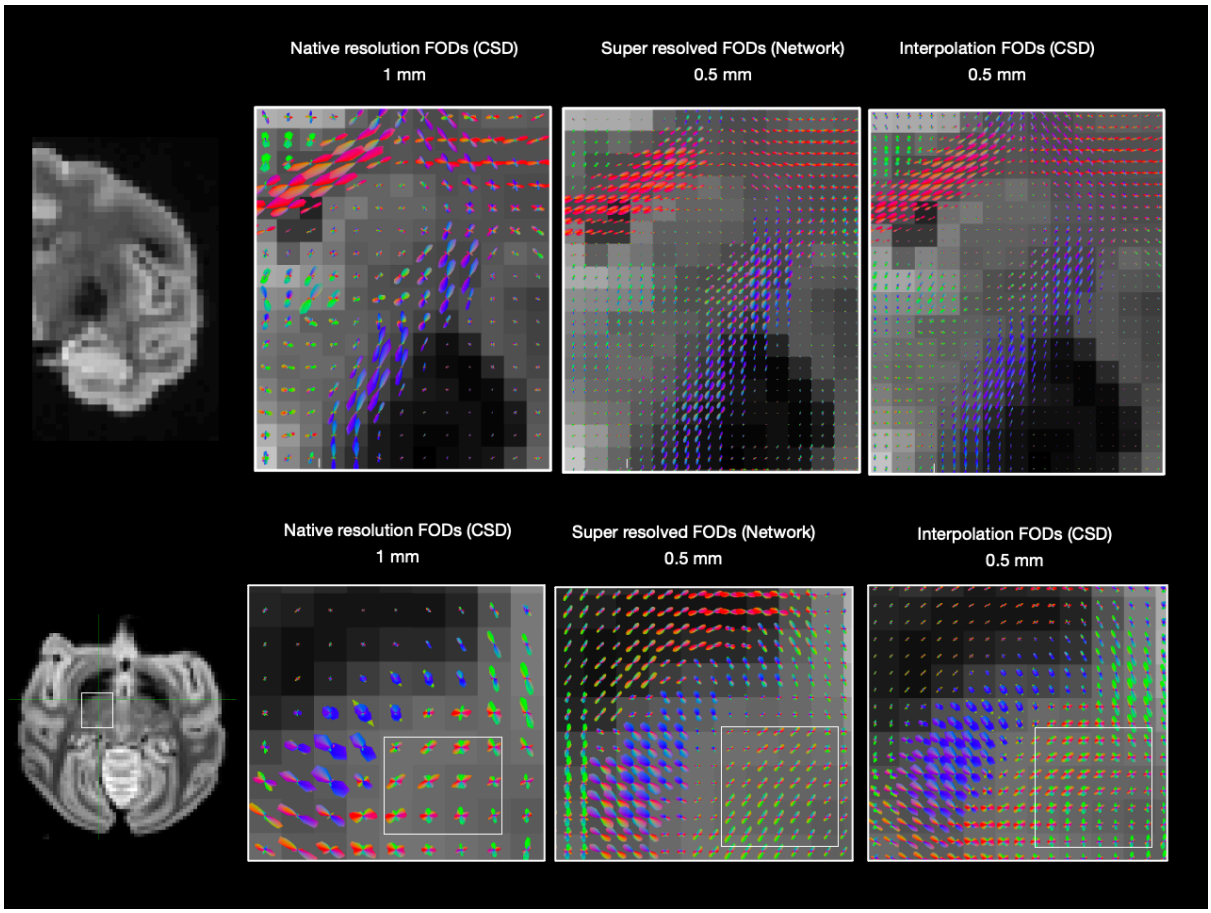


Figure 6.5: **Application to postmortem macaque dMRI at 1 mm.**
FODs are shown for native-resolution CSD (Left), super-resolved FODs obtained from the network (Middle), and super-resolved FODs produced by linear interpolation (Right). Network super-resolved FODs shows fewer crossing fibres in the corticospinal region (Top). In the thalamus (Bottom), the network allocated multiple fibre populations of crossing-fibre voxels to distinct spatial locations while maintaining smooth spatial transitions between voxels.

Figure 6.6 shows the network applied to unseen postmortem macaque data from the same macaque brain at 1 mm but with higher b-values and higher angular resolution (at b=10 ms/μm^2 with 1000 diffusion gradient directions paired with 0.5 mm co-registered structural MRI). The network estimated FODs at 0.5 mm isotropic resolution across the entire brain which shows enhanced resolution and anatomical details compared to the CSD FODs at 1 mm. The results below in this section are all based on these FODs.

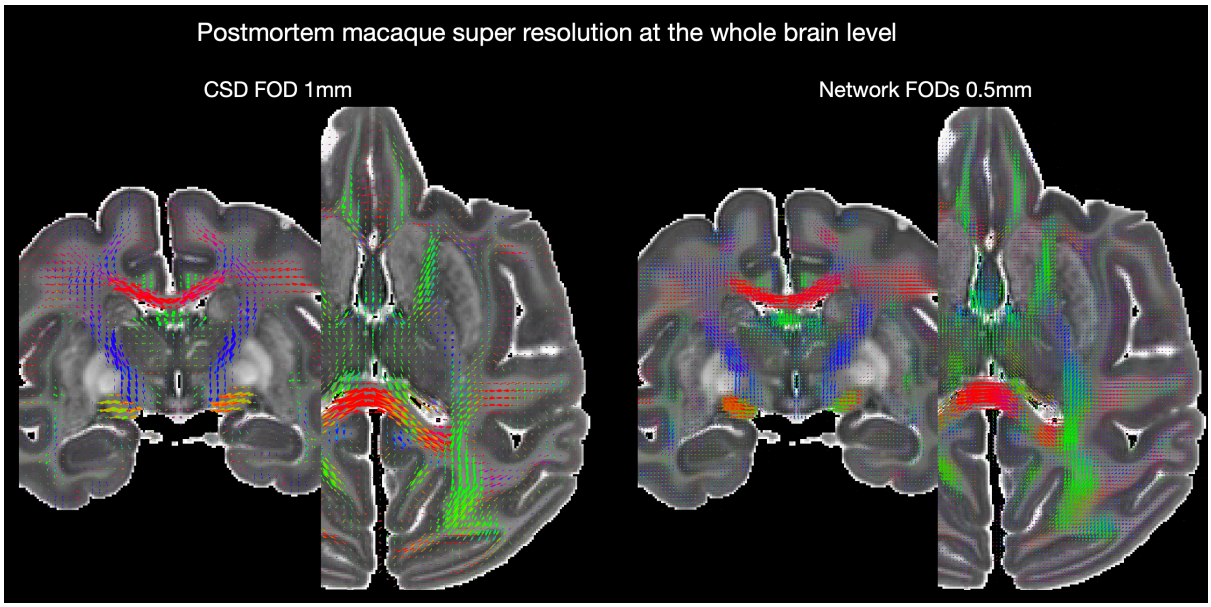


Figure 6.6: Application to postmortem macaque dMRI at 1 mm with b=10 ms/μm^2. We evaluated the network in estimating 0.5 mm FODs from 1 mm dMRI (b=10 ms/μm^2 with 1000 diffusion gradient directions) and 0.5 mm structural MRI. Whole-brain FODs generated by the network were compared to those obtained using CSD, demonstrating the network's ability to achieve high resolution and enhance anatomical details.

Figure 6.7 shows a zoomed-in region of the calcarine sulcus within the occipital lobe, where fibre architecture exhibits pronounced curvature, as demonstrated by the corresponding PLI. Despite the limited directional information in the 1 mm input dMRI, our network reconstructed this complex architecture with large curvature during FOD estimation.

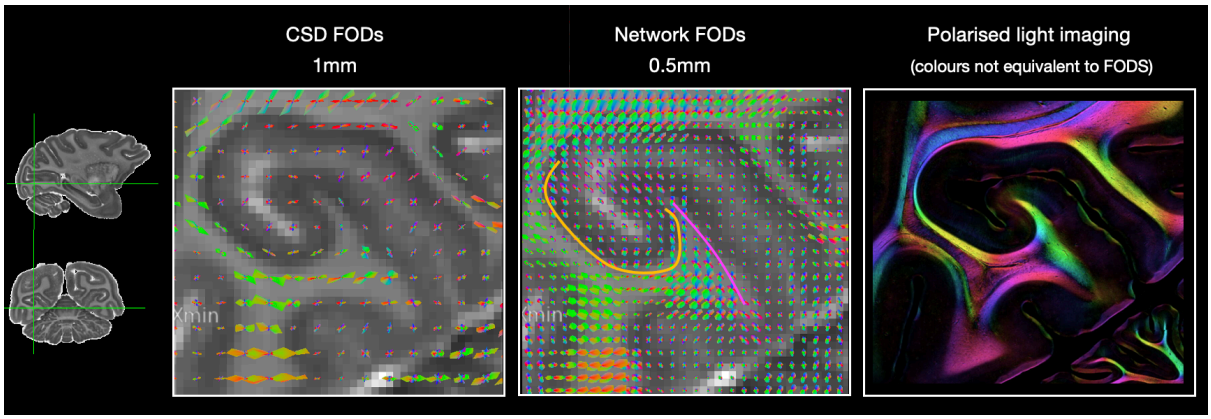


Figure 6.7: **Reconstruction of fibre orientations in the calcarine sulcus.** FODs estimated using the super-resolved microscopy-informed network at 0.5 mm resolution were compared to those derived from CSD at 1 mm resolution. The network FODs exhibit closer alignment with anatomical details as observed in PLI within the calcarine sulcus of the occipital lobe and as evidenced by the continuous FOD patterns (yellow and pink annotation). These results highlight the network's ability to preserve intricate fibre architecture despite the limitations of the original low-resolution data.

However, there are some regions where the network failed. As illustrated in Figure 6.8, the fibre orientation within the brainstem reveals a striping pattern in ultra-high-resolution MRI data (Henssen et al., 2019) (Figure 6.8 Right). This pattern arises from intersecting white matter pathways, including superior-inferior oriented tracts (e.g. corticospinal and pontocerebellar fibres) and right-left oriented tracts (e.g., medial lemniscus) which form intricate crossing fibre configurations. Notably, this pattern is absent in native-resolution FOD at 1 mm isotropic resolution. However, despite super-resolution, the network failed to reconstruct these striping and crossing architectures, a limitation also observed in interpolation FODs with CSD. These results highlight a challenge in resolving crossing fibre populations in densely packed regions.

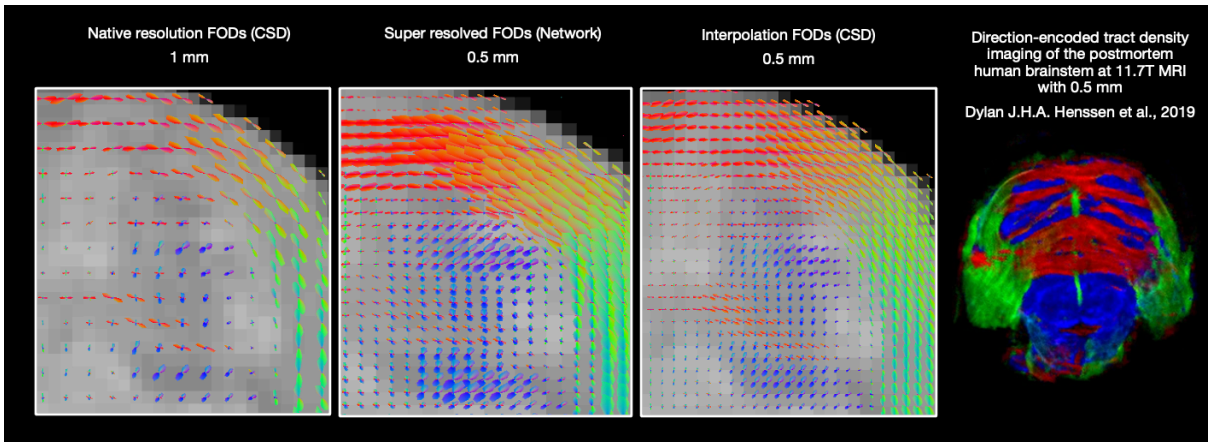


Figure 6.8 Super resolved fibre orientation in the brainstem.
The complex and intricate fibre crossings in the brainstem present a significant challenge for accurate dMRI fibre orientation estimation. Dylan et al. 2019(Henssen et al., 2019) demonstrated ultra-high-resolution acquisitions in the human brain stem that revealed a striping fibre pattern. However, our method could only capture it as a crossing fibre, not spatially resolved fibre bundles, limiting the ability to clearly determine the underlying structure.

Figure 6.9 shows how the network FODs at 0.5 mm can be used to successfully reconstruct white matter tracts via tractography, including optic radiation, corticospinal tract and fornix.

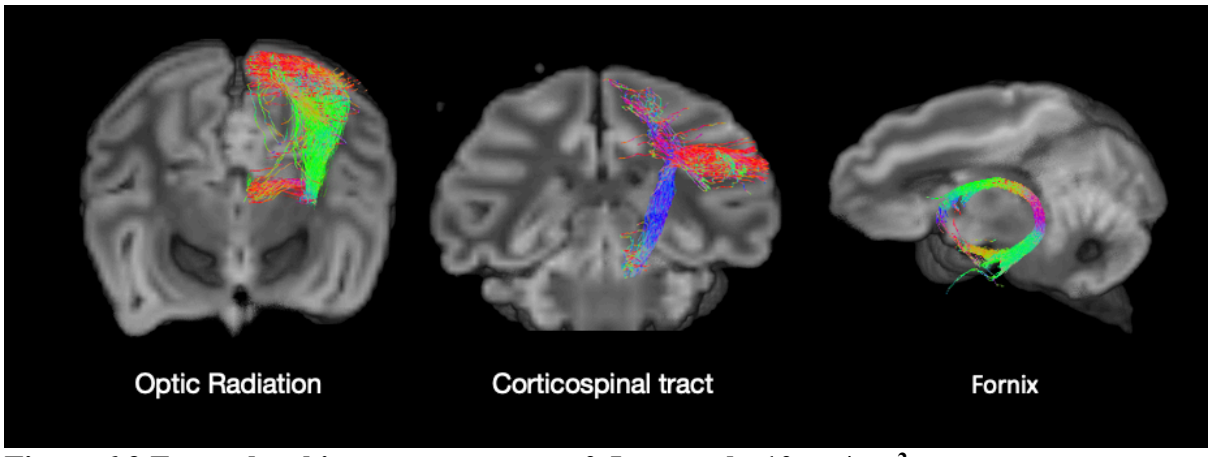


Figure 6.9 Example white matter tracts at 0.5 mm at b=10 ms/μm^2.
White matter tracts were reconstructed using tractography from network-derived FODs, estimated from the dMRI at 1 mm and b=10 ms/μm^2 .

6.3.3 Application to the in-vivo macaque data

Figure 6.10 shows that the network was applied to in-vivo macaque data (1 mm dMRI and 0.5 mm structural MRI). Notably, this in-vivo data had lower SNR than the postmortem data used previously, as evidenced by the b0 images. Importantly, the network was able to recover super-resolved and anatomically plausible FODs in most of the regions, even given the low SNR inputs. These preliminary results demonstrate that the network is invariant to tissue state (in-vivo versus postmortem) in macaque. However, some FODs are missing or have low amplitudes, which are incorrectly estimated and will be addressed in future work.

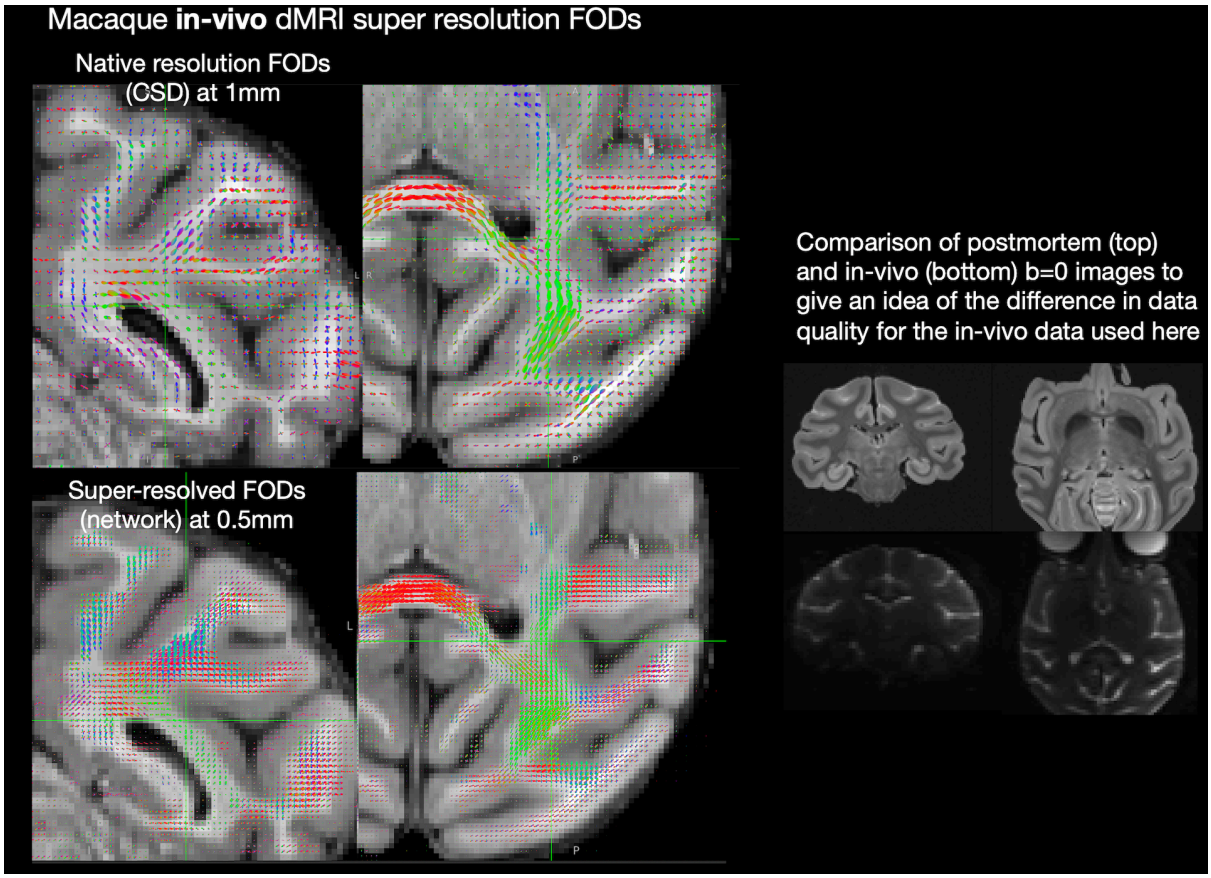


Figure 6.10: Super-resolved FODs in in-vivo macaque at 1 mm.
Low-quality in-vivo dMRI (1 mm) and co-registered structural MRI (0.5 mm) were used to estimate FODs at a resolution of 0.5 mm. The figure presents coronal (Left) and axial views (Middle) comparing FODs derived from native-resolution CSD FODs at 1 mm with the network super-resolved FODs at 0.5mm. The right panel illustrates the contrast in data quality between in-vivo and postmortem dMRI, highlighting the differences in signal-to-noise ratio and resolution.

6.3.4 Application to the in-vivo human data

Figure 6.11 shows the application of the network adapted to in-vivo human UK Biobank data through unsupervised domain adaptation using 2 mm single-shell dMRI and 1 mm structural MRI. The super-resolved FODs exhibited improved spatial resolution and preserved anatomical plausible FODs and crossing fibres in regions such as the central semiovale and hippocampus.

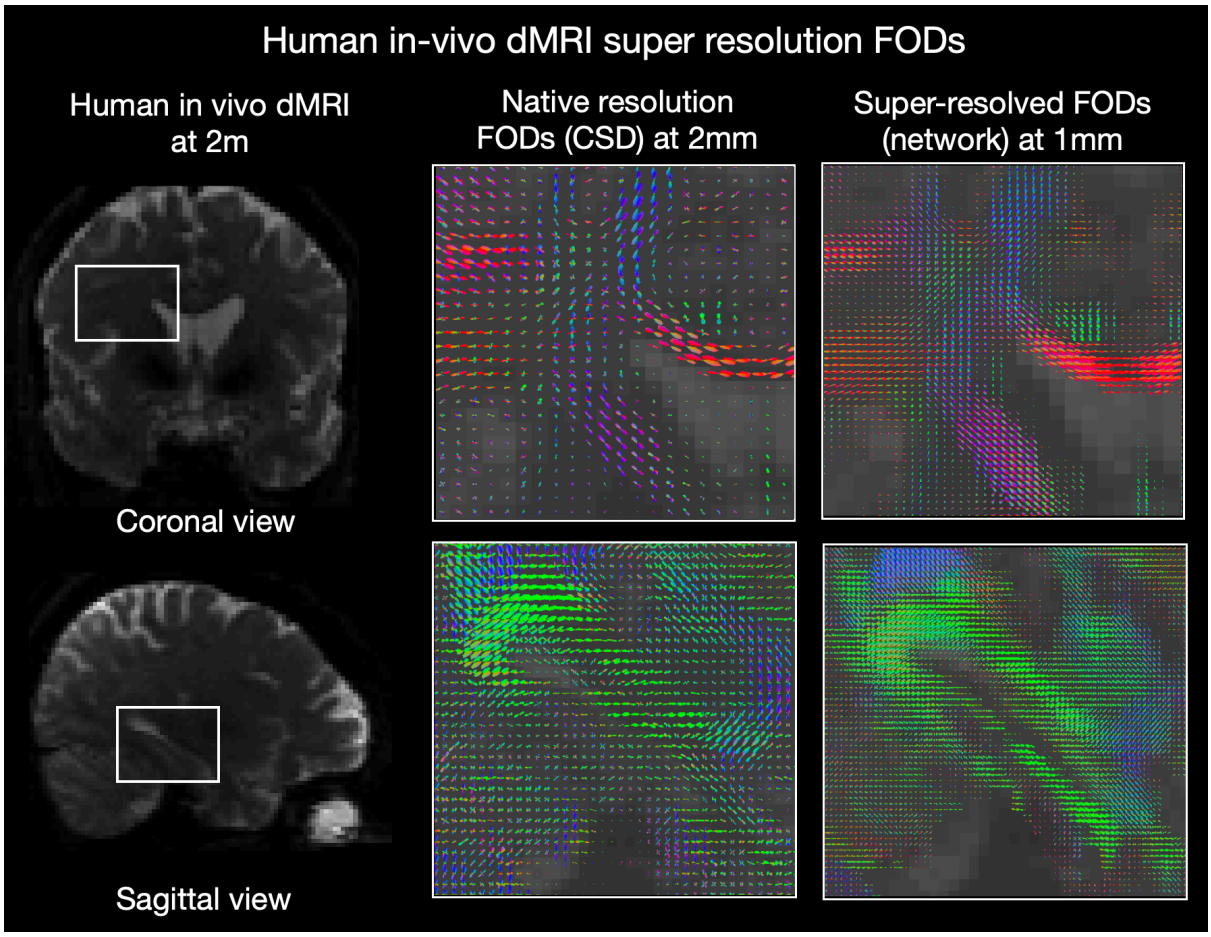


Figure 6.11: Super-resolved FODs in in-vivo human.
The network was adapted for the in-vivo human data with unsupervised domain adaptation using single-shell in-vivo dMRI (2 mm) and structural imaging (1 mm) from the UKB data. FODs at the native resolution of 2 mm estimated using CSD are compared with the network super-resolved FODs at 1mm. FODs are in coronal (Top) for central semiovale, and sagittal (Bottom) view showing the hippocampus.

6.4 Discussion

This study investigates whether deep learning based multi-modal super-resolution can leverage microscopy-derived information to enhance fibre orientation estimation in MRI. We propose a novel microscopy-informed super-resolution framework designed for single-shell in-vivo dMRI paired with structural MRI when microscopy is unavailable. The approach integrates low-resolution dMRI with high-resolution structural MRI (twice the spatial resolution of dMRI). Critically, FOD predictions are implicitly informed by microscopy through training on hybrid MRI-microscopy FODs derived from the BigMac dataset enabling cross-species and cross-tissue state generalisability. To our knowledge, this represents the

first cross-species, multimodal deep learning framework achieving super-resolved FODs by transferring microscopy-derived insights to dMRI.

Our framework has several key advantages over conventional approaches. First, we include both dMRI and structural MRI where structural MRI provides high-resolution tissue boundary information at twice the spatial resolution of input dMRI. Second, microscopy provides distinct advantages over conventional interpolation approaches. Microscopy-guided super-resolution enables spatially informed allocation of fibre orientations. Unlike linear interpolation which assumes linear intensity between voxels when upsampling the dMRI data, our microscopy-informed approach leverages subvoxel fibre architecture to resolve crossing fibres at high resolution while preserving spatial smoothness. This is demonstrated through direct comparisons showing that interpolation-based upsampling (e.g., linear) fails to disambiguate complex fibre configurations in thalamus (Figure 6.5), whereas microscopy information guides anatomically plausible orientation distributions. Third, the microscopy-informed network in effect learns the fibre response function (FRF) which is the diffusion signal profile for a single fibre population relating the diffusion signal to the FOD. The network learns the FRF in a data-driven manner whilst CSD assumes a uniform response function across all white matter regions. The CSD FRF assumption is likely invalid if we consider how microstructure and myelin vary across the brain. By deriving response functions directly from the joint analysis of dMRI-microscopy hybrid FODs, our method accounts for regional variations in the response function related to e.g. fibre packing density and myelination. To our knowledge, this work is the first to unify dMRI, structural MRI, and microscopy into a single super-resolution framework, resolving complex fibre architectures beyond the limitations of both classical interpolation and CSD-based techniques.

The domain adaptation architecture enhances the network's generalisability to shifts in data distribution, where similar methods have previously been used to mitigate scanner-specific variability for data harmonisation (Dinsdale et al., 2021). Figure 6.10 illustrates differences between in-vivo and postmortem dMRI data with in-vivo scans exhibiting higher noise levels and reduced data quality. The network was pre-trained to capture invariant representation across both in-vivo and postmortem MRI domains in macaque, regardless of these changes in data quality. Importantly, the 1 mm macaque dMRI resolution approximates the 2.5 mm resolution typical in human studies when scaled by brain size, highlighting the translational potential of our approach. The proposed method was next adapted to in-vivo human dMRI

data: single-shell diffusion encoding, 2 mm isotropic resolution, and a total acquisition time (dMRI + structural MRI) under 15 minutes. Our results demonstrate robust cross-species transferability: the network leveraged macaque-derived microscopy information to reconstruct high-resolution FODs from human data, despite inherent interspecies variability in MRI acquisitions. By demonstrating robust super-resolution performance on low-quality and limited datasets, this framework shows potential for future clinical translation, particularly in scenarios where high-resolution acquisitions are not feasible.

One limitation of our approach arises from inherent uncertainties in the super-resolution process, particularly in regions of complex fibre architecture. Although structural MRI provides high-resolution anatomical guidance, it is one-dimensional, lacking explicit information about multi-directional fibre organisation. This shortfall becomes pronounced in neuroanatomical regions with complex fibre architecture such as the brainstem. The super-resolution network knows nothing about these crossing configurations and fails to reconstruct them. The challenges of resolving complex fibre architecture are exacerbated by the small, tight packed and curved fibre bundles inside the brain, which often fall below the spatial resolution of clinical dMRI (typically 2 mm isotropic). At such resolutions, intra-voxel signal averaging occurs across multiple fibre populations, making it difficult to disentangle or reconstruct different fibre populations. Furthermore, the pons and brainstem exhibit heterogeneous tissue composition, with white matter fibres intermixing with and passing through adjacent grey matter regions. This complexity makes these areas particularly susceptible to partial volume effects (Haines and Mihailoff, 2018). As a result, the network's ability to infer accurate orientation distributions in these regions is compromised (Figure 6.8). These limitations highlight a fundamental constraint of super-resolution methodologies: when microstructural complexity exceeds the informational capacity of both diffusion and structural MRI—neither of which directly provides precise spatial localisation of subvoxel fibre geometry—orientation estimation becomes less accurate.

A second limitation of our network in its current form is that it requires the input of a higher-resolution structural MRI, alongside the dMRI data. We included the structural because it can inform tissue boundaries at higher resolution and thus aid the super-resolution. Our network currently requires the input structural MRI to be twice the dMRI resolution. For datasets where this is not the case (eg. HCP provides dMRI at 1.25 mm isotropic resolution paired with structural MRI at 0.7 mm), the structural data must first be upsampled, which could

result in minor errors or misestimation (Essen et al., 2013). Further, the structural and dMRI images must be co-aligned when input into the network, where misregistration errors could introduce inaccuracies. A similar network without the structural input could easily be created and a thorough examination of the added benefit of the structural MRI is planned for future work.

While the microscopy-informed super-resolution network presented in this chapter demonstrates initial feasibility, its applications to in-vivo macaque and human data remain preliminary. Future studies are necessary to conduct rigorous validation across datasets. First, a comparative analysis will be conducted to evaluate network performance when trained with versus without structural MRI inputs, which will clarify the impact of structural MRI as input. Additionally, the network architecture was adapted from the previous chapter, and further refinement of the main network architecture will be explored to better suit super-resolution the task. Second, we will compare microscopy-informed super-resolved FODs with alternative deep learning based super-resolution techniques, which are also analysis-based super-resolution methods designed to enhance standard quality datasets. High-resolution FODs from ultra-high field MRI will be used as the ground truth (Barisano et al., 2019; Beaujoin et al., 2018; Pisharady et al., 2024). This comparative analysis will highlight the strengths and limitations of utilising microscopy information during the training process. Third, we aim to extend the application of the microscopy-informed super-resolution network to dMRI datasets with limited resolution or shorter scan times. Particular focus will be placed on clinically critical targets, such as the fibre connections between the subthalamic nucleus and globus pallidus internus—key regions in deep brain stimulation (Lyons, 2011; Zhang et al., 2019) which are difficult to resolve at low spatial resolutions. Tractography, including fibre tracking in subcortical regions such as hippocampus tractography, will be used to evaluate if the microscopy information is beneficial to better tractography in humans. Furthermore, we aim to explore the feasibility of achieving higher super-resolution factors, such as a three-fold increase (eg. super-resolve dMRI data with an input resolution of 0.6 mm to produce FODs at 0.2 mm) to further investigate the utility of super-resolution FODs in improving in-vivo fibre tracking precision. By addressing these limitations, our super-resolution framework holds significant potential to advance tractography quality in clinical settings where conventional high-resolution acquisitions remain impractical.

Conclusion

In summary, this study introduces a novel deep learning framework designed to enhance FOD resolution in diffusion MRI by integrating postmortem microscopy information. The method addresses a critical limitation in neuroimaging: resolving intricate white matter architectures with super-resolution, such as those in the internal capsule and thalamus, where standard low-resolution dMRI fails to disentangle. This advancement establishes a foundation for translating high-resolution neuroanatomical insights from microscopy into MRI, with the potential to refine the characterisation of brain connectivity in living humans. Further validation and optimisation of the framework are needed to better position it as an important tool for research and diagnostic neuroimaging.

7

Future direction and final remarks

Table of Contents

7. 1 Future work *171*
7.1.1 Application and validation on PS-OCT 171
7.1.2 Improvement of the deep learning framework 173
7.1.3 Applications to larger datasets 175
7.2 Final remarks *175*

Foreword

This thesis investigates integrative methods for estimating fibre orientations from diffusion MRI. Our primary goal is to transfer microscopy-derived information to dMRI, through cross-species and cross-modality framework.

Chapter 3 introduces a hybrid tractography method that combines dMRI and microscopy data through a data-fusion approach, utilising the complementary strengths of these modalities. **Chapter 4** extends microscopy-derived knowledge beyond datasets where MRI and microscopy are acquired from the same brain to typical in-vivo MRI in another macaque brain through deep learning. **Chapter 5** adapts this deep learning framework to in-vivo human data, ensuring cross-species applicability to single-shell dMRI. Collectively, we present approaches leveraging microscopy information to improve the accuracy of brain connectivity mapping with non-invasive dMRI in humans. In **Chapter 6**, we apply domain adaptation techniques to achieve super-resolution in dMRI. A network trained on microscopy data at resolutions exceeding that of MRI shows the potential to super-resolve the MRI-derived fibre orientations.

Together, these methods introduced in this thesis advance the accuracy and resolution of fibre orientations in dMRI, thus improving fibre tracking, adding valuable insights for future tractography development and showing promise for applications in clinical diagnosis and therapeutic planning.

7. 1 Future work

This thesis presents two primary contributions: (1) the integration of dMRI and microscopy to leverage the complementary strengths of both modalities, and (2) the transfer of knowledge from microscopy to dMRI to improve accuracy or achieve super-resolution in fibre orientation estimation. Future directions include (1) further validation of our methods by incorporating additional microscopy techniques, such as polarisation-sensitive optical coherence tomography (PS-OCT)(Wang et al., 2010), (2) improving the microscopy-informed deep learning framework by better integrating microscopy knowledge, and (3) extending its applications to larger datasets.

7.1.1 Application and validation on PS-OCT

Our previous work aligns well with large ongoing research programmes including the BRAIN Initiative, the BRAIN Initiative Connectivity Across Scales (BRAIN CONNECTS)(Ngai, 2024), and BigBrain project (Amunts et al., 2013). These projects aim to establish ‘roadmaps’ of structural brain connectivity across species including humans. These initiatives involve deep phenotyping of select brains via extensive MRI and microscopy, where combining multiple technologies offers the promise of brain connectivity mapping with great details. Building on this alignment with our work, our next step is to integrate our data fusion methods and the deep learning models with the datasets obtained by these initiatives. This will not only allow us to generate detailed wiring diagrams of primate brains with their extensive microscopy data but also further improve the robustness and generalisability of our methods.

One of the primary research aims of the CONNECTS programme is to obtain PS-OCT and ultra-high field diffusion MRI from the same macaque brain for comparison with anatomical tract tracing to generate an accurate wiring diagram. PS-OCT, like PLI, utilises the birefringence of the myelin to measure the alterations of light polarisation. While this thesis primarily focuses on PLI, PS-OCT offers several advantages which will be discussed in the

following section. As part of the BRAIN CONNECTS team, we will have access to valuable PS-OCT and dMRI data. Therefore, we aim to explore its potential to enhance our methods by investigating 1) the feasibility and quality of hybrid dMRI-PS-OCT tractography and 2) using PS-OCT and PLI to train a microscopy-informed deep learning model.

PS-OCT setup and advantages: PS-OCT utilises blockface sectioning, which means images are captured for each exposed surface before the tissue is sliced. This technique preserves structural integrity and mitigates slice-specific distortions common in traditional serial sectioning, ensuring greater accuracy in volumetric reconstruction. PS-OCT operates similarly to ultrasound, transmitting waves (in this case, light) through tissues and analysing the backscattered signals. The delay of the signals provides information on how the light interacts with the tissue, revealing structural details. By exploiting the birefringence of myelin sheath surrounding axons, PS-OCT enables the differentiation of grey and white matter and facilitates the measurement of fibre orientations. With in-plane resolutions as fine as 15 μm and slice thicknesses of 100–200 μm, PS-OCT typically provides higher spatial resolution and deeper penetration compared to PLI (Wang et al., 2018). While PLI is predominantly used in research investigations, PS-OCT has broader applications, both in-vivo and ex-vivo imaging, with clinical uses such as assessing ocular fibrous tissues and cancer tissues (Pircher et al., 2011).

Applications of PS-OCT: PS-OCT can delineate distinct contrasts for myeloarchitecture and cytoarchitecture, enabling detailed mapping of cortical layers, subcortical regions, and fibre tracts in both human (Wang et al., 2014) and mouse brains (Nakaji et al., 2008). For instance, in the cerebellar cortex, PS-OCT can clearly distinguish between the molecular and granular layers, with well-defined layer boundaries (Wang et al., 2018). Furthermore, specific cell types, such as the Purkinje cell layer, are clearly visible. PS-OCT can capture either 2D or 3D fibre orientations depending on the setups, and with the structure tensor analysis, it enables the generation of 2D or 3D tractography (H. Wang et al., 2015). Notably, tractography has been demonstrated in both deep and superficial white matter with complex fibre architectures (Jones et al., 2020). These capabilities highlight the potential of PS-OCT for mapping brain connectivity with great details.

Future use of PS-OCT: We will use the hybrid MRI-microscopy method proposed in Chapter 3, to combine the in-plane orientation from 2D PS-OCT with the through-plane

orientation from ultra-high field dMRI, constructing hybrid MRI-PS-OCT fibre orientations in the macaque brain. Subsequently, we will assess whether the hybrid PS-OCT orientations provide novel insights into brain connectivity that remain difficult to uncover when each modality is used in isolation. We will also compare it against 3D anatomical tract tracing(Xu et al., 2021), considered the gold standard, from the CONNECTS programme to evaluate the accuracy and specificity of our tractography method.

Furthermore, we will train our microscopy-informed deep learning with both hybrid dMRI-PS-OCT data and hybrid dMRI-PLI data. By utilising this large dataset that incorporates variations across individual macaques, the model may be better generalised across different subjects and brain structures.

7.1.2 Improvement of the deep learning framework

In Chapters 4, 5, and 6, we proposed deep learning techniques to model the relationship between dMRI and microscopy-informed fibre orientations. However, a limitation of this approach is that deep learning remains a black-box process, making it challenging to understand how microscopy data is utilised within the model.

To address this, we aim to explore the deep learning framework by explicitly incorporating prior knowledge from microscopy which may enhance the interpretability of the model, and the accuracy of fibre orientation estimates derived from dMRI. We will explore two different strategies to more effectively leverage microscopy data.

First, instead of using hybrid dMRI-PLI orientations as labels during model training, we will directly utilise 2D microscopy data and construct the loss function by projecting MRI fibre orientation onto the microscopy plane. This method prevents information pooling (combining fibre orientation at the microscopy resolution into dMRI resolution) during constructing the hybrid dMRI-PLI orientations which will provide subvoxel fibre architecture. In addition, the loss function may be designed to penalise deviations from tissue-specific properties—such as maintaining fibre continuity in white matter within a certain neighbourhood or enforcing angular constraints for FODs near grey matter boundaries. These constraints will help ensure that dMRI-derived fibre orientation estimates remain consistent with known histological features.

Second, we will investigate the reinforcement learning (RL) approach for estimating fibre orientations by leveraging a feedback-driven optimisation process (Figure 7.1). In this framework, the estimation problem is formulated as a sequential decision-making task, where fibre orientation predictions are iteratively refined based on a reward signal. RL models the system dynamics by updating the state (S_t) based on the selected action (A_t), resulting in a new state (S_{t+1}) with the environment providing feedback on if the action improves the fibre orientations or not. For our estimation, the state (S_t) represents the fibre orientation at a given location (x,y) and angle θ along with the orientations of its neighbouring fibres. This formulation enables the effective incorporation of neighbouring fibre orientation information.

The action (A_t) involves either increasing, decreasing or maintaining the current orientation angle. The reward function is designed to promote smooth transitions while penalising discontinuities, ensuring spatial consistency in the estimated orientations. Through trial-and-error interactions, the RL model progressively improves fibre orientation predictions. In addition, asymmetric FODs can be applied as an action to better distinguish sub-voxel patterns including crossing, fanning etc (Wu et al., 2020).

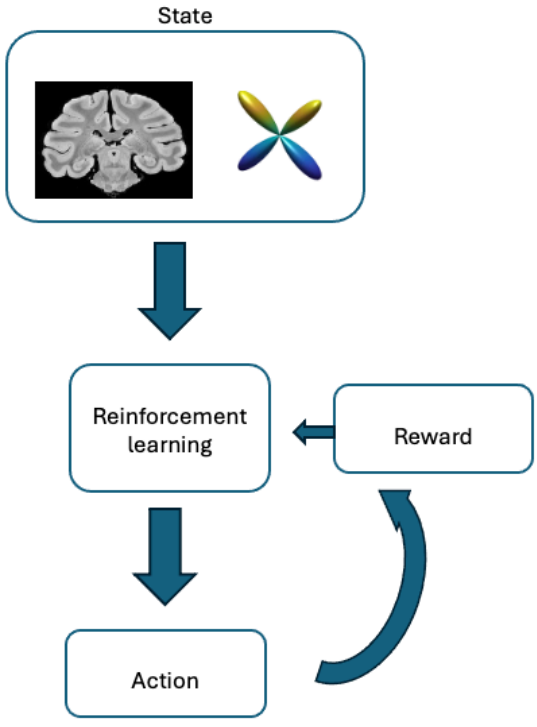


Figure 7.1: Reinforcement learning framework

State: The state encodes the fibre orientation and its neighbours capturing local spatial context. **Action**: At each step, the agent adjusts the target orientation angle via discrete actions (increase, decrease, maintain). **Reward-Driven optimisation**: A reward function penalises angular discontinuities and facilitates smooth spatial transitions.

7.1.3 Applications to larger datasets

We have demonstrated that the network trained on macaque data can be adapted for human data from both the HCP and the UKB. However, our results were based on a limited number of subjects. Moving forward, we plan to extend the application of the network to a larger cohort of human subjects to evaluate its ability for detecting subtle effects—such as the association between imaging phenotypes and non-imaging phenotypes within the UKB—that may be challenging to identify using traditional methods. This approach will advance our understanding of how brain microstructure relates to non-imaging factors, such as lifestyle and diseases, while also improving our ability to predict specific phenotypes and disease outcomes.

7.2 Final remarks

This thesis highlights the successful transfer of knowledge from microscopy in the BigMac dataset to humans using integrative methods of data fusion and deep learning. By using a cross-species, multi-scale, multi-modal approach, we address challenges in improving the accuracy of brain connectivity mapping. The rapid progress in deep learning creates significant potential to improve the accuracy of tractography for both basic and clinical neuroscience.

Reference list

Abraham, A., Milham, M.P., Di Martino, A., Craddock, R.C., Samaras, D., Thirion, B., Varoquaux, G., 2017. Deriving reproducible biomarkers from multi-site resting-state data: An Autism-based example. NeuroImage 147, 736–745. https://doi.org/10.1016/j.neuroimage.2016.10.045

Aja-Fernández, S., Martín-Martín, C., Planchuelo-Gómez, Á., Faiyaz, A., Uddin, M.N., Schifitto, G., Tiwari, A., Shigwan, S.J., Kumar Singh, R., Zheng, T., Cao, Z., Wu, D., Blumberg, S.B., Sen, S., Goodwin-Allcock, T., Slator, P.J., Yigit Avci, M., Li, Z., Bilgic, B., Tian, Q., Wang, X., Tang, Z., Cabezas, M., Rauland, A., Merhof, D., Manzano Maria, R., Campos, V.P., Santini, T., Da Costa Vieira, M.A., HashemizadehKolowri, S., DiBella, E., Peng, C., Shen, Z., Chen, Z., Ullah, I., Mani, M., Abdolmotalleby, H., Eckstrom, S., Baete, S.H., Filipiak, P., Dong, T., Fan, Q., De Luis-García, R., Tristán-Vega, A., Pieciak, T., 2023. Validation of deep learning techniques for quality augmentation in diffusion MRI for clinical studies. NeuroImage Clin. 39, 103483. https://doi.org/10.1016/j.nicl.2023.103483

Alexander, D.C., Dyrby, T.B., Nilsson, M., Zhang, H., 2019. Imaging brain microstructure with diffusion MRI: practicality and applications. NMR Biomed. 32, e3841. https://doi.org/10.1002/nbm.3841

Alexander, D.C., Zikic, D., Ghosh, A., Tanno, R., Wottschel, V., Zhang, J., Kaden, E., Dyrby, T.B., Sotiropoulos, S.N., Zhang, H., Criminisi, A., 2017. Image quality transfer and applications in diffusion MRI. NeuroImage 152, 283–298. https://doi.org/10.1016/j.neuroimage.2017.02.089

Alom, M.Z., Taha, T.M., Yakopcic, C., Westberg, S., Sidike, P., Nasrin, M.S., Hasan, M., Van Essen, B.C., Awwal, A.A.S., Asari, V.K., 2019. A State-of-the-Art Survey on Deep Learning Theory and Architectures. Electronics 8, 292. https://doi.org/10.3390/electronics8030292

Alzubaidi, L., Zhang, J., Humaidi, A.J., Al-Dujaili, A., Duan, Y., Al-Shamma, O., Santamaría, J., Fadhel, M.A., Al-Amidie, M., Farhan, L., 2021. Review of deep learning: concepts, CNN architectures, challenges, applications, future directions. J. Big Data 8, 53. https://doi.org/10.1186/s40537-021-00444-8

Ambrosen, K.S., Eskildsen, S.F., Hinne, M., Krug, K., Lundell, H., Schmidt, M.N., Van Gerven, M.A.J., Mørup, M., Dyrby, T.B., 2020. Validation of structural brain connectivity networks: The impact of scanning parameters. NeuroImage 204, 116207. https://doi.org/10.1016/j.neuroimage.2019.116207

Amunts, K., Lepage, C., Borgeat, L., Mohlberg, H., Dickscheid, T., Rousseau, M.-É., Bludau, S., Bazin, P.-L., Lewis, L.B., Oros-Peusquens, A.-M., Shah, N.J., Lippert, T., Zilles, K., Evans, A.C., 2013. BigBrain: An Ultrahigh-Resolution 3D Human Brain Model. Science 340, 1472–1475. https://doi.org/10.1126/science.1235381

Anthofer, J., Steib, K., Fellner, C., Lange, M., Brawanski, A., Schlaier, J., 2014. The variability of atlas-based targets in relation to surrounding major fibre tracts in thalamic deep brain stimulation. Acta Neurochir. (Wien) 156, 1497–1504. https://doi.org/10.1007/s00701-014-2103-z

Ardesch, D.J., Scholtens, L.H., de Lange, S.C., Roumazeilles, L., Khrapitchev, A.A., Preuss, T.M., Rilling, J.K., Mars, R.B., van den Heuvel, M.P., 2022. Scaling Principles of White Matter Connectivity in the Human and Nonhuman Primate Brain. Cereb. Cortex N. Y. N 1991 32, 2831–2842. https://doi.org/10.1093/cercor/bhab384

Asan, A.S., McIntosh, J.R., Carmel, J.B., 2022. Targeting Sensory and Motor Integration for Recovery of Movement After CNS Injury. Front. Neurosci. 15.

Assaf, Y., Pasternak, O., 2008. Diffusion Tensor Imaging (DTI)-based White Matter Mapping in Brain Research: A Review. J. Mol. Neurosci. 34, 51–61. https://doi.org/10.1007/s12031-007-0029-0

Axer, H., 2011. Microstructural analysis of human white matter architecture using polarized light imaging: views from neuroanatomy. Front. Neuroinformatics 5. https://doi.org/10.3389/fninf.2011.00028

Axer, H., Axer, M., Krings, T., Keyserlingk, D.G. v, 2001. Quantitative estimation of 3-D fiber course in gross histological sections of the human brain using polarized light. J. Neurosci. Methods 105, 121–131. https://doi.org/10.1016/S0165-0270(00)00349-6

Axer, M., Amunts, K., Grässel, D., Palm, C., Dammers, J., Axer, H., Pietrzyk, U., Zilles, K., 2011a. A novel approach to the human connectome: Ultra-high resolution mapping of fiber tracts in the brain. NeuroImage 54, 1091–1101. https://doi.org/10.1016/j.neuroimage.2010.08.075

Axer, M., Graessel, D., Kleiner, M., Dammers, J., Dickscheid, T., Reckfort, J., Huetz, T., Eiben, B., Pietrzyk, U., Zilles, K., Amunts, K., 2011b. High-Resolution Fiber Tract Reconstruction in the Human Brain by Means of Three-Dimensional Polarized Light Imaging. Front. Neuroinformatics 5.

Aydogan, D.B., Shi, Y., 2018. Tracking and validation techniques for topographically organized tractography. NeuroImage 181, 64–84. https://doi.org/10.1016/j.neuroimage.2018.06.071

Baldassarre, A., Lewis, C.M., Committeri, G., Snyder, A.Z., Romani, G.L., Corbetta, M., 2012. Individual variability in functional connectivity predicts performance of a perceptual task. Proc. Natl. Acad. Sci. 109, 3516–3521. https://doi.org/10.1073/pnas.1113148109

Barisano, G., Sepehrband, F., Ma, S., Jann, K., Cabeen, R., Wang, D.J., Toga, A.W., Law, M., 2019. Clinical 7 T MRI: Are we there yet? A review about magnetic resonance imaging at ultra-high field. Br. J. Radiol. 92, 20180492. https://doi.org/10.1259/bjr.20180492

Basser, P.J., Jones, D.K., 2002. Diffusion-tensor MRI: theory, experimental design and data analysis – a technical review. NMR Biomed. 15, 456–467. https://doi.org/10.1002/nbm.783

Basser, P.J., Mattiello, J., LeBihan, D., 1994. MR diffusion tensor spectroscopy and imaging. Biophys. J. 66, 259–267. https://doi.org/10.1016/S0006-3495(94)80775-1

Bastiani, M., Cottaar, M., Dikranian, K., Ghosh, A., Zhang, H., Alexander, D.C., Behrens, T.E., Jbabdi, S., Sotiropoulos, S.N., 2017. Improved tractography using asymmetric fibre orientation distributions. NeuroImage 158, 205–218. https://doi.org/10.1016/j.neuroimage.2017.06.050

Baumann, N., Pham-Dinh, D., 2001. Biology of Oligodendrocyte and Myelin in the Mammalian Central Nervous System. Physiol. Rev. 81, 871–927. https://doi.org/10.1152/physrev.2001.81.2.871

Beaujoin, J., Palomero-Gallagher, N., Boumezbeur, F., Axer, M., Bernard, J., Poupon, F., Schmitz, D., Mangin, J.-F., Poupon, C., 2018. Post-mortem inference of the human hippocampal connectivity and microstructure using ultra-high field diffusion MRI at 11.7 T. Brain Struct. Funct. 223, 2157–2179. https://doi.org/10.1007/s00429-018-1617-1

Beaulieu, C., 2002. The basis of anisotropic water diffusion in the nervous system - a technical review. NMR Biomed. 15, 435–455. https://doi.org/10.1002/nbm.782

Behrens, T.E.J., Berg, H.J., Jbabdi, S., Rushworth, M.F.S., Woolrich, M.W., 2007. Probabilistic diffusion tractography with multiple fibre orientations: What can we gain? NeuroImage 34, 144–155. https://doi.org/10.1016/j.neuroimage.2006.09.018

Behrens, T.E.J., Woolrich, M.W., Jenkinson, M., Johansen-Berg, H., Nunes, R.G., Clare, S., Matthews, P.M., Brady, J.M., Smith, S.M., 2003. Characterization and propagation of uncertainty in diffusion-weighted MR imaging. Magn. Reson. Med. 50, 1077–1088. https://doi.org/10.1002/mrm.10609

Belyk, M., Eichert, N., McGettigan, C., 2021. A dual larynx motor networks hypothesis. Philos. Trans. R. Soc. B Biol. Sci. 376, 20200392. https://doi.org/10.1098/rstb.2020.0392

Benabid, A.L., 2003. Deep brain stimulation for Parkinson's disease. Curr. Opin. Neurobiol. 13, 696–706. https://doi.org/10.1016/j.conb.2003.11.001

Berger, C., Bauer, M., Wittig, H., Scheurer, E., Lenz, C., 2022. Post mortem brain temperature and its influence on quantitative MRI of the brain. Magma N. Y. N 35, 375–387. https://doi.org/10.1007/s10334-021-00971-8

Bigun, J., Bigun, T., Nilsson, K., 2004. Recognition by symmetry derivatives and the generalized structure tensor. IEEE Trans. Pattern Anal. Mach. Intell. 26, 1590–1605. https://doi.org/10.1109/TPAMI.2004.126

Bihan, D.L., 2007. The 'wet mind': water and functional neuroimaging. Phys. Med. Biol. 52, R57–R90. https://doi.org/10.1088/0031-9155/52/7/R02

Block, K.T., Uecker, M., Frahm, J., 2007. Undersampled radial MRI with multiple coils. Iterative image reconstruction using a total variation constraint. Magn. Reson. Med. 57, 1086–1098. https://doi.org/10.1002/mrm.21236

Brown, R., 1828. XXVII. *A brief account of microscopical observations made in the months of June, July and August* 1827, *on the particles contained in the pollen of plants; and on the general existence of active molecules in organic and inorganic bodies*. Philos. Mag. 4, 161–173. https://doi.org/10.1080/14786442808674769

Budde, M.D., Annese, J., 2013. Quantification of anisotropy and fiber orientation in human brain histological sections. Front. Integr. Neurosci. 7, 3. https://doi.org/10.3389/fnint.2013.00003

Budde, M.D., Frank, J.A., 2012a. Examining brain microstructure using structure tensor analysis of histological sections. NeuroImage 63, 1–10. https://doi.org/10.1016/j.neuroimage.2012.06.042

Budde, M.D., Frank, J.A., 2012b. Examining brain microstructure using structure tensor analysis of histological sections. NeuroImage 63, 1–10. https://doi.org/10.1016/j.neuroimage.2012.06.042

Calabrese, E., 2016. Diffusion Tractography in Deep Brain Stimulation Surgery: A Review. Front. Neuroanat. 10. https://doi.org/10.3389/fnana.2016.00045

Calamante, F., Tournier, J.-D., Jackson, G.D., Connelly, A., 2010. Track-density imaging (TDI): Super-resolution white matter imaging using whole-brain track-density mapping. NeuroImage 53, 1233–1243. https://doi.org/10.1016/j.neuroimage.2010.07.024

Caminiti, R., Girard, G., Battaglia-Mayer, A., Borra, E., Schito, A., Innocenti, G.M., Luppino, G., 2021. The Complex Hodological Architecture of the Macaque Dorsal Intraparietal Areas as Emerging from Neural Tracers and DW-MRI Tractography. eneuro 8, ENEURO.0102-21.2021. https://doi.org/10.1523/ENEURO.0102-21.2021

Chad J. Donahue, Stamatios N. Sotiropoulos, Saad Jbabdi, Moises Hernandez-Fernandez, Timothy E. Behrens, Tim B. Dyrby, Timothy Coalson, Henry Kennedy, Kenneth Knoblauch, David C. Van Essen, Matthew F. Glasser, 2016. Using Diffusion Tractography to Predict Cortical Connection Strength and Distance: A Quantitative

Comparison with Tracers in the Monkey. J. Neurosci. 36, 6758. https://doi.org/10.1523/JNEUROSCI.0493-16.2016

Chamberland, M., Tax, C.M.W., Jones, D.K., 2018. Meyer's loop tractography for image-guided surgery depends on imaging protocol and hardware. NeuroImage Clin. 20, 458–465. https://doi.org/10.1016/j.nicl.2018.08.021

Chen, Y., Xie, Y., Zhou, Z., Shi, F., Christodoulou, A.G., Li, D., 2018. Brain MRI super resolution using 3D deep densely connected neural networks, in: 2018 IEEE 15th International Symposium on Biomedical Imaging (ISBI 2018). Presented at the 2018 IEEE 15th International Symposium on Biomedical Imaging (ISBI 2018), IEEE, Washington, DC, pp. 739–742. https://doi.org/10.1109/ISBI.2018.8363679

Cheng, B., Liu, M., Zhang, D., Munsell, B.C., Shen, D., 2015. Domain Transfer Learning for MCI Conversion Prediction. IEEE Trans. Biomed. Eng. 62, 1805–1817. https://doi.org/10.1109/TBME.2015.2404809

Chi, J.G., Dooling, E.C., Gilles, F.H., 1977. Gyral development of the human brain. Ann. Neurol. 1, 86–93. https://doi.org/10.1002/ana.410010109

Choe, A.S., Stepniewska, I., Colvin, D.C., Ding, Z., Anderson, A.W., 2012. Validation of diffusion tensor MRI in the central nervous system using light microscopy: quantitative comparison of fiber properties. NMR Biomed. 25, 900–908. https://doi.org/10.1002/nbm.1810

Cicimen, A.G., Tregidgo, H.F.J., Figini, M., Messaritaki, E., McNabb, C.B., Palombo, M., Evans, C.J., Cercignani, M., Jones, D.K., Alexander, D.C., 2024. Image Quality Transfer of Diffusion MRI Guided By High-Resolution Structural MRI. https://doi.org/10.48550/ARXIV.2408.03216

Côté, M.-A., Girard, G., Boré, A., Garyfallidis, E., Houde, J.-C., Descoteaux, M., 2013. Tractometer: Towards validation of tractography pipelines. Med. Image Anal. 17, 844–857. https://doi.org/10.1016/j.media.2013.03.009

Cottaar, M., Bastiani, M., Boddu, N., Glasser, M.F., Haber, S., van Essen, D.C., Sotiropoulos, S.N., Jbabdi, S., 2021. Modelling white matter in gyral blades as a continuous vector field. NeuroImage 227, 117693. https://doi.org/10.1016/j.neuroimage.2020.117693

Dale, A.M., Fischl, B., Sereno, M.I., 1999. Cortical Surface-Based Analysis: I. Segmentation and Surface Reconstruction. NeuroImage 9, 179–194. https://doi.org/10.1006/nimg.1998.0395

D'Arceuil, H.E., Westmoreland, S., De Crespigny, A.J., 2007. An approach to high resolution diffusion tensor imaging in fixed primate brain. NeuroImage 35, 553–565. https://doi.org/10.1016/j.neuroimage.2006.12.028

Das Balken-System oder die Hirnschenkel-Organisation im großen Gehirn., 1809. . Arch. Für Physiol.

Delettre, C., Messé, A., Dell, L.-A., Foubet, O., Heuer, K., Larrat, B., Meriaux, S., Mangin, J.-F., Reillo, I., De Juan Romero, C., Borrell, V., Toro, R., Hilgetag, C.C., 2019. Comparison between diffusion MRI tractography and histological tract-tracing of cortico-cortical structural connectivity in the ferret brain. Netw. Neurosci. 3, 1038–1050. https://doi.org/10.1162/netn_a_00098

Dell'Acqua, F., 2024. Handbook of Diffusion MR Tractography: Imaging Methods, Biophysical Models, Algorithms and Applications, 1st ed. ed. Elsevier Science & Technology, Chantilly.

Dell'Acqua, F., Rizzo, G., Scifo, P., Clarke, R.A., Scotti, G., Fazio, F., 2007. A Model-Based Deconvolution Approach to Solve Fiber Crossing in Diffusion-Weighted MR Imaging. IEEE Trans. Biomed. Eng. 54, 462–472. https://doi.org/10.1109/TBME.2006.888830

Dell'Acqua, F., Simmons, A., Williams, S.C.R., Catani, M., 2013. Can spherical deconvolution provide more information than fiber orientations? Hindrance modulated orientational anisotropy, a true-tract specific index to characterize white matter diffusion: Hindrance Modulated Orientational Anisotropy. Hum. Brain Mapp. 34, 2464–2483. https://doi.org/10.1002/hbm.22080

Dell'Acqua, F., Tournier, J. -Donald, 2019. Modelling white matter with spherical deconvolution: How and why? NMR Biomed. 32, e3945. https://doi.org/10.1002/nbm.3945

Deng, Y., Hung, K.S.Y., Lui, S.S.Y., Chui, W.W.H., Lee, J.C.W., Wang, Y., Li, Z., Mak, H.K.F., Sham, P.C., Chan, R.C.K., Cheung, E.F.C., 2019. Tractography-based classification in distinguishing patients with first-episode schizophrenia from healthy individuals. Prog. Neuropsychopharmacol. Biol. Psychiatry 88, 66–73. https://doi.org/10.1016/j.pnpbp.2018.06.010

Denk, W., Horstmann, H., 2004. Serial Block-Face Scanning Electron Microscopy to Reconstruct Three-Dimensional Tissue Nanostructure. PLOS Biol. 2, null. https://doi.org/10.1371/journal.pbio.0020329

Deutsch, G.K., Dougherty, R.F., Bammer, R., Siok, W.T., Gabrieli, J.D.E., Wandell, B., 2005. Children's Reading Performance is Correlated with White Matter Structure Measured by Diffusion Tensor Imaging. Cortex 41, 354–363. https://doi.org/10.1016/S0010-9452(08)70272-7

Dhollander, T., Clemente, A., Singh, M., Boonstra, F., Civier, O., Duque, J.D., Egorova, N., Enticott, P., Fuelscher, I., Gajamange, S., Genc, S., Gottlieb, E., Hyde, C., Imms, P., Kelly, C., Kirkovski, M., Kolbe, S., Liang, X., Malhotra, A., Mito, R., Poudel, G., Silk, T.J., Vaughan, D.N., Zanin, J., Raffelt, D., Caeyenberghs, K., 2021. Fixel-based Analysis of Diffusion MRI: Methods, Applications, Challenges and Opportunities. NeuroImage 241, 118417. https://doi.org/10.1016/j.neuroimage.2021.118417

Dhollander, T., Mito, R., Raffelt, D., Connelly, A., 2019. Improved white matter response function estimation for 3-tissue constrained spherical deconvolution.

Dhollander, T., Raffelt, D., Connelly, A., 2016. Unsupervised 3-tissue response function estimation from single-shell or multi-shell diffusion MR data without a co-registered T1 image.

Dinsdale, N.K., Jenkinson, M., Namburete, A.I.L., 2021. Deep learning-based unlearning of dataset bias for MRI harmonisation and confound removal. NeuroImage 228, 117689. https://doi.org/10.1016/j.neuroimage.2020.117689

Dohmen, M., Menzel, M., Wiese, H., Reckfort, J., Hanke, F., Pietrzyk, U., Zilles, K., Amunts, K., Axer, M., 2015. Understanding fiber mixture by simulation in 3D Polarized Light Imaging. NeuroImage 111, 464–475. https://doi.org/10.1016/j.neuroimage.2015.02.020

Donahue, C.J., Sotiropoulos, S.N., Jbabdi, S., Hernandez-Fernandez, M., Behrens, T.E., Dyrby, T.B., Coalson, T., Kennedy, H., Knoblauch, K., Van Essen, D.C., Glasser, M.F., 2016. Using Diffusion Tractography to Predict Cortical Connection Strength and Distance: A Quantitative Comparison with Tracers in the Monkey. J. Neurosci. 36, 6758–6770. https://doi.org/10.1523/JNEUROSCI.0493-16.2016

Dyer, E.L., Roncal, W.G., Prasad, J.A., Fernandes, H.L., Gürsoy, D., Andrade, V.D., Fezzaa, K., Xiao, X., Vogelstein, J.T., Jacobsen, C., Körding, K.P., Kasthuri, N., 2017. Quantifying Mesoscale Neuroanatomy Using X-Ray Microtomography. eNeuro 4. https://doi.org/10.1523/ENEURO.0195-17.2017

Dyrby, T.B., Søgaard, L.V., Parker, G.J., Alexander, D.C., Lind, N.M., Baaré, W.F.C., Hay-Schmidt, A., Eriksen, N., Pakkenberg, B., Paulson, O.B., Jelsing, J., 2007. Validation

of in vitro probabilistic tractography. NeuroImage 37, 1267–1277. https://doi.org/10.1016/j.neuroimage.2007.06.022

Edgar, J.M., Griffiths, I.R., 2009. Chapter 5 - White Matter Structure: A Microscopist's View, in: Johansen-Berg, H., Behrens, T.E.J. (Eds.), Diffusion MRI. Academic Press, San Diego, pp. 74–103. https://doi.org/10.1016/B978-0-12-374709-9.00005-5

Eichner, C., Paquette, M., Müller-Axt, C., Bock, C., Budinger, E., Gräßle, T., Jäger, C., Kirilina, E., Lipp, I., EBC Consortium, Data Analysis and Writing, Brain Extraction, Møller, T., Olofsson-Sannö, K., Morawski, M., Rusch, H., Wenk, P., Weiskopf, N., Wittig, R.M., Crockford, C., Friederici, A.D., Anwander, A., 2024. Detailed mapping of the complex fiber structure and white matter pathways of the chimpanzee brain. Nat. Methods 21, 1122–1130. https://doi.org/10.1038/s41592-024-02270-1

Eickhoff, S.B., Yeo, B.T.T., Genon, S., 2018. Imaging-based parcellations of the human brain. Nat. Rev. Neurosci. 19, 672–686. https://doi.org/10.1038/s41583-018-0071-7

Einstein, A., 1905. On the motion required by the molecular kinetic theory of heat of small particles suspended in a stationary liquid. Ann. Phys. 17, 549.

Essen, D.C.V., Smith, S.M., Barch, D.M., Behrens, T.E.J., Yacoub, E., Ugurbil, K., 2013. The WU-Minn Human Connectome Project: An overview. NeuroImage 80, 62–79. https://doi.org/10.1016/j.neuroimage.2013.05.041

Felleman, D.J., Van Essen, D.C., 1991. Distributed hierarchical processing in the primate cerebral cortex. Cereb. Cortex N. Y. N 1991 1, 1–47. https://doi.org/10.1093/cercor/1.1.1-a

Fillard, P., Descoteaux, M., Goh, A., Gouttard, S., Jeurissen, B., Malcolm, J., Ramirez-Manzanares, A., Reisert, M., Sakaie, K., Tensaouti, F., Yo, T., Mangin, J.-F., Poupon, C., 2011. Quantitative evaluation of 10 tractography algorithms on a realistic diffusion MR phantom. NeuroImage 56, 220–234. https://doi.org/10.1016/j.neuroimage.2011.01.032

Filley, C.M., Fields, R.D., 2016. White matter and cognition: making the connection. J. Neurophysiol. 116, 2093–2104. https://doi.org/10.1152/jn.00221.2016

Fischl, B., 2012. FreeSurfer. 20 YEARS FMRI 62, 774–781. https://doi.org/10.1016/j.neuroimage.2012.01.021

Fischl, B., Sereno, M.I., Dale, A.M., 1999. Cortical Surface-Based Analysis: II: Inflation, Flattening, and a Surface-Based Coordinate System. NeuroImage 9, 195–207. https://doi.org/10.1006/nimg.1998.0396

Friedrich, P., Forkel, S.J., Amiez, C., Balsters, J.H., Coulon, O., Fan, L., Goulas, A., Hadj-Bouziane, F., Hecht, E.E., Heuer, K., Jiang, T., Latzman, R.D., Liu, X., Loh, K.K., Patil, K.R., Lopez-Persem, A., Procyk, E., Sallet, J., Toro, R., Vickery, S., Weis, S., Wilson, C.R.E., Xu, T., Zerbi, V., Eickoff, S.B., Margulies, D.S., Mars, R.B., Thiebaut De Schotten, M., 2021. Imaging evolution of the primate brain: the next frontier? NeuroImage 228, 117685. https://doi.org/10.1016/j.neuroimage.2020.117685

Gahm, J.K., Shi, Y., 2019. Surface-based Tracking of U-fibers in the Superficial White Matter. Med. Image Comput. Comput.-Assist. Interv. MICCAI Int. Conf. Med. Image Comput. Comput.-Assist. Interv. 11766, 538–546.

Gallyas, F., 1971. Silver staining of Alzheimer's neurofibrillary changes by means of physical development. Acta Morphol. Acad. Sci. Hung. 19, 1–8.

Ganin, Y., Ustinova, E., Ajakan, H., Germain, P., Larochelle, H., Laviolette, F., Marchand, M., Lempitsky, V., 2017. Domain-Adversarial Training of Neural Networks, in: Csurka, G. (Ed.), Domain Adaptation in Computer Vision Applications. Springer International Publishing, Cham, pp. 189–209. https://doi.org/10.1007/978-3-319-58347-1_10

Garman, R.H., 2011. Histology of the Central Nervous System. Toxicol. Pathol. 39, 22–35. https://doi.org/10.1177/0192623310389621

Georgiadis, M., Menzel, M., Reuter, J.A., Born, D.E., Kovacevich, S.R., Alvarez, D., Taghavi, H.M., Schroeter, A., Rudin, M., Gao, Z., Guizar-Sicairos, M., Weiss, T.M., Axer, M., Rajkovic, I., Zeineh, M.M., 2023. Imaging crossing fibers in mouse, pig, monkey, and human brain using small-angle X-ray scattering. Acta Biomater. 164, 317–331. https://doi.org/10.1016/j.actbio.2023.04.029

Georgiadis, M., Schroeter, A., Gao, Z., Guizar-Sicairos, M., Novikov, D.S., Fieremans, E., Rudin, M., 2020. Retrieving neuronal orientations using 3D scanning SAXS and comparison with diffusion MRI. NeuroImage 204, 116214. https://doi.org/10.1016/j.neuroimage.2019.116214

Gersing, A.S., Cervantes, B., Knebel, C., Schwaiger, B.J., Kirschke, J.S., Weidlich, D., Claudi, C., Peeters, J.M., Pfeiffer, D., Rummeny, E.J., Karampinos, D.C., Woertler, K., 2020. Diffusion tensor imaging and tractography for preoperative assessment of benign peripheral nerve sheath tumors. Eur. J. Radiol. 129, 109110. https://doi.org/10.1016/j.ejrad.2020.109110

Girard, G., Aydogan, D.B., Dell'Acqua, F., Leemans, A., Descoteaux, M., Sotiropoulos, S.N., 2025. Chapter 14 - Probabilistic tractography, in: Dell'Acqua, F., Descoteaux, M., Leemans, A. (Eds.), Handbook of Diffusion MR Tractography. Academic Press, pp. 257–274. https://doi.org/10.1016/B978-0-12-818894-1.00030-6

Girard, G., Caminiti, R., Battaglia-Mayer, A., St-Onge, E., Ambrosen, K.S., Eskildsen, S.F., Krug, K., Dyrby, T.B., Descoteaux, M., Thiran, J.-P., Innocenti, G.M., 2020. On the cortical connectivity in the macaque brain: A comparison of diffusion tractography and histological tracing data. NeuroImage 221, 117201. https://doi.org/10.1016/j.neuroimage.2020.117201

Girard, G., Daducci, A., Petit, L., Thiran, J.-P., Whittingstall, K., Deriche, R., Wassermann, D., Descoteaux, M., 2017. AxTract: Toward microstructure informed tractography. Hum. Brain Mapp. 38, 5485–5500. https://doi.org/10.1002/hbm.23741

Glickstein, M., 2006. Golgi and Cajal: The neuron doctrine and the 100th anniversary of the 1906 Nobel Prize. Curr. Biol. 16, R147–R151. https://doi.org/10.1016/j.cub.2006.02.053

Goubran, M., Leuze, C., Hsueh, B., Aswendt, M., Ye, L., Tian, Q., Cheng, M.Y., Crow, A., Steinberg, G.K., McNab, J.A., Deisseroth, K., Zeineh, M., 2019. Multimodal image registration and connectivity analysis for integration of connectomic data from microscopy to MRI. Nat. Commun. 10, 5504. https://doi.org/10.1038/s41467-019-13374-0

Gray, E.G., 1969. Electron Microscopy of Excitatory and Inhibitory Synapses: A Brief Review, in: Akert, K., Waser, P.G. (Eds.), Mechanisms of Synaptic Transmission, Progress in Brain Research. Elsevier, pp. 141–155. https://doi.org/10.1016/S0079-6123(08)63235-5

Greenspan, H., Oz, G., Kiryati, N., Peled, S., 2002. MRI inter-slice reconstruction using super-resolution. Magn. Reson. Imaging 20, 437–446. https://doi.org/10.1016/S0730-725X(02)00511-8

Guan, H., Liu, M., 2022. Domain Adaptation for Medical Image Analysis: A Survey. IEEE Trans. Biomed. Eng. 69, 1173–1185. https://doi.org/10.1109/TBME.2021.3117407

Guerreiro, J., Tomás, P., Garcia, N., Aidos, H., 2023. Super-resolution of magnetic resonance images using Generative Adversarial Networks. Comput. Med. Imaging Graph. 108, 102280. https://doi.org/10.1016/j.compmedimag.2023.102280

Guevara, M., Guevara, P., Román, C., Mangin, J.-F., 2020. Superficial white matter: A review on the dMRI analysis methods and applications. NeuroImage 212, 116673. https://doi.org/10.1016/j.neuroimage.2020.116673

Guo, Z., Zheng, Y., Zhang, Y., 2022. CLARITY techniques based tissue clearing: types and differences. Folia Morphol. 81, 1–12. https://doi.org/10.5603/FM.a2021.0012

Haber, S.N., Lynd-Balta, E., Mitchell, S.J., 1993. The organization of the descending ventral pallidal projections in the monkey. J. Comp. Neurol. 329, 111–128. https://doi.org/10.1002/cne.903290108

Haines, D.E., Mihailoff, G.A., 2018. Fundamental neuroscience for basic and clinical applications, 5th ed. ed. Elsevier, Philadelphia.

Hansen, J.Y., Shafiei, G., Markello, R.D., Smart, K., Cox, S.M.L., Nørgaard, M., Beliveau, V., Wu, Y., Gallezot, J.-D., Aumont, É., Servaes, S., Scala, S.G., DuBois, J.M., Wainstein, G., Bezgin, G., Funck, T., Schmitz, T.W., Spreng, R.N., Galovic, M., Koepp, M.J., Duncan, J.S., Coles, J.P., Fryer, T.D., Aigbirhio, F.I., McGinnity, C.J., Hammers, A., Soucy, J.-P., Baillet, S., Guimond, S., Hietala, J., Bedard, M.-A., Leyton, M., Kobayashi, E., Rosa-Neto, P., Ganz, M., Knudsen, G.M., Palomero-Gallagher, N., Shine, J.M., Carson, R.E., Tuominen, L., Dagher, A., Misic, B., 2022. Mapping neurotransmitter systems to the structural and functional organization of the human neocortex. Nat. Neurosci. 25, 1569–1581. https://doi.org/10.1038/s41593-022-01186-3

Hartig, R., Glen, D., Jung, B., Logothetis, N.K., Paxinos, G., Garza-Villarreal, E.A., Messinger, A., Evrard, H.C., 2021. The Subcortical Atlas of the Rhesus Macaque (SARM) for neuroimaging. NeuroImage 235, 117996. https://doi.org/10.1016/j.neuroimage.2021.117996

Hedges, V., 2022. Introduction to Neuroscience, Open textbook library. Michigan State University, Place of publication not identified.

Henssen, D.J.H.A., Mollink, J., Kurt, E., Van Dongen, R., Bartels, R.H.M.A., Gräβel, D., Kozicz, T., Axer, M., Van Cappellen Van Walsum, A.-M., 2019. Ex vivo visualization of the trigeminal pathways in the human brainstem using 11.7T diffusion MRI combined with microscopy polarized light imaging. Brain Struct. Funct. 224, 159–170. https://doi.org/10.1007/s00429-018-1767-1

Hermundstad, A.M., Bassett, D.S., Brown, K.S., Aminoff, E.M., Clewett, D., Freeman, S., Frithsen, A., Johnson, A., Tipper, C.M., Miller, M.B., Grafton, S.T., Carlson, J.M., 2013. Structural foundations of resting-state and task-based functional connectivity in the human brain. Proc. Natl. Acad. Sci. 110, 6169–6174. https://doi.org/10.1073/pnas.1219562110

Honey, C.J., Sporns, O., Cammoun, L., Gigandet, X., Thiran, J.P., Meuli, R., Hagmann, P., 2009. Predicting human resting-state functional connectivity from structural connectivity. Proc. Natl. Acad. Sci. 106, 2035–2040. https://doi.org/10.1073/pnas.0811168106

Howard, A., 2020. Microstructure imaging with diffusion MRI and microscopy.

Howard, A.F.D., Huszar, I.N., Smart, A., Cottaar, M., Daubney, G., Hanayik, T., Khrapitchev, A.A., Mars, R.B., Mollink, J., Scott, C., Sibson, N.R., Sallet, J., Jbabdi, S., Miller, K.L., 2023. An open resource combining multi-contrast MRI and microscopy in the macaque brain. Nat. Commun. 14, 4320. https://doi.org/10.1038/s41467-023-39916-1

Howard, A.FD., Mollink, J., Kleinnijenhuis, M., Pallebage-Gamarallage, M., Bastiani, M., Cottaar, M., Miller, K.L., Jbabdi, S., 2019. Joint modelling of diffusion MRI and microscopy. NeuroImage 201, 116014. https://doi.org/10.1016/j.neuroimage.2019.116014

Huszar, I., Pallebage-Gamarallage, M., Bangerter-Christensen, S., Brooks, H., Fitzgibbon, S., Foxley, S., Hiemstra, M., Howard, A.F.D., Jbabdi, S., Kor, D.Z.L., Leonte, A., Mollink, J., Smart, A., Tendler, B.C., Turner, M.R., Ansorge, O., Miller, K.L., Jenkinson, M., 2023a. Tensor image registration library: Deformable registration of stand-alone histology images to whole-brain post-mortem MRI data. NeuroImage 265, 119792. https://doi.org/10.1016/j.neuroimage.2022.119792

Huszar, I., Smart, A., Jenkinson, M., Howard, A.FD., Miller, K., 2022. Deformable Registration of Serial Micrographs to Post-Mortem MRI in the BigMac Dataset Using TIRL, in: ISMRM 30th Annual Meeting. Presented at the The International Society for Magnetic Resonance in Medicine, London.

Huszar, I., Zhu, S., Smart, A., Jbabdi, S., Miller, K., Howard, A., 2023b. The joint registration of multiple microscopy contrasts to MRI in the BigMac dataset, in: ISMRM 31th Annual Meeting. Presented at the The International Society for Magnetic Resonance in Medicine, Toronto.

Jbabdi, S., Sotiropoulos, S.N., Haber, S.N., Van Essen, D.C., Behrens, T.E., 2015. Measuring macroscopic brain connections in vivo. Nat. Neurosci. 18, 1546–1555. https://doi.org/10.1038/nn.4134

Jenkinson, M., Bannister, P., Brady, M., Smith, S., 2002. Improved Optimization for the Robust and Accurate Linear Registration and Motion Correction of Brain Images. NeuroImage 17, 825–841. https://doi.org/10.1006/nimg.2002.1132

Jenkinson, M., Beckmann, C.F., Behrens, T.E.J., Woolrich, M.W., Smith, S.M., 2012. FSL. NeuroImage 62, 782–790. https://doi.org/10.1016/j.neuroimage.2011.09.015

Jenkinson, M., Smith, S., 2001. A global optimisation method for robust affine registration of brain images. Med. Image Anal. 5, 143–156. https://doi.org/10.1016/S1361-8415(01)00036-6

Jespersen, S.N., Kroenke, C.D., Østergaard, L., Ackerman, J.J.H., Yablonskiy, D.A., 2007. Modeling dendrite density from magnetic resonance diffusion measurements. NeuroImage 34, 1473–1486. https://doi.org/10.1016/j.neuroimage.2006.10.037

Jeurissen, B., Tournier, J.-D., Dhollander, T., Connelly, A., Sijbers, J., 2014. Multi-tissue constrained spherical deconvolution for improved analysis of multi-shell diffusion MRI data. NeuroImage 103, 411–426. https://doi.org/10.1016/j.neuroimage.2014.07.061

Johansen-Berg, H., Behrens, T.E.J., 2014. Diffusion MRI: from quantitative measurement to in-vivo neuroanatomy, 2nd ed. ed. Elsevier Science, Amsterdam.

Johnson, G.A., Tian, Y., Ashbrook, D.G., Cofer, G.P., Cook, J.J., Gee, J.C., Hall, A., Hornburg, K., Kaczorowski, C.C., Qi, Y., Yeh, F.-C., Wang, N., White, L.E., Williams, R.W., 2023. Merged magnetic resonance and light sheet microscopy of the whole mouse brain. Proc. Natl. Acad. Sci. 120, e2218617120. https://doi.org/10.1073/pnas.2218617120

Jones, R., Grisot, G., Augustinack, J., Magnain, C., Boas, D.A., Fischl, B., Wang, H., Yendiki, A., 2020. Insight into the fundamental trade-offs of diffusion MRI from polarization-sensitive optical coherence tomography in ex vivo human brain. NeuroImage 214, 116704. https://doi.org/10.1016/j.neuroimage.2020.116704

Kádár, A., Wittmann, G., Liposits, Z., Fekete, C., 2009. Improved method for combination of immunocytochemistry and Nissl staining. J. Neurosci. Methods 184, 115–118. https://doi.org/10.1016/j.jneumeth.2009.07.010

Kamagata, K., Andica, C., Kato, A., Saito, Y., Uchida, W., Hatano, T., Lukies, M., Ogawa, T., Takeshige-Amano, H., Akashi, T., Hagiwara, A., Fujita, S., Aoki, S., 2021. Diffusion Magnetic Resonance Imaging-Based Biomarkers for Neurodegenerative Diseases. Int. J. Mol. Sci. 22, 5216. https://doi.org/10.3390/ijms22105216

Karamov, R., Martulli, L.M., Kerschbaum, M., Sergeichev, I., Swolfs, Y., Lomov, S.V., 2020. Micro-CT based structure tensor analysis of fibre orientation in random fibre composites versus high-fidelity fibre identification methods. Compos. Struct. 235, 111818. https://doi.org/10.1016/j.compstruct.2019.111818

Karimi, D., Vasung, L., Jaimes, C., Machado-Rivas, F., Warfield, S.K., Gholipour, A., 2021. Learning to estimate the fiber orientation distribution function from diffusion-weighted MRI. NeuroImage 239, 118316. https://doi.org/10.1016/j.neuroimage.2021.118316

Kirilina, E., Helbling, S., Morawski, M., Pine, K., Reimann, K., Jankuhn, S., Dinse, J., Deistung, A., Reichenbach, J.R., Trampel, R., Geyer, S., Müller, L., Jakubowski, N., Arendt, T., Bazin, P.-L., Weiskopf, N., 2020. Superficial white matter imaging: Contrast mechanisms and whole-brain in vivo mapping. Sci. Adv. 6, eaaz9281. https://doi.org/10.1126/sciadv.aaz9281

Klingler, J., 1935. Erleichterung der makrokopischen Präparation des Gehirns durch den Gefrierprozess.

Knickmeyer, R.C., Gouttard, S., Kang, C., Evans, D., Wilber, K., Smith, J.K., Hamer, R.M., Lin, W., Gerig, G., Gilmore, J.H., 2008. A Structural MRI Study of Human Brain Development from Birth to 2 Years. J. Neurosci. 28, 12176–12182. https://doi.org/10.1523/JNEUROSCI.3479-08.2008

Konstantopoulos, K., Giakoumettis, D., 2023. Chapter 1 - Basic knowledge on neuroanatomy and neurophysiology of the central nervous system, in: Konstantopoulos, K., Giakoumettis, D. (Eds.), Neuroimaging in Neurogenic Communication Disorders. Academic Press, pp. 1–30. https://doi.org/10.1016/B978-0-12-823875-2.00004-9

Kreilkamp, B.A.K., Weber, B., Richardson, M.P., Keller, S.S., 2017. Automated tractography in patients with temporal lobe epilepsy using TRActs Constrained by UnderLying Anatomy (TRACULA). NeuroImage Clin. 14, 67–76. https://doi.org/10.1016/j.nicl.2017.01.003

Kretschmann, H.J., 1988. Localisation of the corticospinal fibres in the internal capsule in man. J. Anat. 160, 219–225.

Kuan, L., Li, Y., Lau, C., Feng, D., Bernard, A., Sunkin, S.M., Zeng, H., Dang, C., Hawrylycz, M., Ng, L., 2015. Neuroinformatics of the Allen Mouse Brain Connectivity Atlas. Methods 73, 4–17. https://doi.org/10.1016/j.ymeth.2014.12.013

Larsen, L., Griffin, L.D., GRäßel, D., Witte, O.W., Axer, H., 2007. Polarized light imaging of white matter architecture. Microsc. Res. Tech. 70, 851–863. https://doi.org/10.1002/jemt.20488

Le Bihan, D., Johansen-Berg, H., 2012. Diffusion MRI at 25: exploring brain tissue structure and function. NeuroImage 61, 324–341. https://doi.org/10.1016/j.neuroimage.2011.11.006

LeCun, Y., Bengio, Y., Hinton, G., 2015. Deep learning. Nature 521, 436–444. https://doi.org/10.1038/nature14539

Lee, M.H., Smyser, C.D., Shimony, J.S., 2013. Resting-state fMRI: a review of methods and clinical applications. AJNR Am. J. Neuroradiol. 34, 1866–1872. https://doi.org/10.3174/ajnr.A3263

Lein, E.S., Hawrylycz, M.J., Ao, N., Ayres, M., Bensinger, A., Bernard, A., Boe, A.F., Boguski, M.S., Brockway, K.S., Byrnes, E.J., Chen, Lin, Chen, Li, Chen, T.-M., Chi Chin, M., Chong, J., Crook, B.E., Czaplinska, A., Dang, C.N., Datta, S., Dee, N.R., Desaki, A.L., Desta, T., Diep, E., Dolbeare, T.A., Donelan, M.J., Dong, H.-W., Dougherty, J.G., Duncan, B.J., Ebbert, A.J., Eichele, G., Estin, L.K., Faber, C., Facer, B.A., Fields, R., Fischer, S.R., Fliss, T.P., Frensley, C., Gates, S.N., Glattfelder, K.J., Halverson, K.R., Hart, M.R., Hohmann, J.G., Howell, M.P., Jeung, D.P., Johnson,

R.A., Karr, P.T., Kawal, R., Kidney, J.M., Knapik, R.H., Kuan, C.L., Lake, J.H., Laramee, A.R., Larsen, K.D., Lau, C., Lemon, T.A., Liang, A.J., Liu, Y., Luong, L.T., Michaels, J., Morgan, J.J., Morgan, R.J., Mortrud, M.T., Mosqueda, N.F., Ng, L.L., Ng, R., Orta, G.J., Overly, C.C., Pak, T.H., Parry, S.E., Pathak, S.D., Pearson, O.C., Puchalski, R.B., Riley, Z.L., Rockett, H.R., Rowland, S.A., Royall, J.J., Ruiz, M.J., Sarno, N.R., Schaffnit, K., Shapovalova, N.V., Sivisay, T., Slaughterbeck, C.R., Smith, S.C., Smith, K.A., Smith, B.I., Sodt, A.J., Stewart, N.N., Stumpf, K.-R., Sunkin, S.M., Sutram, M., Tam, A., Teemer, C.D., Thaller, C., Thompson, C.L., Varnam, L.R., Visel, A., Whitlock, R.M., Wohnoutka, P.E., Wolkey, C.K., Wong, V.Y., Wood, M., Yaylaoglu, M.B., Young, R.C., Youngstrom, B.L., Feng Yuan, X., Zhang, B., Zwingman, T.A., Jones, A.R., 2007. Genome-wide atlas of gene expression in the adult mouse brain. Nature 445, 168–176. https://doi.org/10.1038/nature05453

Liang, Z., Arefin, T.M., Lee, C.H., Zhang, J., 2023. Using mesoscopic tract-tracing data to guide the estimation of fiber orientation distributions in the mouse brain from diffusion MRI. NeuroImage 270, 119999. https://doi.org/10.1016/j.neuroimage.2023.119999

Liang, Z., Zhang, J., 2023. Mouse brain MR super-resolution using a deep learning network trained with optical imaging data. Front. Radiol. 3, 1155866. https://doi.org/10.3389/fradi.2023.1155866

Liu, X., Yoo, C., Xing, F., Oh, H., Fakhri, G.E., Kang, J.-W., Woo, J., 2022. Deep Unsupervised Domain Adaptation: A Review of Recent Advances and Perspectives. https://doi.org/10.48550/ARXIV.2208.07422

Lucena, O., Vos, S.B., Vakharia, V., Duncan, J., Ashkan, K., Sparks, R., Ourselin, S., 2021. Enhancing the estimation of fiber orientation distributions using convolutional neural networks. Comput. Biol. Med. 135, 104643. https://doi.org/10.1016/j.compbiomed.2021.104643

Lyons, M.K., 2011. Deep brain stimulation: current and future clinical applications. Mayo Clin. Proc. 86, 662–672. https://doi.org/10.4065/mcp.2011.0045

Maaten, L. van der, Hinton, G., 2008. Visualizing Data using t-SNE. J. Mach. Learn. Res. 9, 2579–2605.

Maffei, C., Girard, G., Schilling, K.G., Aydogan, D.B., Adluru, N., Zhylka, A., Wu, Y., Mancini, M., Hamamci, A., Sarica, A., Teillac, A., Baete, S.H., Karimi, D., Yeh, F.-C., Yildiz, M.E., Gholipour, A., Bihan-Poudec, Y., Hiba, B., Quattrone, Andrea, Quattrone, Aldo, Boshkovski, T., Stikov, N., Yap, P.-T., de Luca, A., Pluim, J., Leemans, A., Prabhakaran, V., Bendlin, B.B., Alexander, A.L., Landman, B.A., Canales-Rodríguez, E.J., Barakovic, M., Rafael-Patino, J., Yu, T., Rensonnet, G., Schiavi, S., Daducci, A., Pizzolato, M., Fischi-Gomez, E., Thiran, J.-P., Dai, G., Grisot, G., Lazovski, N., Puch, S., Ramos, M., Rodrigues, P., Prčkovska, V., Jones, R., Lehman, J., Haber, S.N., Yendiki, A., 2022a. Insights from the IronTract challenge: Optimal methods for mapping brain pathways from multi-shell diffusion MRI. NeuroImage 257, 119327. https://doi.org/10.1016/j.neuroimage.2022.119327

Maffei, C., Girard, G., Schilling, K.G., Aydogan, D.B., Adluru, N., Zhylka, A., Wu, Y., Mancini, M., Hamamci, A., Sarica, A., Teillac, A., Baete, S.H., Karimi, D., Yeh, F.-C., Yildiz, M.E., Gholipour, A., Bihan-Poudec, Y., Hiba, B., Quattrone, Andrea, Quattrone, Aldo, Boshkovski, T., Stikov, N., Yap, P.-T., de Luca, A., Pluim, J., Leemans, A., Prabhakaran, V., Bendlin, B.B., Alexander, A.L., Landman, B.A., Canales-Rodríguez, E.J., Barakovic, M., Rafael-Patino, J., Yu, T., Rensonnet, G., Schiavi, S., Daducci, A., Pizzolato, M., Fischi-Gomez, E., Thiran, J.-P., Dai, G., Grisot, G., Lazovski, N., Puch, S., Ramos, M., Rodrigues, P., Prčkovska, V., Jones,

R., Lehman, J., Haber, S.N., Yendiki, A., 2022b. Insights from the IronTract challenge: Optimal methods for mapping brain pathways from multi-shell diffusion MRI. NeuroImage 257, 119327. https://doi.org/10.1016/j.neuroimage.2022.119327

Maffei, C., Girard, G., Schilling, K.G., Aydogan, D.B., Adluru, N., Zhylka, A., Wu, Y., Mancini, M., Hamamci, A., Sarica, A., Teillac, A., Baete, S.H., Karimi, D., Yeh, F.-C., Yildiz, M.E., Gholipour, A., Bihan-Poudec, Y., Hiba, B., Quattrone, Andrea, Quattrone, Aldo, Boshkovski, T., Stikov, N., Yap, P.-T., De Luca, A., Pluim, J., Leemans, A., Prabhakaran, V., Bendlin, B.B., Alexander, A.L., Landman, B.A., Canales-Rodríguez, E.J., Barakovic, M., Rafael-Patino, J., Yu, T., Rensonnet, G., Schiavi, S., Daducci, A., Pizzolato, M., Fischi-Gomez, E., Thiran, J.-P., Dai, G., Grisot, G., Lazovski, N., Puch, S., Ramos, M., Rodrigues, P., Prčkovska, V., Jones, R., Lehman, J., Haber, S.N., Yendiki, A., 2022c. Insights from the IronTract challenge: Optimal methods for mapping brain pathways from multi-shell diffusion MRI. NeuroImage 257, 119327. https://doi.org/10.1016/j.neuroimage.2022.119327

Maier-Hein, K.H., Neher, P.F., Houde, J.-C., Côté, M.-A., Garyfallidis, E., Zhong, J., Chamberland, M., Yeh, F.-C., Lin, Y.-C., Ji, Q., Reddick, W.E., Glass, J.O., Chen, D.Q., Feng, Y., Gao, C., Wu, Y., Ma, J., He, R., Li, Q., Westin, C.-F., Deslauriers-Gauthier, S., González, J.O.O., Paquette, M., St-Jean, S., Girard, G., Rheault, F., Sidhu, J., Tax, C.M.W., Guo, F., Mesri, H.Y., Dávid, S., Froeling, M., Heemskerk, A.M., Leemans, A., Boré, A., Pinsard, B., Bedetti, C., Desrosiers, M., Brambati, S., Doyon, J., Sarica, A., Vasta, R., Cerasa, A., Quattrone, A., Yeatman, J., Khan, A.R., Hodges, W., Alexander, S., Romascano, D., Barakovic, M., Auría, A., Esteban, O., Lemkaddem, A., Thiran, J.-P., Cetingul, H.E., Odry, B.L., Mailhe, B., Nadar, M.S., Pizzagalli, F., Prasad, G., Villalon-Reina, J.E., Galvis, J., Thompson, P.M., Requejo, F.D.S., Laguna, P.L., Lacerda, L.M., Barrett, R., Dell'Acqua, F., Catani, M., Petit, L., Caruyer, E., Daducci, A., Dyrby, T.B., Holland-Letz, T., Hilgetag, C.C., Stieltjes, B., Descoteaux, M., 2017. The challenge of mapping the human connectome based on diffusion tractography. Nat. Commun. 8, 1349. https://doi.org/10.1038/s41467-017-01285-x

Maller, J.J., Welton, T., Middione, M., Callaghan, F.M., Rosenfeld, J.V., Grieve, S.M., 2019. Revealing the Hippocampal Connectome through Super-Resolution 1150-Direction Diffusion MRI. Sci. Rep. 9, 2418. https://doi.org/10.1038/s41598-018-37905-9

Markov, N.T., Ercsey-Ravasz, M.M., Ribeiro Gomes, A.R., Lamy, C., Magrou, L., Vezoli, J., Misery, P., Falchier, A., Quilodran, R., Gariel, M.A., Sallet, J., Gamanut, R., Huissoud, C., Clavagnier, S., Giroud, P., Sappey-Marinier, D., Barone, P., Dehay, C., Toroczkai, Z., Knoblauch, K., Van Essen, D.C., Kennedy, H., 2012a. A Weighted and Directed Interareal Connectivity Matrix for Macaque Cerebral Cortex. Cereb. Cortex 24, 17–36. https://doi.org/10.1093/cercor/bhs270

Markov, N.T., Ercsey-Ravasz, M.M., Ribeiro Gomes, A.R., Lamy, C., Magrou, L., Vezoli, J., Misery, P., Falchier, A., Quilodran, R., Gariel, M.A., Sallet, J., Gamanut, R., Huissoud, C., Clavagnier, S., Giroud, P., Sappey-Marinier, D., Barone, P., Dehay, C., Toroczkai, Z., Knoblauch, K., Van Essen, D.C., Kennedy, H., 2012b. A Weighted and Directed Interareal Connectivity Matrix for Macaque Cerebral Cortex. Cereb. Cortex 24, 17–36. https://doi.org/10.1093/cercor/bhs270

Markov, N.T., Misery, P., Falchier, A., Lamy, C., Vezoli, J., Quilodran, R., Gariel, M.A., Giroud, P., Ercsey-Ravasz, M., Pilaz, L.J., Huissoud, C., Barone, P., Dehay, C., Toroczkai, Z., Van Essen, D.C., Kennedy, H., Knoblauch, K., 2010. Weight Consistency Specifies Regularities of Macaque Cortical Networks. Cereb. Cortex 21, 1254–1272. https://doi.org/10.1093/cercor/bhq201

Mars, R.B., Neubert, F.-X., Verhagen, L., Sallet, J., Miller, K.L., Dunbar, R.I.M., Barton, R.A., 2014. Primate comparative neuroscience using magnetic resonance imaging: promises and challenges. Front. Neurosci. 8. https://doi.org/10.3389/fnins.2014.00298

Mars, R.B., Sotiropoulos, S.N., Passingham, R.E., Sallet, J., Verhagen, L., Khrapitchev, A.A., Sibson, N., Jbabdi, S., 2018. Whole brain comparative anatomy using connectivity blueprints. eLife 7, e35237. https://doi.org/10.7554/eLife.35237

Masís, J., Mankus, D., Wolff, S.B.E., Guitchounts, G., Joesch, M., Cox, D.D., 2018. A micro-CT-based method for quantitative brain lesion characterization and electrode localization. Sci. Rep. 8, 5184. https://doi.org/10.1038/s41598-018-23247-z

Melissa Clare O'Donoghue, Jasmine Blane, Grace Gillis, Robert Mitchell, Karen Lindsay, Juliet Semple, Pieter M Pretorius, Ludovica Griffanti, Jane Fossey, Vanessa Raymont, Lola Martos, Clare E Mackay, 2023. Oxford brain health clinic: protocol and research database. BMJ Open 13, e067808. https://doi.org/10.1136/bmjopen-2022-067808

Melozzi, F., Bergmann, E., Harris, J.A., Kahn, I., Jirsa, V., Bernard, C., 2019. Individual structural features constrain the mouse functional connectome. Proc. Natl. Acad. Sci. 116, 26961–26969. https://doi.org/10.1073/pnas.1906694116

Menzel, M., Michielsen, K., De Raedt, H., Reckfort, J., Amunts, K., Axer, M., 2015. A Jones matrix formalism for simulating three-dimensional polarized light imaging of brain tissue. J. R. Soc. Interface 12, 20150734. https://doi.org/10.1098/rsif.2015.0734

Meyer, A., 1970. Karl Friedrich Burdach and his place in the history of neuroanatomy. J. Neurol. Neurosurg. Psychiatry 33, 553–561. https://doi.org/10.1136/jnnp.33.5.553

Miller, A.K.H., Alston, R.L., Corsellis, J.A.N., 1980. VARIATION WITH AGE IN THE VOLUMES OF GREY AND WHITE MATTER IN THE CEREBRAL HEMISPHERES OF MAN: MEASUREMENTS WITH AN IMAGE ANALYSER. Neuropathol. Appl. Neurobiol. 6, 119–132. https://doi.org/10.1111/j.1365-2990.1980.tb00283.x

Miller, K.L., Alfaro-Almagro, F., Bangerter, N.K., Thomas, D.L., Yacoub, E., Xu, J., Bartsch, A.J., Jbabdi, S., Sotiropoulos, S.N., Andersson, J.L.R., Griffanti, L., Douaud, G., Okell, T.W., Weale, P., Dragonu, I., Garratt, S., Hudson, S., Collins, R., Jenkinson, M., Matthews, P.M., Smith, S.M., 2016. Multimodal population brain imaging in the UK Biobank prospective epidemiological study. Nat. Neurosci. 19, 1523–1536. https://doi.org/10.1038/nn.4393

Miller, K.L., Stagg, C.J., Douaud, G., Jbabdi, S., Smith, S.M., Behrens, T.E.J., Jenkinson, M., Chance, S.A., Esiri, M.M., Voets, N.L., Jenkinson, N., Aziz, T.Z., Turner, M.R., Johansen-Berg, H., McNab, J.A., 2011. Diffusion imaging of whole, post-mortem human brains on a clinical MRI scanner. NeuroImage 57, 167–181. https://doi.org/10.1016/j.neuroimage.2011.03.070

Mollink, J., Kleinnijenhuis, M., Cappellen van Walsum, A.-M. van, Sotiropoulos, S.N., Cottaar, M., Mirfin, C., Heinrich, M.P., Jenkinson, M., Pallebage-Gamarallage, M., Ansorge, O., Jbabdi, S., Miller, K.L., 2017a. Evaluating fibre orientation dispersion in white matter: Comparison of diffusion MRI, histology and polarized light imaging. Neuroimage 157, 561–574. https://doi.org/10.1016/j.neuroimage.2017.06.001

Mollink, J., Kleinnijenhuis, M., Cappellen van Walsum, A.-M. van, Sotiropoulos, S.N., Cottaar, M., Mirfin, C., Heinrich, M.P., Jenkinson, M., Pallebage-Gamarallage, M., Ansorge, O., Jbabdi, S., Miller, K.L., 2017b. Evaluating fibre orientation dispersion in white matter: Comparison of diffusion MRI, histology and polarized light imaging. NeuroImage 157, 561–574. https://doi.org/10.1016/j.neuroimage.2017.06.001

Morecraft, R.J., Herrick, J.L., Stilwell-Morecraft, K.S., Louie, J.L., Schroeder, C.M., Ottenbacher, J.G., Schoolfield, M.W., 2002. Localization of arm representation in the

corona radiata and internal capsule in the non-human primate. Brain 125, 176–198. https://doi.org/10.1093/brain/awf011

Nahirney, P.C., Tremblay, M.-E., 2021. Brain Ultrastructure: Putting the Pieces Together. Front. Cell Dev. Biol. 9, 629503. https://doi.org/10.3389/fcell.2021.629503

Nakaji, H., Kouyama, N., Muragaki, Y., Kawakami, Y., Iseki, H., 2008. Localization of nerve fiber bundles by polarization-sensitive optical coherence tomography. J. Neurosci. Methods 174, 82–90. https://doi.org/10.1016/j.jneumeth.2008.07.004

Nath, V., Pathak, S.K., Schilling, K.G., Schneider, W., Landman, B.A., 2020a. Deep learning estimation of multi-tissue constrained spherical deconvolution with limited single shell DW-MRI, in: Landman, B.A., Išgum, I. (Eds.), Medical Imaging 2020: Image Processing. Presented at the Image Processing, SPIE, Houston, United States, p. 27. https://doi.org/10.1117/12.2549455

Nath, V., Schilling, K.G., Parvathaneni, P., Hansen, C.B., Hainline, A.E., Huo, Y., Blaber, J.A., Lyu, I., Janve, V., Gao, Y., Stepniewska, I., Anderson, A.W., Landman, B.A., 2019. Deep learning reveals untapped information for local white-matter fiber reconstruction in diffusion-weighted MRI. Magn. Reson. Imaging 62, 220–227. https://doi.org/10.1016/j.mri.2019.07.012

Nath, V., Schilling, K.G., Parvathaneni, P., Huo, Y., Blaber, J.A., Hainline, A.E., Barakovic, M., Romascano, D., Rafael-Patino, J., Frigo, M., Girard, G., Thiran, J., Daducci, A., Rowe, M., Rodrigues, P., Prčkovska, V., Aydogan, D.B., Sun, W., Shi, Y., Parker, W.A., Ould Ismail, A.A., Verma, R., Cabeen, R.P., Toga, A.W., Newton, A.T., Wasserthal, J., Neher, P., Maier-Hein, K., Savini, G., Palesi, F., Kaden, E., Wu, Y., He, J., Feng, Y., Paquette, M., Rheault, F., Sidhu, J., Lebel, C., Leemans, A., Descoteaux, M., Dyrby, T.B., Kang, H., Landman, B.A., 2020b. Tractography reproducibility challenge with empirical data (TraCED): The 2017 ISMRM diffusion study group challenge. J. Magn. Reson. Imaging 51, 234–249. https://doi.org/10.1002/jmri.26794

Ngai, J., 2024. BRAIN @ 10: A decade of innovation. Neuron 112, 3003–3006. https://doi.org/10.1016/j.neuron.2024.09.007

Nickerson, L.D., Smith, S.M., Öngür, D., Beckmann, C.F., 2017. Using Dual Regression to Investigate Network Shape and Amplitude in Functional Connectivity Analyses. Front. Neurosci. 11. https://doi.org/10.3389/fnins.2017.00115

Nicole Schubert, Markus Axer, Uwe Pietrzyk, Katrin Amunts, 2017. 3D Polarized Light Imaging Portrayed: Visualization of Fiber Architecture Derived from 3D-PLI, in: Ahmet Mesrur Halefoğlu (Ed.), High-Resolution Neuroimaging. IntechOpen, Rijeka, p. Ch. 3. https://doi.org/10.5772/intechopen.72532

Ning, L., Setsompop, K., Michailovich, O., Makris, N., Westin, C.-F., Rathi, Y., 2015. A Compressed-Sensing Approach for Super-Resolution Reconstruction of Diffusion MRI, in: Ourselin, S., Alexander, D.C., Westin, C.-F., Cardoso, M.J. (Eds.), Information Processing in Medical Imaging, Lecture Notes in Computer Science. Springer International Publishing, Cham, pp. 57–68. https://doi.org/10.1007/978-3-319-19992-4_5

Niogi, 2010. Individual differences in distinct components of attention are linked to anatomical variations in distinct white matter tracts. Front. Neuroanat. https://doi.org/10.3389/neuro.05.002.2010

Noonan, M.P., Sallet, J., Mars, R.B., Neubert, F.X., O'Reilly, J.X., Andersson, J.L., Mitchell, A.S., Bell, A.H., Miller, K.L., Rushworth, M.F.S., 2014. A Neural Circuit Covarying with Social Hierarchy in Macaques. PLOS Biol. 12, e1001940. https://doi.org/10.1371/journal.pbio.1001940

Nozais, V., Forkel, S.J., Petit, L., Talozzi, L., Corbetta, M., Thiebaut De Schotten, M., Joliot, M., 2023. Atlasing white matter and grey matter joint contributions to resting-state networks in the human brain. Commun. Biol. 6, 726. https://doi.org/10.1038/s42003-023-05107-3

Oh, S.W., Harris, J.A., Ng, L., Winslow, B., Cain, N., Mihalas, S., Wang, Q., Lau, C., Kuan, L., Henry, A.M., Mortrud, M.T., Ouellette, B., Nguyen, T.N., Sorensen, S.A., Slaughterbeck, C.R., Wakeman, W., Li, Y., Feng, D., Ho, A., Nicholas, E., Hirokawa, K.E., Bohn, P., Joines, K.M., Peng, H., Hawrylycz, M.J., Phillips, J.W., Hohmann, J.G., Wohnoutka, P., Gerfen, C.R., Koch, C., Bernard, A., Dang, C., Jones, A.R., Zeng, H., 2014. A mesoscale connectome of the mouse brain. Nature 508, 207–214. https://doi.org/10.1038/nature13186

Panesar, S.S., Abhinav, K., Yeh, F.-C., Jacquesson, T., Collins, M., Fernandez-Miranda, J., 2019. Tractography for Surgical Neuro-Oncology Planning: Towards a Gold Standard. Neurotherapeutics 16, 36–51. https://doi.org/10.1007/s13311-018-00697-x

Park, M.C., Belhaj-Saïf, A., Gordon, M., Cheney, P.D., 2001. Consistent features in the forelimb representation of primary motor cortex in rhesus macaques. J. Neurosci. Off. J. Soc. Neurosci. 21, 2784–2792. https://doi.org/10.1523/JNEUROSCI.21-08-02784.2001

Patriat, R., Palnitkar, T., Braun, H., Solomona, O., Harel, N., 2023. Imaging of subcortical deep brain structures with 7T MRI, in: Advances in Magnetic Resonance Technology and Applications. Elsevier, pp. 273–285. https://doi.org/10.1016/B978-0-323-99898-7.00018-3

Paxinos, G., Petrides, M., Evrard, H.C., 2024. The Rhesus Monkey Brain in Stereotaxic Coordinates, 4th ed. ed. Elsevier Science & Technology, San Diego.

Penfield, W., Boldrey, E., 1937. SOMATIC MOTOR AND SENSORY REPRESENTATION IN THE CEREBRAL CORTEX OF MAN AS STUDIED BY ELECTRICAL STIMULATION. Brain 60, 389–443. https://doi.org/10.1093/brain/60.4.389

Petersen, K.J., Reid, J.A., Chakravorti, S., Juttukonda, M.R., Franco, G., Trujillo, P., Stark, A.J., Dawant, B.M., Donahue, M.J., Claassen, D.O., 2018. Structural and functional connectivity of the nondecussating dentato-rubro-thalamic tract. NeuroImage 176, 364–371. https://doi.org/10.1016/j.neuroimage.2018.04.074

Petersen, M., Frey, B.M., Mayer, C., Kühn, S., Gallinat, J., Hanning, U., Fiehler, J., Borof, K., Jagodzinski, A., Gerloff, C., Thomalla, G., Cheng, B., 2022. Fixel based analysis of white matter alterations in early stage cerebral small vessel disease. Sci. Rep. 12, 1581. https://doi.org/10.1038/s41598-022-05665-2

Phillips, O.R., Joshi, S.H., Piras, F., Orfei, M.D., Iorio, M., Narr, K.L., Shattuck, D.W., Caltagirone, C., Spalletta, G., Di Paola, M., 2016. The superficial white matter in Alzheimer's disease. Hum. Brain Mapp. 37, 1321–1334. https://doi.org/10.1002/hbm.23105

Pichat, J., Iglesias, J.E., Yousry, T., Ourselin, S., Modat, M., 2018. A Survey of Methods for 3D Histology Reconstruction. Med. Image Anal. 46, 73–105. https://doi.org/10.1016/j.media.2018.02.004

Pilati, N., Barker, M., Panteleimonitis, S., Donga, R., Hamann, M., 2008. A rapid method combining Golgi and Nissl staining to study neuronal morphology and cytoarchitecture. J. Histochem. Cytochem. Off. J. Histochem. Soc. 56, 539–550. https://doi.org/10.1369/jhc.2008.950246

Pircher, M., Hitzenberger, C.K., Schmidt-Erfurth, U., 2011. Polarization sensitive optical coherence tomography in the human eye. Prog. Retin. Eye Res. 30, 431–451. https://doi.org/10.1016/j.preteyeres.2011.06.003

Pisharady, P.K., Yeatts, M., Farooq, H., Johnson, M., Harel, N., Moeller, S., Zimmermann, J., Yacoub, E., Ugurbil, K., Heilbronner, S.R., Lenglet, C., Akkin, T., 2024. Mapping polarization sensitive optical coherence tomography and ultra-high-field diffusion MRI in the macaque brain. https://doi.org/10.1101/2024.04.19.590326

Pouyanfar, S., Sadiq, S., Yan, Y., Tian, H., Tao, Y., Reyes, M.P., Shyu, M.-L., Chen, S.-C., Iyengar, S.S., 2019. A Survey on Deep Learning: Algorithms, Techniques, and Applications. ACM Comput. Surv. 51, 1–36. https://doi.org/10.1145/3234150

Pruessmann, K.P., Weiger, M., Scheidegger, M.B., Boesiger, P., 1999. SENSE: sensitivity encoding for fast MRI. Magn. Reson. Med. 42, 952–962.

Purves, D., Augustine, G.J., Fitzpatrick, D. (Eds.), 2019. Neuroscience, International sixth edition. ed. Sinauer Associates / Oxford University Press, New York.

Qu, L., Li, Y., Xie, P., Liu, L., Wang, Y., Wu, J., Liu, Y., Wang, T., Li, L., Guo, K., Wan, W., Ouyang, L., Xiong, F., Kolstad, A.C., Wu, Z., Xu, F., Zheng, Y., Gong, H., Luo, Q., Bi, G., Dong, H., Hawrylycz, M., Zeng, H., Peng, H., 2022. Cross-modal coherent registration of whole mouse brains. Nat. Methods 19, 111–118. https://doi.org/10.1038/s41592-021-01334-w

Raffelt, D., Tournier, J.-D., Fripp, J., Crozier, S., Connelly, A., Salvado, O., 2011. Symmetric diffeomorphic registration of fibre orientation distributions. NeuroImage 56, 1171–1180. https://doi.org/10.1016/j.neuroimage.2011.02.014

Raffelt, D., Tournier, J.-D., Rose, S., Ridgway, G.R., Henderson, R., Crozier, S., Salvado, O., Connelly, A., 2012. Apparent Fibre Density: A novel measure for the analysis of diffusion-weighted magnetic resonance images. NeuroImage 59, 3976–3994. https://doi.org/10.1016/j.neuroimage.2011.10.045

Ramón y Cajal, S., 1995. Histology of the nervous system of man and vertebrates, History of neuroscience. Oxford University Press, New York.

Reckfort, J., Wiese, H., Pietrzyk, U., Zilles, K., Amunts, K., Axer, M., 2015. A multiscale approach for the reconstruction of the fiber architecture of the human brain based on 3D-PLI. Front. Neuroanat. 9. https://doi.org/10.3389/fnana.2015.00118

Rheault, F., St-Onge, E., Sidhu, J., Maier-Hein, K., Tzourio-Mazoyer, N., Petit, L., Descoteaux, M., 2019. Bundle-specific tractography with incorporated anatomical and orientational priors. NeuroImage 186, 382–398. https://doi.org/10.1016/j.neuroimage.2018.11.018

Robinson, E.C., Jbabdi, S., Glasser, M.F., Andersson, J., Burgess, G.C., Harms, M.P., Smith, S.M., Van Essen, D.C., Jenkinson, M., 2014. MSM: A new flexible framework for Multimodal Surface Matching. NeuroImage 100, 414–426. https://doi.org/10.1016/j.neuroimage.2014.05.069

Rojkova, K., Volle, E., Urbanski, M., Humbert, F., Dell'Acqua, F., Thiebaut De Schotten, M., 2016. Atlasing the frontal lobe connections and their variability due to age and education: a spherical deconvolution tractography study. Brain Struct. Funct. 221, 1751–1766. https://doi.org/10.1007/s00429-015-1001-3

Rowe, M., Zhang, H.G., Oxtoby, N., Alexander, D.C., 2013. Beyond crossing fibers: tractography exploiting sub-voxel fibre dispersion and neighbourhood structure. Inf. Process. Med. Imaging Proc. Conf. 23, 402–413. https://doi.org/10.1007/978-3-642-38868-2_34

Saini, F., Dell'Acqua, F., Strydom, A., 2022. Structural Connectivity in Down Syndrome and Alzheimer's Disease. Front. Neurosci. 16. https://doi.org/10.3389/fnins.2022.908413

Saleem, K.S., Avram, A.V., Glen, D., Yen, C.C.-C., Ye, F.Q., Komlosh, M., Basser, P.J., 2021. High-resolution mapping and digital atlas of subcortical regions in the macaque monkey based on matched MAP-MRI and histology. NeuroImage 245, 118759. https://doi.org/10.1016/j.neuroimage.2021.118759

Saleem, K.S., Logothetis, N., 2012. A combined MRI and histology atlas of the rhesus monkey brain in stereotaxic coordinates, 2nd ed., with horizontal, coronal, and Sagittal series. ed. Elsevier/AP, Amsterdam.

Sallet, J., Noonan, M.P., Thomas, A., O'Reilly, J.X., Anderson, J., Papageorgiou, G.K., Neubert, F.X., Ahmed, B., Smith, J., Bell, A.H., Buckley, M.J., Roumazeilles, L., Cuell, S., Walton, M.E., Krug, K., Mars, R.B., Rushworth, M.F.S., 2020. Behavioral flexibility is associated with changes in structure and function distributed across a frontal cortical network in macaques. PLOS Biol. 18, e3000605. https://doi.org/10.1371/journal.pbio.3000605

Scheffer, L.K., Xu, C.S., Januszewski, M., Lu, Z., Takemura, Shin-ya, Hayworth, K.J., Huang, G.B., Shinomiya, K., Maitlin-Shepard, J., Berg, S., Clements, J., Hubbard, P.M., Katz, W.T., Umayam, L., Zhao, T., Ackerman, D., Blakely, T., Bogovic, J., Dolafi, T., Kainmueller, D., Kawase, T., Khairy, K.A., Leavitt, L., Li, P.H., Lindsey, L., Neubarth, N., Olbris, D.J., Otsuna, H., Trautman, E.T., Ito, M., Bates, A.S., Goldammer, J., Wolff, T., Svirskas, R., Schlegel, P., Neace, E., Knecht, C.J., Alvarado, C.X., Bailey, D.A., Ballinger, S., Borycz, J.A., Canino, B.S., Cheatham, N., Cook, M., Dreher, M., Duclos, O., Eubanks, B., Fairbanks, K., Finley, S., Forknall, N., Francis, A., Hopkins, G.P., Joyce, E.M., Kim, S., Kirk, N.A., Kovalyak, J., Lauchie, S.A., Lohff, A., Maldonado, C., Manley, E.A., McLin, S., Mooney, C., Ndama, M., Ogundeyi, O., Okeoma, N., Ordish, C., Padilla, N., Patrick, C.M., Paterson, T., Phillips, E.E., Phillips, E.M., Rampally, N., Ribeiro, C., Robertson, M.K., Rymer, J.T., Ryan, S.M., Sammons, M., Scott, A.K., Scott, A.L., Shinomiya, A., Smith, C., Smith, K., Smith, N.L., Sobeski, M.A., Suleiman, A., Swift, J., Takemura, Satoko, Talebi, I., Tarnogorska, D., Tenshaw, E., Tokhi, T., Walsh, J.J., Yang, T., Horne, J.A., Li, F., Parekh, R., Rivlin, P.K., Jayaraman, V., Costa, M., Jefferis, G.S., Ito, K., Saalfeld, S., George, R., Meinertzhagen, I.A., Rubin, G.M., Hess, H.F., Jain, V., Plaza, S.M., 2020. A connectome and analysis of the adult *Drosophila* central brain. eLife 9, e57443. https://doi.org/10.7554/eLife.57443

Schiavi, S., Ocampo-Pineda, M., Barakovic, M., Petit, L., Descoteaux, M., Thiran, J.-P., Daducci, A., 2020. A new method for accurate in vivo mapping of human brain connections using microstructural and anatomical information. Sci. Adv. 6, eaba8245. https://doi.org/10.1126/sciadv.aba8245

Schilling, K., Gao, Y., Janve, V., Stepniewska, I., Landman, B.A., Anderson, A.W., 2017a. Can increased spatial resolution solve the crossing fiber problem for diffusion MRI? NMR Biomed. 30. https://doi.org/10.1002/nbm.3787

Schilling, K., Gao, Y., Janve, V., Stepniewska, I., Landman, B.A., Anderson, A.W., 2017b. Confirmation of a gyral bias in diffusion MRI fiber tractography. Hum. Brain Mapp. 39, 1449–1466. https://doi.org/10.1002/hbm.23936

Schilling, K.G., Chad, J.A., Chamberland, M., Nozais, V., Rheault, F., Archer, D., Li, M., Gao, Y., Cai, L., Del'Acqua, F., Newton, A., Moyer, D., Gore, J.C., Lebel, C., Landman, B.A., 2023. White matter tract microstructure, macrostructure, and associated cortical gray matter morphology across the lifespan. https://doi.org/10.1101/2023.09.25.559330

Schilling, K.G., Daducci, A., Maier-Hein, K., Poupon, C., Houde, J.-C., Nath, V., Anderson, A.W., Landman, B.A., Descoteaux, M., 2019a. Challenges in diffusion MRI tractography – Lessons learned from international benchmark competitions. Magn. Reson. Imaging 57, 194–209. https://doi.org/10.1016/j.mri.2018.11.014

Schilling, K.G., Gao, Y., Christian, M., Janve, V., Stepniewska, I., Landman, B.A., Anderson, A.W., 2019b. A Web-Based Atlas Combining MRI and Histology of the

Squirrel Monkey Brain. Neuroinformatics 17, 131–145. https://doi.org/10.1007/s12021-018-9391-z

Schilling, K.G., Gao, Y., Stepniewska, I., Janve, V., Landman, B.A., Anderson, A.W., 2019c. Histologically derived fiber response functions for diffusion MRI vary across white matter fibers—An ex vivo validation study in the squirrel monkey brain. NMR Biomed. 32, e4090. https://doi.org/10.1002/nbm.4090

Schilling, K.G., Grussu, F., Ianus, A., Hansen, B., Howard, A.F.D., Barrett, R.L.C., Aggarwal, M., Michielse, S., Nasrallah, F., Syeda, W., Wang, N., Veraart, J., Roebroeck, A., Bagdasarian, A.F., Eichner, C., Sepehrband, F., Zimmermann, J., Soustelle, L., Bowman, C., Tendler, B.C., Hertanu, A., Jeurissen, B., Verhoye, M., Frydman, L., Van De Looij, Y., Hike, D., Dunn, J.F., Miller, K., Landman, B.A., Shemesh, N., Anderson, A., McKinnon, E., Farquharson, S., Dell'Acqua, F., Pierpaoli, C., Drobnjak, I., Leemans, A., Harkins, K.D., Descoteaux, M., Xu, D., Huang, H., Santin, M.D., Grant, S.C., Obenaus, A., Kim, G.S., Wu, D., Le Bihan, D., Blackband, S.J., Ciobanu, L., Fieremans, E., Bai, R., Leergaard, T.B., Zhang, J., Dyrby, T.B., Johnson, G.A., Cohen-Adad, J., Budde, M.D., Jelescu, I.O., 2025. Considerations and recommendations from the ISMRM diffusion study group for preclinical diffusion MRI : Part 2—Ex vivo imaging: Added value and acquisition. Magn. Reson. Med. mrm.30435. https://doi.org/10.1002/mrm.30435

Schilling, K.G., Nath, V., Hansen, C., Parvathaneni, P., Blaber, J., Gao, Y., Neher, P., Aydogan, D.B., Shi, Y., Ocampo-Pineda, M., Schiavi, S., Daducci, A., Girard, G., Barakovic, M., Rafael-Patino, J., Romascano, D., Rensonnet, G., Pizzolato, M., Bates, A., Fischi, E., Thiran, J.-P., Canales-Rodríguez, E.J., Huang, C., Zhu, H., Zhong, L., Cabeen, R., Toga, A.W., Rheault, F., Theaud, G., Houde, J.-C., Sidhu, J., Chamberland, M., Westin, C.-F., Dyrby, T.B., Verma, R., Rathi, Y., Irfanoglu, M.O., Thomas, C., Pierpaoli, C., Descoteaux, M., Anderson, A.W., Landman, B.A., 2019d. Limits to anatomical accuracy of diffusion tractography using modern approaches. NeuroImage 185, 1–11. https://doi.org/10.1016/j.neuroimage.2018.10.029

Schilling, K.G., Tax, C.M.W., Rheault, F., Landman, B.A., Anderson, A.W., Descoteaux, M., Petit, L., 2022. Prevalence of white matter pathways coming into a single white matter voxel orientation: The bottleneck issue in tractography. Hum. Brain Mapp. 43, 1196–1213. https://doi.org/10.1002/hbm.25697

Scholz, J., Klein, M.C., Behrens, T.E.J., Johansen-Berg, H., 2009. Training induces changes in white-matter architecture. Nat. Neurosci. 12, 1370–1371. https://doi.org/10.1038/nn.2412

Seehaus, A., Roebroeck, A., Bastiani, M., Fonseca, L., Bratzke, H., Lori, N., Vilanova, A., Goebel, R., Galuske, R., 2015. Histological validation of high-resolution DTI in human post mortem tissue. Front. Neuroanat. 9. https://doi.org/10.3389/fnana.2015.00098

Shapson-Coe, A., Januszewski, M., Berger, D.R., Pope, A., Wu, Y., Blakely, T., Schalek, R.L., Li, P.H., Wang, S., Maitin-Shepard, J., Karlupia, N., Dorkenwald, S., Sjostedt, E., Leavitt, L., Lee, D., Troidl, J., Collman, F., Bailey, L., Fitzmaurice, A., Kar, R., Field, B., Wu, H., Wagner-Carena, J., Aley, D., Lau, J., Lin, Z., Wei, D., Pfister, H., Peleg, A., Jain, V., Lichtman, J.W., 2024. A petavoxel fragment of human cerebral cortex reconstructed at nanoscale resolution. Science 384, eadk4858. https://doi.org/10.1126/science.adk4858

Shastin, D., Genc, S., Parker, G.D., Koller, K., Tax, C.M.W., Evans, J., Hamandi, K., Gray, W.P., Jones, D.K., Chamberland, M., 2022. Surface-based tracking for short association fibre tractography. NeuroImage 260, 119423. https://doi.org/10.1016/j.neuroimage.2022.119423

Sitek, K.R., Gulban, O.F., Calabrese, E., Johnson, G.A., Lage-Castellanos, A., Moerel, M., Ghosh, S.S., De Martino, F., 2019. Mapping the human subcortical auditory system using histology, postmortem MRI and in vivo MRI at 7T. eLife 8, e48932. https://doi.org/10.7554/eLife.48932

Smith, S.M., Elliott, L.T., Alfaro-Almagro, F., McCarthy, P., Nichols, T.E., Douaud, G., Miller, K.L., 2020. Brain aging comprises many modes of structural and functional change with distinct genetic and biophysical associations. eLife 9, e52677. https://doi.org/10.7554/eLife.52677

Soltani, M.H., Pichardo, R., Song, Z., Sangha, N., Camacho, F., Satyamoorthy, K., Sangueza, O.P., Setaluri, V., 2005. Microtubule-associated protein 2, a marker of neuronal differentiation, induces mitotic defects, inhibits growth of melanoma cells, and predicts metastatic potential of cutaneous melanoma. Am. J. Pathol. 166, 1841–1850. https://doi.org/10.1016/S0002-9440(10)62493-5

Son, S.-J., Kim, M., Park, H., 2016. Imaging analysis of Parkinson's disease patients using SPECT and tractography. Sci. Rep. 6, 38070. https://doi.org/10.1038/srep38070

Sporns, O., 2013. The human connectome: Origins and challenges. NeuroImage 80, 53–61. https://doi.org/10.1016/j.neuroimage.2013.03.023

Sporns, O., Tononi, G., Kötter, R., 2005. The Human Connectome: A Structural Description of the Human Brain. PLoS Comput. Biol. 1, e42. https://doi.org/10.1371/journal.pcbi.0010042

Stanisz, G.J., Wright, G.A., Henkelman, R.M., Szafer, A., 1997. An analytical model of restricted diffusion in bovine optic nerve. Magn. Reson. Med. 37, 103–111. https://doi.org/10.1002/mrm.1910370115

Stephan, K.E., Schlagenhauf, F., Huys, Q.J.M., Raman, S., Aponte, E.A., Brodersen, K.H., Rigoux, L., Moran, R.J., Daunizeau, J., Dolan, R.J., Friston, K.J., Heinz, A., 2017. Computational neuroimaging strategies for single patient predictions. NeuroImage 145, 180–199. https://doi.org/10.1016/j.neuroimage.2016.06.038

St-Onge, E., Daducci, A., Girard, G., Descoteaux, M., 2018. Surface-enhanced tractography (SET). NeuroImage 169, 524–539. https://doi.org/10.1016/j.neuroimage.2017.12.036

Tendler, B.C., Hanayik, T., Ansorge, O., Bangerter-Christensen, S., Berns, G.S., Bertelsen, M.F., Bryant, K.L., Foxley, S., van den Heuvel, M.P., Howard, A.F., Huszar, I.N., Khrapitchev, A.A., Leonte, A., Manger, P.R., Menke, R.A., Mollink, J., Mortimer, D., Pallebage-Gamarallage, M., Roumazeilles, L., Sallet, J., Scholtens, L.H., Scott, C., Smart, A., Turner, M.R., Wang, C., Jbabdi, S., Mars, R.B., Miller, K.L., 2022. The Digital Brain Bank, an open access platform for post-mortem imaging datasets. eLife 11, e73153. https://doi.org/10.7554/eLife.73153

Thiebaut De Schotten, M., Dell'Acqua, F., Valabregue, R., Catani, M., 2012. Monkey to human comparative anatomy of the frontal lobe association tracts. Cortex 48, 82–96. https://doi.org/10.1016/j.cortex.2011.10.001

Thomas, C., Ye, F.Q., Irfanoglu, M.O., Modi, P., Saleem, K.S., Leopold, D.A., Pierpaoli, C., 2014. Anatomical accuracy of brain connections derived from diffusion MRI tractography is inherently limited. Proc. Natl. Acad. Sci. 111, 16574–16579. https://doi.org/10.1073/pnas.1405672111

Thorn, K., 2016. A quick guide to light microscopy in cell biology. Mol. Biol. Cell 27, 219–222. https://doi.org/10.1091/mbc.e15-02-0088

Tobolsky, A.V., 1955. Stress Relaxation, Birefringence and the Structure of Gelatin and Other Polymeric Gels. J. Phys. Chem. 59, 575–575. https://doi.org/10.1021/j150528a026

Tournier, J.-D., Calamante, F., Connelly, A., 2010. Improved probabilistic streamlines tractography by 2nd order integration over fibre orientation distributions., in:

Proceedings of the International Society for Magnetic Resonance in Medicine. Presented at the International Society for Magnetic Resonance in Medicine.

Tournier, J.-D., Calamante, F., Connelly, A., 2007. Robust determination of the fibre orientation distribution in diffusion MRI: Non-negativity constrained super-resolved spherical deconvolution. NeuroImage 35, 1459–1472. https://doi.org/10.1016/j.neuroimage.2007.02.016

Tournier, J.-D., Calamante, F., Gadian, D.G., Connelly, A., 2004. Direct estimation of the fiber orientation density function from diffusion-weighted MRI data using spherical deconvolution. NeuroImage 23, 1176–1185. https://doi.org/10.1016/j.neuroimage.2004.07.037

Tournier, J.-D., Smith, R., Raffelt, D., Tabbara, R., Dhollander, T., Pietsch, M., Christiaens, D., Jeurissen, B., Yeh, C.-H., Connelly, A., 2019. MRtrix3: A fast, flexible and open software framework for medical image processing and visualisation. NeuroImage 202, 116137. https://doi.org/10.1016/j.neuroimage.2019.116137

Tullo, S., Devenyi, G.A., Patel, R., Park, M.T.M., Collins, D.L., Chakravarty, M.M., 2018. Warping an atlas derived from serial histology to 5 high-resolution MRIs. Sci. Data 5, 180107. https://doi.org/10.1038/sdata.2018.107

Van Dyken, P.C., Khan, A.R., Palaniyappan, L., 2024. Imaging of the superficial white matter in health and disease. Imaging Neurosci. 2, 1–35. https://doi.org/10.1162/imag_a_00221

Van Essen, D.C., Dierker, D.L., 2007. Surface-Based and Probabilistic Atlases of Primate Cerebral Cortex. Neuron 56, 209–225. https://doi.org/10.1016/j.neuron.2007.10.015

Van Essen, D.C., Donahue, C.J., Coalson, T.S., Kennedy, H., Hayashi, T., Glasser, M.F., 2019. Cerebral cortical folding, parcellation, and connectivity in humans, nonhuman primates, and mice. Proc. Natl. Acad. Sci. U. S. A. 116, 26173–26180. https://doi.org/10.1073/pnas.1902299116

Van Essen, D.C., Smith, J., Glasser, M.F., Elam, J., Donahue, C.J., Dierker, D.L., Reid, E.K., Coalson, T., Harwell, J., 2017. The Brain Analysis Library of Spatial maps and Atlases (BALSA) database. Data Shar. Part II 144, 270–274. https://doi.org/10.1016/j.neuroimage.2016.04.002

van Opbroek, A., Ikram, M.A., Vernooij, M.W., de Bruijne, M., 2015. Transfer Learning Improves Supervised Image Segmentation Across Imaging Protocols. IEEE Trans. Med. Imaging 34, 1018–1030. https://doi.org/10.1109/TMI.2014.2366792

Van Waesberghe, J.H.T.M., Kamphorst, W., De Groot, C.J.A., Van Walderveen, M.A.A., Castelijns, J.A., Ravid, R., Lycklama Nijeholt, G.J., Van Der Valk, P., Polman, C.H., Thompson, A.J., Barkhof, F., 1999. Axonal loss in multiple sclerosis lesions: Magnetic resonance imaging insights into substrates of disability. Ann. Neurol. 46, 747–754. https://doi.org/10.1002/1531-8249(199911)46:5<747::AID-ANA10>3.0.CO;2-4

Versace, A., Hitchens, T.K., Wallace, C.T., Watkins, S.C., D'Aiuto, L., 2024. 11.7T Diffusion Magnetic Resonance Imaging and Tractography to Probe Human Brain Organoid Microstructure. Biol. Psychiatry Glob. Open Sci. 4, 100344. https://doi.org/10.1016/j.bpsgos.2024.100344

Vu, A.T., Auerbach, E., Lenglet, C., Moeller, S., Sotiropoulos, S.N., Jbabdi, S., Andersson, J., Yacoub, E., Ugurbil, K., 2015. High resolution whole brain diffusion imaging at 7 T for the Human Connectome Project. NeuroImage 122, 318–331. https://doi.org/10.1016/j.neuroimage.2015.08.004

Wachinger, C., Golland, P., Kremen, W., Fischl, B., Reuter, M., 2015. BrainPrint: A discriminative characterization of brain morphology. NeuroImage 109, 232–248. https://doi.org/10.1016/j.neuroimage.2015.01.032

Wachinger, C., Reuter, M., 2016. Domain adaptation for Alzheimer's disease diagnostics. NeuroImage 139, 470–479. https://doi.org/10.1016/j.neuroimage.2016.05.053

Wagle Shukla, A., Okun, M.S., 2014. Surgical treatment of Parkinson's disease: patients, targets, devices, and approaches. Neurother. J. Am. Soc. Exp. Neurother. 11, 47–59. https://doi.org/10.1007/s13311-013-0235-0

Wang, D., Buckner, R.L., Fox, M.D., Holt, D.J., Holmes, A.J., Stoecklein, S., Langs, G., Pan, R., Qian, T., Li, K., Baker, J.T., Stufflebeam, S.M., Wang, K., Wang, X., Hong, B., Liu, H., 2015. Parcellating cortical functional networks in individuals. Nat. Neurosci. 18, 1853–1860. https://doi.org/10.1038/nn.4164

Wang, H., Al-Qaisi, M.K., Akkin, T., 2010. Polarization-maintaining fiber based polarization-sensitive optical coherence tomography in spectral domain. Opt. Lett. 35, 154. https://doi.org/10.1364/OL.35.000154

Wang, H., Lenglet, C., Akkin, T., 2015. Structure tensor analysis of serial optical coherence scanner images for mapping fiber orientations and tractography in the brain. J. Biomed. Opt. 20, 036003. https://doi.org/10.1117/1.JBO.20.3.036003

Wang, H., Magnain, C., Wang, R., Dubb, J., Varjabedian, A., Tirrell, L.S., Stevens, A., Augustinack, J.C., Konukoglu, E., Aganj, I., Frosch, M.P., Schmahmann, J.D., Fischl, B., Boas, D.A., 2018. as-PSOCT: Volumetric microscopic imaging of human brain architecture and connectivity. NeuroImage 165, 56–68. https://doi.org/10.1016/j.neuroimage.2017.10.012

Wang, H., Zhu, J., Reuter, M., Vinke, L.N., Yendiki, A., Boas, D.A., Fischl, B., Akkin, T., 2014. Cross-validation of serial optical coherence scanning and diffusion tensor imaging: a study on neural fiber maps in human medulla oblongata. NeuroImage 100, 395–404. https://doi.org/10.1016/j.neuroimage.2014.06.032

Warrington, S., Bryant, K.L., Khrapitchev, A.A., Sallet, J., Charquero-Ballester, M., Douaud, G., Jbabdi, S., Mars, R.B., Sotiropoulos, S.N., 2020. XTRACT - Standardised protocols for automated tractography in the human and macaque brain. NeuroImage 217, 116923. https://doi.org/10.1016/j.neuroimage.2020.116923

Wasserthal, J., Neher, P., Maier-Hein, K.H., 2018a. TractSeg - Fast and accurate white matter tract segmentation. NeuroImage 183, 239–253. https://doi.org/10.1016/j.neuroimage.2018.07.070

Wasserthal, J., Neher, P.F., Maier-Hein, K.H., 2018b. Tract orientation mapping for bundle-specific tractography. https://doi.org/10.48550/ARXIV.1806.05580

White, J.G., Southgate, E., Thomson, J.N., Brenner, S., 1986. The structure of the nervous system of the nematode *Caenorhabditis elegans*. Philos. Trans. R. Soc. Lond. B Biol. Sci. 314, 1–340. https://doi.org/10.1098/rstb.1986.0056

Wu, D., Zhang, J., 2016. In vivo mapping of macroscopic neuronal projections in the mouse hippocampus using high-resolution diffusion MRI. NeuroImage 125, 84–93. https://doi.org/10.1016/j.neuroimage.2015.10.051

Wu, M., Lu, L.H., Lowes, A., Yang, S., Passarotti, A.M., Zhou, X.J., Pavuluri, M.N., 2014a. Development of superficial white matter and its structural interplay with cortical gray matter in children and adolescents. Hum. Brain Mapp. 35, 2806–2816. https://doi.org/10.1002/hbm.22368

Wu, M., Lu, L.H., Lowes, A., Yang, S., Passarotti, A.M., Zhou, X.J., Pavuluri, M.N., 2014b. Development of superficial white matter and its structural interplay with cortical gray matter in children and adolescents. Hum. Brain Mapp. 35, 2806–2816. https://doi.org/10.1002/hbm.22368

Wu, W., Poser, B.A., Douaud, G., Frost, R., In, M.-H., Speck, O., Koopmans, P.J., Miller, K.L., 2016. High-resolution diffusion MRI at 7T using a three-dimensional multi-slab acquisition. NeuroImage 143, 1–14. https://doi.org/10.1016/j.neuroimage.2016.08.054

Wu, Y., Hong, Y., Feng, Y., Shen, D., Yap, P.-T., 2020. Mitigating gyral bias in cortical tractography via asymmetric fiber orientation distributions. Med. Image Anal. 59, 101543. https://doi.org/10.1016/j.media.2019.101543

Wysiadecki, G., Clarke, E., Polguj, M., Haładaj, R., Żytkowski, A., Topol, M., 2019. Klingler's method of brain dissection: review of the technique including its usefulness in practical neuroanatomy teaching, neurosurgery and neuroimaging. Folia Morphol. 78, 455–466. https://doi.org/10.5603/FM.a2018.0113

Xiao, Y., Fonov, V., Chakravarty, M.M., Beriault, S., Al Subaie, F., Sadikot, A., Pike, G.B., Bertrand, G., Collins, D.L., 2017. A dataset of multi-contrast population-averaged brain MRI atlases of a Parkinson′s disease cohort. Data Brief 12, 370–379. https://doi.org/10.1016/j.dib.2017.04.013

Xu, Fang, Shen, Y., Ding, L., Yang, C.-Y., Tan, H., Wang, H., Zhu, Q., Xu, R., Wu, F., Xiao, Y., Xu, C., Li, Q., Su, P., Zhang, L.I., Dong, H.-W., Desimone, R., Xu, Fuqiang, Hu, X., Lau, P.-M., Bi, G.-Q., 2021. High-throughput mapping of a whole rhesus monkey brain at micrometer resolution. Nat. Biotechnol. 39, 1521–1528. https://doi.org/10.1038/s41587-021-00986-5

Yamada, K., Akazawa, K., Yuen, S., Goto, M., Matsushima, S., Takahata, A., Nakagawa, M., Mineura, K., Nishimura, T., 2010. MR Imaging of Ventral Thalamic Nuclei. Am. J. Neuroradiol. 31, 732–735. https://doi.org/10.3174/ajnr.A1870

Yeatman, J.D., Dougherty, R.F., Myall, N.J., Wandell, B.A., Feldman, H.M., 2012. Tract Profiles of White Matter Properties: Automating Fiber-Tract Quantification. PLOS ONE 7, e49790. https://doi.org/10.1371/journal.pone.0049790

Yendiki, A., Aggarwal, M., Axer, M., Howard, A.F.D., van Walsum, A.-M. van C., Haber, S.N., 2022. Post mortem mapping of connectional anatomy for the validation of diffusion MRI. NeuroImage 256, 119146. https://doi.org/10.1016/j.neuroimage.2022.119146

Zeng, R., Lv, J., Wang, H., Zhou, L., Barnett, M., Calamante, F., Wang, C., 2022. FOD-Net: A deep learning method for fiber orientation distribution angular super resolution. Med. Image Anal. 79, 102431. https://doi.org/10.1016/j.media.2022.102431

Zhang, C., Pan, Y., Wang, L., Wang, T., Zhang, J., Zhou, H., Hu, W., Sun, B., Ramirez-Zamora, A., Li, D., 2019. Globus pallidus internus deep brain stimulation improves axial symptoms of Parkinson patients after long-term subthalamic nucleus stimulation: A case series study. Interdiscip. Neurosurg. 18, 100516. https://doi.org/10.1016/j.inat.2019.100516

Zhang, F., Daducci, A., He, Y., Schiavi, S., Seguin, C., Smith, R.E., Yeh, C.-H., Zhao, T., O'Donnell, L.J., 2022. Quantitative mapping of the brain's structural connectivity using diffusion MRI tractography: A review. NeuroImage 249, 118870. https://doi.org/10.1016/j.neuroimage.2021.118870

Zhang, F., Wu, Y., Norton, I., Rigolo, L., Rathi, Y., Makris, N., O'Donnell, L.J., 2018. An anatomically curated fiber clustering white matter atlas for consistent white matter tract parcellation across the lifespan. NeuroImage 179, 429–447. https://doi.org/10.1016/j.neuroimage.2018.06.027

Zheng, H., Qu, X., Bai, Z., Liu, Y., Guo, D., Dong, J., Peng, X., Chen, Z., 2017. Multi-contrast brain magnetic resonance image super-resolution using the local weight similarity. BMC Med. Imaging 17, 6. https://doi.org/10.1186/s12880-016-0176-2

Zhu, S., Huszar, I.N., Cottaar, M., Daubney, G., Eichert, N., Hanayik, T., Khrapitchev, A.A., Mars, R.B., Mollink, J., Sallet, J., Scott, C., Smart, A., Jbabdi, S., Miller, K.L., Howard, A.F.D., 2025. Imaging the structural connectome with hybrid MRI-microscopy tractography. Med. Image Anal. 102, 103498. https://doi.org/10.1016/j.media.2025.103498